A TACTICAL GRADE MEMS ACCELEROMETER

A THESIS SUBMITTED TO
THE GRADUATE SCHOOL OF NATURAL AND APPLIED SCIENCES
OF
MIDDLE EAST TECHNICAL UNIVERSITY

BY

ILKER ENDER OCAK

IN PARTIAL FULFILLMENT OF THE REQUIREMENTS
FOR
THE DEGREE OF DOCTOR OF PHILOSOPHY
IN
ELECTRICAL AND ELECTRONICS ENGINEERING

SEPTEMBER 2010

Approval of the thesis:

A TACTICAL GRADE MEMS ACCELEROMETER

submitted by **İLKER ENDER OCAK** in partial fulfillment of the requirements for the degree of **Doctor of Philosophy in Electrical and Electronics Engineering Department, Middle East Technical University** by,

Prof. Dr. Canan Özgen ____________________
Dean, Graduate School of **Natural and Applied Sciences**

Prof. Dr. İsmet Erkmen ____________________
Head of Department, **Electrical and Electronics Eng.**

Prof. Dr. Tayfun Akın ____________________
Supervisor, **Electrical and Electronics Eng. Dept., METU**

Examining Committee Members

Prof. Dr. Cengiz Beşikçi ____________________
Electrical and Electronics Eng. Dept., METU

Prof. Dr. Tayfun Akın ____________________
Electrical and Electronics Eng. Dept., METU

Assoc. Prof. Dr. Haluk Külah ____________________
Electrical and Electronics Eng. Dept., METU

Assist. Prof. Dr. Yakup Özkazanç ____________________
Electrical and Electronics Eng. Dept., HACETTEPE Ü.

Assist. Prof. Dr. Barış Bayram ____________________
Electrical and Electronics Eng. Dept., METU

Date: 16.09.2010

I hereby declare that all information in this document has been obtained and presented in accordance with academic rules and ethical conduct. I also declare that, as required by these rules and conduct, I have fully cited and referenced all referenced material and results that are not original to this work.

Name, Surname: İlker Ender OCAK

Signature:

ABSTRACT

A TACTICAL GRADE MEMS ACCELEROMETER

Ocak, İlker Ender

Ph. D., Department of Electrical and Electronics Engineering

Supervisor: Prof. Dr. Tayfun Akın

September 2010, 266 pages

Micromachining technologies enabled the use of miniaturized transducers in many high technology sensing systems. These transducers have many advantages like small-size, low-cost and high-reliability. One of the applications micro-machined transducers are used is inertial navigation systems, where the exact position of a moving frame is continuously monitored by tracking the linear and angular motions of the frame. Other than navigation applications, inertial sensors are used in health and military applications as well as consumer electronics. Today accelerometers capable of measuring accelerations from 0.5g-1g range up to several thousand g's are commercially available in the market which have been fabricated using micromachining technologies. The aim of this research is to develop such a state-of-the-art micro-machined accelerometer system, whose performance is expected to reach tactical-grade level.

In order to achieve these performance values a MATLAB algorithm is developed to optimize the accelerometer performances in the desired levels. Expected performance parameters of the designed accelerometer structures are extracted from the simulations done by both Coventorware finite element modeling tool and MATLAB. Designed structures are then fabricated with silicon-on-glass, dissolved wafer and dissolved epitaxial wafer processes. These fabrication results are compared and it is observed that highest yield accelerometers are fabricated with the SOG process. But these accelerometers could not be able to satisfy tactical grade performance parameters. Best performances are obtained with DWP, but due to high internal stress, yield of the sensors were very low. DEWP increased the yield of this process from 2-3% to 45-50% but the expected operation range of the designs dropped to ±12.5g range. Using the fabricated accelerometers in DEWP a three axial accelerometer package is prepared and tests results proved that this three axial accelerometer system was satisfying the tactical grade requirements. In addition to these a three axial monolithic accelerometer fabrication technique is proposed and sensors are designed which are suitable for this process.

Best performances achieved with single axis accelerometers were 153µg/√Hz noise floor, 50µg bias drift, 0.38% non-linearity and a maximum operation range of 33.5g which has the higher dynamic range among its counterparts in the literature. Performance results achieved with the three axes accelerometer were ~150µg bias drift, <200µg/√Hz noise density, ~0.4% non-linearity with higher than ±10g operation range.

ÖZ

TAKTİK SEVİYE MEMS İVMEÖLÇER

Ocak, İlker Ender

Doktora, Elektrik ve Elektronik Mühendisliği Bölümü

Tez Yöneticisi: Prof. Dr. Tayfun Akın

Eylül 2010, 266 sayfa

Mikro işleme teknolojilerinin gelişimi minyatür duyargaların yüksek teknoloji ürünü sistemlerde kullanımını olası hale getirmiştir. Bu tip duyargaların küçük boyut, düşük fiyat ve yüksek güvenilirlik gibi birçok avantajı bulunmaktadır. Mikro işlenmiş algılayıcıların kullanıldığı alanlardan birisi doğrusal ve açısal hareketler sergileyen bir nesnenin tam pozisyonunun ivmeölçer ve dönüölçerler vasıtasıyla izlenmesini öngören ataletsel seyrüsefer uygulamalarıdır. Seyrüsefer uygulamaları dışında ataletsel duyargalar, askeri, sağlık ve tüketici uygulamaları alanlarında da kullanılmaktadır. Günümüzde mikro işleme teknolojileri ile üretilmiş 0,5-1g ivme seviyelerinden birkaç bin ivme seviyelerine kadar ölçüm yapabilen ivmeölçerler piyasada ticari olarak bulunabilmektedirler. Bu çalışmanın amacı da teknolojide ki en son gelişmelere paralel olarak, mikro işleme teknikleri ile geliştirilmiş, taktik seviye bir ivmeölçer sistemi oluşturmaktır.

Bu performans değerlerine ulaşabilmek için, ivmeölçer performansını istenen seviye aralığında optimize edecek bir MATLAB algoritması geliştirilmiştir. Tasarlanan ivmeölçerlerin beklenen performans değerleri de COVENTORWARE sonlu eleman modelleme aracı ve MATLAB tarafından çıkarılmıştır. Tasarlanan yapılar daha sonra cam-üstü-silikon, çözülmüş pul işleme ve çözülmüş epitaksiyel pul işleme süreçleri ile üretilmiştir. Bu üretim sonuçları karşılaştırılmış ve en yüksek verimliliğin cam-üstü-silikon üretim süreci ile elde edildiği gözlemlenmiştir. Fakat bu süreç il üretilen ivmeölçerler taktik seviye performans parametrelerini sağlayamamaktadır. En iyi performans değerleri ise çözülmüş pul işleme süreci ile elde edilmiştir, fakat yapısal katmaları içerisinde bulunan gerilim sebebiyle bu üretim sürecinin verimliliği çok düşük olmuştur. Çözülmüş epitaksiyel pul süreci üretim verimini 2-3% seviyelerinden, 45-50% seviyelerine çıkarmıştır, fakat beklenen çalışma aralığı değeri ±12.5g seviyesine gerilemiştir. Bu üretimden çıkan ivmeölçerler kullanılarak üç eksenli bir ivmeölçer paketi hazırlanmış ve yapılan testler ile performansının taktik seviye isterleri karşıladığı gösterilmiştir. Bunların yanında üç eksenli aynı tabanda üretilebilen bir ivmeölçer üretim teknolojisi de önerilmiş ve bu teknolojiye uygun duyarga tasarımları yapılmıştır.

Tek eksende üretilen ivmeölçerler ile elde edilen en iyi performans değerleri 153µg/√Hz gürültü yoğunluğu, 50µg sabit kayma kararsızlığı, 0.38% doğrusallıktan sapma oranı ve ±33.5g çalışma aralığıdır ki, literatürde yer alan benzerlerinden daha yüksek bir dinamik ölçüm aralığı değerine sahiptir. 3 eksenli ivmeölçer paketi ile elde edilen performans değerleri ise ~150µg sabit kayma kararsızlığı, <200µg/√Hz gürültü yoğunluğu, ~0,4% doğrusallıktan sapma oranı ve ±10g'den büyük çalışma aralığıdır.

To the Memory of My Grandmothers

Bedia Koyuncu and Raife Ocak

ACKNOWLEDGEMENTS

First and foremost, I would like to thank my supervisor, Prof. Dr. Tayfun Akın for the valuable guidance and advices through my PhD. study. He inspired me greatly and his willingness to motivate contributed tremendously to this thesis.

I also would like to thank, Assoc. Prof. Haluk Külah for encouraging and motivating me during my studies, Dr. Said Emre Alper for helping me understanding the basics of mechanical sensors and sharing his ideas on micro fabrication technologies and Orhan Ş. Akar for his great support and unequalled contributions to my processes.

I am indebted to my many colleagues who helped me during my studies even in the most hopeless times and I am especially grateful to Mehmet Akif Erişmiş, Reha Kepenek, Serdar Tez, Uğur Sönmez, and Osman Aydın for their contributions on accelerometer studies and I also would like to thank Kanber Mithat Silay, Kıvanç Azgın, Korhan Şahin, Yüksel Temiz, Emre Şahin, Burak Eminoğlu, Erdinç Tatar, and Mert Torunbalcı for their invaluable helps during my studies on inertial sensors.

I also would like to thank my friends Dr. Erkan Alpman and Dr. Kemal Şafak Demirci whom I started this road together, for their never ending friendship. I would like to thank my collegues Dr. Yusuf Tanrıkulu, Dr. Murat Tepegöz, Dr. Kağan Topalli, Dr. Mehmet Ünlü, Dr. Özge Zorlu, İpek İstanbulluoğlu Turhan, Ömer Özgür Yıldırım, Fehmi Çivitci, Halil İbrahim Atasoy, Batuhan Dayanık, Alperen Toprak, Kerem Kapucu, Emre Kültürsay, Ufuk Şenveli, Alp Oğuz, İlker Comart, Başak Kebapçı, Dinçay Akçören, Şeniz Esra Küçük, Ercihan İncetürkmen, Ömer Bayraktar, Ufuk Temoçin, Ekrem Bayraktar, Gürkan Yılmaz and Cavid Musayev for providing a stimulating and fun environment. The times we spent together were invaluable and the memories will never be forgotten.

I would like to thank TÜBİTAK for supporting this PhD. Thesis with the scholarship they provided.

I offer my special thanks to Melike Özer who was always supporting me with her care and friendship during my studies.

And finally, I owe my deepest gratitude to my father M. Ragıp Ocak, to my mother A. Ayşın Ocak, to my dear brother R. Soner Ocak, to my grandfathers Hulusi Koyuncu and Ekrem Ocak and to my grandmothers Bedia Koyuncu and Raife Ocak for raising me as the person I currently am and never withholding their love and support.

TABLE OF CONTENTS

LIST OF FIGURES

FIGURES

LIST OF TABLES

TABLES

CHAPTER 1

INTRODUCTION

In the dark ages, people used various primitive methods like the length of shadow, direction of the polar star or behavior of other animals in order to find their directions. In the modern world with the improving technology, humans can find their way with far more advanced techniques. Today with the satellites orbiting around the earth, position of any object can be determined with perfect accuracy. In addition to orbiting satellites, various sensors like accelerometers and gyroscopes are also integrated to modern time devices. With the invention of the MEMS technology, these sensors are decreased in size such that the position tracking devices can now be carried in pockets.

Studies on micro electro mechanical sensors started in early 1950's by companies Kulite, Microsystems and Honeywell with the knowledge based from Bell Laboratories. These companies are considered as discoverers of first MEMS pressure sensors. After the discovery of the sensors, in 1960's commercialization sped up and some important electric companies of that era like General Electric's, Fairchild, Westinghouse and Endevco also started to work in micro electro mechanical sensor fabrication business.

With the growing demand, market for micro sensors expanded incredibly in 1970's. In this period main concern was to decrease the fabrication costs and expand the application areas of MEMS sensors. Many known and new companies like IBM, IC Transducers, National Semiconductors, GM Delco, Texas Instruments, and Motorola started to share this expanding market. In this era several universities also started in depth research on micro sensors. J. Angell and J. Meindl et al. started the first studies of MEMS sensors in Stanford University towards the end of 1970’s.

In 1980’s, Steven Senturia et al. in M.I.T, R. Muller and R. White et al. in U.C. Berkeley, W. Ko in Case-Western Reserve, and K.D. Wise in University of Michigan was the frontier researchers in their universities in MEMS sensors and these names are known as the pioneers of the MEMS technology of today. New micromachining techniques are developed during the studies in this period and sensor variety increased considerably. Many old and new companies joined to work on MEMS technology in order to have their share from the market. Figure 1.1 shows the historical genealogy of MEMS sensors and actuators between 1954 -1990 [1].

After 1990’s improvement of accelerometers and other MEMS sensors are accelerated. More companies entered the MEMS fabrication market some of which are ST Microelectronics, Analog Devices, Bosch, Sensortec, Citizen, Freescale, Fujitsu, Fuji Electric, Fuji, Hitachi Metals, Hokuriku Denko, HSG-IMIT, Infineon, Invensense, Kionix, Micro Infinity, Mitsubishi, Murata, Samsung, and SONY. Today the size of the MEMS market reaches over 6 Billion’s dollar per year and it is projected to grow over 8 Billion’s dollar in 3 years after the market decline about 15% in 2008 and 2009. Figure 1.2 shows the distribution of MEMS market by application between 2006 -2013 [2]. The variety of the products also expanded greatly and MEMS sensors having various functions are currently serving the needs for customers for different applications. Figure 1.3 shows the distribution of MEMS market by devices between 2006 -2013 [2]. It can be seen from this figure that accelerometers share a big portion of the market together with pressure sensors and inkjet print heads in today’s MEMS technology.

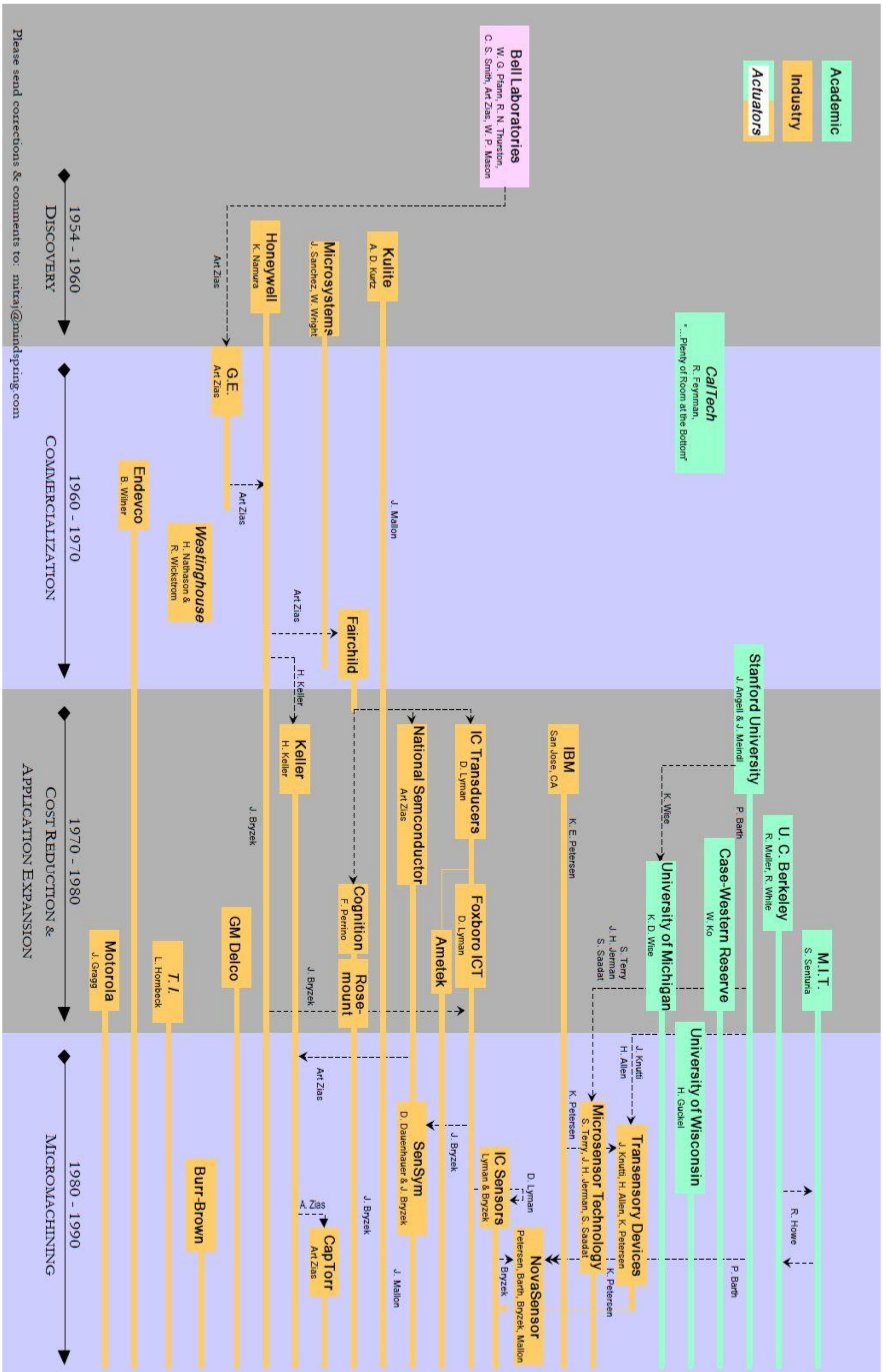

Figure 1.1: Historical genealogy of MEMS sensors and actuators in 1954-1990 [1].

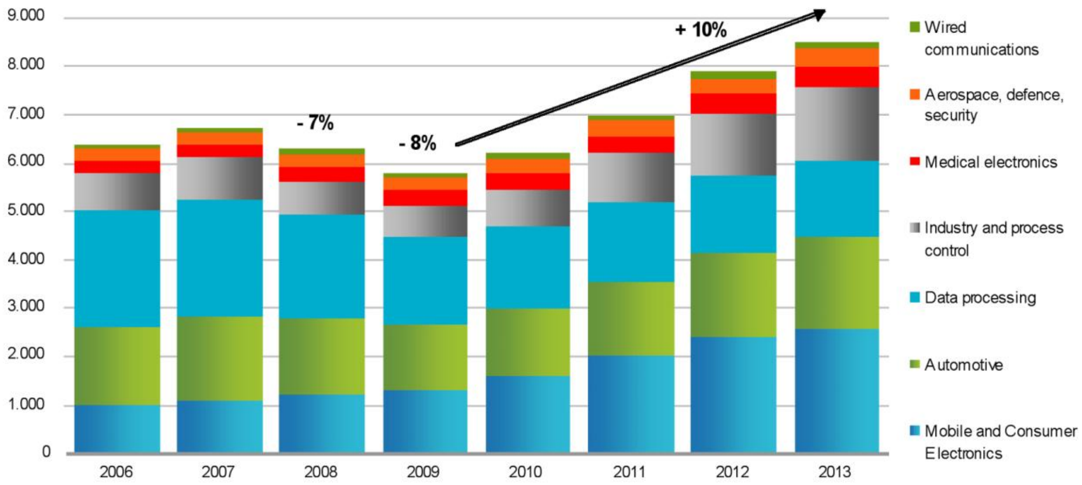

Figure 1.2: Distribution of MEMS market by application in 2006-2013 [2].

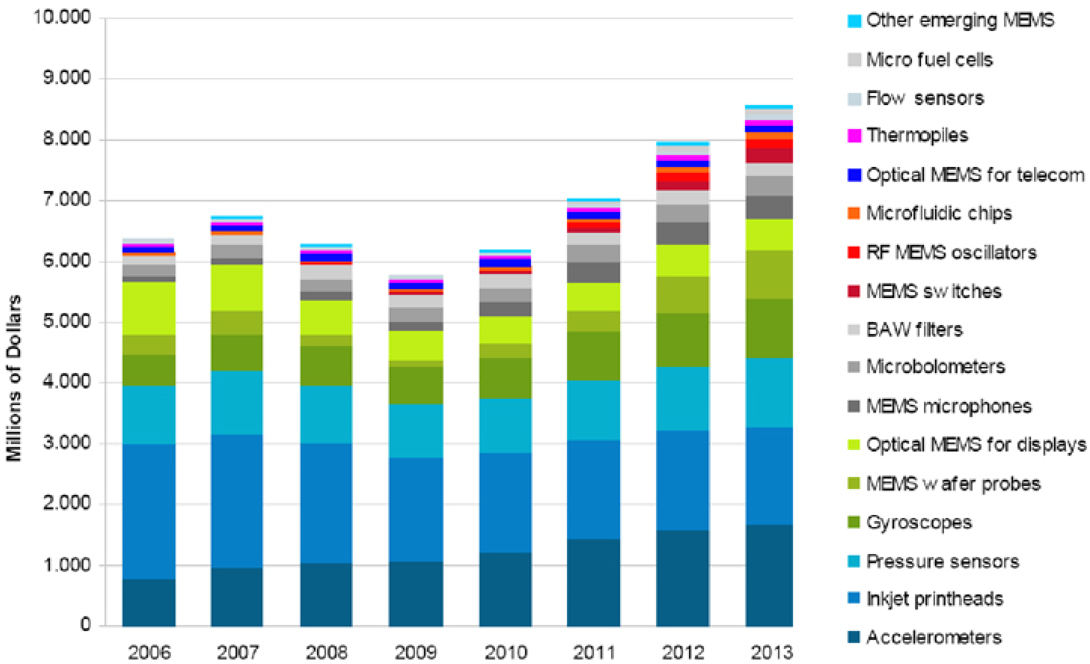

Figure 1.3: Distribution of MEMS market by devices in 2006-2013 [2].

1.1 Application Areas of Microaccelerometers

Tracking the position of an object is an important engineering problem in modern world. Micromachined inertial sensors have been the subject of intensive research for over four decades to solve the need for tracking the movements of various objects. Today micromachined inertial sensors find many application areas in which the cost of these sensors is a little concern, such as military and aerospace systems.

Mass production of precision inertial sensors at very low costs created an opportunity to use these sensors in automotive industry for safety systems such as airbag release, seat belts control, active suspension and traction control. Latest improvements created many application areas for these sensors like anti-jitter platform stabilization for video-cameras, virtual reality applications with head mounted displays and data gloves, GPS back-up systems, shock monitoring during the shipment of sensitive goods, novel computer input devices, electronic toys and many others [3] - [5].

Performance requirements of accelerometers vary for different applications. These sensors are typically specified by their sensitivity, maximum operation range, frequency response, resolution, full-scale nonlinearity, offset, off-axis sensitivity, and shock survivability. Since micromachined accelerometers are used in a wide range of applications, their required specifications are also application dependent and cover a rather broad spectrum. For instance, for microgravity measurements devices with a range of operation greater than 0.1 g, a resolution of less than 1μg in a frequency range of zero frequency to 1 Hz are desired, while in ballistic and impact sensing applications, a range of over 10 000 g with a resolution of less than 1 g in a 50 kHz bandwidth is required.

Industrial applications require inertial sensors for testing and conditioning purposes. As an example, accelerometers are put into computer hard drives for detecting the external shocks. Due to the fact that high shock values may cause damage to the read/write head of the device, the accelerometer may suspend the operation of the drive when there is an excessive external shock [6] - [8]. The performance of the accelerometers used for this kind of applications is not as critical as those used for military applications, but the cost of the sensors should be reasonably low.

The medical applications use inertial sensors and IMUs for monitoring the physical body activities such as absolute position of the leg segments or heart monitoring [6], [9], [10]. Again in this area, the performance of the sensors is not as critical as those used for military applications, but power consumption and small volume are more important.

The consumer applications include the automotive applications, entertainment applications, and consumer navigation applications. These applications need low-cost IMUs with relatively low performance to detect the position of an object [6]. In all these applications, small sensor volume is the key factor which can be satisfied by using micromachined inertial sensors

Therefore, micromachined inertial sensors are highly preferred in all the applications listed in this section for their low cost, low power consumption, and high reliability as well as satisfactory performance.

Table 1.1 summarizes typical performance parameters of accelerometers with medium resolution for automotive applications and high performance for inertial navigation applications [4]. Figure 1.4 shows the acceleration-bandwidth performance requirements of different application areas for accelerometers [3].

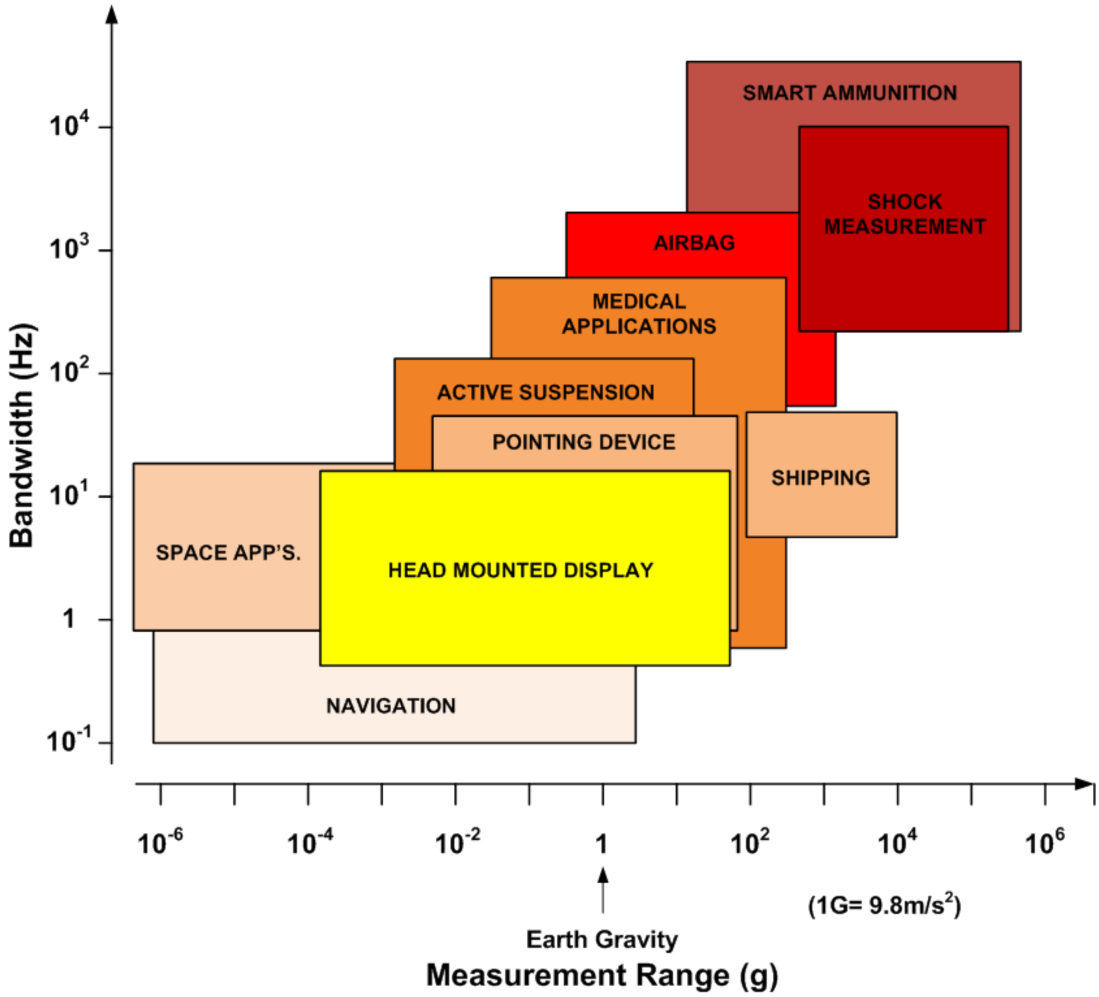

Figure 1.4: Acceleration-bandwidth performance requirements of different application areas for accelerometers [3].

Table 1.1: Typical specifications of accelerometers for automotive and inertial navigation applications [4].

Parameter	Automotive	Navigation
Range	±50g(airbag) ±2g (vehicle stability system)	±1g
Frequency Range	DC-400Hz	DC-100Hz
Resolution	<100mg (airbag) <10mg (vehicle stability system)	<4μg
Off-axis Sensitivity	<5%	<0.1%
Nonlinearity	<2%	<0.1%
Max. Shock in 1msec	>2000g	>10g
Temperature Range	-40^{o}C to 85^{o}C	-40^{o}C to 85^{o}C
TC of Offset	<60mg/^{o}C	<50μg/^{o}C
TC of Sensitivity	900ppm/^{o}C	±50ppm/^{o}C

1.2 Classification of MEMS Accelerometers

MEMS accelerometers can be mainly classified into eight groups according to their sensing mechanisms:

1. Capacitive
2. Optical
3. Piezoresistive
4. Piezoelectric
5. Thermal
6. Tunneling current
7. Resonant
8. Magnetic

In capacitive accelerometers, when an external acceleration is applied suspended proof mass of the system moves in the reverse direction with the proof mass. Proof mass displacement is detected with the change in the capacitance between the capacitive fingers placed on each side of the sensors.

Optical inertial sensors are rather difficult to fabricate but show high performances. The major advantages for optical inertial sensors are that they are immune to electromagnetic interference and they can operate at high temperatures. They show high performances but fabrication of light emitting and sensing components using micromachining techniques is not easy [11].

Piezoresistive sensing scheme is widely used in accelerometers. Sensors using piezoresistive materials are easy to fabricate and they have simple readout circuitries. However, their sensitivity is low, and their temperature dependency is high compared to capacitive sensors [4]. Therefore, they are not preferred for high performance applications.

The operation of piezoelectric sensors requires an external stress similar to the piezoresistive sensors. The sensitive material stores a charge on itself proportional to this external stress. Charge storage capability of the piezoelectric sensors makes them active devices, theoretically providing them to generate their own power and provides low power sensor design. In addition to this, the fabrication of piezoelectric sensors is as easy as piozoresistive sensors enabling low cost sensor realization. However, the main disadvantage of the piezoelectric sensors is that they do not have a DC response due to the fact that the charge stored on the piezoelectric material leaks away under a constant stress. Therefore, low frequency operation is not possible. This fact makes it difficult to realize piezoelectric accelerometers since accelerometers are generally used to sense low frequency accelerations [12].

In thermal accelerometers proof mass of the accelerometer is a hot air bubble which is placed between two electrodes. When there is not any input acceleration, temperature difference between the electrodes is fixed. However, when an external acceleration is applied, hot air bubble moves and the temperature difference changes between the electrodes. Hence, the acceleration is converted to the temperature difference. This temperature difference is sensed and acceleration is detected [13].

Another type of accelerometer is resonant type accelerometer which directly finds the applied force to the proof mass. Proof mass of the sensor is vibrated at its natural resonance frequency and the inertial force caused by external acceleration changes the resonance frequency of the system. By finding the shift in the resonance frequency, magnitude of the acceleration can be extracted [14].

Tunneling type accelerometers have a very low noise, wide bandwidth, and are highly sensitive. This type of accelerometers use tunneling current that occurs between two conductive layers located very close to each other. The distance between these electrodes should be about 10 Å to create a tunneling current. When there is an external acceleration, one of the conductive layers moves and the tunneling current is changed [15]. With this type of accelerometers very low noise levels could be achieved, but high drift values, fabrication complexity, and high cost prevent tunneling accelerometers to be widely used in the industry.

In summary, there are a number of approaches to implement accelerometers, but the widely used one is the capacitive approach, as it is suitable for MEMS fabrication techniques. Capacitive sensors have important advantages compared to other types of inertial sensors. They have simple structure and hence low fabrication cost. In addition, they provide low power consumption, high sensitivity, and high reliability as well as low nonlinearity, low temperature dependency, low noise, and low drift. Capacitive sensors are widely preferred in consumer application due to their high performance, reliability, and low cost. Capacitive interfaces have several attractive features. In most micromachining technologies no or minimal additional processing is needed. Capacitors operate both as sensors and actuators. Excellent sensitivity has been demonstrated, and the transduction mechanism is intrinsically insensitive to temperature [16].

1.3 History of MEMS Capacitive Accelerometers

The improvement of MEMS accelerometers started back in early 1980's. With the research done in several universities like Stanford, Berkeley, Caltech, and Michigan, knowledge about the MEMS accelerometers flourished and first publications are issued in this period. In 1983 F. Rudolf published the first known capacitive micro accelerometer paper which was about a capacitive accelerometer plate suspended by two springs and behaves like both an electrode and a proof mass at the same time [17]. After the first reported capacitive accelerometers, first closed loop readout circuit for capacitive accelerometers is reported by M. Van Paemel in 1989 [18]. In his study he showed that closed loop configuration has two advantages for accelerometer systems which are adjustable operation range and expandable operation bandwidth. In 1990 H. Seidel et al. designed, fabricated and tested a highly symmetrical differential accelerometer which can operate in ±5g range and has a minimum resolvable acceleration value of 1mg [19]. In that same year, F. Rudolf et al. made another publication which is about a high precision accelerometer with μg resolution. This accelerometer was for spacecraft applications which is able to measure in ±0.1g range and has a resolution of less than 1μg in 1Hz bandwidth [20]. In 1991, E. Peeters et al. showed that high pressure while sealing accelerometers after fabrication is better for low non-linearity, which increases the damping and stability of the device. They also showed that Helium is preferred over air or nitrogen as the sealing atmosphere because of its higher ionization energy and lower molecular weight which allows higher pressures for a given damping. This accelerometer showed 80dB dynamic range with in ±50g measurement range [21]. In 1992, W. Yun and R.T. Howe designed a monolithic accelerometer with a closed loop, Σ-Δ modulated force feedback control loop. Although the performance of the system is not presented in the publication, it was stated that a high dynamic range can be achieved with Σ-Δ modulated force feedback control loop architecture [22]. In 1994, E. Abbaspour-Sani et al. fabricated a novel electromagnetic accelerometer. This accelerometer was using coil like windings on both side of suspended structures and with the applied acceleration induction of current on one side increases with decreasing plate spacing. Although they were able to measure high operation ranges like ±50g, resolution of the system was bad and in order to have higher dynamic range, windings should be increased on each side which increases the complexity of the process [23].

Later in 1995 first SOI capacitive accelerometer which has a swastika shaped spring architecture and 10μm structural thickness, which is able to detect accelerations in z-direction, is reported by Y. Matsumoto et al. [24]. Same year two other groups developed and published monolithic surface micromachined accelerometer chips with force-feedback operation. First group, K.H.–L. Chau et al., developed an accelerometer system for low g applications [25]. Accelerometer had a ±5g measurement range and 600μg/√Hz noise floor. Other group, B. Wenk et al., designed and tested their accelerometer system in ±100g acceleration range and had a 100mg resolution with less than 1% non-linearity [26].

In 1996, M. E. Lemkin and B. E. Boser developed a surface micromachined fully differential capacitive accelerometer. With careful design and detailed analysis, this accelerometer achieved a noise floor of 500μg/√Hz, but the measurement range was limited with ±3.5g [27].

In 1997, B.P. van Drieënhuizen et al fabricated an accelerometer with fusion bonding and DRIE processes. Structures in this study are defined by DRIE process after thinning the silicon wafers up to 20-200μm structural thicknesses. A second order sigma-delta closed loop readout architecture is used together with the mechanical sensor. Unfortunately 35mg resolution can be achieved for a 5g full scale range which has a poor 44 dB dynamic range [28]. N. Yazdi and K. Najafi, in that same year, developed an accelerometer structure to achieve μg resolutions. In this study, they assumed the main noise component of an accelerometer system as the mechanical noise and they try to decrease it my increasing mass and decreasing damping of the accelerometer. They also used trench refill technique in order to stiffen the top and bottom electrodes. Figure 1.5 shows the mechanical structure and SEM pictures of the vertical axis accelerometer fabricated in this study. Although their aim was to achieve high resolution structures, they were unable to present any performance results in their studies [29]. B.P. Van Drieënhuizen and N.I. Maluf published a paper on a high resolution single crystal silicon accelerometer using silicon fusion bonding and deep reactive ion etching. Their aim was to fabricate CMOS compatible, low cost, high resolution accelerometers. But the noise floor of the fabricated accelerometer which has a full scale range of ±2g is reported as 80μg/√Hz which was 13 times larger than the estimated mechanical noise of the system [30]. B. Ha et al. reported an area variable capacitive accelerometer with separate force rebalancing electrodes. In this structure sense electrodes are placed beneath the moving mass and the acceleration is detected by changing capacitive area of the electrodes. Since the feedback electrodes also have variable capacitive type architecture continuous feedback voltage is applied to the proof mass of the accelerometer. The performance of this accelerometer is measured as 274μg/√Hz with in ±9g full scale operation range [31].

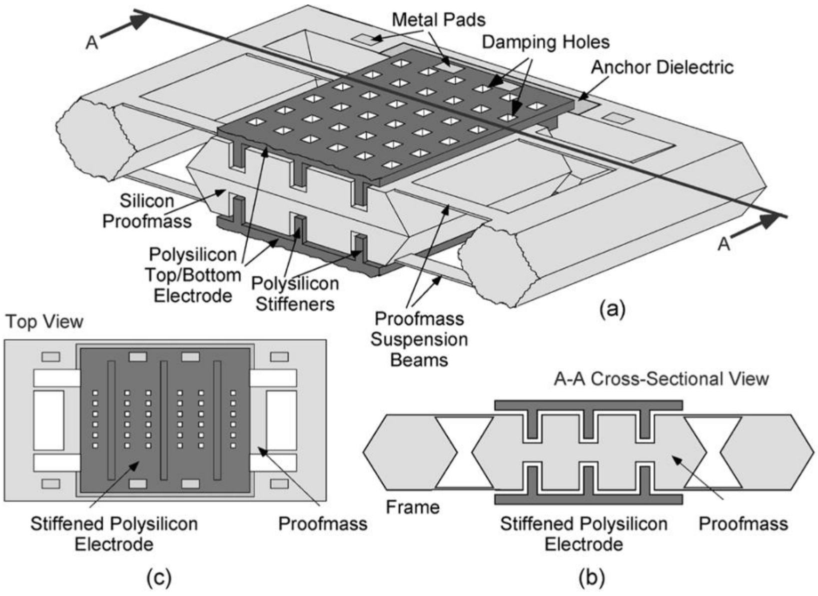

Figure 1.5: Fabricated mechanical structure and SEM pictures of the vertical axis accelerometer [29].

G. Zhang et al. worked on a monolithic lateral capacitive accelerometer with closed loop sigma-delta readout architecture in 1999. Their aim was to solve the inherent buckling problem of sensors after post CMOS processing. Instead of canceling the internal stress or placing some electrodes to pull the structure on the opposite direction of the buckling, they designed such a structure that after buckling fingers became parallel and completely overlapping. Tests performed after the fabrication showed that rest capacitance lost is still 67.5% and measured noise floor is 500μg/√Hz which is ~1.5 times the expected capacitance value. The full scale operation range of the accelerometer was not reported in the publication [32]. Same year N. Yazdi, A. Salian and K. Najafi published a paper to prove that sub-μg resolution can be obtained without vacuum packaging. For this purpose they proposed new sensor architecture with a fixed electrode, a movable electrode and proof mass. This way they could increase the mass of the structure further and decreased the mechanical noise to 0.18μg/√Hz theoretical level without decreasing the damping of the structure. But they were unable to report any test results about the noise level they could reach with a readout circuit [33].

In 2000, H. Xie and G. Fedder reported a z-axis accelerometer which is able to measure with comb finger type capacitive sensing architecture. The device is designed to achieve ±600g linear measurement range with 0.6μg/√Hz noise floor. But the usual problem with the monolithic accelerometers with post CMOS fabrication is also observed in this publication and due to huge stress in the sensor devices buckle greatly and could only achieve ±27g with 6mg/√Hz noise floor [34]. H. Luo, G.K. Fedder and R.L. Carley have another publication same year on lateral CMOS MEMS accelerometer. Design of the sensor, force-feedback architecture and experimental test results are described in detail and sensor achieved ±13g operation range with 1mg/√Hz noise floor [35]. A. Salian et al. reported a hybrid silicon micro accelerometer system with CMOS interface circuit. Sensor used in this paper was previously published in [15]. With the new readout circuit which can both used in closed and open loop modes, system demonstrated 20μg/√Hz noise floor with in ±1.2 g range with 5V supply [36].

In 2001, H. Goldberg et al. reported an extremely low noise accelerometer with custom ASIC circuitry. A closed loop 5th order sigma delta readout circuit is used as the output stage of the accelerometer system. This accelerometer was specifically designed to measure seismic recordings and has a full scale measurement range of ±0.2g with 30ng/√Hz noise floor [37]. S. Wei et al. worked on a large operation range accelerometer system and designed a sensing system which is able to operate in ±60g range. In their publication, noise floor of the system was measured as 3mg/√Hz, drift was less than 10mg and short term drift was as low as 3mg [38].

In 2002, R. Toda et al. worked on a novel spherical 3 axis accelerometer in Japan. Sensors are fabricated with totally noval spherical silicon micro machining techniques [39] and spherical mass of the sensor levitates in the air during the operation of the accelerometer. Figure 1.6 shows the cross sectional view of the accelerometer. Test results indicate that the noise level of the accelerometer is measured as 40μg/√Hz with in ±2g measurement range and has a very high linearity [40].

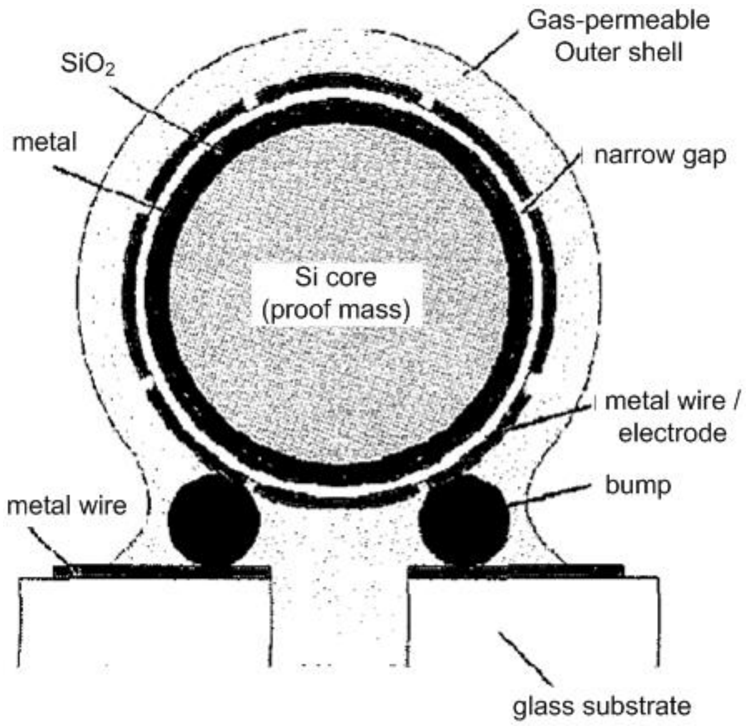

Figure 1.6: Cross-sectional view of the spherical accelerometer

In 2003, Ki-Ho Han and Young-Ho Cho reported a navigation grade accelerometer system with novel branched finger electrode architecture. In their study effects of varying voltage and pressure on accelerometer are observed. Figure 1.7 shows the novel branched finger electrode architecture. Tests showed that the micro accelerometer system developed by the authors demonstrated 5.5±0.72μg/√Hz noise floor with in ±2g operation range [41].

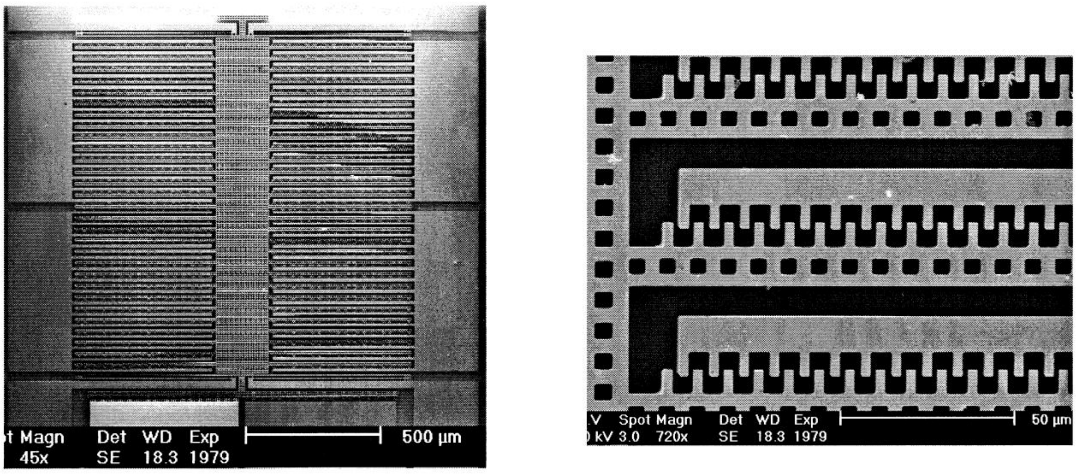

(a) (b)

Figure 1.7: Novel branched finger electrode architecture [41].

Same year H. Külah and J. Chae worked on novel accelerometer and readout architectures. In two different publications mechanical and electrical components are explained in detail. During the fabrication of the accelerometer both bulk and surface micromachining techniques are employed and huge proof mass of the accelerometer fabricated with anisotropic bulk micromachining is suspended to anchors with poly silicon spring structures. Figure 1.8 shows top and cross sectional views of the mechanical structure fabricated in University of Michigan [42]. In order to detect acceleration a multistage second order sigma delta readout circuit is used. In the first stage of the architecture coarse acceleration measurement is done and the output pulse signal is processed and converted to analog and fed into second stage after multiplying with a proper gain. Second stage is used as the fine acceleration measurement. Both stages use different accelerometers which means two identical accelerometers are required for a single system to operate. Test results showed that in ±1.35g full scale range with 5V supply, the readout circuit can resolve 1.5μg/√Hz open loop noise. Unfortunately closed loop noise performance was not presented in the paper [43]. B.V. Amini et al. reported an SOI capacitive accelerometer with 40μm structural thickness and is fabricated with a simple backside dry release process. The interface IC was fabricated at National Semiconductors 0.25μm process and is able to operate at 1MHz clock frequency. Tests of this study presented 110μg/√Hz noise floor with in ±2g range [44].

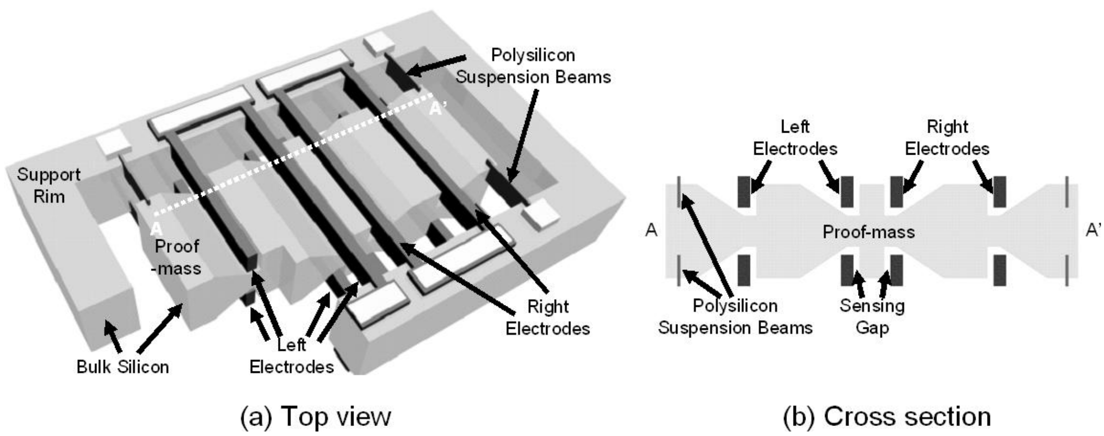

Figure 1.8: Top and cross sectional views of the mechanical structure fabricated in University of Michigan [42].

In 2004, J. Wu, G.K. Fedder and L.R. Carley made a publication on a low noise, low offset capacitive sensing amplifier for monolithic CMOS MEMS accelerometer. Chopper stabilization, AC offset calibration and DC offset cancelation techniques are used during the design of this novel readout architecture. A prototype accelerometer designed to test with this circuit achieved 50μg/√Hz noise floor with in ±6g operation range [45]. Unlike the readout architectures using reference capacitors to match the capacitors on sensors, B.V. Amini proposed a new method to divide accelerometer electrodes on each side and use the resulting four capacitors on the sensor to construct the full bridge structure. By this way, proof mass voltage does not need to be switched and can be a fixed voltage which reduces the charge injection noise, and removes the need to place exact same external capacitances in order to match the sensor capacitances. With this new architecture, they were able to measure in ±2g full scale range with 4.4μg/√Hz noise floor [46]. T. Tsuchiya and H. Funabashi reported a z-axis differential capacitive SOI accelerometer. Difference of this accelerometer from its counterparts in literature is that it employs vertical comb electrodes in order to detect acceleration differentially. They invented a new fabrication technique employing two layer masking of epitaxial layer of the SOI wafer and with time controlled two step deep reactive ion etching. Figure 1.9 shows the technique to fabricate z-axis SOI accelerometer with vertical comb electrodes. Although this structure is novel and makes it possible to fabricate three axes accelerometers on the same substrate, achieved sensitivity value is 1.3fF/g which makes it impossible to measure high ranges [47].

In 2005, J. Chae, H. Külah and K. Najafi published a monolithic three axes micro-g micromachined silicon capacitive micro accelerometer. They joined the previously fabricated lateral and vertical axes accelerometers with poly silicon connectors [29], [42] in order to achieve a three axes micro accelerometer structure. Figure 1.9 shows the joined three axes monolithic accelerometer structure. The reported noise floors for lateral accelerometers were 1.6μg/√Hz and for vertical accelerometer 1.08μg/√Hz in ~±1g measurement range [48]. Same group, same year published another article about a CMOS-compatible high aspect ratio silicon-on-glass in-plane micro-accelerometer. These sensors are fabricated on 120μm thick silicon substrate with 3.4μm finger spacing. After fabrication, 2nd order $\Sigma - \Delta$ readout circuit is connected with SOG accelerometer on a glass substrate. Figure 1.11 shows the technique to interconnect SOG accelerometer to its readout circuit using the metal pads on a glass substrate. Performance of the system is tested with readout circuit and noise level is found as 79.1μg/√Hz in ±1g operation range while the expected noise level was 14.6μg/√Hz [49]. Reason of this discrepancy is not given in the aforementioned publication.

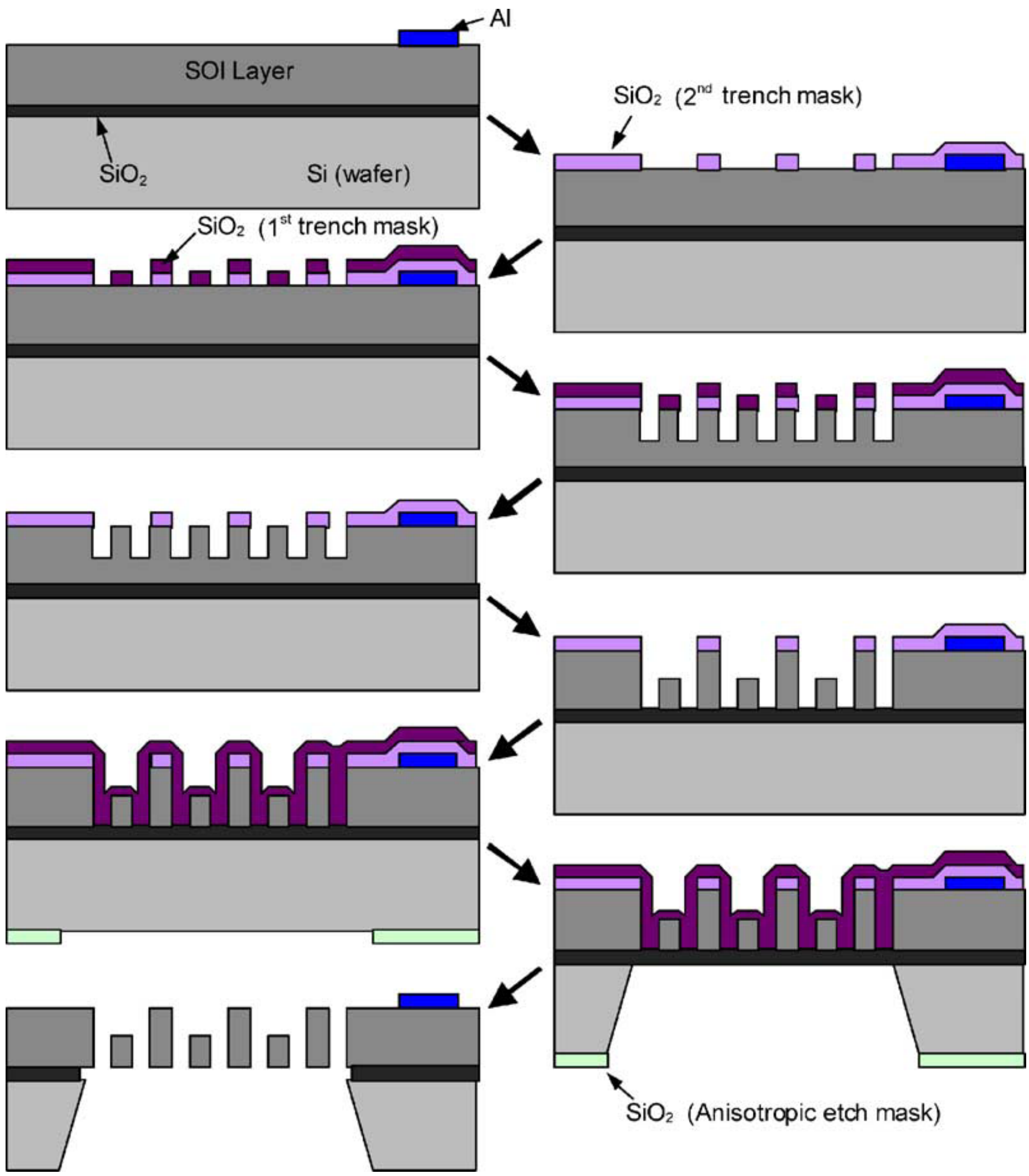

Figure 1.9: Technique to fabricate z-axis SOI accelerometer with vertical comb electrodes [47].

Other than the performance improvement studies in 2005, many novel structures are also reported. H. Rödjegard et al. issued a novel study about an SOI monolithic accelerometer able to measure in three axes. Unlike conventional accelerometers this accelerometer utilizes 4 suspended structures placed orthogonally instead of a mass and fingers. These structures are designed such that when acceleration is applied in x-, y- or z- direction, capacitance on accelerometer changes differentially in the indicated directions. Figure 1.11 shows the mechanical structure of novel three axis monolithic accelerometer and Figure 1.12 shows the technique to fabricate this novel three axis SOI accelerometer structure. Although structure is very unique and resemble none of the accelerometers previously reported, test results showed that the sensitivity results are very low. Sensitivity values are measured as 1.51fF/g which is not enough for high measurement range operation [50].

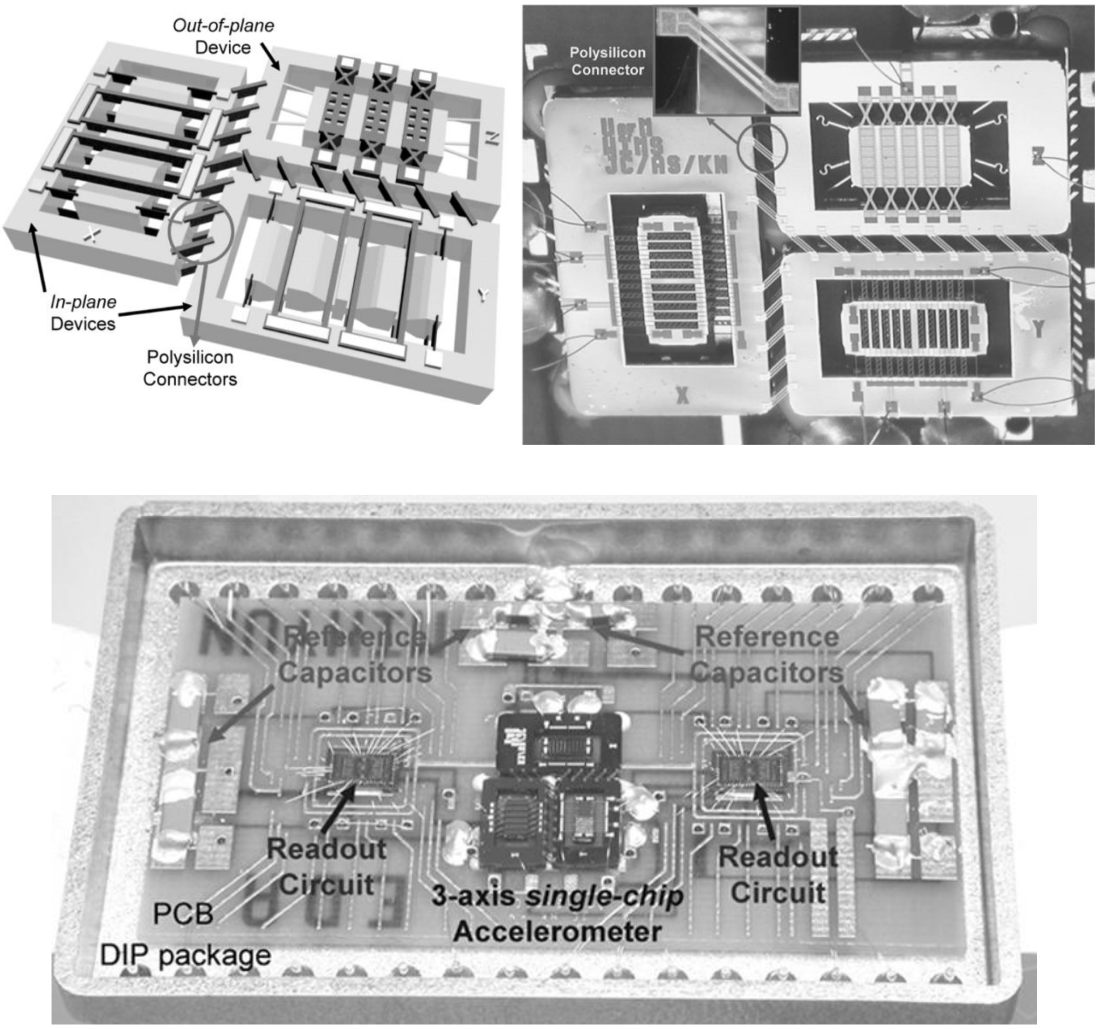

Figure 1.10: Joined three axes monolithic accelerometer structure and SEM pictures fabricated in University of Michigan [48].

H. Ko et al. reported a two chip implemented, wafer level hermetic packaged, tactical and inertial grade accelerometer. Accelerometer is fabricated using sacrificial bulk micro machining process. Accelerometers are than hermetically packaged at wafer level using glass-silicon anodic bonding. This sensor is than connected to open-loop readout circuit which can be trimmed with EEPROM, therefore die to die variation originating from fabrication is canceled this way.

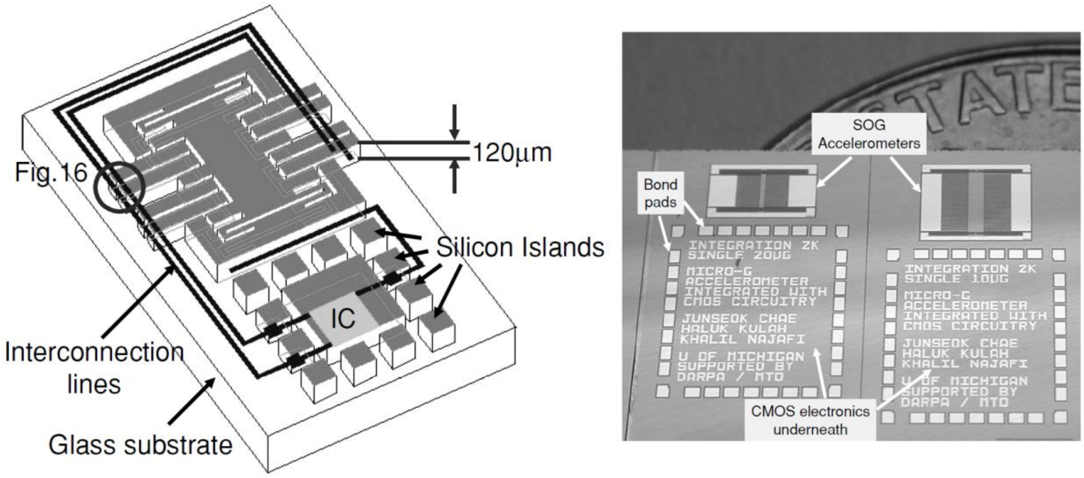

Figure 1.11: Technique to interconnect SOG accelerometer to its readout circuit using the metal pads on a glass substrate [49].

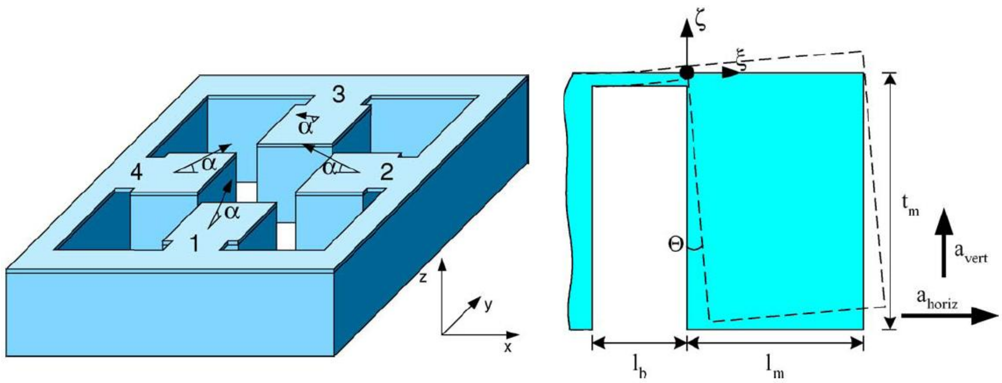

Figure 1.12: Mechanical structure of novel three axis monolithic SOI accelerometer

Normally capacitive accelerometers with varying gap fingers are non-linear if open loop readout architecture is employed. In order to overcome this problem varying overlap area is used as the sensing mechanism of this accelerometer. Test results indicated 1.92µg/√Hz noise floor in 500Hz bandwidth with ±10g operation range and 0.1% non-linearity in this range [51]. Another structure, a novel z-axis accelerometer is also reported by C. Weiping et al. Z-axis capacitive accelerometer is fabricated by anisotropic bulk micromachining of silicon wafers. In order to form top and bottom electrodes, glass wafers coated with Cr/Au is bonded to the silicon proof mass. Figure 1.14 shows the cross-sectional structural view of this z-axis accelerometer encapsulated in glass wafers. This way both top and bottom electrodes are formed for the sensor to measure in z-direction and sensor is protected from external effects [52].

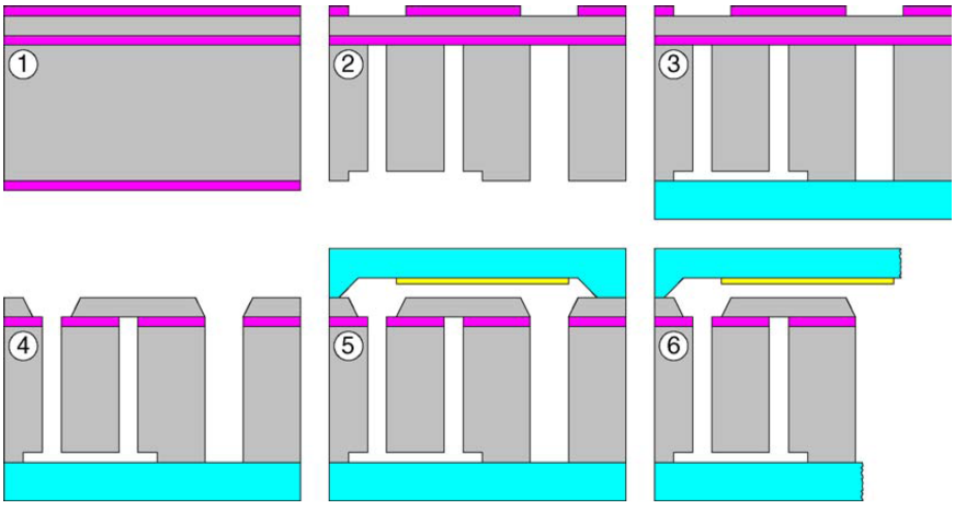

Figure 1.13: (1) Oxidized SOI; (2) DRIE-etching of the handle layer in two steps and patterning of the oxide; (3) anodic bonding to glass; (4) TMAH-etching of the epi layer and removal of oxide; (5) anodic bonding of glass with the detection electrodes; (6) dicing in two steps. [50]

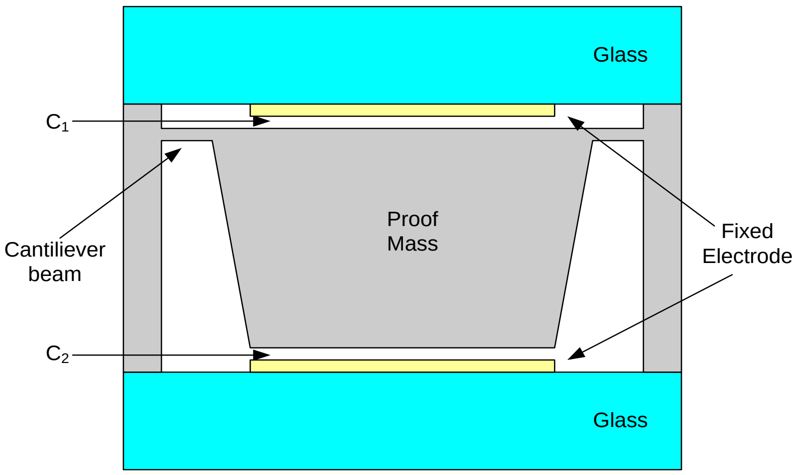

Figure 1.14: Cross-sectional view of z-axis accelerometer encapsulated in glass wafers [52].

Another novel idea for detecting the acceleration was proposed by H. Yang et al. which rely on determining the pull-in voltage of the suspended proof mass. Figure 1.14 shows the structure of novel x-axis pull-in type accelerometer. During the operation of the accelerometer, proof mass which is connected to the anchor with a soft spring oscillates between detection electrode 1 and detection electrode 2, by the voltages applied to the driving electrodes. When the proof mass hits the detection electrodes, pull-in period is observed and difference between two pull-in periods of detection electrode 1 and 2 gives the externally applied acceleration. When no acceleration is applied, difference between pull-in periods will be 0. When acceleration is applied, mass will deflect to one side and pull-in duration in that side will decrease while it will increase on the other side. Although the architecture is very novel, tests results showed that the relation between pull-in duration and acceleration was difficult to measure due to high driving voltage and short life time [53].

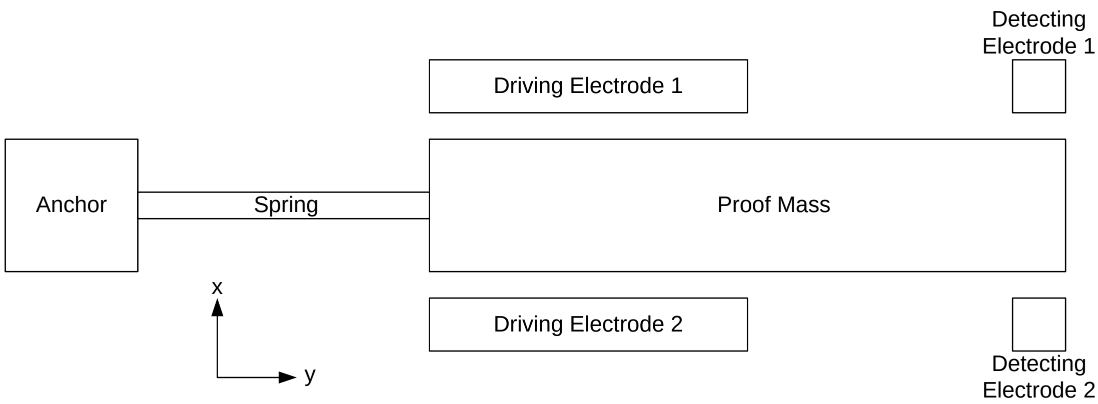

Figure 1.15: Structure of novel x-axis pull-in type accelerometer [53].

Lastly a new varying area capacitive accelerometer was reported in 2005 by B. Bais et al. Instead of capacitive fingers, several electrodes are placed beneath the proof mass of the accelerometer, and the overlap of the mass and these electrodes form the capacitances of accelerometer. Figure 1.16 shows the conceptual design of the varying area capacitive accelerometer. Fabrication of the accelerometers was not done and tests results are not presented but sensitivity and mechanical noise calculations were promising for high performance accelerometer systems [54].

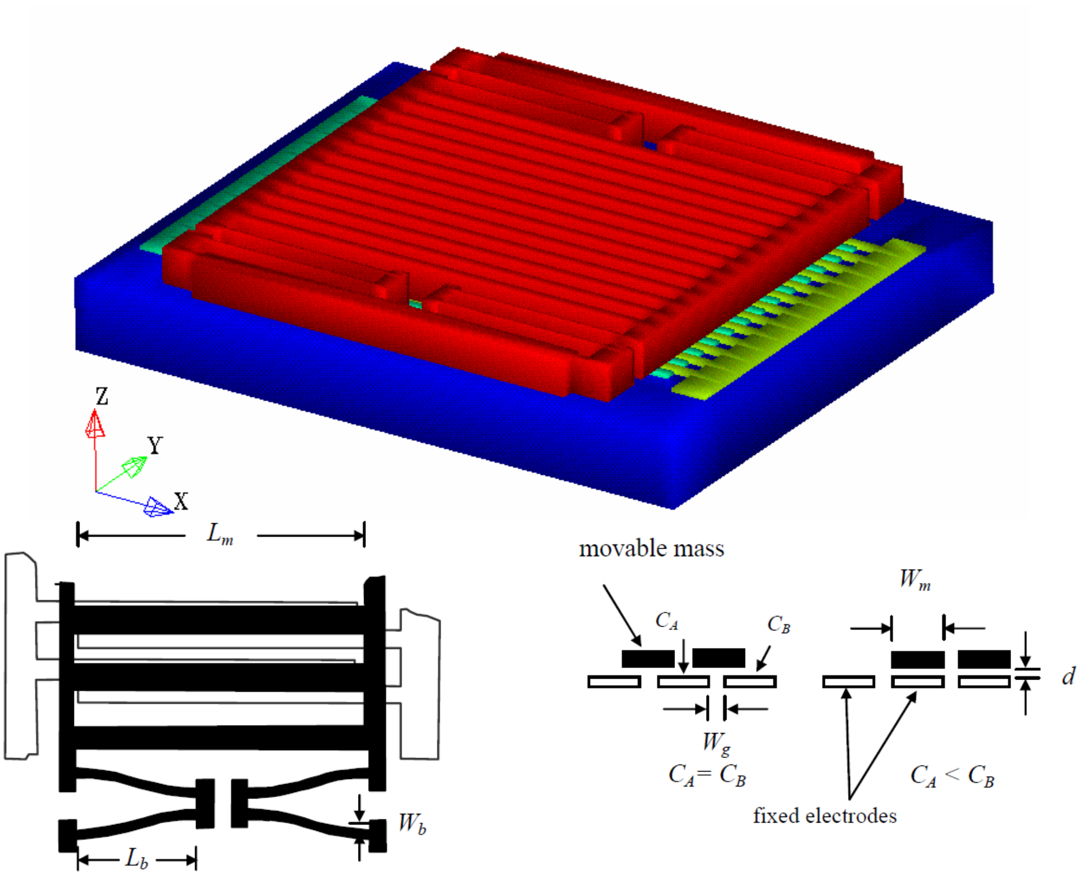

Figure 1.16: Conceptual design of the area changed capacitive accelerometer [54].

In 2006, an accelerometer having a higher dynamic range or better noise floor was not reported. But publications on novel structural designs continued to be published. This year, Y. Liu et al. reported an accelerometer structure having biaxial measurement capability. They integrated two lateral axis accelerometers into a single accelerometer and saved from space, but on the other hand this structure suffered much from the cross-axis sensitivity [55]. Figure 1.17 shows the top and 3D view of the bilateral axis accelerometer designed by Y. Liu et al.

Also a new readout circuit is reported in 2006 by D. Fang et al. In this publication a novel dual-chopper amplifier for CMOS MEMS capacitive accelerometers is reported. This circuit operates in open-loop mode and together with the accelerometer they achieved 50µg/√Hz with in ±8g range. The major disadvantage of open loop architecture is its non-linearity and the full range non-linearity of the system was not reported in the paper [56].

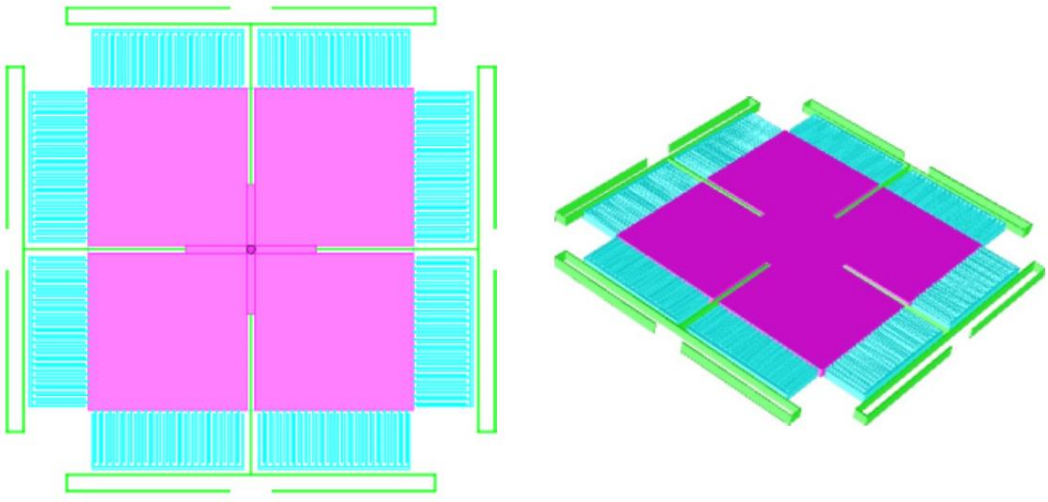

Figure 1.17: Top and 3D view of the bilateral axis accelerometer designed by Y. Liu et al. [55]

In 2007, F. Xiao et al. developed a new technique to fabricate proof mass springs by wet etching. Advantages of this technique are that fabrication of the accelerometers become easier and since <111> surfaces are used as the self etch stop, fabrication results are measured to be very close to design calculations. On the other hand unlike defining the structures with DRIE, this technique has very limited usage since it is not suitable for fabrication of the very different spring structures. In the journal only doubly clamped springs could be fabricated and 678Hz theoretical resonance frequency is measured as 696Hz after fabrication [57]. Figure 1.18 shows the general structural overview of the accelerometer developed by F. Xiao et al and Figure 1.19 describes the novel fabrication technique of the springs by self etch stop technique.

Previously T. Tsuchiya and H. Funabashi reported a novel z-axis SOI accelerometer fabricated by two steps DRIE etching of the structural layer [47]. This time H. Hamaguchi et al. modified the structure such that it could measure acceleration in all three axes. This was achieved by adding varying gap capacitance fingers orthogonally on each side of the proof mass and device is able to measure differentially in all three axes. Figure 1.19 shows the SEM pictures of capacitive three axes SOI accelerometer with vertical comb fingers developed by H. Hamaguchi et. al. Measured sensitivities were 1.04fF/g on x and y axes and 1.14fF/g on z axis which are very low and not suitable for high measurement range applications [58].

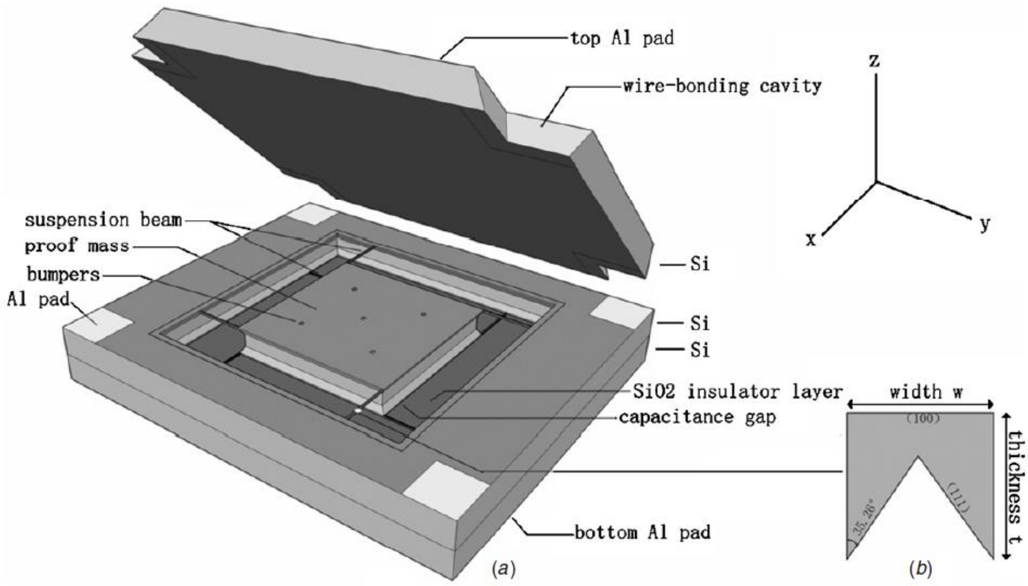

Figure 1.18: Structural of the accelerometer developed by F. Xiao et. al. [57]

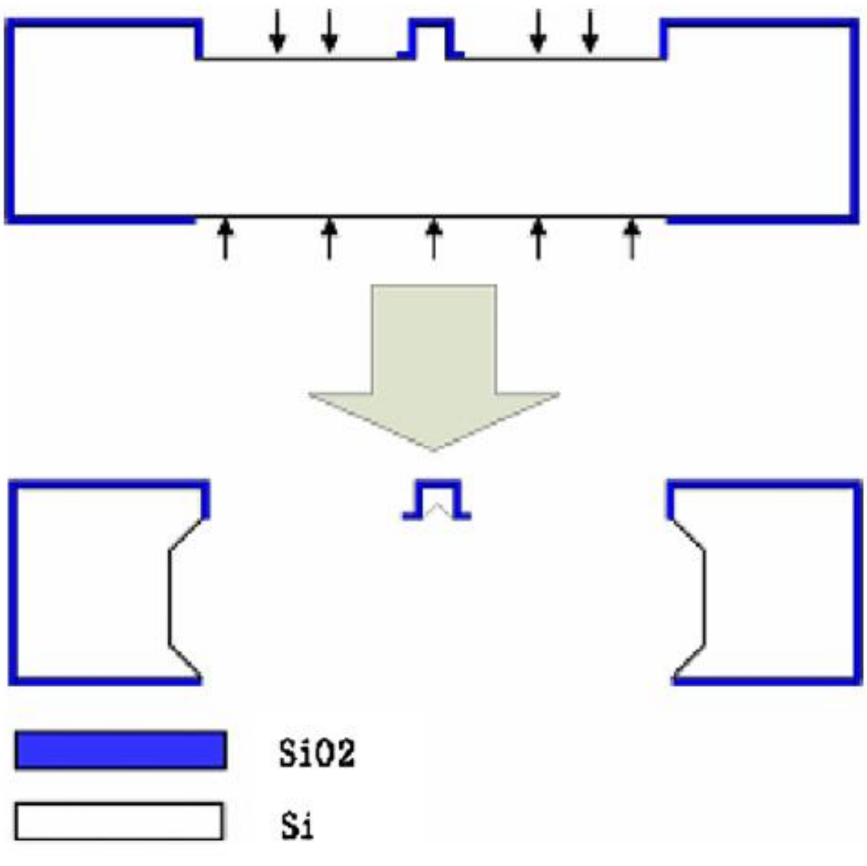

Figure 1.19: Novel self etch stop fabrication technique of the springs [57].

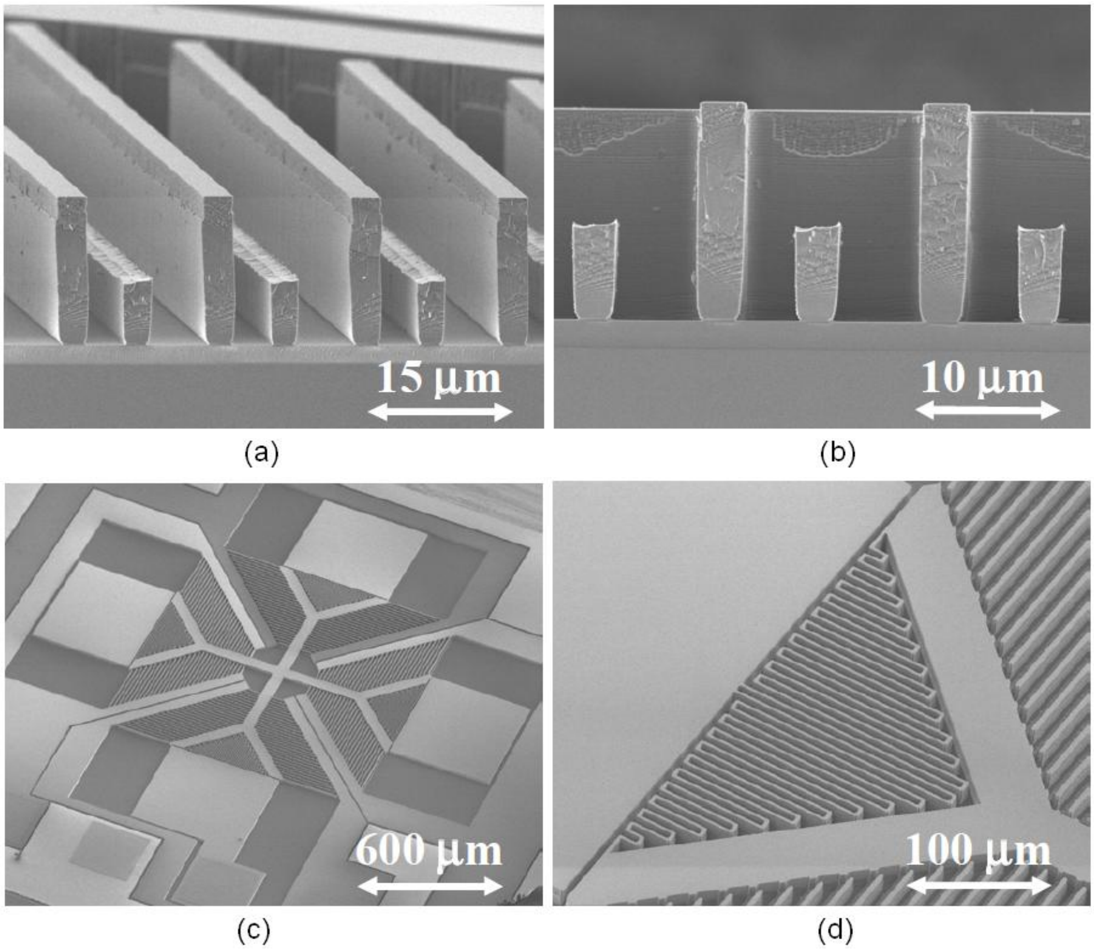

Figure 1.20: SEM pictures of capacitive three axes SOI accelerometer with vertical comb fingers developed by H. Hamaguchi et. al. [58]

R. Abdolvand, B. Vakili and F. Ayazi reported an in-plane accelerometer able to measure sub-micron gravity with reduced capacitive gaps and extra seismic mass. In order to decrease the mechanical noise of an accelerometer one should either decrease the damping or increase the mass of the sensor. In this study with a new technique developed by authors, capacitive gaps can be narrowed by post DRIE poly-silicon deposition. With the help of this technique capacitive gaps having 10µm spacing is decreased to 4-4.5µm after ~3µm poly-silicon deposition. In addition to this, the region of handle layer beneath the suspended proof mass is protected and not etched during the fabrication. This way accelerometer proof mass is increased considerably in order to decrease the mechanical noise. Figure 1.20 shows the schematic 3D view of the capacitive SOI accelerometer with sub-micro-gravity resolution and figure 1.21 shows SEM pictures of the cross section of a sense gap after poly-silicon deposition. Measured noise floor of the accelerometer when tested with open loop readout circuit was 213ng/√Hz; bias instability was 8µg in 3 hours and had a bandwidth of 200Hz [59].

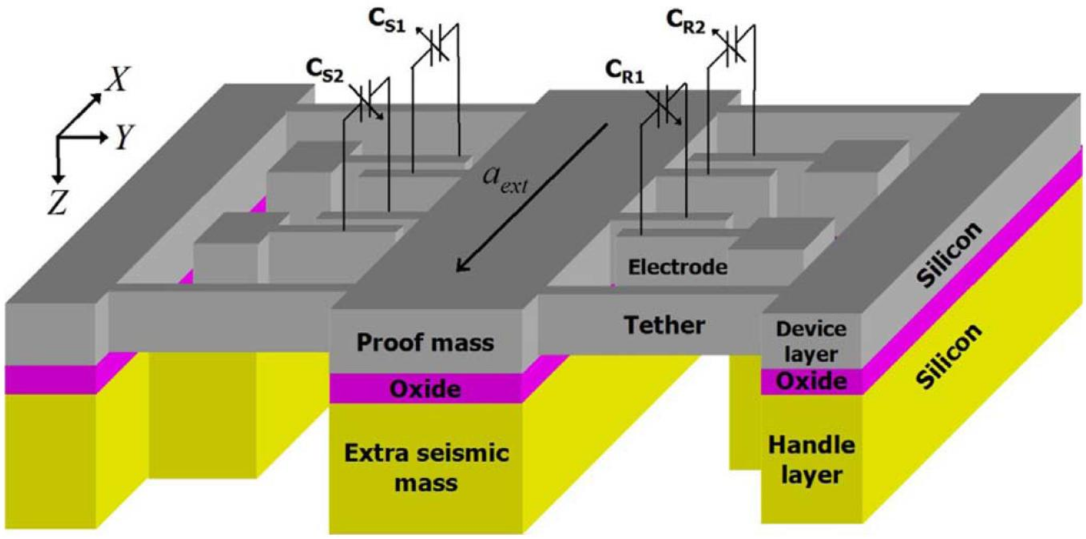

Figure 1.21: Schematic 3D view of the capacitive SOI accelerometer with sub-micro-gravity resolution [59].

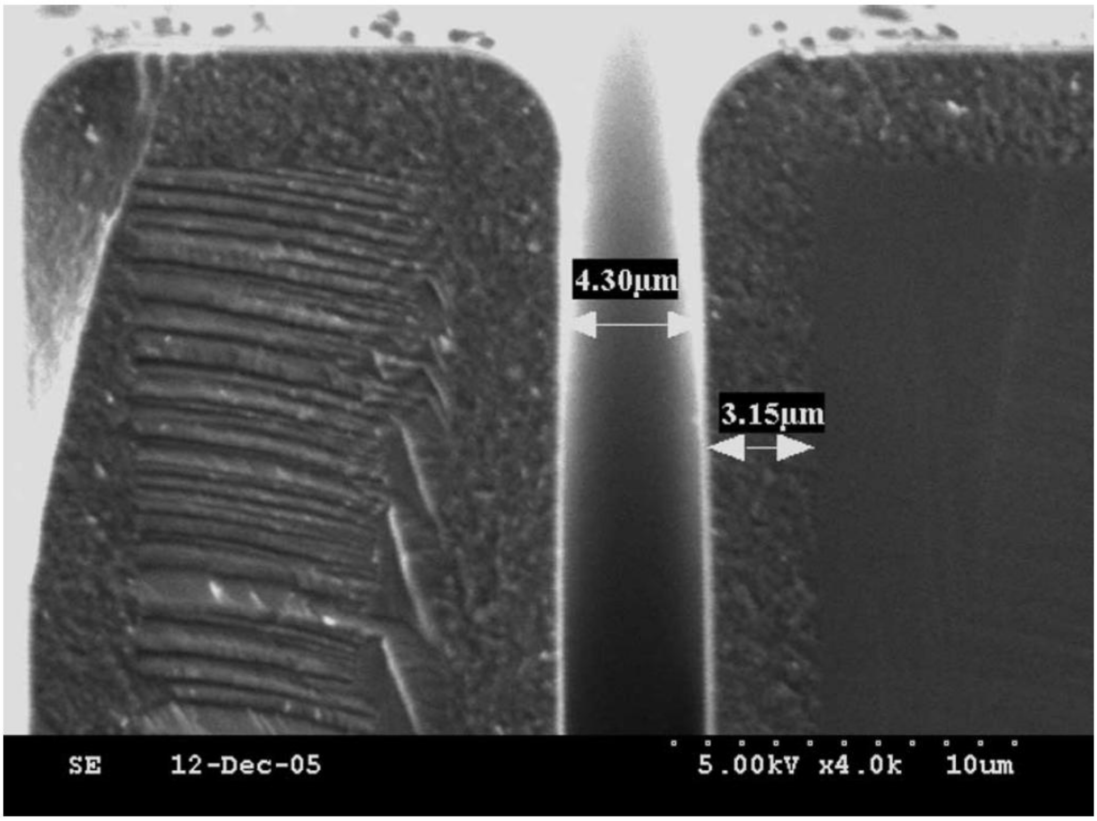

Figure 1.22: SEM pictures of the cross section of a sense gap after poly-silicon deposition [59].

Besides the improvements in mechanical structures two other readout circuits were also reported claiming to improve the performance of the accelerometers in 2007. First readout IC was published by M. Paavola et al. and it was a 62µA interface ASIC for 3-axis capacitive micro-accelerometers. Measured noise floors for this readout circuit were 460µg/√Hz for the x-axis and 550µg/√Hz in y and z-axes and the measurement range for all these axes were ±4g [60]. Second readout IC was published by L. Aaltonen et al. and it was continues time interface for closed-loop accelerometers. The integrated part of the interface includes oscillator and readout circuitry but does not contain controllers and references. Those components were added to the circuit externally. Noise floor obtained with this IC was 400ng/√Hz but the measurement range was limited with in ±1.5g range [61].

In 2008, Y. W. Hsu et al. reported a capacitive low-g three axes accelerometer, fabricated with SOG bulk micro-machining and DRIE techniques. In this architecture proof mass of each axis has a frame like structure surrounding another axis. Figure 1.23 shows the structure of capacitive low-g three axis accelerometer reported by Y.W. Hsu. In this structure the inner accelerometer is the y-axis while the intermediate mass belongs to x-axis and the outmost frame is the mass of the z-axis accelerometer. Figure 1.24 shows the z-axis movement of the outmost frame of capacitive low-g three axis accelerometer reported by Y.W. Hsu. The frame is suspended with a lever beam at the middle of the accelerometer and with the applied acceleration capacitance between the mass and the electrodes on the glass substrate changes. With this mechanism it is possible to measure acceleration differentially in z-axis. Fabricated accelerometers were tested with a simple open-loop capacitance-to-voltage converter circuit and noise floors were found as 138, 159, and 49µg/√Hz in ±2g operation range [62]. A. Wung et al. published their novel work on a tri-axial high-g CMOS MEMS capacitive accelerometer array this year. Designed accelerometers were using an array of cantilever structures, electrically connected in parallel for capacitive sensing which was designed to be used as shock sensors. System was tested in ±200g range with open-loop readout circuit. Calculated noise performance of the system in open loop mode was 2.66mg/√Hz and 1.33mg/√Hz for lateral and vertical accelerometers, but the test results were not presented in the conference. Figure 1.25 shows the SEMs of lateral and vertical CMOS-MEMS high-g capacitive accelerometer array [63].

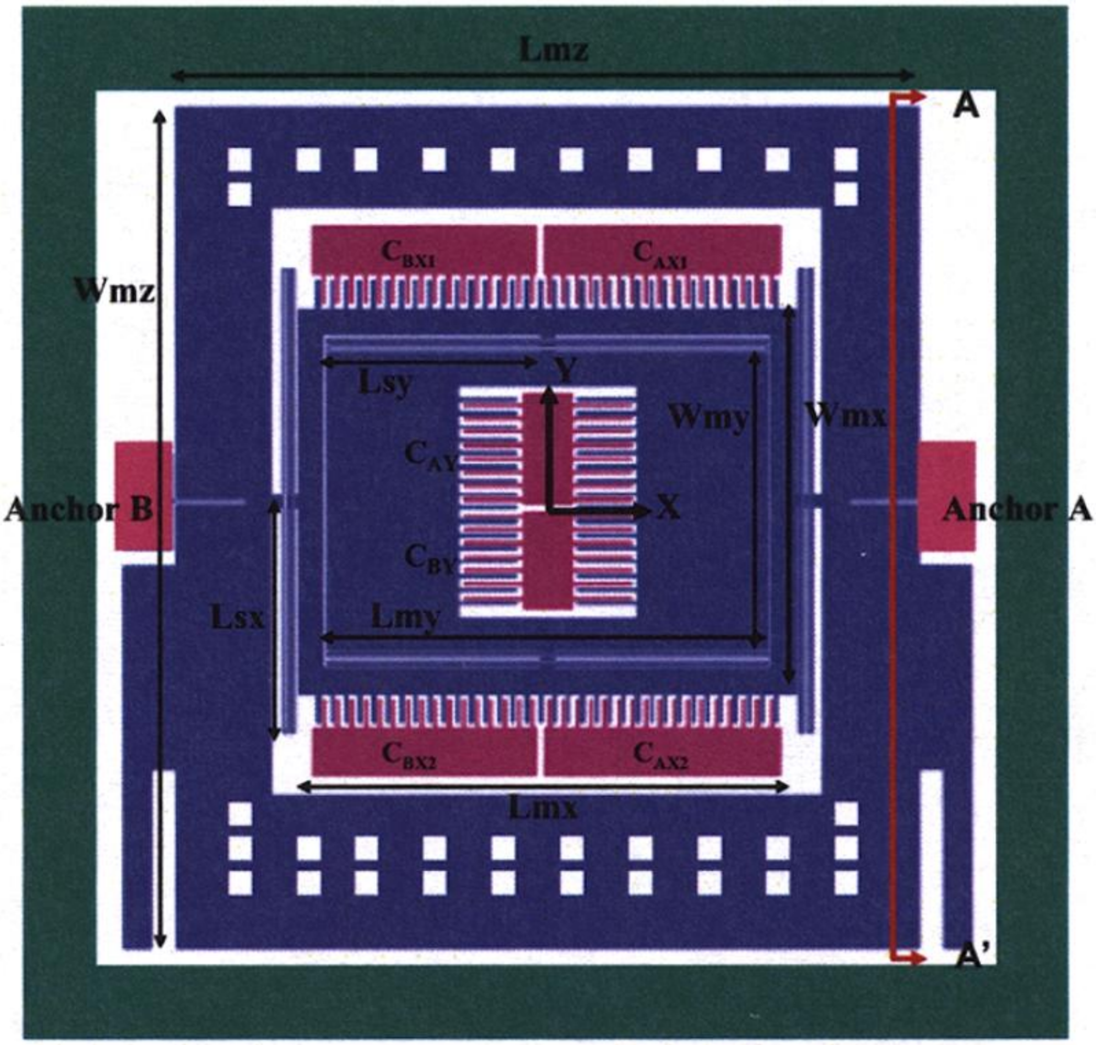

Figure 1.23: Structure of capacitive low-g three axis accelerometer reported by Y.W. Hsu [62].

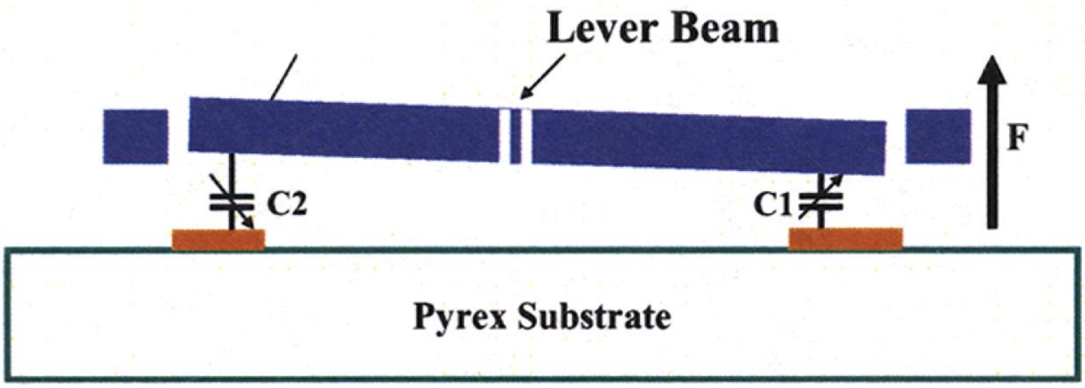

Figure 1.24: Z-axis movement of the outmost frame of capacitive low-g three axis accelerometer reported by Y.W. Hsu [62].

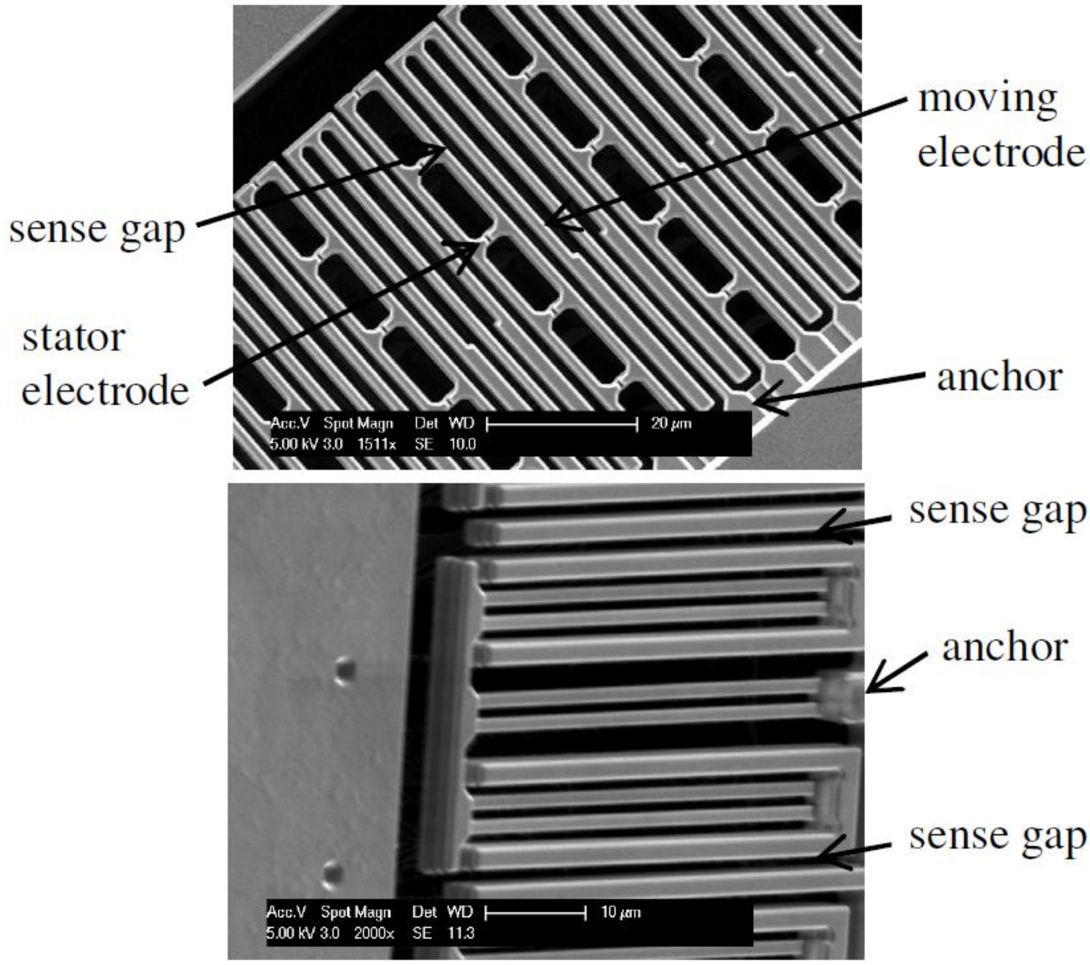

Figure 1.25: SEM pictures of lateral and vertical CMOS-MEMS high-g capacitive accelerometer array [63].

C.M. Sun et al. published a journal on CMOS capacitive accelerometer performance improvement same year which was about optimizing the finger number / proof mass density ratio. In their study in order to increase the sensitivity of the accelerometer some part of the proof mass is replaced with capacitive fingers and remaining mass is decreased to some extent by opening holes on it. Figure 1.25 shows the SEM pictures of the previous accelerometer design and the improved design by replacing mass with additional fingers. This way operation range of the accelerometer is increased up to ±10g range, but the noise floor is measured as 100mg/√Hz [64].

Lastly W. Huang et al. from China reported an interface IC for capacitive accelerometer sensors which was fabricated with 6μm bipolar process in 2008. IC was operating with ±6V, ± 18V and consists of an active square wave generator, a symmetrical voltage reference, a low-capacitance high-impedance voltage buffer, demodulation block, pre-amplifier, and a self-testing module. At a supply voltage of 15V, test results together with the readout IC was 581μg/√Hz noise floor, 54 mg drift in 30 minutes and total power consumption was 48mW. Unfortunately operation range of the accelerometer was not reported in the publication [65].

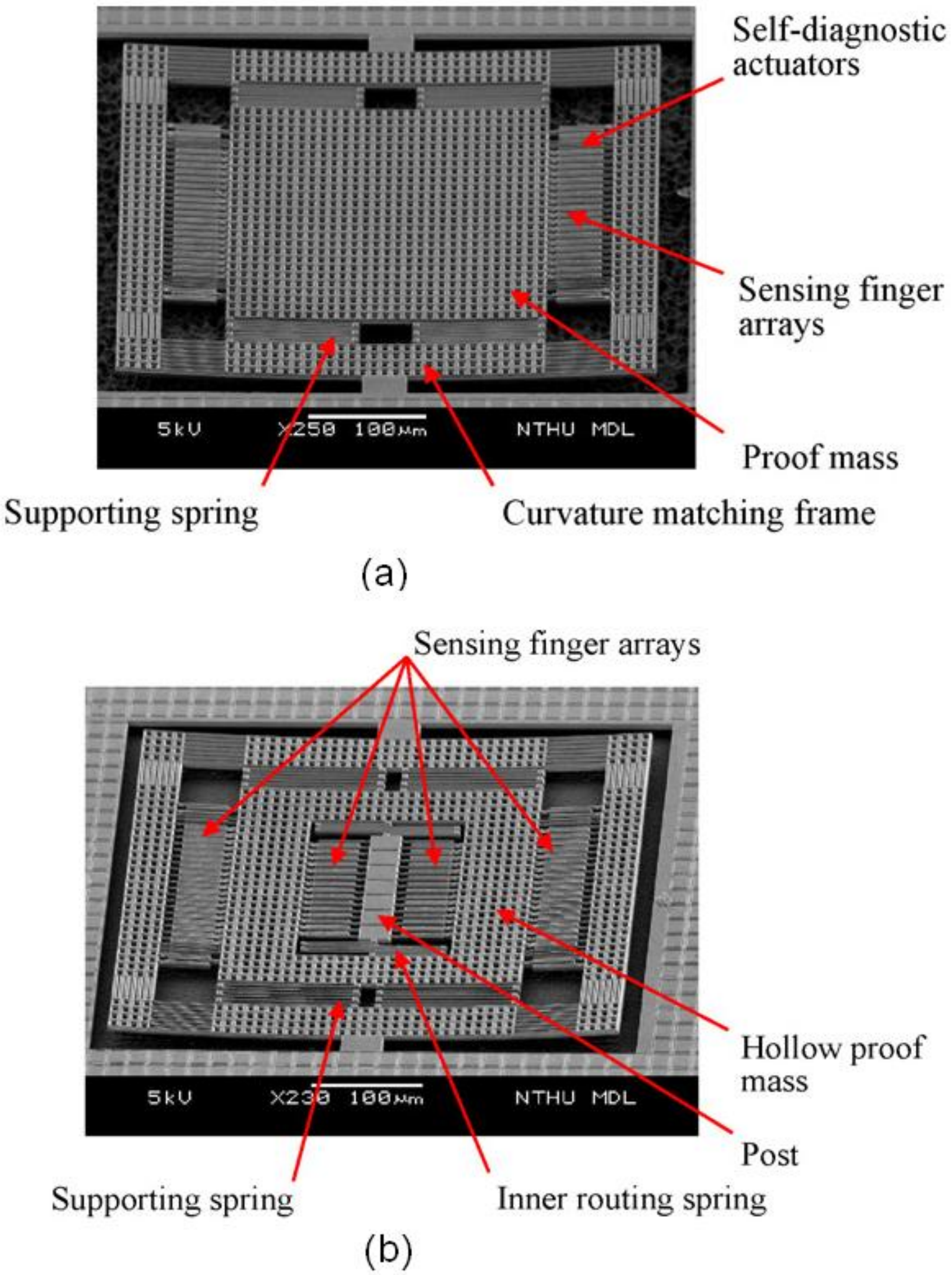

Figure 1.26: SEM pictures of (a) previous accelerometer design and (b) improved design with mass is replaced with additional fingers reported by C.M. Sun et al. [64].

In 2009 many innovative ideas are reported all around the world. Y. Hirata et al. reported a newly developed z-axis capacitive accelerometer which has a unique sensing mechanism by which the displacement of an inertial mass caused by acceleration in the z-axis direction is converted into the rotational displacement of a pair of detection plates. Figure 1.26 shows the acceleration detection mechanism of the sensor developed by Y. Hirata et al. and figure 1.27 shows the schematic drawing and SEM picture of the novel z-axis accelerometer. Sensor was designed for acceleration range of ±200g but the performance tests were not presented in the publication [66].

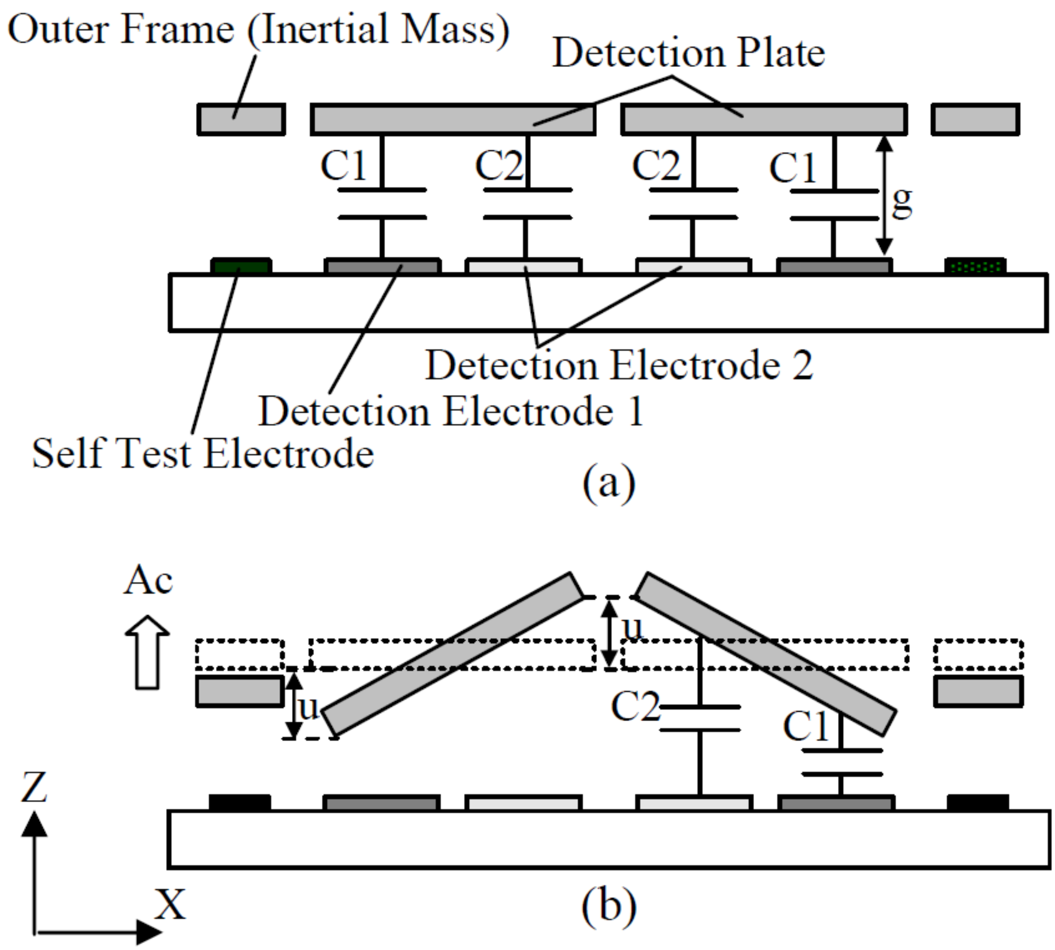

Figure 1.27: Acceleration detection mechanism of the sensor developed by Y. Hirata et al. [66]

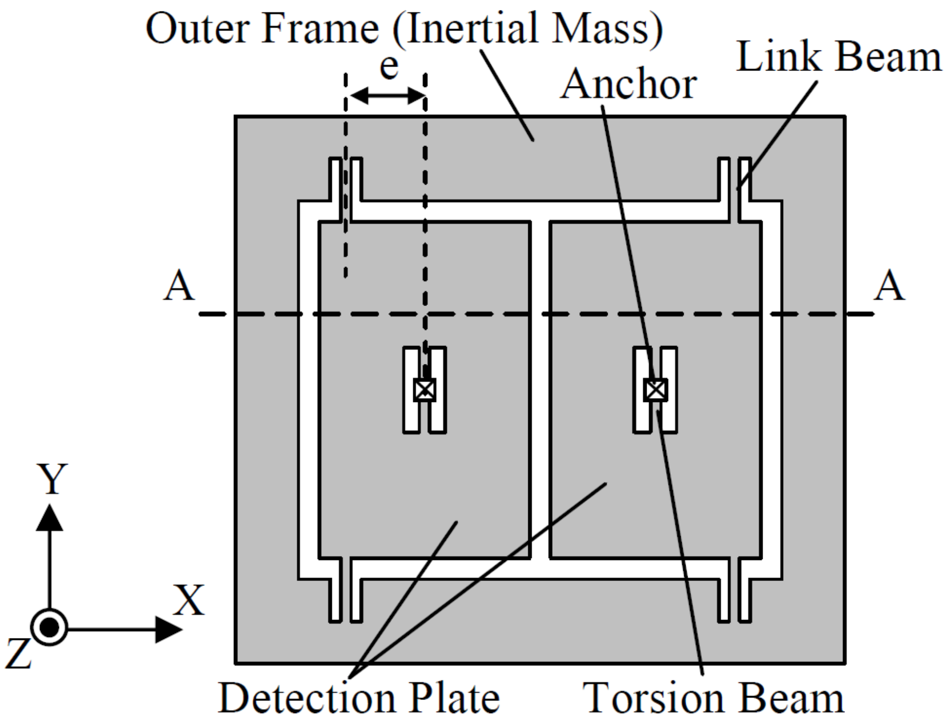

(a)

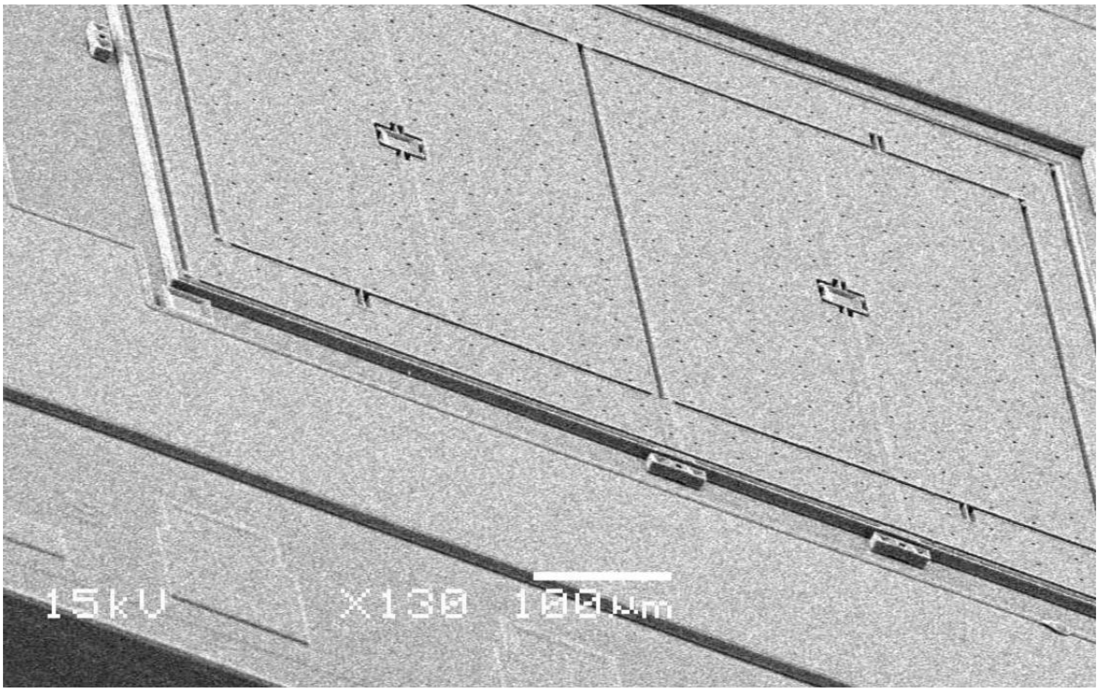

(b)

Figure 1.28: (a) Schematic drawing of the novel z-axis capacitive accelerometer (b) SEM picture of the novel z-axis capacitive accelerometer developed by Y. Hirata et al. [66].

C.P. Hsu et al. reported an implementation of a novel z-axis accelerometer on an SOI wafer. Instead of overlapping full parallel plates this accelerometer contains specially designed gap-closing differential sensing electrodes. In addition to these the electrical connection between the device and handle silicon layers of the SOI wafer is provided by metal-via's. This z-axis accelerometer is fabricated and characterized by authors and during the performance tests MS3110 universal capacitive readout IC is used. The noise floor and measurement range of the accelerometer is found to be 760μg/√Hz and ±1g respectively. Figure 1.28 shows the schematic of differential z-axis electrodes and the silver pastes used as via between epitaxial and handle layers of accelerometer and figure 1.29 shows the accelerometer placed and wire bonded in a ceramic package where silver dots are the silver epoxy paste used as via's [67].

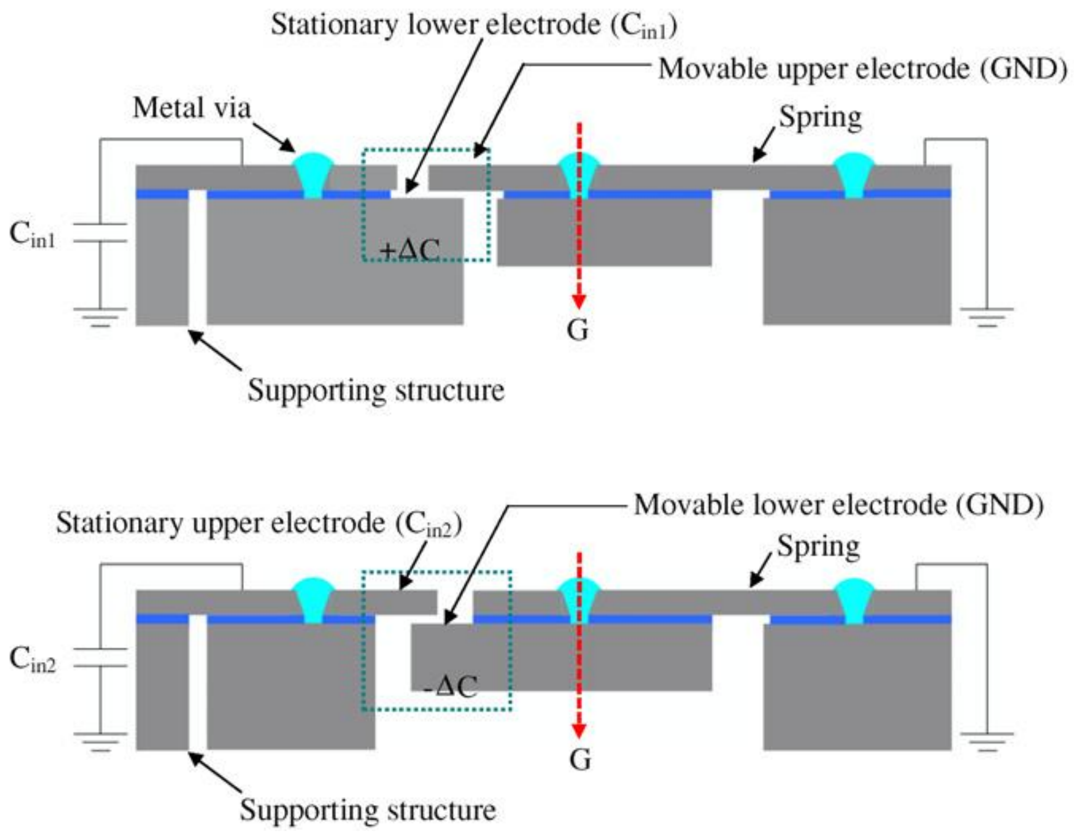

Figure 1.29: Schematic of differential z-axis electrodes and the silver pastes used as via between epitaxial and handle layers of accelerometer [67]

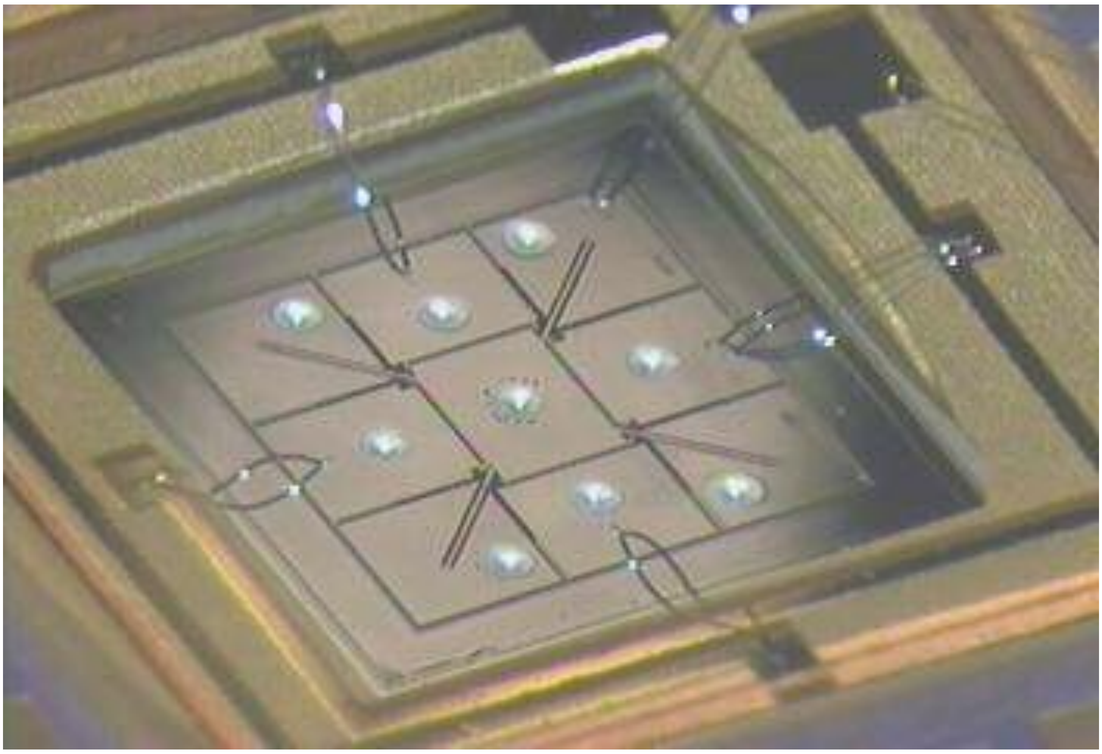

Figure 1.30: Accelerometer placed and wire bonded in a ceramic package where silver dots are the silver epoxy paste used as via's [67].

D Linxi et al. developed a novel MEMS inertial sensor with enhanced sensing capacitors. In this new design a different type of capacitive fingers are used in order to both increase the sensitivity and decrease the damping of the accelerometers. This way mechanical noise of the accelerometer is reduced and capacitive area is increased. Fabrication of these sensors was done with usual silicon-on-glass process and features are defined with DRIE. Test results indicated that the quality factor of the device based on the slide-film damping effect is 514, which shows that the enhanced capacitors can reduce mechanical noise. Sensitivity of the fabricated accelerometers are found as 0,492pF/g . Figure 1.31 shows the SEM pictures of improved comb finger structure in order to enhance sensitivity and decrease mechanical noise [68].

Another important study in 2009 was by C.-M. Sun et al. who reported a novel single proof mass tri-axis capacitive CMOS MEMS accelerometer to reduce the die size of the three axes sensor. In this study a serpentine spring is designed to reduce the cross axis sensitivity of the z-axis accelerometer. In addition to these a magnetic self testing interface is also placed for z-axis. Measurement results show that sensitivities (non-linearity) of etch direction are 0.53mV/G (2.64%) of X-axis, 0.28mV/G (3.15%) of Y-axis, and 0.2mV/G (3.36%) of Z-axis. The cross-axis sensitivities range from 1% to 8.3%, and the measurement range is between 0.8-6G, respectively. Figure 1.31 shows the conceptual design of the single mass, three axes CMOS MEMS accelerometer produced by C.-M. Sun et al. [69].

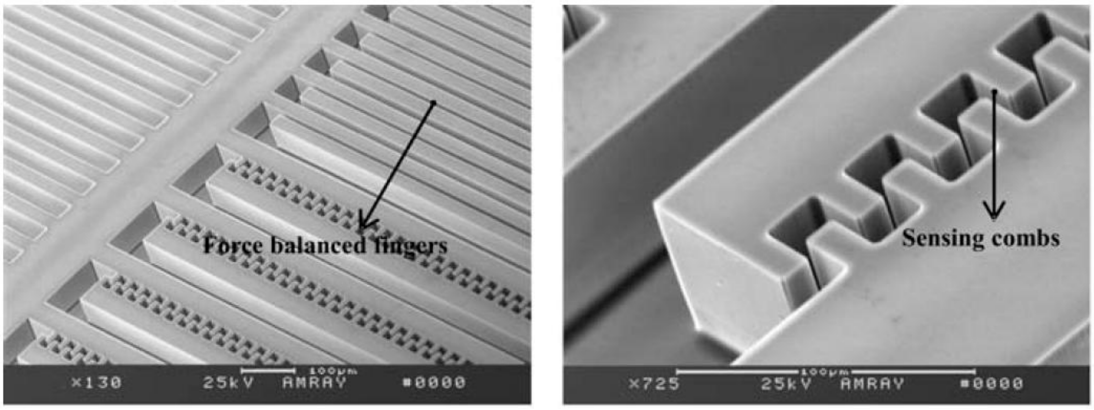

Figure 1.31: SEM pictures of improved comb finger structure in order to enhance sensitivity and decrease mechanical noise [68].

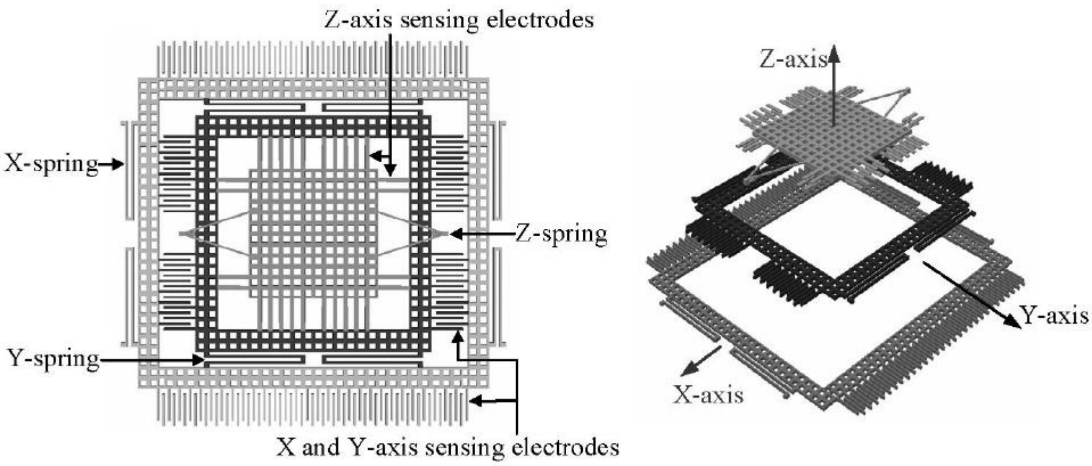

Figure 1.32: conceptual design of the single mass, three axes CMOS MEMS accelerometer produced by C.-M. Sun et al. [69].

In 2010, C.-M. Sun et al. published another paper about the device reported in [69]. This time noise performance of each axis is measured and reported as 120µg/√Hz in x-direction, 271µg/√Hz in y-direction and 357µg/√Hz in z-direction with in ±0.8-6g measurement range [70].

Finally in 2010, Colibrys one of the leading MEMS inertial sensors company published an article about one of their commercial accelerometers. Reported sensor has navigation grade performance and was read in closed loop mode with second order sigma-delta multi-bit and high order 1-bit sigma-delta modulators. The accelerometers were fabricated with bulk micromachining through anisotropic etching of silicon which increases the yield and repeatability of the manufacturing process. Tests results showed that accelerometers developed and reported by Colibrys is able to measure in ±11.7g range with 1.7μg/√Hz noise level. Sensor has a maximum measurement bandwidth of 400Hz and its bias instability was also measured as 100μg in 24 hours [71].

In this section of the thesis, most important publications from 1983 to today are summarized. In these publications authors usually give emphasis to the sensitivity of the fabricated accelerometers, though sensitivity is not a performance parameter and does not indicate anything on its own. Sensitivity is a measure of various important parameters like operation range or noise of the system but its meaningful when either used with the mass of the accelerometer or the spacing between the capacitive fingers. Another important issue is that most of the publications just indicate the noise floor or resolution of the reported systems without mentioning the measurement range which again does not completely reflect the real performance. Noise floor or resolution of the system is a merit for the possible application areas of that particular accelerometer system but since noise and measurement range of an accelerometer are inversely proportional, the real parameter indicating the challenge factor of the design is the dynamic range of the accelerometer which is defined by the ratio of the measurement range to the noise floor. Therefore all these publications throughout the literature should be classified according to their measurement range and noise floor as their primary performance parameters in order to evaluate them correctly. Table 1.2 lists all the measurement range, noise level and dynamic range of accelerometers investigated in this section of the thesis.

Table 1.2: Measurement range, noise level and dynamic range of accelerometers searched in the literature. (Lines with yellow color shows the accelerometers with open loop readout architecture, line with blue color has 5th order Σ−Δ readout circuit)

Year	Author(s)	Measurement Range (g)	Noise Floor (g/√Hz)	Dynamic Range (dB)
1990	F. Rudolf et. al.	0,1	1,0E-06	106
1990	H. Seidel et. al.	5,0	1,0E-03	80
1991	E. Peeters et. al.	50,0	1,0E-02	80
1995	K.H.-L. Chau et. al.	5,0	6,0E-04	84
1995	B. Wenk et. al.	150,0	1,6E-03	105
1996	M.E. Lemkin et. al.	3,5	5,0E-04	83
1997	B.P. Van Drieënhuizen	2,0	8,0E-05	94
1997	B.P. Van Drieënhuizen	5,0	1,1E-03	79
1997	B. Ha	9,0	2,7E-04	96
2000	A. Salian et. al.	1,2	2,0E-05	102
2000	H. Luo, G.K. Fedder, R.L. Carley	13,0	1,0E-03	88
2000	H. Xie and G.K. Fedder	27,0	6,0E-03	79
2001	H. Goldberg et. al.	0,2	3,0E-08	142
2001	S. Wei et. al.	60,0	3,0E-03	92
2002	R. Toda et. al.	2,0	4,0E-05	100
2003	Ki-Ho Han and Young-Ho Cho	2,0	5,5E-06	117
2003	B.V. Amini et. al.	2,0	1,1E-04	91
2003	H. Külah and J. Chae et. al.	1,4	1,5e-06	125
2004	B.V. Amini et. al.	2,0	4,4E-06	119
2004	J. Wu, G.K. Fedder and L.R.Carley	6,0	5,0E-05	108
2005	J. Chae, H. Külah and K. Najafi	1,0	7,9E-05	88
2005	H. Ko et. al.	10	1,9E-06	140
2006	D. Fang et. al.	8,0	5,0E-05	110
2007	L. Aaltonen et al.	1,5	4,0E-07	138
2007	M. Paavola et. al.	4,0	4,6E-04	85
2008	Y. W. Hsu et al.	2,0	4,9E-05	98
2008	A. Wung et. al.	200	1,3e-03	110
2009	C.P.Hsu et. al.	1,0	7,6E-04	68
2010	Colibrys (fifth order readout circuit)	11,7	1,7E-06	143
2010	C.-M.Sun et. al.	6,0	2,7E-04	93

1.4 Objectives of This Study

Literature on capacitive micro accelerometers is extensively studied and the lack of tactical grade accelerometer optimization is observed. Up to now many accelerometers are reported in navigation grade having superior sub micro-g noise performances. Many tactical grade accelerometers are also reported but their dynamic range characteristic could not match with the navigation grade accelerometers.

Aim of this study was the optimization and fabrication of tactical grade accelerometers that could achieve high dynamic range. In order to complete this study, following goals are achieved in the given order.

- Readout circuit that will be used together with the accelerometers is decided: Open-loop readout architectures allow designing low noise accelerometer systems but their non-linearity characteristics are very bad for high operation ranges. Since the aim of the study was to fabricate tactical grade accelerometers, and non-linearity of the system is an important parameter, closed loop type readout architecture is decided to be used with the system. Closed loop accelerometers have superior linearity, and bandwidth characteristics with enhanced measurement range. Noise performance of closed loop structures is worse than the open loop counterparts, but with a proper design dynamic range can be maximized.
- Proper fabrication method is chosen for high performance accelerometers: In order to achieve high performance tactical grade accelerometers, high aspect ratio devices should be fabricated with great accuracy. Therefore with trial and error, many different fabrication procedures should be tried and an optimum method has to be found for the fabrication of high performance tactical grade accelerometers.
- An optimization algorithm is developed in order to maximize the dynamic range of the accelerometer: After deciding the readout circuit and fabrication technique, performance limiting factors of the system is extracted. Boundaries for noise performance and measurement range are formulized and an optimization algorithm is written in MATLAB in order to design optimum accelerometer.

- Sensor and system level tests: After the fabrication of sensors, they are tested at system level in order to see if the fabricated accelerometers meet the design parameters. The one satisfying the design parameters are connected to a second order sigma-delta ($\Sigma-\Delta$) readout circuit for system level testing. During these tests noise, measurement range, linearity and bias drift of the accelerometers are found.
- Three axis packaging of single axis accelerometers are done: Fabricated and tested accelerometers are connected in three orthogonal axes on an alumina substrate specifically designed for this purpose. This substrate is than placed in a package to form a three axes accelerometer which can be tested by connecting to an external readout circuitry. Tests at system level are performed and all there axes of the accelerometer are characterized.
- Three axis monolithic accelerometer fabrication: While constructing the three axes accelerometer system using three single axis accelerometers many problems are encountered like the difficulty to orthogonally place all three sensors or the cross axis misalignment. In order to solve these problems a new monolithic three axes accelerometer fabrication method is developed. With this new fabrication technology all three accelerometers can be fabricated at the same time, and no further processing is required during packaging in order to integrate them orthogonally.

During this study, several fabrication techniques are tried and at the end of this study a high performance, high dynamic range tactical grade accelerometer could be fabricated successfully. This accelerometer achieved 153µg/√Hz noise level in ±33.5g measurement range. Table 1.3 lists the estimated and measured performance parameters of the accelerometer presented in this thesis. In order to evaluate the performance of this accelerometer, it is compared with the similar sensors in the literature. Figure 1.33 shows the graphical view of the measurement range and noise characteristics of accelerometers presented in Table 1.2. Figure 1.34 shows the enlarged version of the same graph for lower noise margins and measurement ranges. As it can be seen from these graphs, single axis accelerometer presented in this thesis achieved a performance which could not be previously achieved and it demonstrates the lowest noise performance among the accelerometers that can measure in high operation ranges.

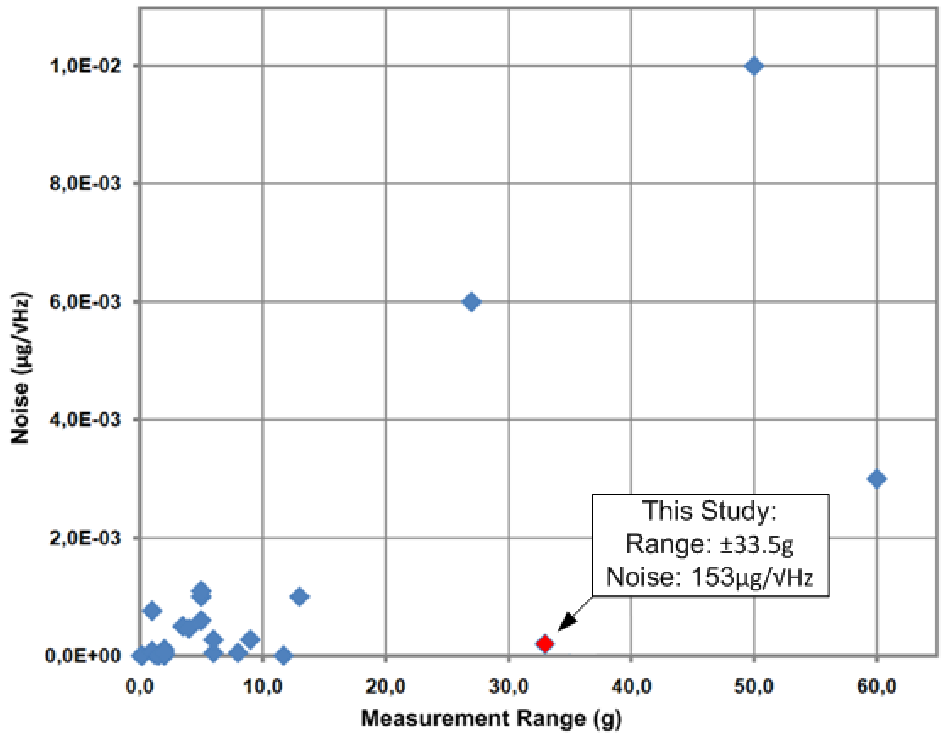

Figure 1.33: Graphical view of the measurement range and noise characteristics of accelerometers presented in table 1.2.

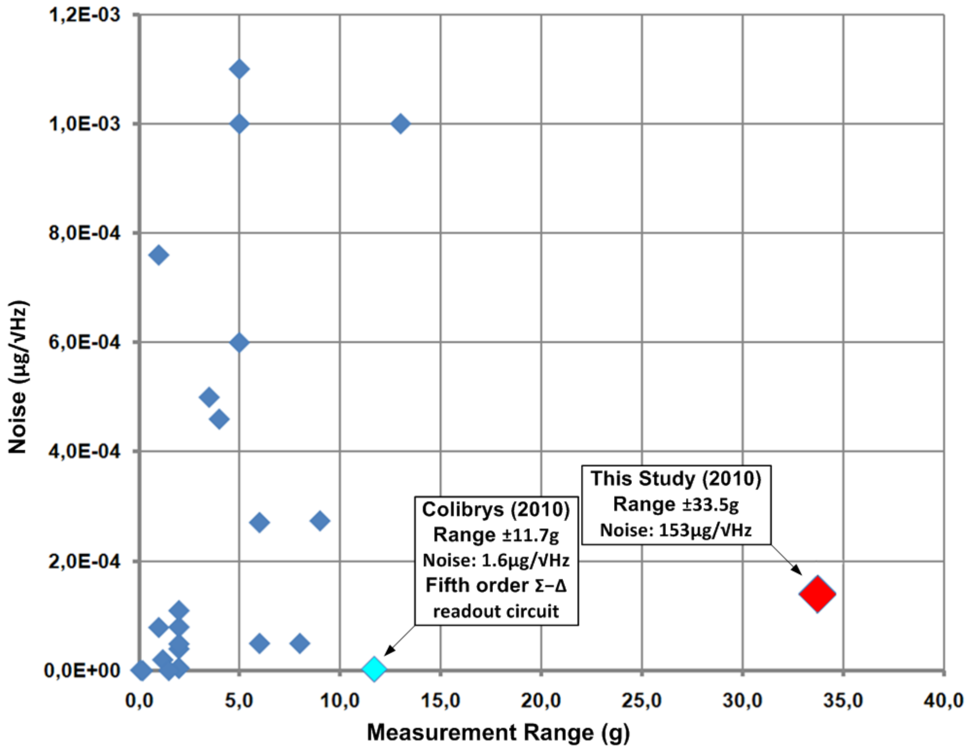

Figure 1.34: Enlarged graphical view of the measurement range and noise characteristics of accelerometers presented in table 1.2

Figure 1.35 shows the dynamic range vs. measurement range of the accelerometers in the literature given in table 1.2. According to this graph there are only two accelerometers in the literature reported so far that is beyond the boundaries of the trend line among the accelerometers reported so far. One of them is reported by Colibrys in 2010, which utilizes a fifth order Σ−Δ readout circuitry, and the other one is the accelerometer system reported in this thesis.

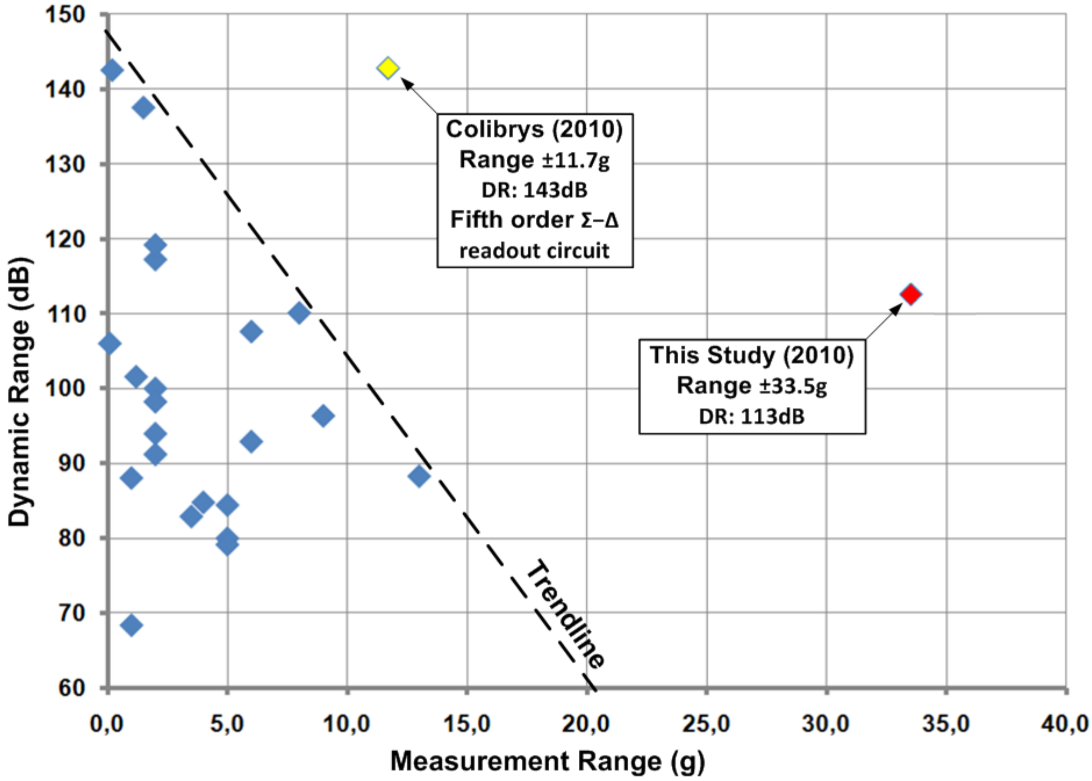

Figure 1.35: Dynamic range vs. measurement range of the accelerometers in the literature given in table 1.2.

Table 1.3: Estimated and measured performance parameters of the accelerometer presented in this thesis.

PARAMETER	GOAL	MEASURED PERFORMANCE
Operation Range (g)	<±39g	±33.5g
Noise Floor (μg/√Hz)	<150μg/√Hz	153 μg/√Hz
Bias Drift (μg)	<500μg	50μg
Non-Linearity (%)	<0.5%	0.38%
Dynamic Range (dB)	114	113

Contributions of this thesis to the literature can be summarized as:

- Measurement range, closed loop oriented noise and dead zone concepts are verified with a model constructed in MATLAB. It is proved that measurement range and dead zone of the closed loop accelerometer system matches with the mathematical models in the literature but the mass residual motion of the system does not match with equations given in the literature. Reason of this mismatch is the assumptions made during the mass residual motion calculations in the literature.
- A MATLAB Code is written to optimize a high performance, high dynamic range, and low noise system for a fixed die size.
- Designed optimum accelerometers are fabricated with three different fabrication techniques results are compared, problems related with each fabrication is identified and several solutions are proposed.
- A high performance tactical grade single axis accelerometer is fabricated with dissolved wafer process. System level tests of this accelerometer revealed ±33.5g operation range, 153μg/√Hz noise density, 50μg bias drift and 0.38% non-linearity. This accelerometer has 113dB dynamic range which surpasses its counterparts in the literature.
- A new monolithic three axial accelerometer fabrication technique is developed. This process involves 9 masks with advanced fabrication steps. New accelerometer designs are made for this process that can measure in lateral and vertical directions at the same time.

1.5 Outline of the Thesis

There are a total of 7 chapters in this thesis. First chapter is the introduction to history of accelerometer and has a detailed literature search about the navigation and tactical grade accelerometers. After describing the application areas and classification of accelerometers, chapter concludes with the objectives achieved and contributions added to the literature.

Second chapter starts with the basic second order accelerometer theory. Later in the chapter mechanical accelerometer is modeled by calculating its basic elements together with its open and closed loop readout architectures.

Third chapter describes all the performance parameters that a designer should care during the design of a capacitive MEMS accelerometer. Each performance parameter is described in detail and mathematical formulations are presented for modeling the parameters like noise, range, and bandwidth.

Fourth chapter explains three different fabrication processes used in this study in order to fabricate accelerometers. Designs for each fabrication process and the SEM pictures detailing the results of each fabrication are also given in this chapter.

In fifth chapter test results of fabricated sensors for each fabrication process are given. Sensor and system level tests of accelerometers are presented and these results are compared with the design parameters calculated in the fourth chapter.

In the sixth chapter the new SOI^2 process developed in the scope of this study is described. In this 9 mask process; purpose of each mask is described in detail. Expected performance parameters of the designed lateral and vertical axis accelerometers are also presented.

Finally in the seventh chapter thesis is concluded with the summary of the PhD. study. In addition to this, goals achieved and the future works that can be done in order to improve the performance of the accelerometers are given.

CHAPTER 2

THEORY AND MODELING OF CAPACITIVE MEMS ACCELEROMETERS

This chapter introduces the basic theory and modeling of capacitive micro accelerometers.

2.1 Basic Theory of Capacitive Accelerometers

MEMS capacitive accelerometers measure acceleration by detecting the amount of deflection of a proof mass, resulting from an applied external acceleration. A MEMS capacitive accelerometer is composed of 3 main mechanical structures which are proof mass, springs and capacitive fingers. Main movable element is the proof mass of the accelerometer and it is attached to the fixed anchor regions with the springs of the accelerometer. There are a number of capacitive finger like structures, attached on sides of the proof mass and with the motion of the proof mass capacitances on each side of the accelerometer changes. Finding the applied acceleration is achieved by detecting the change of capacitance. Figure 2.1 shows a typical structure of a capacitive MEMS accelerometer. Whenever acceleration is applied on the sensitive axis of the accelerometer, capacitance on one side of the accelerometer increases while the other side decreases. This type of finger orientation allows conversion of the capacitance change to output voltage in a differential manner which increases the sensitivity of the system by a factor of 2.

There are two different methods to detect the capacitance change of the accelerometer. First method is the open loop detection which directly measures the change of the capacitance on both sides of the proof mass. Readout circuits operating in open loop detection mode are very simple and capacitance change is converted to voltage with a front-end charge integrator block. Second method is the closed loop detection mode and in this mode instead of measuring capacitance change directly, readout circuit detects the amount of force required to hold the proof mass of the accelerometer in its rest position. This type of readout circuit detects the deflection of the accelerometer with a charge integrating circuit as in the open loop case, but this information is then converted to force and fed to the accelerometer in order to stabilize the proof mass. Both of these methods will be described in detail in section 3 of this thesis.

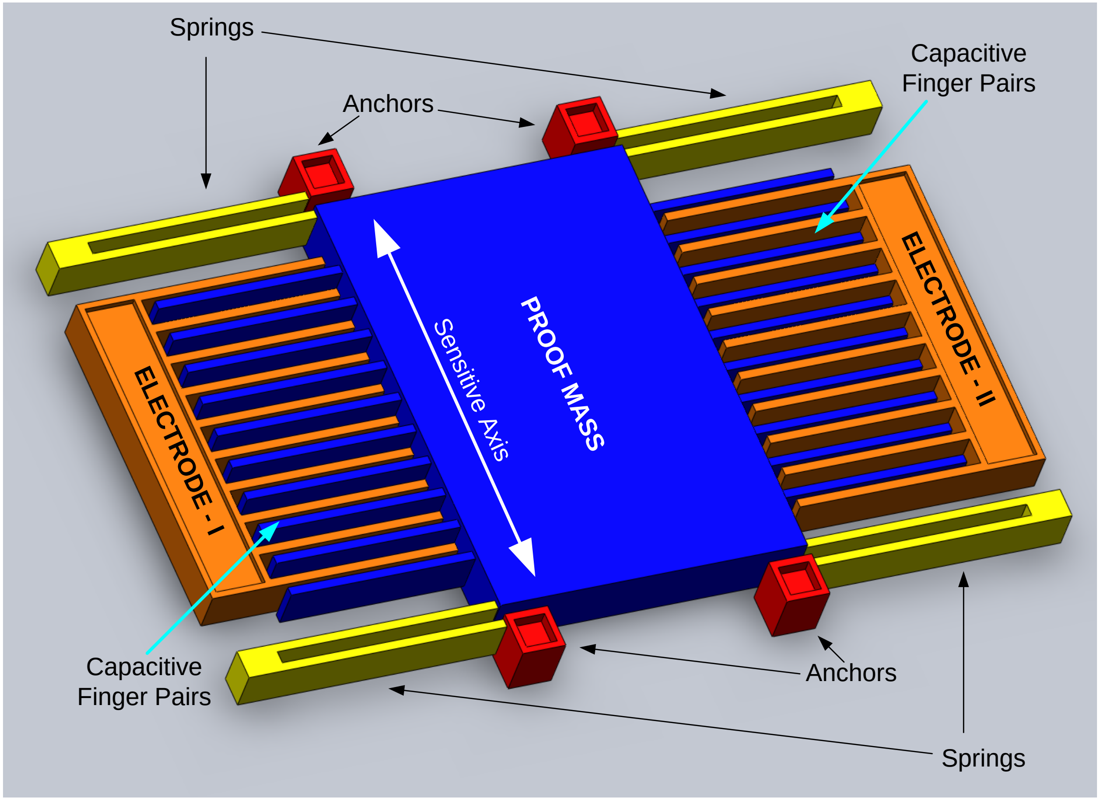

Figure 2.1: Typical MEMS capacitive accelerometer structure

2.2 Modeling of Capacitive Accelerometers

As described in the previous section, micro accelerometers have three basic building blocks. Using these three basic building blocks accelerometers can be modeled as a second order spring-damper system as shown in figure 2.2. Model of this kind of accelerometers can be extracted as

$$F = m.a_{applied} = m\ddot{x} + b\dot{x} + kx \quad (2.1)$$

where "m" is the mass of the moving body, "b" is quantity defining the air damping between the capacitive fingers, which hinders the movement of the proof mass and "k" is the stiffness of the spring constants.

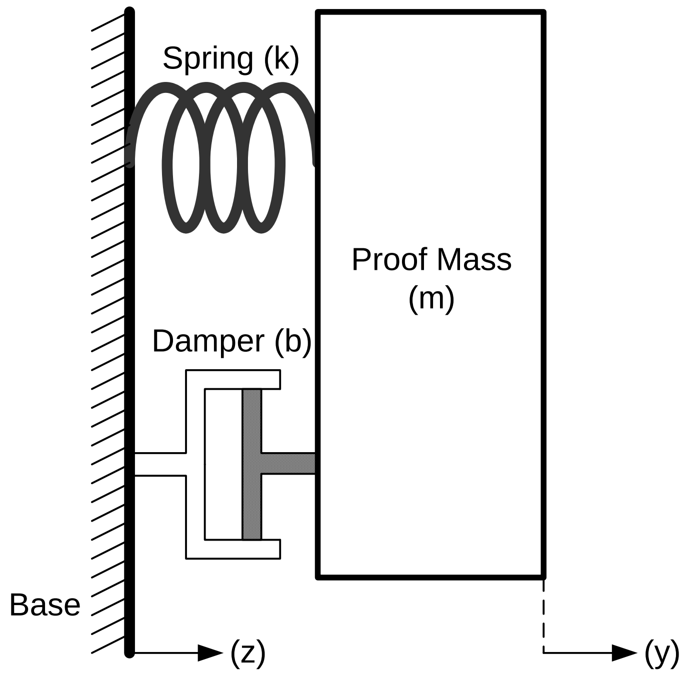

Figure 2.2: Second order spring damper accelerometer model

In order to find the amount of deflection with respect to an externally applied acceleration, we can further simplify 2.1 as

$$\frac{x}{a_{applied}} = \frac{1}{s^2 + {}^{b}/_{m}\, s + {}^{k}/_{m}} \quad (2.2)$$

which can be used as the second order mechanical model of a capacitive accelerometer in simulation tools like MATLAB. Using this second order equation, the resonance frequency and quality factor of the accelerometer system can be calculated as:

$$w_0 = \sqrt{\frac{k}{m}} \quad (2.3)$$

$$Q = \frac{w_0 . m}{b} \tag{2.4}$$

where w_0 is the resonance frequency, Q is the quality factor, k is the spring constant, m is the proof mass, and b is the damping of the accelerometer system. The magnitude and phase response of the proof mass motion with respect to input acceleration can be derived as:

$$\left|\frac{X(jw)}{a(jw)}\right| = \frac{1}{\sqrt{(w_0^2 - w^2)^2 + \left(\frac{w . w_0}{Q}\right)^2}} \tag{2.5}$$

$$\prec \frac{X(jw)}{a(jw)} = \tan^{-1}\left(\frac{\frac{w . w_0}{Q}}{w_0^2 - w^2}\right) \tag{2.6}$$

If acceleration and velocity is also needed to be accessed during the sensor simulations, a more sophisticated model can be implemented instead of a simple second order transfer function of the accelerometer. Figure 2.3 shows a more detailed second order model of an accelerometer with nonlinear damping. Although including nonlinear damping parameter converges the real time system better, effect of this non-linearity can be considered negligible and a simple second order transfer function block is enough for system level simulations.

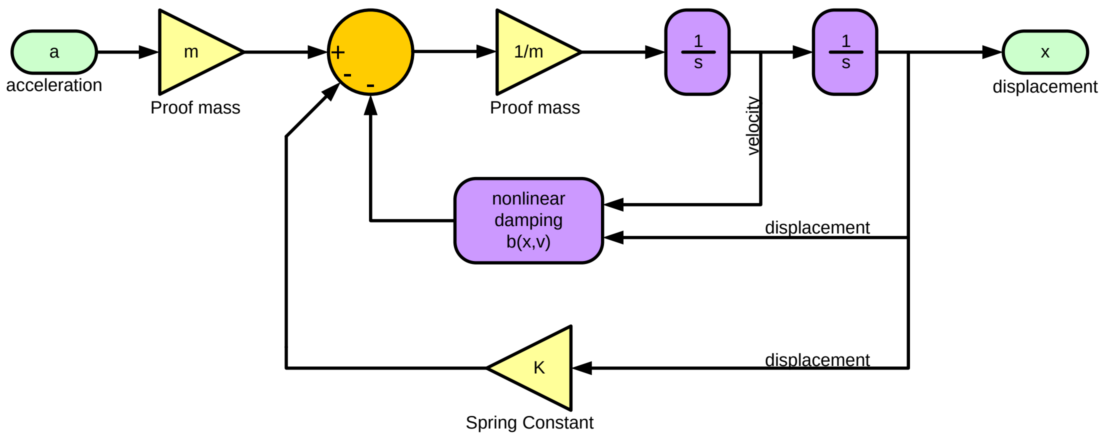

Figure 2.3: Second order model of an accelerometer with nonlinear damping.

2.2.1 Calculation of Total Mass

Total mass of the accelerometer is an important parameter while determining the operation range and mass residual motion of the accelerometer. With increased mass, amount of force that should be applied by the readout circuit, in order to balance the accelerometer in its rest position also increases. In other words when the proof mass of the accelerometer increases the maximum operation range decreases both in open and closed loop mode of operations.

During the design of an accelerometer total mass of the suspended structure can be calculated by adding the masses of the fingers and the proof mass. Sometimes during the design due to area limitations or space requirement for fingers, total mass can be larger than needed. In order to decrease mass, etch holes can be placed throughout the proof mass. Figure 2.4 shows the suspended structures of accelerometer with etch holes. Total mass of this structure can be calculated by adding the masses of the regions colored with blue. Note that while calculating the total mass, masses of the springs and anchors can be neglected.

The total mass of the accelerometer given in figure 2.3 can be calculated as follows:

$$m = \left[(PMW.PML) + \left(2.N_{finger}.FL.FW\right) - (N_{etchhole}.\pi.r_{etchhole}{}^{2})\right].h.d \qquad (2.7)$$

where PMW is the width of the proof mass, PML is the length of the proof mass, N_{finger} is the total number of fingers on each side of the accelerometer, FL is the length of the fingers, FW is the width of the fingers, $N_{etchhole}$ is the number of etch holes opened on the proof mass, $r_{etchhole}$ is the radius of each etch hole opened on the proof mass, h is the thickness of the structure and d is the density of silicon.

For some different accelerometer topologies fingers and the proof mass may not be determined as distinctively as given in the example above. But the general idea of calculating the mass of the accelerometer still holds.

2.2.2 Flexure Design and Spring Constant Estimation

In MEMS microstructures like accelerometers, gyroscopes and resonators, spring constant of the structure play an important role in determining the performances of the sensors. The performance of the sensor is related with the easiness in the movement of the proof mass in the sensitive axis and also with the difficulty in the movement of the proof mass in the other axes. Hence, determining the spring constants in all directions is an important design step.

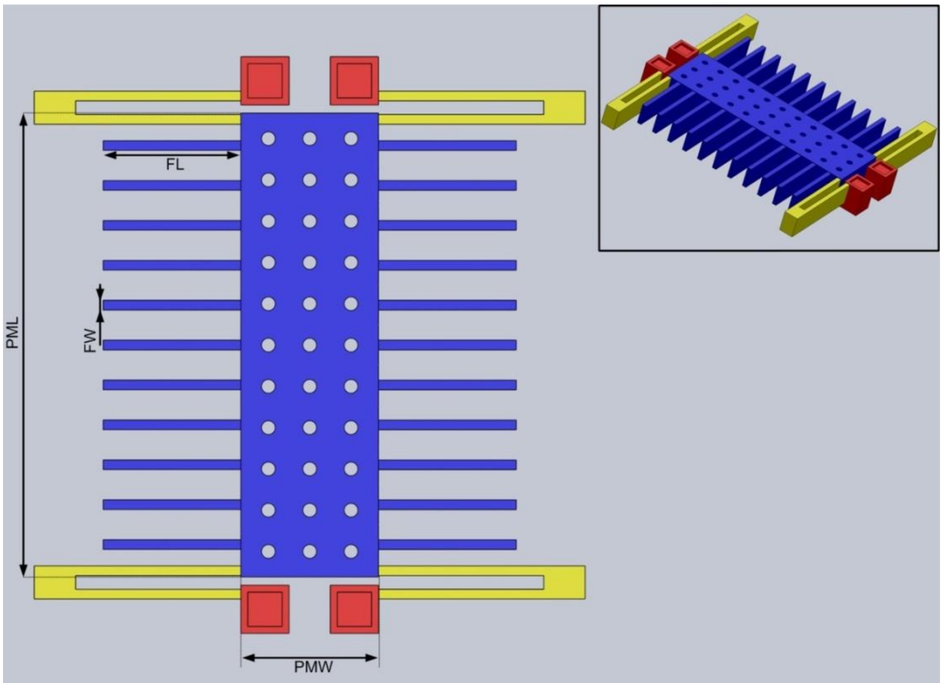

Figure 2.4: Suspended structures of an accelerometer with etch holes.

The spring constant in its relative axis depends on how the beam is bent. If the beam bends in a way that the parallelism of the fixed end and the free end is disturbed, it is called "Deflection of a Cantilever (unguided) Beam". If the parallelism is preserved, then the condition is called "Deflection of a Guided Beam." Figure 2.5 shows both guided and unguided beams in their deflected forms.

Deflection of an unguided cantilever beam condition is the basic condition to be analyzed. (Figure 2.5.a) The spring constants for this condition along each direction are calculated as:

$$k_x = \frac{Ehw^3}{l^3} \qquad k_y = \frac{Ehw^3}{4l^3} \qquad k_z = \frac{Ewh^3}{4l^3} \tag{2.8}$$

where the index of spring constant denotes the direction of the applied force which bends the beam, E is the Young's Modulus, h is the thickness, w is the width, and l is the length of the beam.

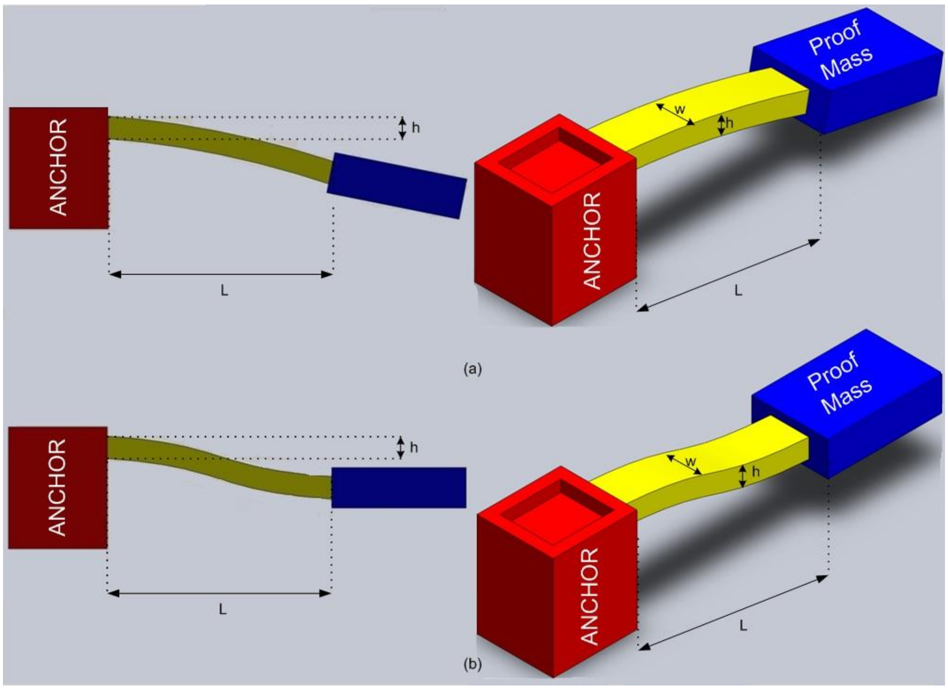

Figure 2.5: Guided and unguided beams in their deflected forms. (a) Unguided beam (b) Guided beam

Spring constants of more complex architectures having many springs can be calculated by concept of connecting springs in parallel and series configurations. Figure 2.6 shows series and parallel connected springs and the resulting spring constants of each configuration. In case figure 2.6.a springs are connected in parallel configuration. Equivalent spring constant for this case can be calculated by adding the individual spring constants as:

$$k_{eq} = k_1 + k_2 \tag{2.9}$$

When the springs are connected in series as given in figure 2.6.b, then the equivalent spring constant of the structure can be calculated as:

$$k_{eq} = {k_1 . k_2}\big/{k_1 + k_2} \tag{2.10}$$

By knowing the spring constant of each beam individually, spring constant of all complex structures can be calculated using the concepts of series and parallel connection of springs.

Spring constant of a guided beam can be calculated as series connection of two half length unguided beams. Figure 2.7 shows a guided beam divided in two unguided segments for the ease of spring constant calculation. In this form the two segments are assumed to be two separate unguided springs connected in series configuration and the spring constant is calculated as given in equation 2.11.

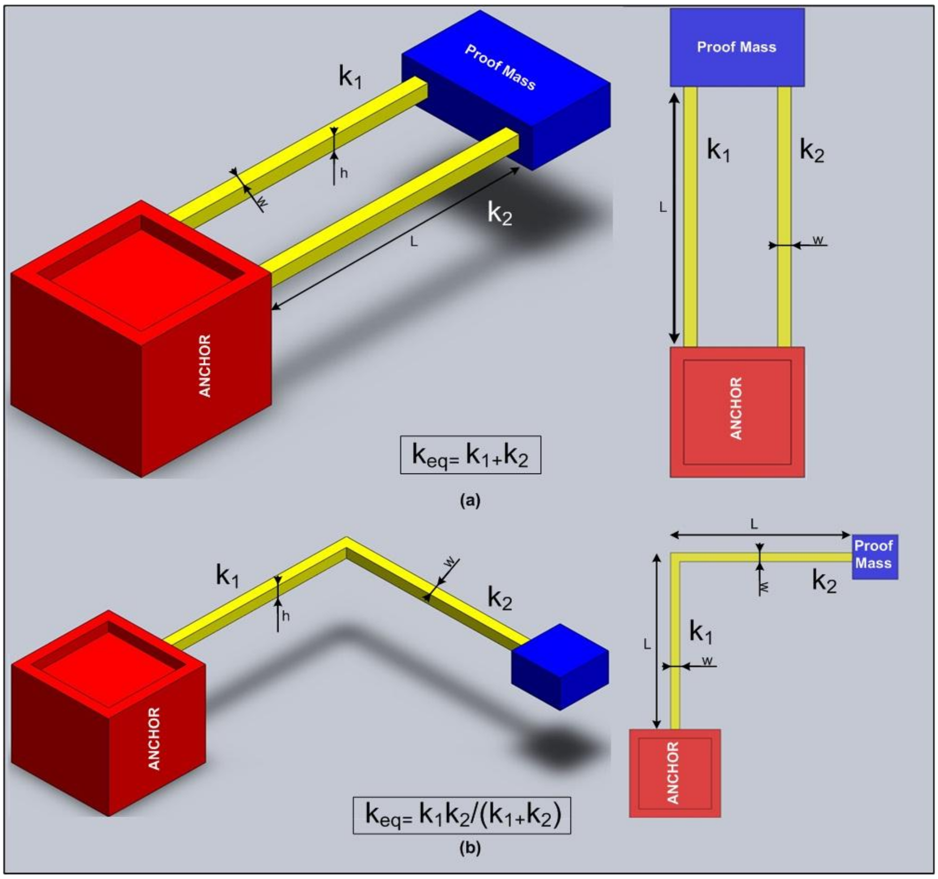

Figure 2.6: Series and parallel connected springs and the resulting spring constants of each configuration (a) springs in parallel configuration (b) springs in series configuration

$$k_1 = k_2 = k = \frac{Ehw^3}{4l^3} \quad ; \quad l = \frac{L}{2} \tag{2.11}$$

$$k_{eq} = \frac{k_1.k_2}{k_1 + k_2} = \frac{k}{2} \tag{2.12}$$

$$k_{eq} = \frac{Ehw^3}{L^3} \tag{2.13}$$

where k_1 and k_2 are the spring constants of each unguided segment of the guided spring, E is the Young's Modulus, h is the thickness, w is the width and L is the length of the spring.

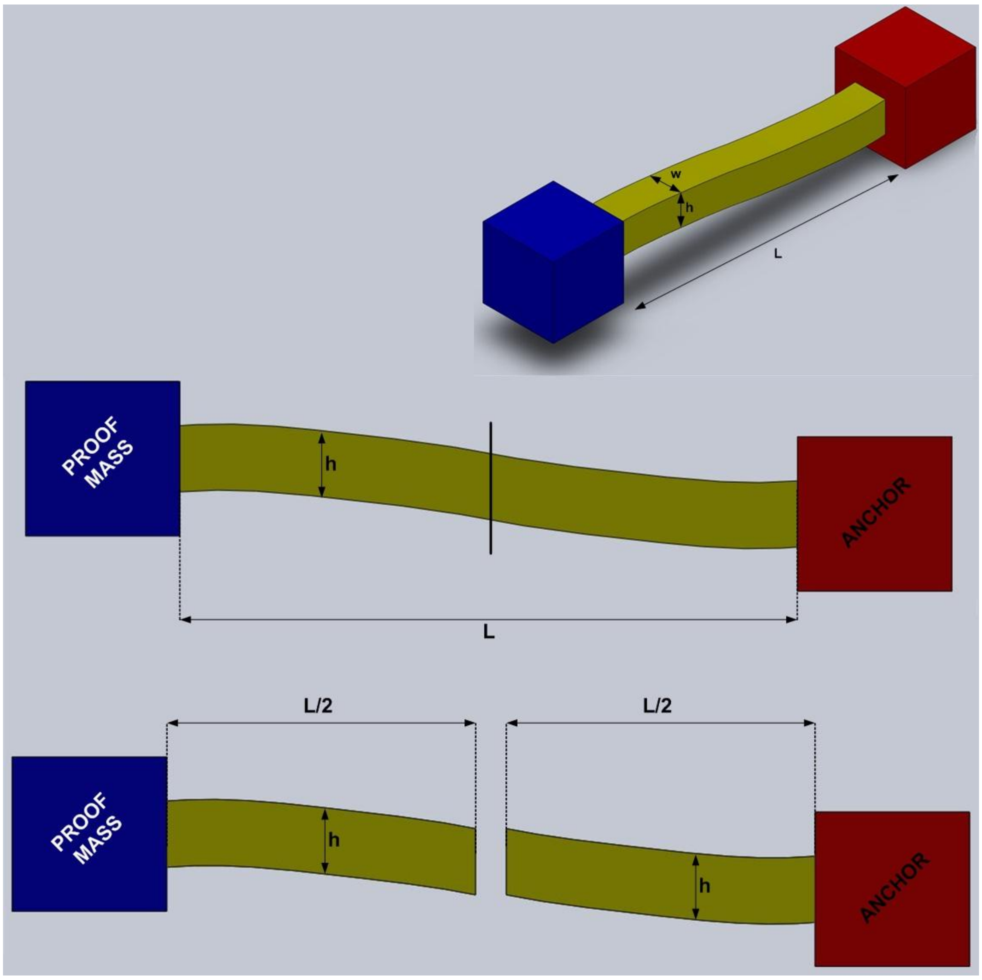

Figure 2.7: Series connected half clamped beams forming a fixed-guided end beam.

Spring constants for various shape beams can be extracted similarly using parallel and series connection of different springs. Figure 2.8 shows lateral beam structures used in this thesis study and calculated respective spring constants. One important note is that the free ends of these beams move in a way that the parallelism of the free end with respect to the fixed end is preserved. This can be achieved by symmetrical beam allocations around the proof mass. Another important note is the rigidity of the truss regions. If the truss regions remain rigid when the beam deflects, we assume that all the sub-beams behave as guided beams. In this study, the truss region widths are designed to be at least 4 times wider than the beam widths to preserve the rigidity of the truss regions.

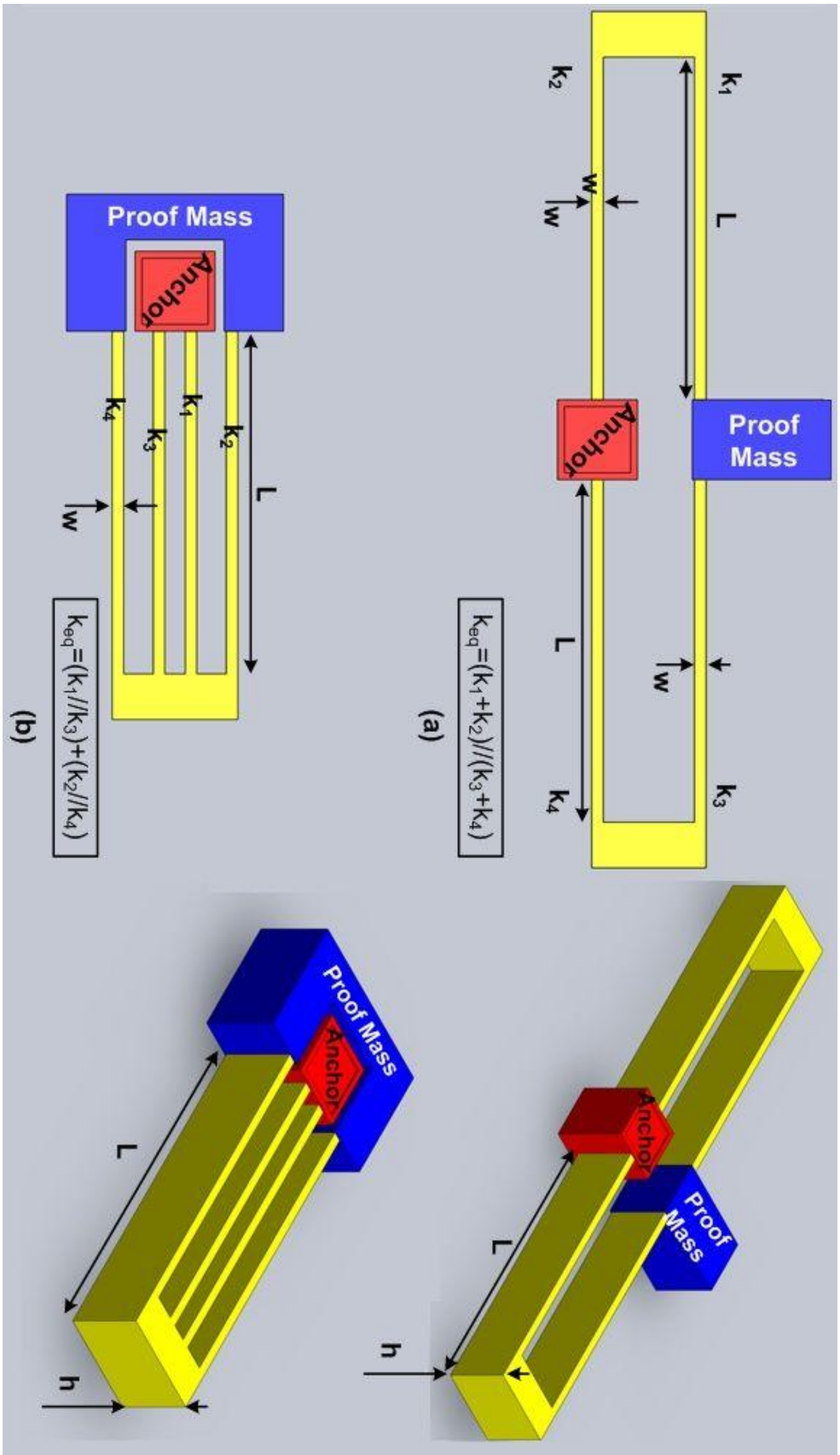

Figure 2.8: Different spring structures used in this study and calculated resultant spring constants.

2.2.3 Damping Coefficient Estimation

Damping coefficient includes all energy dissipative effects during the operation of a micromechanical device. These effects may be the viscous air damping, structural material losses, energy loss through the anchors, etc. At atmospheric pressure, viscous air damping is the dominant dissipative process. At vacuum levels, the effect of air damping can be neglected but then the other dissipative processes, most of which are related with the structural material, determines the damping coefficient. The losses associated with the structural material require deep mechanical analysis, and extend beyond the scope of this thesis work.

The motion of a typical lateral accelerometer is in the direction parallel to the substrate surface. The major damping mechanism for a laterally moving accelerometer operating under the atmospheric pressure is the squeeze film damping between the capacitive fingers. There are also other minor damping mechanisms like slide film damping which can be neglected compared with the squeeze film damping for a micromachined lateral accelerometer. Figure 2.9 illustrate both slide and squeeze film damping mechanisms. In slide-film damping, the motion of the mass is in lateral direction and there is a friction between the upper & lower surfaces of the mass and the air molecules. In squeeze-film damping, the motion of the mass is in such a way that the air molecules between the mass and the substrate are squeezed and they try to escape from the decreasing volume under the mass.

In order to calculate the damping coefficient for a micromachined accelerometer, Couette damping and squeeze film damping can be calculated separately and added in order to find the total damping of the system. Assuming a Newtonian Gas existence in the environment, Couette and squeeze film damping can be calculated as follows [72]:

$$b_{Couette} = \mu_p . p . \frac{A}{y_0} \tag{2.14}$$

where $\mu_p = 3.7 \times 10^{-4}$ is the viscosity constant for air, p is the air pressure, A is the overlap area of the plates, y_0 is the plate separation, and

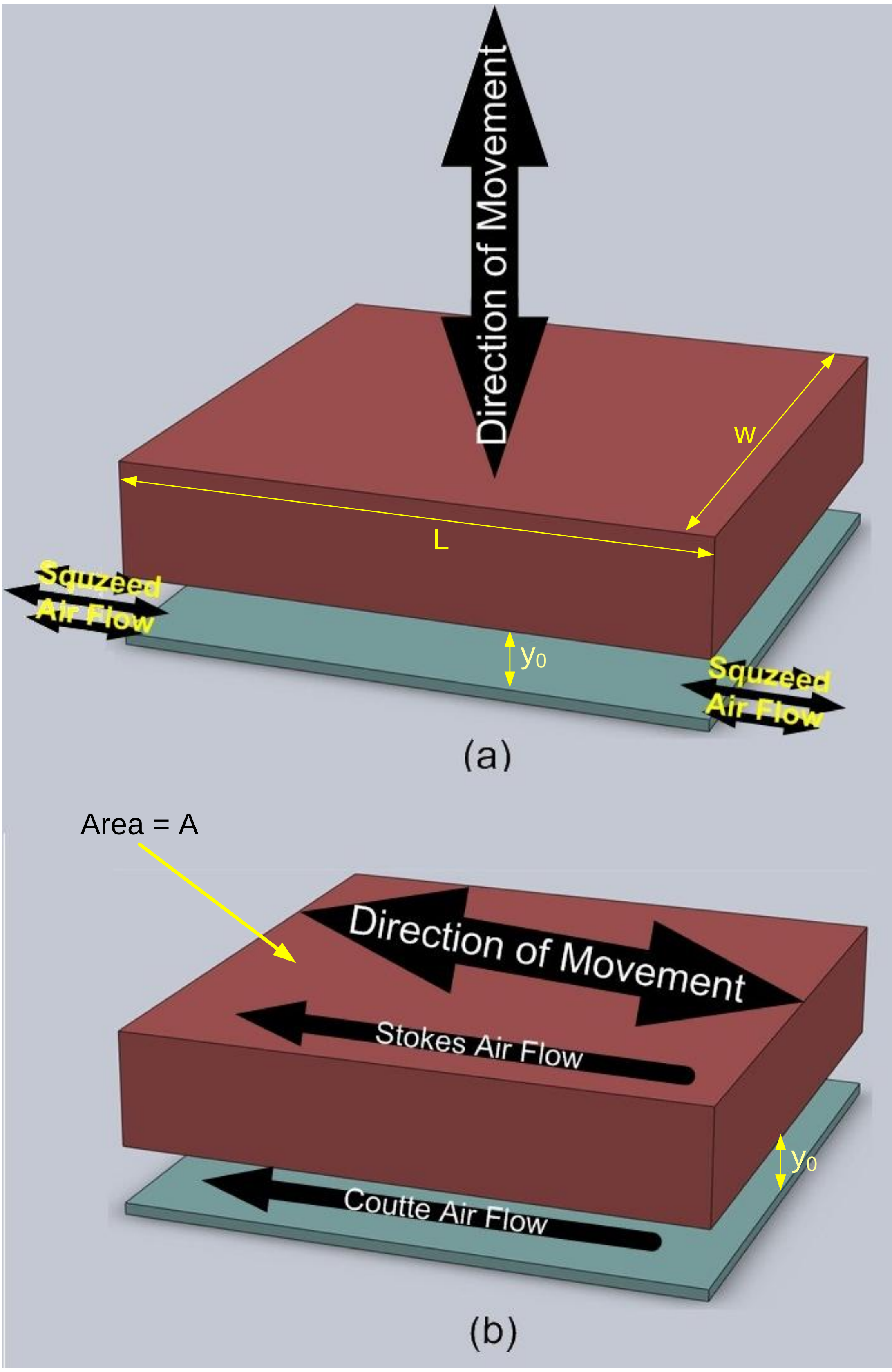

Figure 2.9: Illustration of the (a) slide-film and (b) squeeze-film damping mechanisms.

$$b_{Squeeze} = \mu_p . p . \frac{7 . L . w^3}{y_0^3} \quad (2.15)$$

where L is the length of the capacitive fingers and w is the width of the squeezed area.

Using the above formulas, the damping associated with the capacitive fingers on both sides of the accelerometer is calculated and added together to find the total damping coefficient of the accelerometer. Therefore total damping of a lateral capacitive accelerometer can be calculated as:

$$b = \mu_p . p . \left(\frac{A_{pm}}{y_0} + \frac{14 . N . L . h^3}{g_0^3} + \frac{14 . (N-1) . L . h^3}{g_1^3} \right) \quad (2.16)$$

where μ_p is the viscosity of the air, p is the ambient pressure, A_{pm} is the surface area of all suspended structures, y_0 is the spacing between the accelerometer mass and glass substrate, N is the number of capacitive fingers, L is the length of capacitive fingers, h is the structural thickness, g_0 is the small spacings and g_1 is the large spacings between the capacitive fingers.

2.3 Modeling of Accelerometer Readout Circuits

Two types of readout circuits can be used to detect the amount of capacitance change of the accelerometers. First type is the open-loop readout architecture which directly converts the amount of capacitance change into analog output voltage [4], [73]. This topology has a simple architecture and low noise but poor linearity, limited operation range and narrow bandwidth. Second type is the closed loop $\Sigma - \Delta$ type readout circuit architecture which detects the acceleration from the deflection of the proof mass and applies a feedback voltage to the accelerometer proof mass in order to stabilize it in its rest position [74], [75]. Closed loop readout architecture have improved bandwidth, linearity and dynamic range with digital bit stream output. On the other hand introduction of closed loop control decreases the resolution of the system [4]. In this section of the thesis both readout architectures will be described in detail together with their advantages and disadvantages.

2.3.1 Open Loop Readout Architecture

Open loop topology is a simple current to voltage converter readout architecture. In this type of architecture, differential capacitance change at the accelerometer is converted to a proportional analog voltage at the front-end charge integrator block. This analog signal has voltage pulses with magnitudes proportional to the applied acceleration, but has small pulse widths. In order to increase the pulse width and converge to a DC signal with same magnitude a sample and hold block is used which also increases the gain of the circuit. Finally with a low pass filter, higher order sinusoidal components are filtered and the acceleration component around 0Hz is extracted. In order to have a better SNR, cut-off frequency of the low pass filter should be decreased and sharpened as much as possible.

The charge integrator at the input detects the charge difference between upper and lower capacitances when two square waves with 180^o phase shift are applied. The integrated charge on the integration capacitance is read as a voltage value from the output of the integrator. Figure 2.10 shows the schematic diagram of the charge integrator circuit.

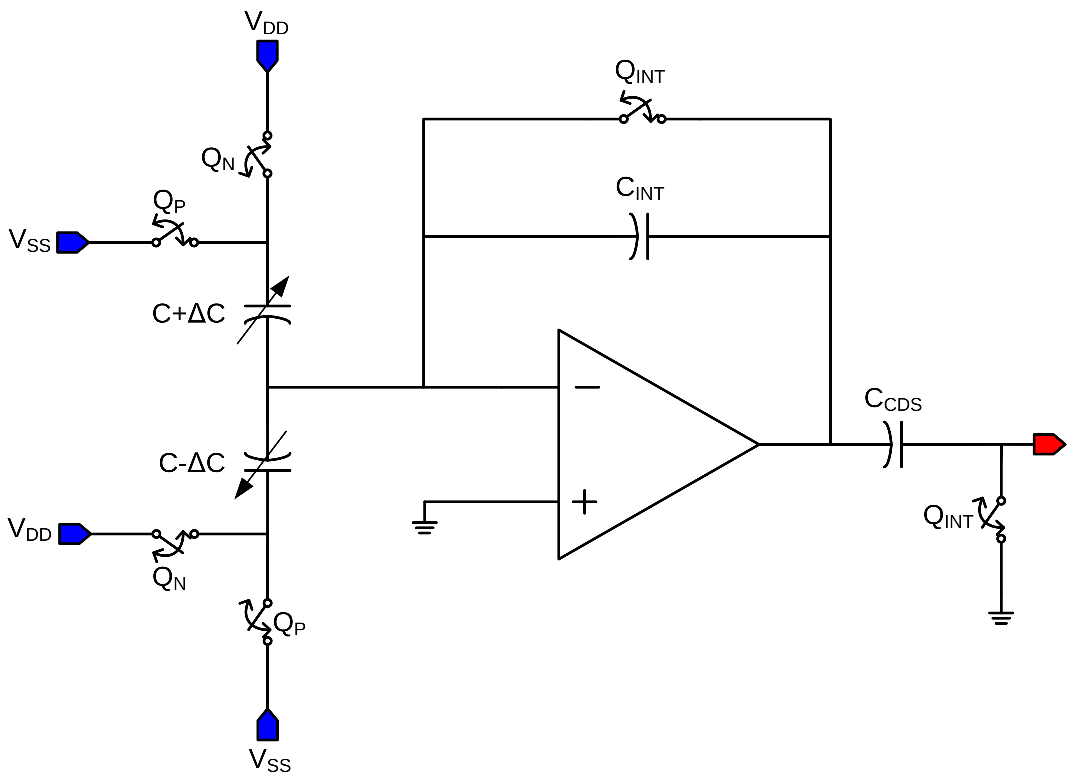

Figure 2.10: Schematic diagram of the charge integrator.

If the capacitive increase in the upper capacitance is ΔC_1, and the capacitance change in the lower capacitance is ΔC_2 then;

$$\Delta C_1 = \frac{\varepsilon_0 . A}{d-x} - \frac{\varepsilon_0 . A}{d} = \frac{\varepsilon_0 . A . x}{d^2 - x . d} \tag{2.17}$$

and

$$\Delta C_2 = \frac{\varepsilon_0 . A}{d} - \frac{\varepsilon_0 . A}{d+x} = \frac{\varepsilon_0 . A . x}{d^2 + x . d} \tag{2.18}$$

where x denotes change of gap between two parallel plates, d is the gap spacing between fingers, ε_0 is the permittivity of the air and A is the capacitance overlap area of the accelerometer.

The operation of the charge integrator block can be divided into two cycles. In charging mode upper bias node is 2.5 volts and lower bias node is -2.5 volts and the total charge on the capacitors is:

$$Q = (V_{DD} - 0)(C + \Delta C_1) + (V_{SS} - 0)(C + \Delta C_2) + (V_{out1} - 0)C_{int} \tag{2.19}$$

In the discharging mode upper bias node is -2.5 volts and lower bias node is 2.5 Volts. Total charge on the capacitors in this mode is:

$$Q = (V_{SS} - 0)(C + \Delta C_1) + (V_{DD} - 0)(C + \Delta C_2) + (V_{out2} - 0)C_{int} \tag{2.20}$$

Total charges in these two cases must be equal. Therefore by equating these two we can conclude that:

$$\begin{aligned} &V_{DD}(C + \Delta C_1) + V_{SS}(C + \Delta C_2) + V_{out1}C_{int} \\ &\qquad = V_{SS}(C + \Delta C_1) + V_{DD}(C + \Delta C_2) + V_{out2}C_{int} \end{aligned} \tag{2.21}$$

$$(V_{DD} - V_{SS})(\Delta C_1 - \Delta C_2) = C_{int}(V_{out2} - V_{out1}) \tag{2.22}$$

$$\Delta V_{out} = \frac{(V_{DD} - V_{SS}).(\Delta C_1 - \Delta C_2)}{C_{int}} \tag{2.23}$$

The important design issue in this type of readout architecture is that the operation range of the accelerometer would be limited by the output of the charge integrator if its value is not chosen properly. The proper value for the charge integration capacitance should be selected such that the maximum possible capacitance change in one direction should create a voltage not larger than $(V_{DD} - V_{SS})/2$ volts. Otherwise the front-end amplifier of the readout circuit saturates at the first stage electronically. This criterion for the open loop readout design can be written as:

$$\frac{C_{int}}{2} > (\Delta C_{1.MAX} - \Delta C_{2.MAX}) \tag{2.24}$$

There is an additional CDS capacitance at the output of the charge integrator. Since the op-amp of the charge integrator is non-ideal, input voltage variation affects the output of the circuit directly. In order to cancel this effect, CDS capacitance is used. CDS capacitance at the output of the circuit is charged with the offset voltage of the op-amp when the integrating capacitance is reset. When the circuit starts to integrate, previously stored offset voltage is automatically subtracted from the output of the circuit which eliminates the input offset voltage. With this method any variation at the input of the charge integrator can be cancelled.

The stage after the charge integrator is a sample and hold circuit. The duty cycle of the charge integrator output is very low. If the charge intergrator output is filtered directly the gain of the circuit would also be very low. Before filtering the signal a Sample and Hold circuit is used to increase the duty cycle of the integrator output. Since the DC component of an AC signal is equal to the average value of that signal, by increasing the duty cycle DC component of the signal can also be increased. Figure 2.11 shows a schematic of a sample and hold circuit. When SnH1 switch is closed and SnH2 switch is opened, sample and hold circuit samples its input to the output until the next clock pulse arrives.

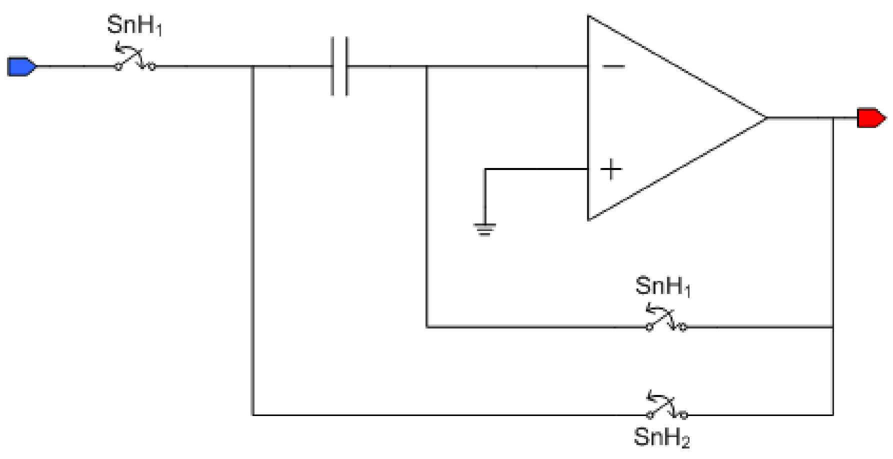

Figure 2.11: Sample and hold stage used in the open loop readout circuit.

After the duty cycle (gain) of the system is increased with the sample and hold block, a low-pass filter is used at the output stage of the circuit in order to obtain the acceleration data. Figure 2.12 shows the structure of a second order Sallen-Key low pass filter.

Transfer function of this type of Low pass filter is as given in (2.25). Gain of the filter is determined by the factor at the numerator of the transfer function. When R4 is selected as zero, the gain of the circuit becomes unity which also decreases the layout area of the circuit.

$$H(f) = \frac{\frac{R_3 + R_4}{R_3}}{(j2\pi f)^2(R_1R_2R_3R_4) + j2\pi f\left(R_1C_1 + R_2C_1 + R_1C_2\left(-\frac{R_4}{R_3}\right)\right) + 1} \tag{2.25}$$

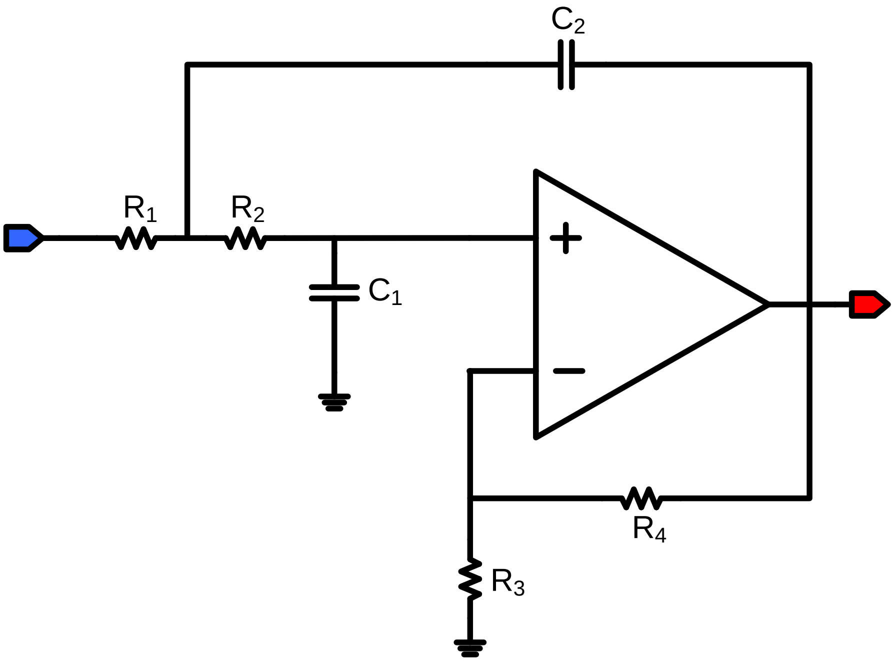

Figure 2.12: Second order Sallen-Key Low-Pass Filter structure.

Corner frequency of the circuit is determined as:

$$FSF.f_c = \frac{1}{2\pi\sqrt{R_2R_3C_1C_2}} \tag{2.26}$$

where FSF stands for the Frequency Scaling Factor, and "f_c" represents the corner frequency. The FSF factor changes according to the structure of the filter and it can be taken as "1" in this case. Therefore the corner frequency of this low pass filter can be directly calculated.

Another important parameter of a Low-Pass filter is the quality factor which can be calculated as;

$$Q = \frac{\sqrt{R_2 R_3 C_1 C_2}}{R_3 C_1 + R_2 C_1 + R_3 C_1 \left(-\frac{R_3 + R_4}{R_3}\right)} \tag{2.27}$$

Low pass filtering block described above is the output stage of the open loop readout circuit architecture. Figure 2.13 shows the overall open loop readout architecture together with the accelerometer model.

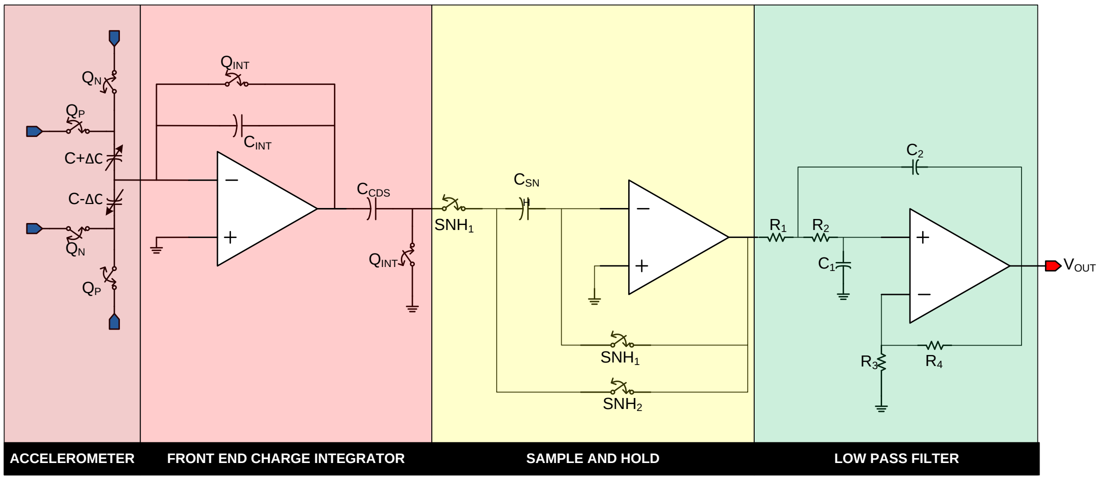

Figure 2.13: The overall open loop readout architecture together with the accelerometer model.

This readout architecture is very simple and can easily be implemented. Since it is operating in open loop mode and the circuit complexity is minimum, noise of the system is just limited with the mechanical noise of the accelerometer and the switching noise of the front-end readout circuit. Therefore this type of reading is suitable for low noise applications. On the other hand, due to the non-linear nature of the sensitivity of the capacitances, accelerometer behaves non-linearly for the high measurement ranges. The bandwidth of the system is also limited either with the accelerometer or low pass filter, both of which could not exceed few kHz.

MATLAB model of the circuit is built in order to perform simulations to understand the theoretical performance limits of the accelerometers like bandwidth, non-linearity, and operation range. Figure 2.14 shows the MATLAB model of second order accelerometer model together with its open loop readout circuit.

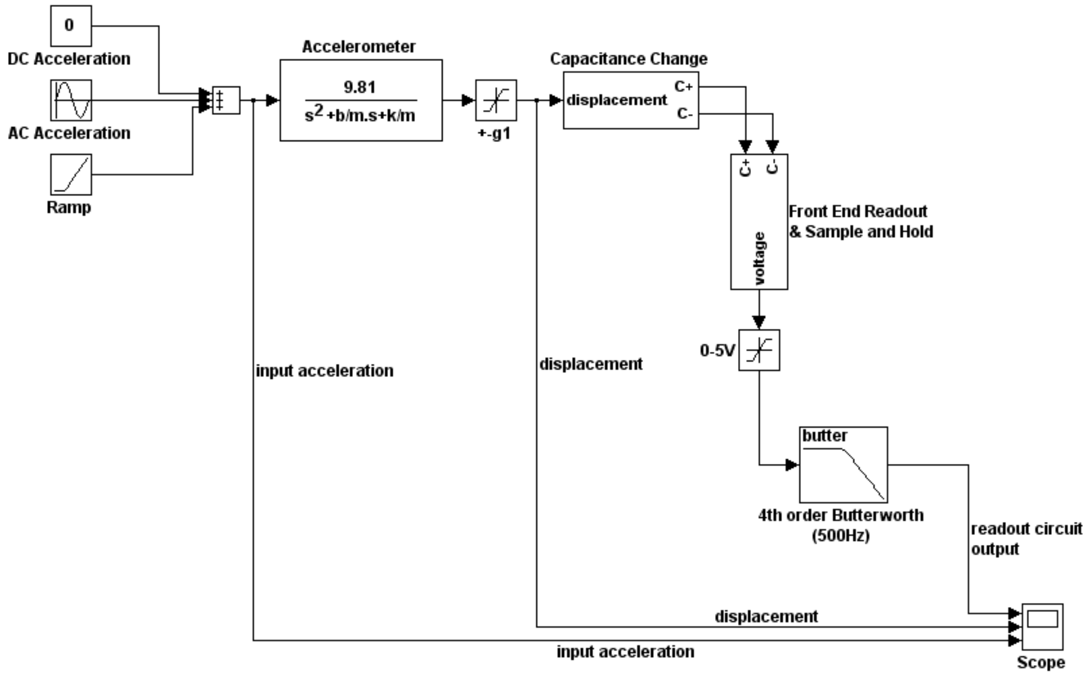

Figure 2.14: MATLAB model of second order accelerometer model with its open loop readout circuit.

During the parameter analysis of accelerometers MATLAB simulations of the open loop accelerometer system is performed on the model given in figure 2.13. Details of these analyses for each accelerometer parameter are given in chapter 3 of this thesis.

2.3.2 Closed Loop Readout Architecture

In the open loop readout structure there were various problems related with the performance of the system that should be solved. The major problems were linearity and the operation range. In accelerometers with open loop readout circuit, output voltage will always be linearly related with the capacitance change of the accelerometer. But the capacitance change of the varying gap accelerometers is non-linear due to its nature. Limitation on the bandwidth of the accelerometer in open loop is another important issue. The low-pass filter at the output of the readout circuit, limits the bandwidth which makes it unusable in most real time applications. In order to solve these problems related with the open loop, closed loop readout architecture can be used [77].

In closed loop readout architecture, readout circuit detects the movement of the accelerometer as in open loop case but in addition to open loop circuit it applies electrostatic force to the proof mass of the accelerometer to prevent its movement. When the external acceleration is increased the duration of force applied to the proof mass also increases and the circuit detects the amount of acceleration as the duration of the force applied to the proof mass. Another advantage of closed loop circuit is the fully digital output with acceleration information sampled at high frequency carrier signal. This provides us the ability to use the output of the circuit directly without any need for analog-to-digital conversion.

Although this circuit has many advantages, poor resolution is the most important disadvantage of the force feedback operation. Since the circuit continuously applies force in order to hold proof mass in its rest position, there is always an oscillation in the proof mass even if there is no input acceleration. This characteristic of the closed loop readout circuit adds a large noise to the output of the system.

Figure 2.15 shows the block diagram of the first stage charge integrator of the second order sigma-delta readout circuit. This block is very similar to the charge integrator stage in the open loop architecture, but instead of single ended output, the integrators operate in differential manner. Charge injected from the capacitors is needed to be integrated in small time duration, since most of the clock period is occupied with the feedback phase in order to increase the measurement range of the accelerometer. In this stage capacitance change is converted to voltage in the differential OTA via the integrating capacitances. The value of integrating capacitances has a direct impact on the sensitivity and resolution of the closed loop accelerometer system. In this circuit schematic the output voltages V_+ and V_- can be calculated as:

$$V_+ = \frac{C_+ - C_{ref}}{C_{int}} . (V_{DD} - V_{SS}) \tag{2.28}$$

$$V_- = \frac{C_- - C_{ref}}{C_{int}} . (V_{SS} - V_{DD}) \tag{2.29}$$

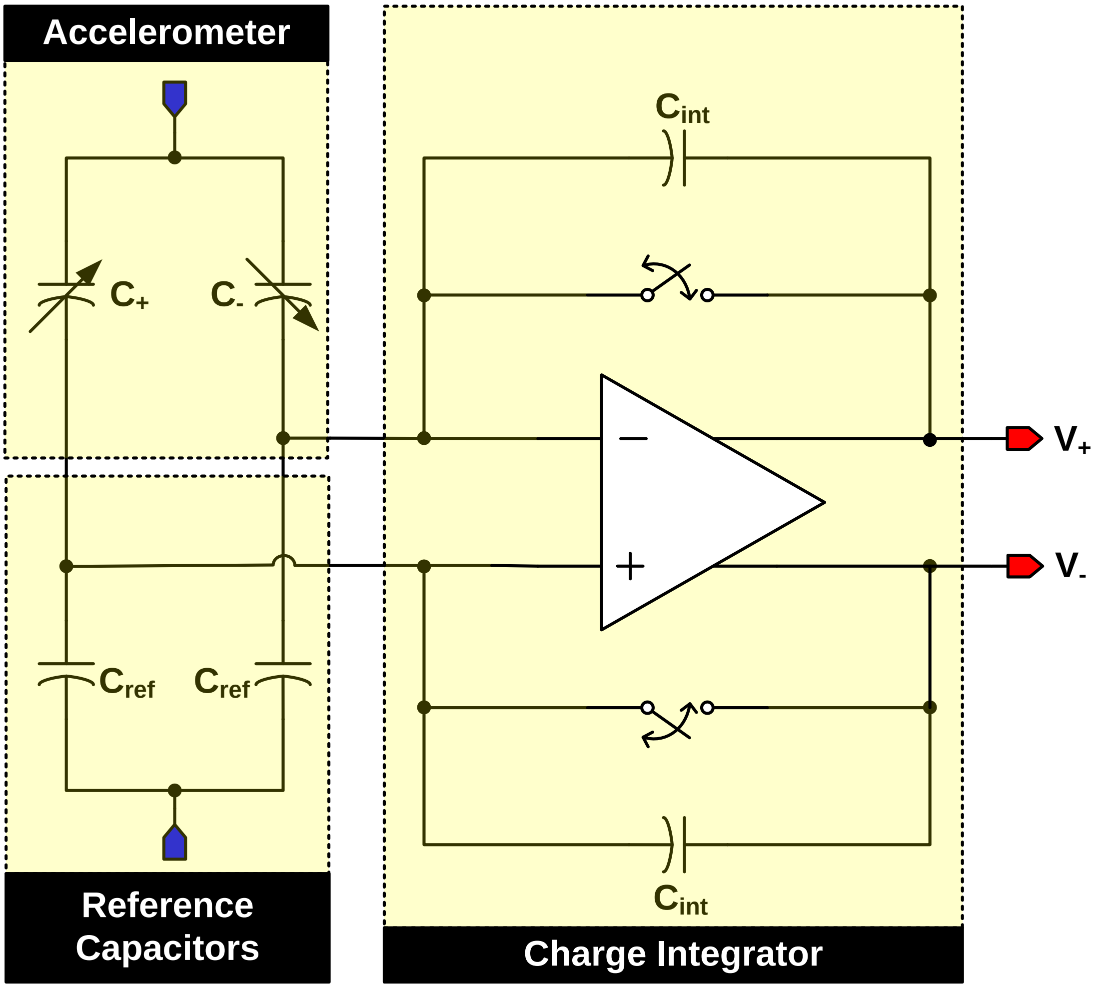

Figure 2.15: Block diagram of typical second order sigma-delta readout circuit

Figure 2.16 shows the block diagram of a compensator circuit used after the charge integrator. Even during the zero input state of the accelerometer due to continuous non-zero feedback force, accelerometer proof mass makes a small oscillation around its rest position. This movement is called the mass residual motion and it is described in detail in the third chapter of this thesis. In order to decrease this undesired motion, circuit should be derived at very high frequencies. However poles arising from the mechanical structure and readout circuit may cause the system settle at a lower frequency which may cause instability. In order to solve this issue a compensator is added at the output of the charge integrator in order to add a zero to the sigma-delta loop. The output voltage of this compensator can be calculated as:

$$V_{out} = V_n - V_{n-1}\frac{C_1}{C_1 + C_2} \tag{2.30}$$

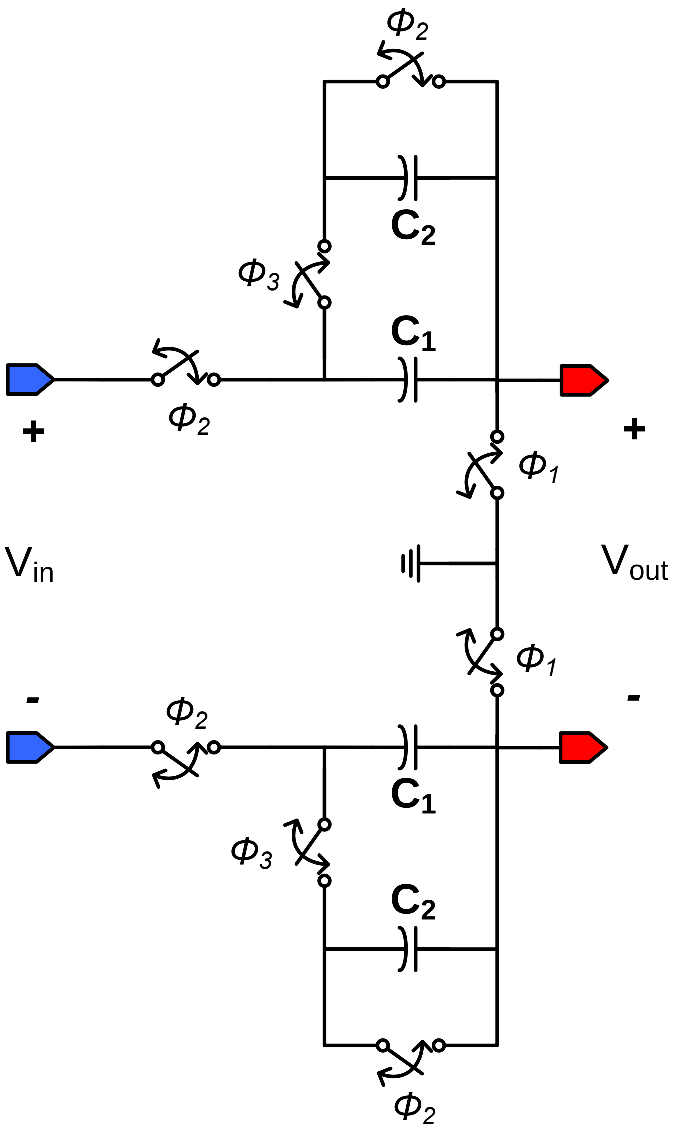

Figure 2.16: Block diagram of the compensator circuit.

A latching comparator is connected at the output of the compensator block as the final stage of the closed-loop sigma delta readout architecture. Comparator should have a latching capability since the two signals that need to be compared appear at a certain interval of the clock pulses. In this interval the two outputs of the compensator block should be compared and the comparator output should be preserved till the next clock cycle. The precision and speed of the latched comparator is also very important to obtain a high sampling rate and high resolution in closed loop sigma-delta modulators.

Differential outputs of the compensator are compared in this stage at very high frequencies and either a "1" or "0" volt logic output is given. This output means that mass of the accelerometer is either deflected in one direction or the other direction. According to the side of the deflection a proper feedback pulse is applied to the proof mass of the accelerometer in order to move it to the opposite direction. With this block closed loop structure of the readout circuit is completed. Figure 2.17 shows the overall closed loop readout architecture together with the accelerometer model.

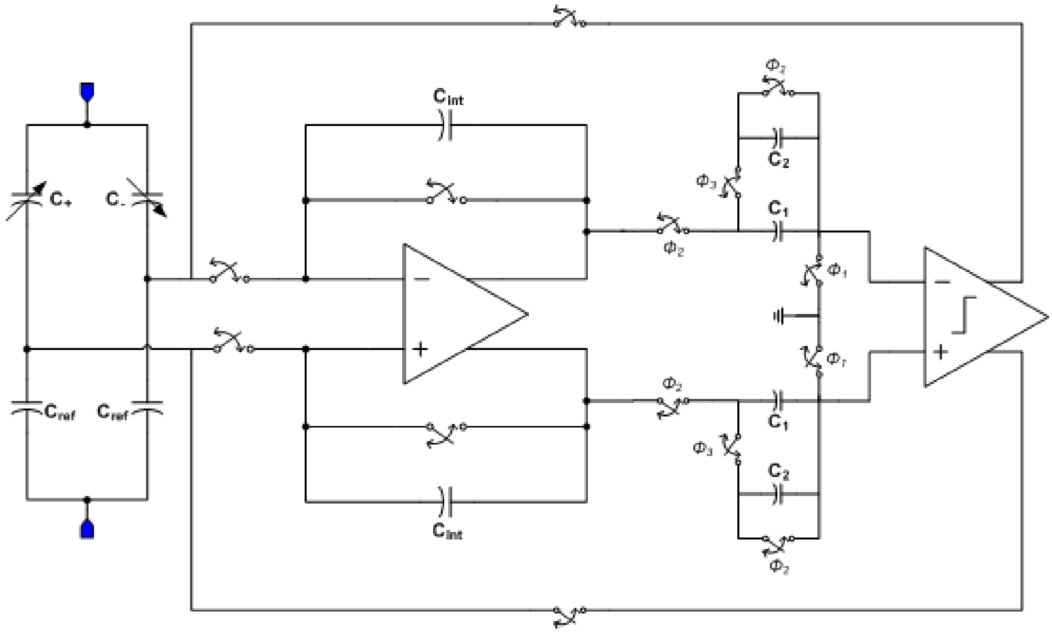

Figure 2.17: Overall closed loop readout architecture together with the accelerometer model.

In closed loop architecture, since the circuit can not be easily formulized like the open-loop case, performing system level simulations before fabrication of the readout circuit and sensor is crucial. For this purpose a detailed MATLAB model is constructed in order to simulate all the important performance parameters. These parameters can be listed as non-linearity, bandwidth, resolution and maximum measurement range. Figure 2.18 shows the overall MATLAB model of the accelerometer and readout circuit which includes all components of the closed loop system. There is also an additional Sinc^3 filter at the output in order to obtain the acceleration data from the one bit pulse stream output. Details of the MATLAB simulations performed for the closed loop architecture are described in section 3 of this thesis.

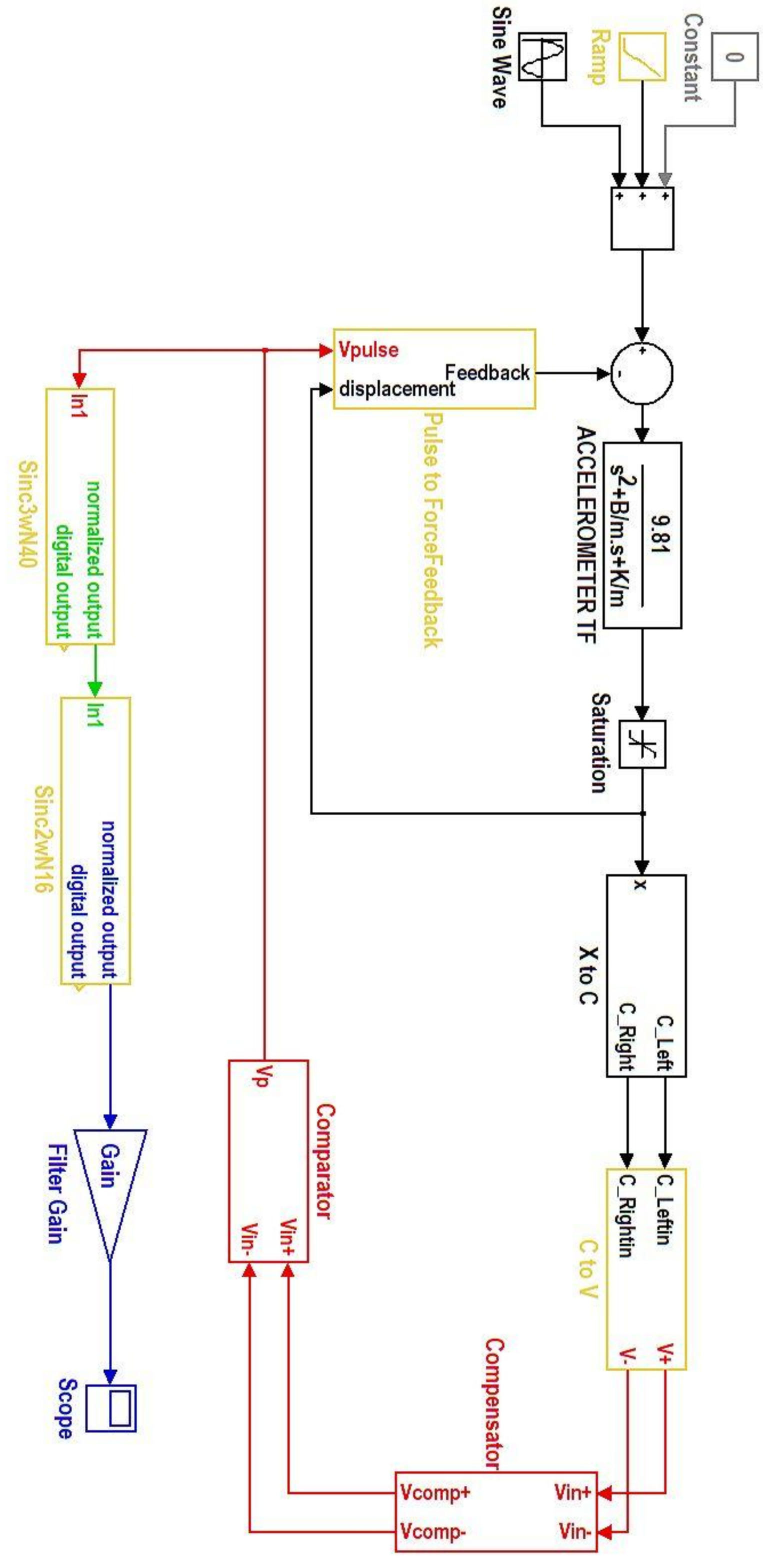

Figure 2.18: Overall MATLAB model of the accelerometer and readout circuit system.

2.4 Summary of the Chapter

In this chapter basic theory of the accelerometers are described in detail. Second order mass, spring and damper model of the accelerometer is given with techniques to calculate each mechanical property. Finally open and closed loop readout architectures are described block by block and the constructed MATLAB models for open and closed loop simulations are presented.

CHAPTER 3

DESIGN OF CAPACITIVE ACCELEROMETER SYSTEMS

Capacitive accelerometers are specifically designed to maximize the change of capacitance with respect to an externally applied acceleration in the direction of its sensitive axis (sensitivity). While increasing the sensitivity, other important parameters of accelerometers should also be taken into consideration. Most important aspects of accelerometers are measurement range, resolution, bandwidth and non-linearity. During the design of a MEMS capacitive accelerometer, trade-offs between each performance parameter should be well understood. In this chapter most important performance parameters of the accelerometers are described in detailed and mechanical and electrical features of the system affecting each performance criteria is analyzed.

3.1 Measurement Range

Measurement range of an accelerometer is the maximum and minimum amount of accelerations that the sensor can detect properly on its sensitive axis. Measurement range concept differs for open and closed loop readout circuit architectures. In open loop mode the spacing between the capacitive fingers determines the operation range of the accelerometer while in closed loop mode it is limited with the amount of feedback force that the circuit can apply.

3.1.1 Open Loop Mode

In open loop mode, accelerometer operation range is limited with the small finger spacing between the capacitive fingers. When acceleration is exerted on the proof mass of the accelerometer, it deflects in the direction such that the capacitances on both sides either increase or decrease. The amount of acceleration where the proof mass is deflected such that the opposing capacitive fingers touch each other is called the maximum measurement range of the accelerometer in open loop mode. Figure 3.1 shows the close-up view of gap and anti-gap spacing of the capacitive fingers. In terms of accelerometer parameters, maximum operation range can be calculated as:

$$Range_{OL} = \frac{k.g_1}{m} \tag{3.1}$$

where k is the spring constant of the accelerometer, g_1 is the small spacing between the capacitive fingers and m is the total mass of the accelerometer.

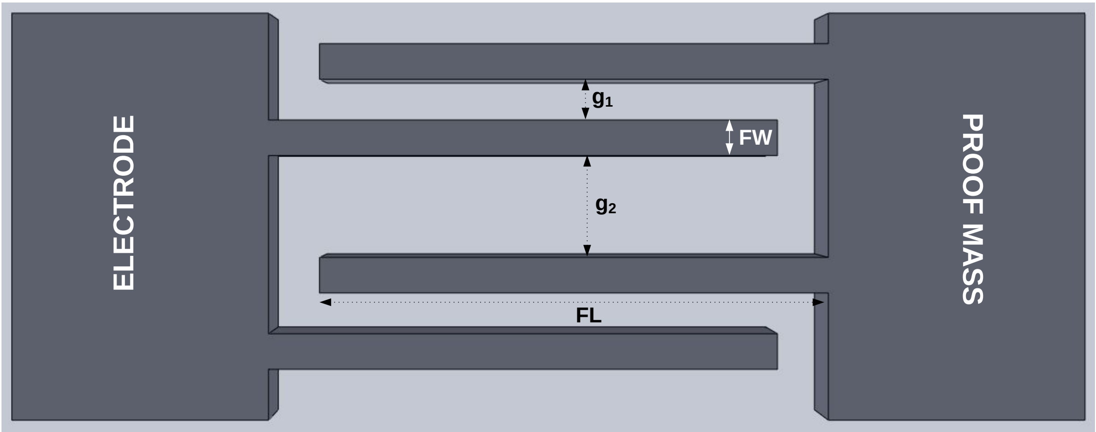

Figure 3.1: Close-up view of gap and anti-gap spacing of capacitive fingers.

In order to verify this issue several MATLAB simulations are performed to see if equation 3.1 reflects the real operation range of the accelerometer system in open loop mode. For this purpose the open loop MATLAB model of the accelerometer given in section 2.3.1 is used. The model used in this simulation used a theoretical accelerometer and a readout circuit with the features given in Table 3.1. According to the equation 3.1 operation range of this accelerometer with open loop readout architecture should be ±25.48g's. Figure 3.2 shows the simulation results of the open loop accelerometer system. An input acceleration of 0-30g is applied to the system and it is seen that the output of the accelerometer readout saturates at ~20.5g's. This is the electrical limit of the accelerometer system where the front-end amplifier output saturates. If the integration capacitance increases, electrical limit also increases and approaches to the mechanical limit which is where the opposing capacitive fingers touch each other. From the simulation results this limit is observed as ~25.5g's where the total proof mass displacement is equal to 2μm's. This simulation results prove that the given measurement range formulation is valid for accelerometers operating with open-loop readout architecture.

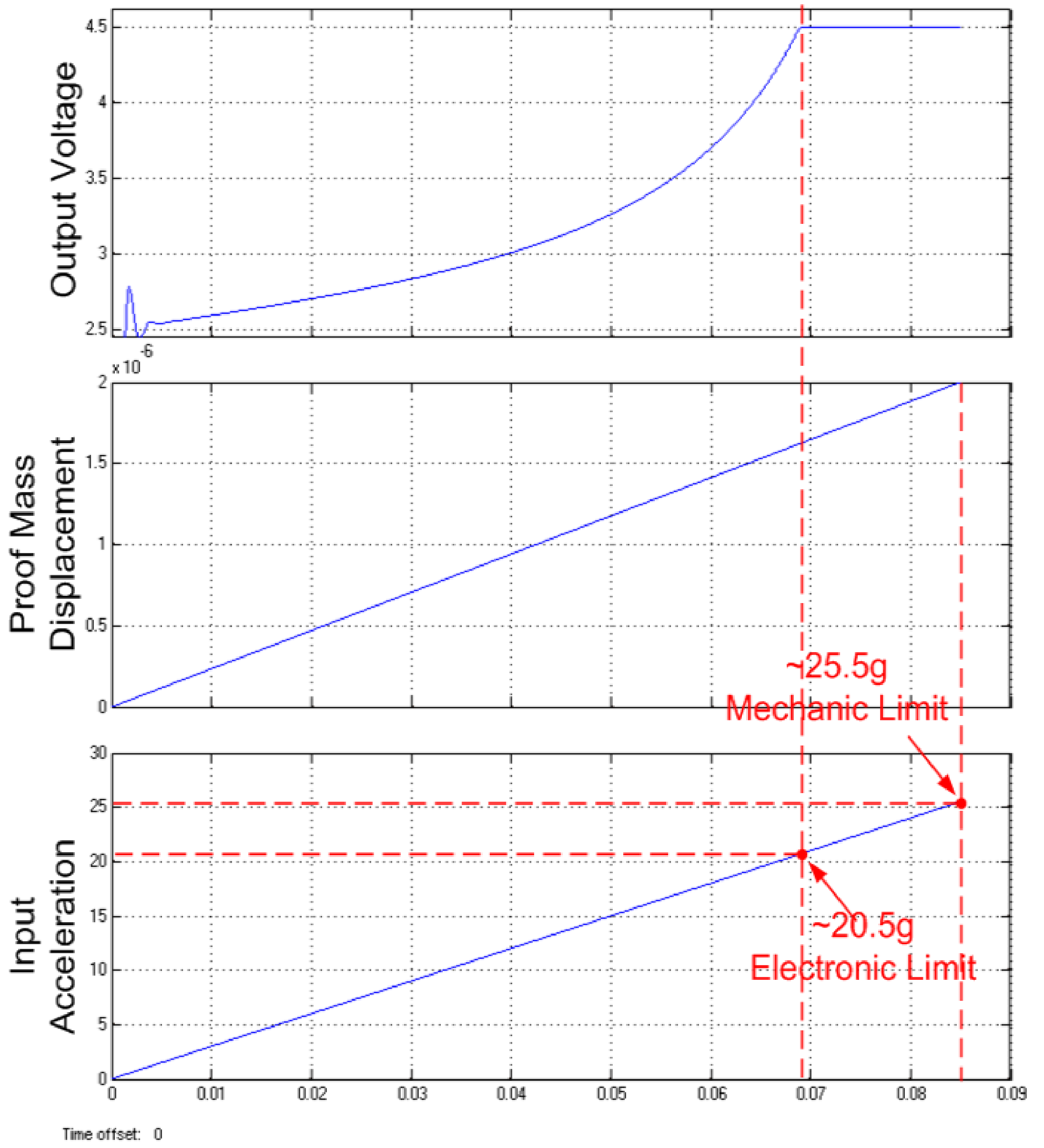

Figure 3.2: Simulation results of the open loop accelerometer system.

3.1.2 Closed Loop Mode

In closed loop mode, readout circuit detects the movement of proof mass resulting from an externally applied acceleration and applies feedback force in order to stabilize proof mass in its rest position. This feedback force is applied as consecutive voltage pulses having either digital high or low levels at high frequencies. The density of high and low voltage pulses at the output bit stream determines the amount of acceleration applied to the accelerometer.

Table 3.1: Theoretical accelerometer and readout circuit features used in open loop circuit MATLAB simulations.

Parameter Name	Value	Parameter Name	Value
Finger Spacing 1	2×10^{-6} m	Spring Constant	50 N/m
Finger Spacing 2	7×10^{-6} m	Damping Coefficient	0.0034
Capacitive Area / finger	5250×10^{-12} m^2	Supply Voltage	5 V
Number of Fingers	300	Integration Capacitance	60 pF
Proof Mass	4×10^{-7} kg		

In closed loop mode, measurement range of the accelerometer is the amount of acceleration that can be suppressed by the feedback force. Applied feedback force is dependent to both readout circuit properties and accelerometer dimensions. Measurement range of the accelerometer in closed loop mode can be calculated as follows:

$$Range_{CL} = \frac{1}{2}.\frac{\partial \mathrm{C}}{\partial \mathrm{x}}.\mathrm{V}^2.\frac{\mathrm{c}}{\mathrm{m}} \tag{3.2}$$

where $\partial C/\partial x$ is the sensitivity of the accelerometer, V is the voltage applied by the readout circuit as the feedback signal, c is the pulse width percentage of the applied feedback voltage and m is the mass of the accelerometer. Feedback signal is a pulse stream having very high frequency compared with the resonance frequency of the accelerometer. Mechanical sensor can't respond to the feedback force directly and resonate at high frequencies. Instead sensor behaves as a low pass filter and only responds to ~0 – 500 Hz band of the feedback force which can be considered as the DC component of the signal. Pulse width percentage parameter in equation 3.2 is placed there in order to calculate the DC component of the signal. Figure 3.3 shows a bit stream output signal sample. For this kind of signal the pulse width percentage can be calculated as in equation 3.3.

$$c = \frac{t_{ff}}{t_i + t_{ff}} \tag{3.3}$$

where t_{ff} is the force feedback time and t_i is the integration time which adds up to a period of the output pulse stream.

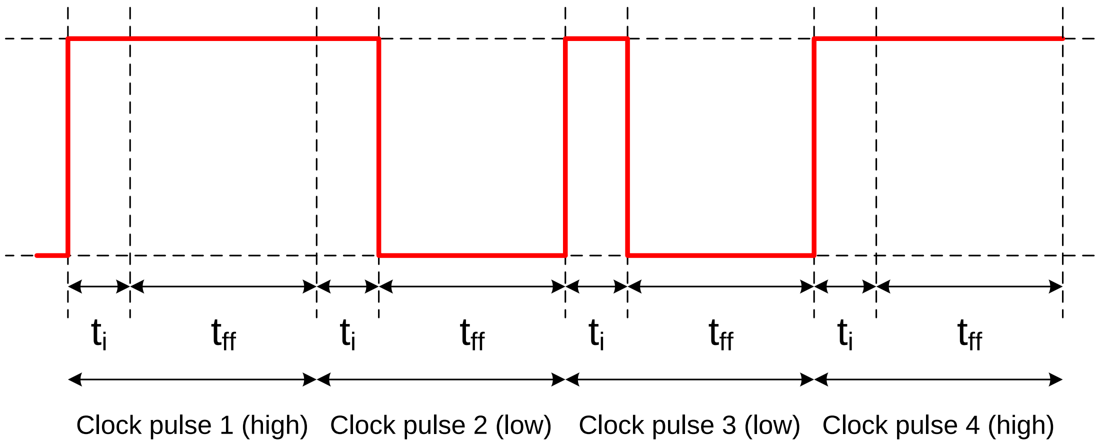

Figure 3.3: A sample of the bit stream output.

Sensitivity of the accelerometer in equation 3.2 is the change of capacitance with respect to the displacement of the mass, and is calculated as:

$$\frac{\partial C}{\partial x} = \frac{N.\varepsilon_0.A}{(g_1 - x)^2} - \frac{N.\varepsilon_0.A}{(g_2 + x)^2} \tag{3.4}$$

where N is the number of capacitive fingers, ε_0 is the permittivity of the air and is equal to 8.85×10^{-12}, A is the capacitive area of each finger, g_1 is the small spacing between capacitive fingers, g_2 is the large spacing between the capacitive fingers and x is the amount of proof mass deflection.

In closed loop mode, the deflection of the proof mass can be neglected for the measurement range estimation since the readout circuit is specifically designed to stop the motion of the accelerometer proof mass. Therefore equation 3.4 can further be simplified to

$$\frac{\partial C}{\partial x} = N.\varepsilon_0.A\frac{(g_2^2 - g_1^2)}{(g_1.g_2)^2} \tag{3.5}$$

It is clear from these results that the operation range is mostly related with the capacitive gap of an accelerometer. In closed loop mode a small gap is preferred in order to increase sensitivity for high operation ranges [78]. The other important parameters are supply voltage and pulse width of the applied feedback voltage. Although mass seems to be an important parameter for operation range adjustment, decreasing the thickness of the accelerometer has no effect on the range since the sensitivity of the accelerometer also decreases with the same amount. Therefore surface area of the proof mass can be used to adjust the operation range of the accelerometer.

In order to verify the measurement range equation for the closed loop mode accelerometer, MATLAB simulations are performed. MATLAB Model used for closed-loop analysis was given in Figure 2.18. Accelerometer used in this simulation was similar to the open-loop case and had the same features. Features of the accelerometer and readout circuit used in the closed loop simulations are given in Table 3.2. With the equation given in 3.2 and 3.5 and assuming the signal pulse width percentage as 60%, the operation range of the accelerometer in closed loop mode is calculated as 56 m/s^2 which is equal to 5.70g. A ramp input is applied to the accelerometer in order to see the response in ±10g range. Figure 3.4 shows the result of the MATLAB ramp input simulation in closed loop mode. It is seen from these simulation results that the output of the closed loop system saturates at 5.76g's. The small difference between the theoretical value and the simulation results can be easily explained by the residual motion of the proof mass due to the applied feedback force.

After verifying the operation range of the accelerometer a sinusoidal acceleration at 10Hz is applied to the accelerometer system with 7g amplitude and the output is monitored. Figure 3.5 shows the response of the closed loop accelerometer system to the sinusoidal acceleration. The output of the system tracks the input acceleration perfectly but for accelerations over 5.7g the output of the system is clipped. This simulation proves the functionality of the MATLAB model and the theoretical calculation of the measurement range.

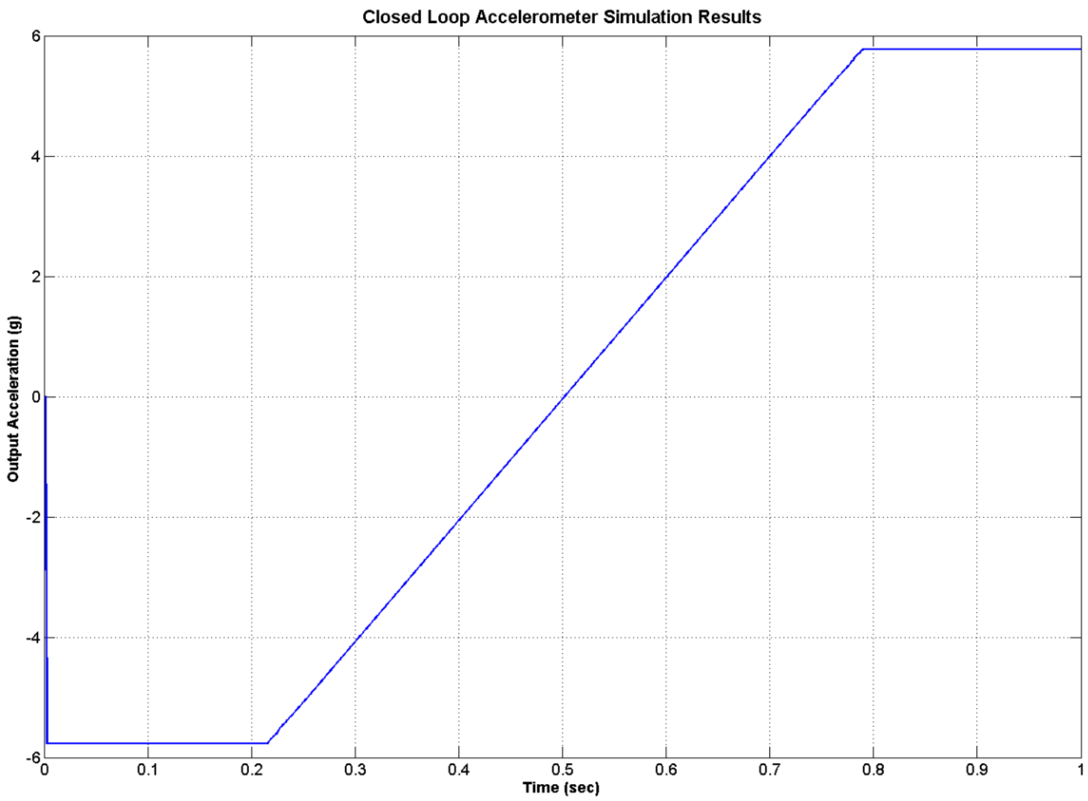

Figure 3.4: Result of the MATLAB ramp input simulation in closed loop mode

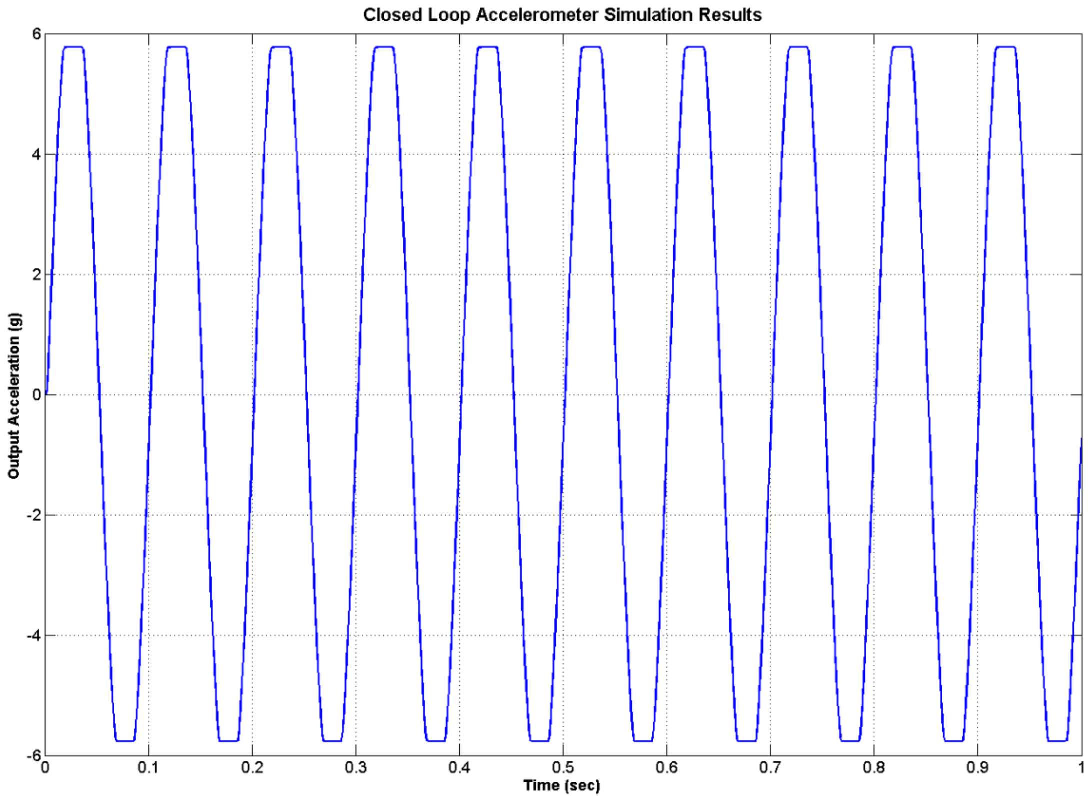

Figure 3.5: Result of the MATLAB sinusoidal input simulation in closed loop mode

Table 3.2: Features of the accelerometer and readout circuit used in the closed loop simulations.

Parameter Name	Value	Parameter Name	Value
Finger Spacing 1	$2x10^{-6}$ m	Spring Constant	50 N/m
Finger Spacing 2	$7x10^{-6}$ m	Damping Coefficient	0.0034
Capacitive Area / finger	$5250x10^{-12}$ m^2	Supply Voltage	5 V
Number of Fingers	300	Int. Capacitance	2 pF
Proof Mass	$4x10^{-7}$ kg	c (pulse width perc.)	60%
		fs	500000 Hz

3.2 Measurement Bandwidth

Like every electromechanical system, accelerometers also have a measurement bandwidth in which the sensor can properly measure the applied acceleration with no higher than 3dB change in the magnitude response. Measurement bandwidth concept differs in open and closed loop operation of accelerometers. In open loop mode the only filter is the accelerometer which has a second order low pass filter characteristic. In closed loop mode high sampling rate of the proof mass position and feedback force, increases the bandwidth of the system up to half of the sampling frequency.

3.2.1 Open Loop Mode

In open loop mode measurement bandwidth of the accelerometer and readout circuit pair is limited with the lower bandwidth of the mechanical sensor or output low pass filter. Mechanical sensor is a second order low pass filter which shapes the frequency response of the whole system. Figure 3.6 shows the magnitude response of a second order spring-damper system having different damping coefficients. Resonance frequency of this system is 100Hz and the plots have 10, 1 and 0.1 quality factors. When the damping of the system decreases, magnitude response around the resonance frequency of the accelerometer becomes sharper and the bandwidth of the accelerometer decreases. On the other hand with increasing damping, accelerometer no longer performs a peak around the resonance frequency and the drop in the magnitude response limits the bandwidth. Bandwidth of the accelerometer has its largest value when the quality factor is selected approximately 1.3. Therefore in an open loop accelerometer design, in order to maximize the bandwidth of the mechanical part of the system, damping should be selected such that:

$$Q = \frac{\sqrt{k.m}}{b} \cong 1.3 \tag{3.6}$$

where k is the spring constant, m is the mass and b is the damping of the accelerometer.

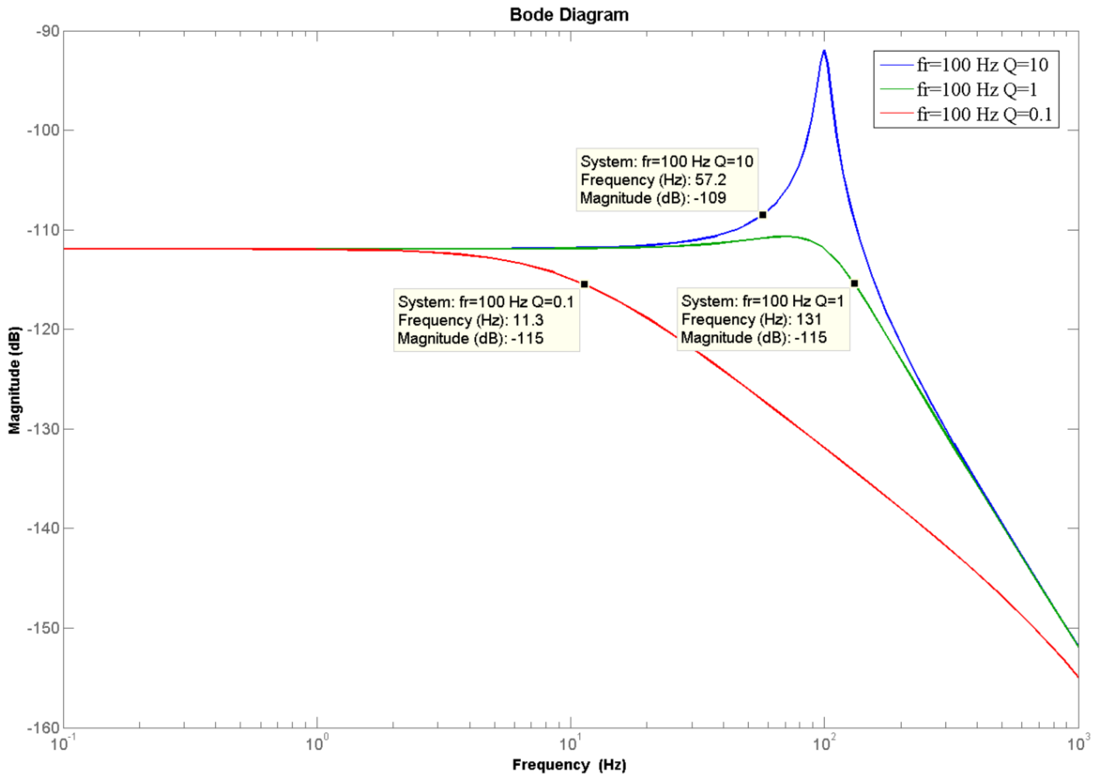

Figure 3.6: Magnitude response of a second order spring damper system having different damping coefficients (resonance frequency = 100 Hz)

Second filter in an open loop system is the electrical low pass filter at the output stage of the readout circuit. As it was described in section 2.3.1 of this thesis, in order to extract the DC component of the integrated signal a low pass filter with low cut-off frequency is required. With this filter the acceleration information is extracted from the output waveform.

Therefore in an open loop system the bandwidth of the system is limited with either the mechanical sensor or electrical readout circuit which has the lowest cut-off frequency.

3.2.2 Closed Loop Mode

In closed loop mode the bandwidth of the system increases with the high sampling frequency. Acceleration and noise information are sampled at very high sampling rates. The output is a series of pulse streams which needs to be low pass filtered preferably with a digital filter in order to extract the meaningful acceleration data from the output pulse stream. Theoretically the maximum bandwidth of the system is limited with half of the sampling frequency which is the Nyquist rate [79]. But the limiting factor on the bandwidth is the resolution of the system. With increasing bandwidth the resolution of the system also decreases significantly. Figure 3.7 shows the trade-off between the bandwidth and resolution in different A/D techniques. In sigma-delta conversion applications relatively low bandwidths are preferred for high resolution systems.

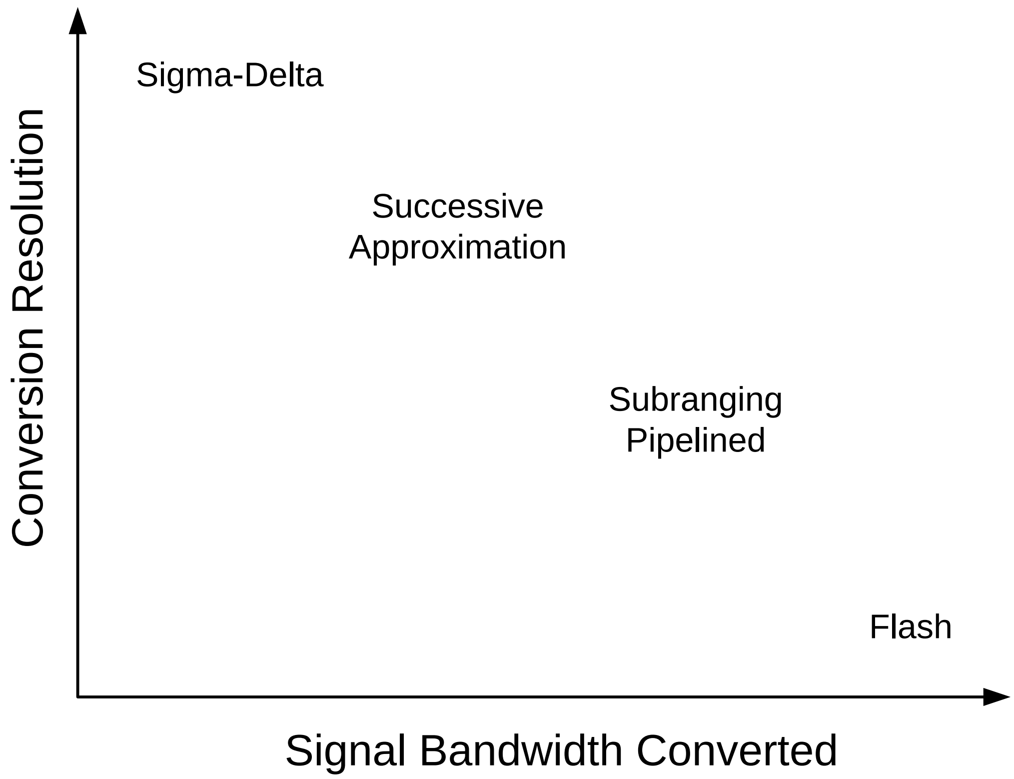

Figure 3.7: Trade-off between the bandwidth and resolution in different A/D techniques [79].

The output of the sigma-delta readout circuit is a bit stream at the circuits own sampling frequency. The meaningful acceleration signal is oversampled in this output bit stream and the noise due to digital conversion is carried to the higher frequencies. Figure 3.8 shows the distribution of acceleration and noise signals on the frequency domain. In order to extract the meaningful acceleration data and filter the noise at high frequencies, a low pass sigma delta demodulator circuit should be used as the final stage which is the deciding component on the bandwidth of closed loop readout architecture.

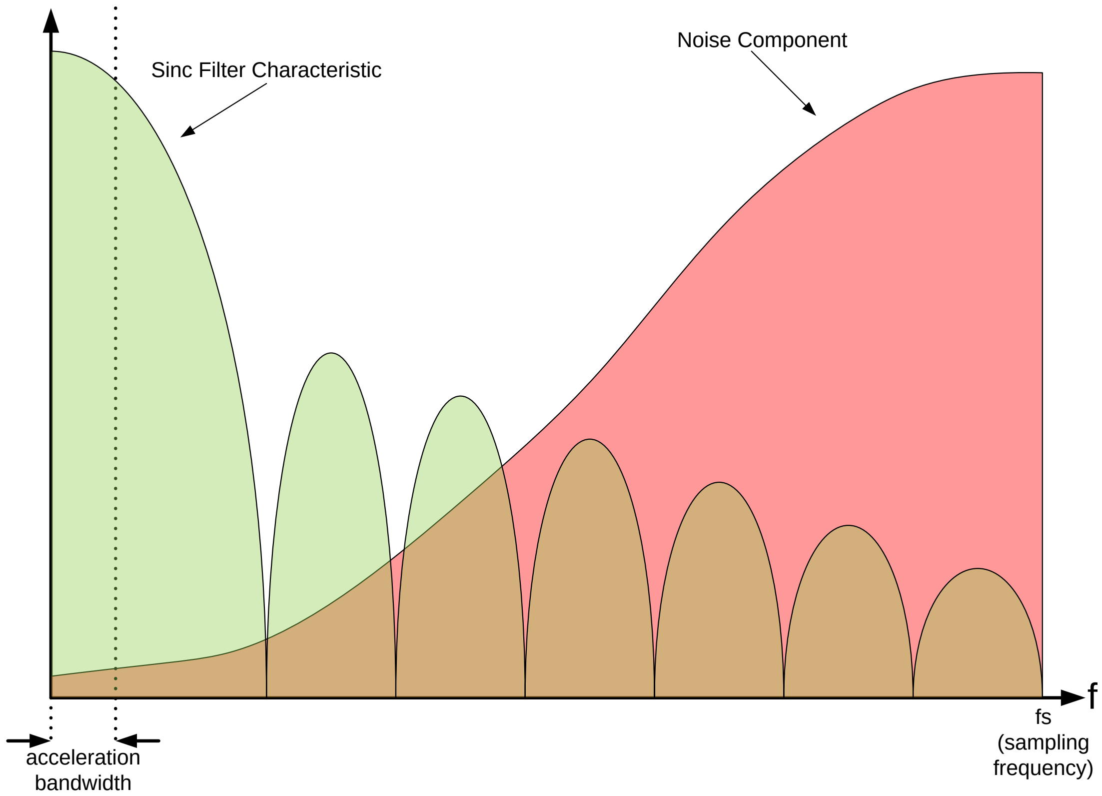

Figure 3.8: Noise component and Sinc filter characteristic of sigma-delta modulator output in frequency domain.

In this study, output bit stream of the readout is filtered with a Sinc demodulator circuit. Sinc filter removes the high frequency noise components of the output and reduces the data rate to the desired value. The order of the Sinc filter depends on the order of the sensing element and readout circuit.

As it was described in section 2 of this thesis, MEMS accelerometer has a transfer function of order 2. The readout circuit doesn’t provide any pole to the system. It converts capacitance change to voltage. Since the readout circuit does not provide any pole, the system has a total of 2 poles coming from sensing element and readout circuitry. The order of the Sinc filter should be at least 1 greater than the order of the system to keep the noise component in the operation range below 0.5dB. Therefore, decimation filter used in this system should be at least a Sinc^3 filter. Comparisons of third order Sinc filter with the first, second and forth order filters are given in figure 3.9. As it's seen from the graph, third order filter has a sharper frequency characteristic compared with the first and second order Sinc filters but forth order filter has a better low pass filter frequency characteristic.

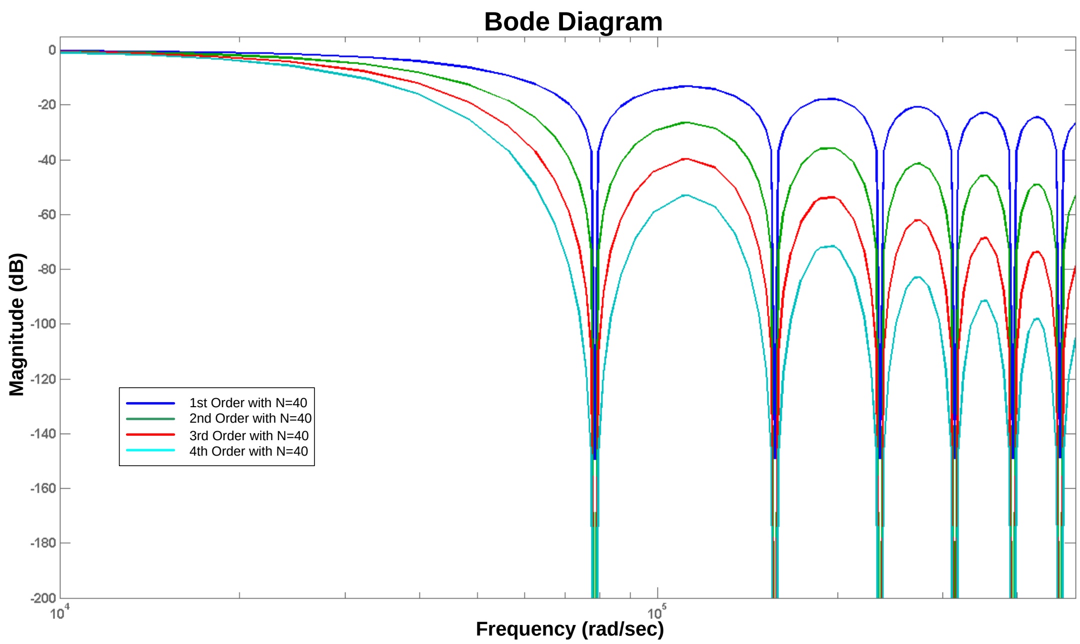

Figure 3.9: Comparisons of third order Sinc filter with the first, second and forth order filters.

The topology of the Sinc^3 filter is shown in figure 3.9.

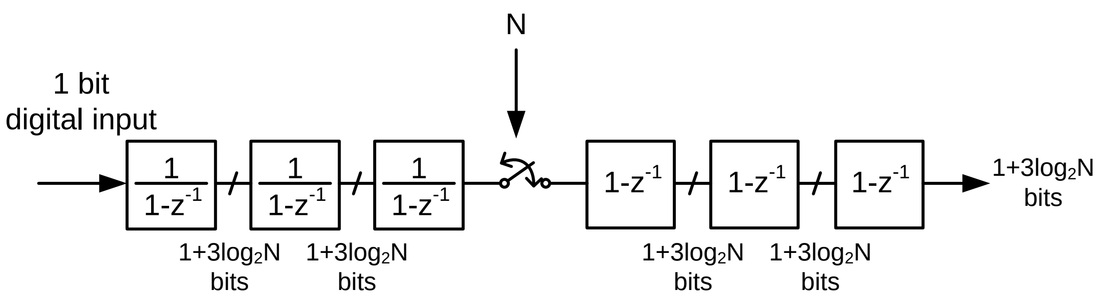

Figure 3.10: Topology of Sinc^3 filter

In this topology there are 3 integrator stages followed by a switch to reduce data rate (decimation) and more differentiator stages at the output. This topology is based on the transfer function of $Sinc^3$ filter as follows:

$$H(z) = \left(\frac{1}{N} . \frac{1 - z^{-N}}{1 - z^{-1}}\right)^3 \qquad (3.7)$$

where N is the decimation ratio of the Sinc filter.

The three integrator stages at the input of the $Sinc^3$ filter integrate the bit stream output of the readout circuit three times. The output of third integrator is sent to differentiator block, but 1 output for each N outputs allowed to pass to the differentiators. By this way, the data rate is reduced by a factor of N. Then the bit stream is differentiated 3 times to obtain the filtered acceleration data.

Another important property of this type of filtering is the output bit number of the circuit can be adjusted easily. By changing the order of the filter and decimation ratio, output bit number can be set to any value using the following equation:

$$output\ bit\ number = b + k. log_2 N \qquad (3.8)$$

where b is the input bit numbers to the Sinc filter (1 bit in single output sigma delta modulators), k is the order of the filter and N is the decimation ratio.

It is also possible to connect these low pass filters in cascaded form in order to adjust the overall decimation ratio or output bit number. In this case the output bits of the first stage Sinc filter is assumed to be fed into the second stage in parallel and the input bit number of the second stage in equation 3.8 (b) is chosen as the output bit number of the first stage. With a two stage Sinc filtering architecture, better control of the cut-off frequency, decimation order and output bit number adjustment is possible.

Sinc filter structure has a very simple architecture and is very easy to implement. But instead of a Sinc filter more complex digital low pass filter’s can also be used for better filtering.

3.3 Resolution (Noise)

Resolution (noise) is the most important performance parameter for an accelerometer system. In order to understand the noise of the overall accelerometer system one should first have an in depth knowledge about the readout circuitry. In this part different noise types will be discussed and methods to calculate these noise sources will be explained.

3.3.1 Open Loop Mode

As all the performance parameters, resolution of the accelerometer system also varies with the readout circuit architecture. In open loop mode accelerometer noise is composed of the accelerometer noise (Brownian Noise), front-end amplifier noise, switching noise and sensor charging reference voltage noise. Following sections describes the properties of each noise source separately.

3.3.1.1 Mechanical Noise of the Accelerometer (Brownian Noise)

Brownian noise is the temperature dependent random motion of the microstructures due to the motion of the gas molecules in fashion of white noise. It is similar to the thermal noise of the resistors in electric circuits [80]. Average mechanical noise of a spring-mass-damper system can be expressed as:

$$a_{mech} = \sqrt{\frac{4.\,k_b.\,T.\,b}{m^2}} \qquad \left({}^{m}\!/_{s^2\sqrt{Hz}}\right) \qquad (3.9)$$

where k_b is the Boltzmann constant, T is the operation temperature, b is the total damping of the system and m is the mass of the second order system [80], [81]. In order to decrease the mechanical noise of an accelerometer either the mass of the sensor should be increased or the damping of the system should be decreased. Increasing the mass of the accelerometer is against the idea of miniaturizing inertial sensors with MEMS technology. On the other hand decreasing the damping of the sensor is against the sensitivity of the accelerometer. Any measure taken to decrease the damping of the sensor will also decrease the sensitivity and measurement range of the sensor but on the other hand it will also decrease the overall system noise.

Therefore there is an important trade-off between noise and sensitivity which should be taken into consideration during the design.

While calculating the resolution of an accelerometer, Brownian Noise of the sensor is an important parameter but its contribution is very low when compared with electrical noise of the readout circuit.

3.3.1.2 Front-End Amplifier Noise

This noise component is due to the first stage charge integrator of the readout circuit which is used to integrate the injected charge from accelerometer due to the change of sensor capacitances. Front-end stage is an operational amplifier and it has a unique noise expression, particular to its topological properties. If a charge integrator which is shown in Figure 3.11, is used as the front-end amplifier of the readout circuit, than the noise expression is sampled, folded and filtered by the amplifier and the equivalent noise at the output of the circuit becomes [82]:

$$V_{front-end} = \sqrt{\frac{16}{3} . \frac{C_s + C_p}{C_{int}} . \frac{k_b T}{C_{out}} . \frac{1}{f_s}} \qquad \left({}^{V}/_{\sqrt{Hz}} \right) \qquad (3.10)$$

where C_s is the sense capacitance of the accelerometer, C_p is the parasitic capacitance at the input of the front-end amplifier, C_{int} is the integrator capacitance connected to the front-end amplifier to integrate the charge injected from accelerometer, C_{out} is the parasitic capacitance connected at the output of the front-end amplifier and f_s is operation frequency of the charge integrator which can also be called as the sampling frequency of the readout circuit.

This noise component is effective in both open and closed loop circuit structures and should be taken into account during the design of mechanical structure since sense capacitance of the accelerometer is a term of this noise source.

3.3.1.3 Switching Noise

This noise component comes from sampling of thermal noise at the switches used in the circuit and it is also known as the kT/C noise [82]. Switching of the integration capacitance dominates the biggest part of this noise component and output referred noise can be expressed as follows:

$$V_{switching} = \sqrt{\frac{4.k_b.T}{f_s.C_{int}}} \qquad \left({}^{V}\!/_{\sqrt{Hz}}\right) \tag{3.11}$$

Like front-end amplifier noise this component should be taken into consideration in both open and closed loop operations. Switching noise does not limit the design of accelerometer since it doesn't have any component related with the mechanical structure of the accelerometer.

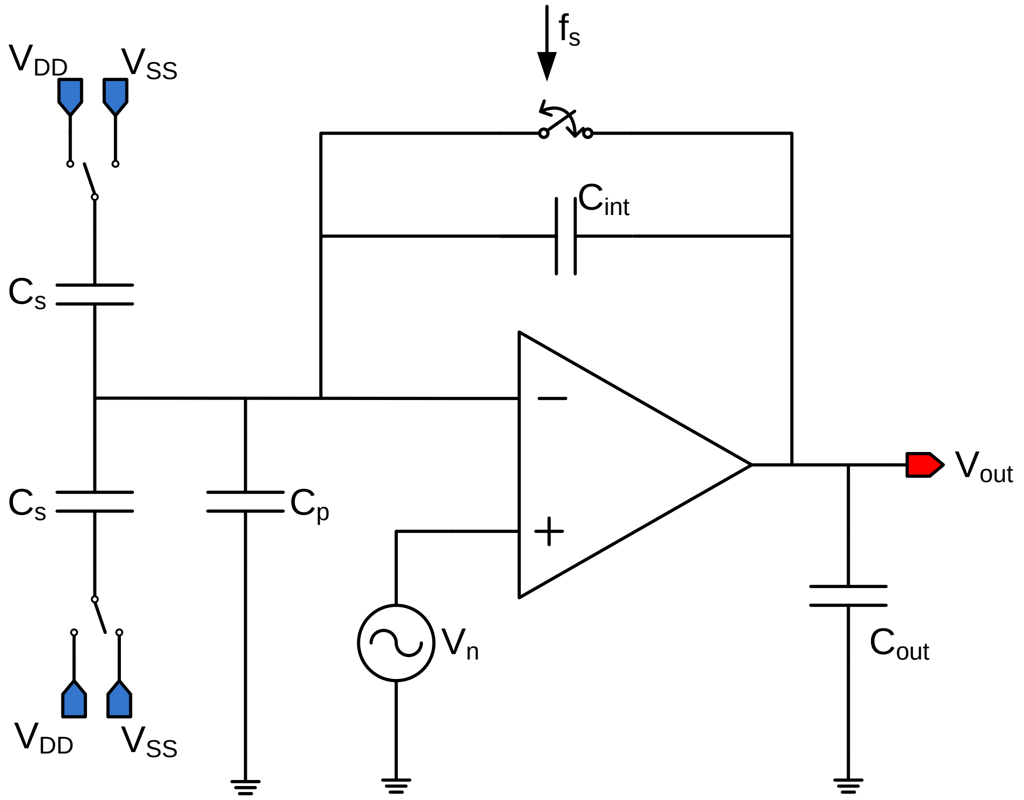

Figure 3.11: Schematic drawing of a charge integrator type front-end amplifier connected to a micromechanical accelerometer.

3.3.1.4 Sensor Charging Reference Voltage Noise

Sensor charging reference voltage noise should be taken into account if a switch capacitor type readout circuit is used to detect the displacement of the proof mass of the accelerometer [83], [84]. The source of the sensor charging reference voltage noise is the reference voltage used to charge and discharge the sensor's fixed capacitances. In order to understand the deflection of the proof mass under an applied external acceleration, electrodes on each side of the accelerometer are charged to a fixed voltage value and then discharged. During the discharging process excess charges are injected from the accelerometer to the readout circuit and these charges are integrated to find an output voltage proportional with the injected charges. Therefore any noise on the reference voltage used to charge the electrodes are directly coupled to the system and contributes to the overall noise. Figure 3.11 shows the simplified circuit schematic to calculate this noise and the output equivalent noise can be calculated using following equation:

$$V_{SCRN} = \sqrt{\frac{2.V_n^2.C_{sw}}{f_s.R_{sw}.{C_{int}}^2}} \qquad \left({}^{V}/_{\sqrt{Hz}}\right) \qquad (3.12)$$

where C_s is the sense capacitance of the sensor, f_s is the sampling frequency of the readout circuit, R_{sw} is the switching resistance, C_{int} is the integration capacitance of the front end amplifier and V_n is the noise associated with the reference voltage used to charge the sensor capacitances. SCRV noise should be taken into account while designing the mechanical sensor since there is a component in the noise expression which is the sense capacitance of the sensor, C_s. This noise expression contributes to the overall noise of the circuit for both open and closed loop of operation.

With this last component of the noise sources all dominant disturbing effects in open loop mode are examined and formulized. The total system noise of the accelerometer can be calculated by adding all noise components. But before doing such integration mathematically, mechanical noise of the accelerometer should be converted to electrical domain from acceleration domain. In order to make such a conversion, measurement range of the accelerometer should be detected first. After calculating the measurement range of the accelerometer with equation 3.1 in open loop mode or with equation 3.2 in closed loop mode, mechanical noise of the accelerometer can be converted to electrical domain as:

$$V_{mech} = a_{mech}.\frac{V_{DD}}{2 \times MR} \qquad \left({}^{V}/_{\sqrt{Hz}}\right) \qquad (3.13)$$

where a_{mech} is the mechanical noise of the accelerometer in acceleration domain which is calculated with equation 3.9, V_{DD} is the supply voltage of the readout which is used to charge and discharge the sensor capacitances in the integration cycle and MR is the measurement range of the accelerometer which is calculated by the other sensor parameters. After calculating the mechanical noise in voltage domain total noise of the system in open loop mode can be calculated as:

$$V_{open-loop} = \sqrt{V_{mech}^2 + V_{front-end}^2 + V_{switching}^2 + V_{SCRN}^2} \qquad \left({}^{V}\!/_{\sqrt{Hz}}\right) \qquad (3.14)$$

This calculated formula can be used in optimization of accelerometer system design in open loop mode of operation.

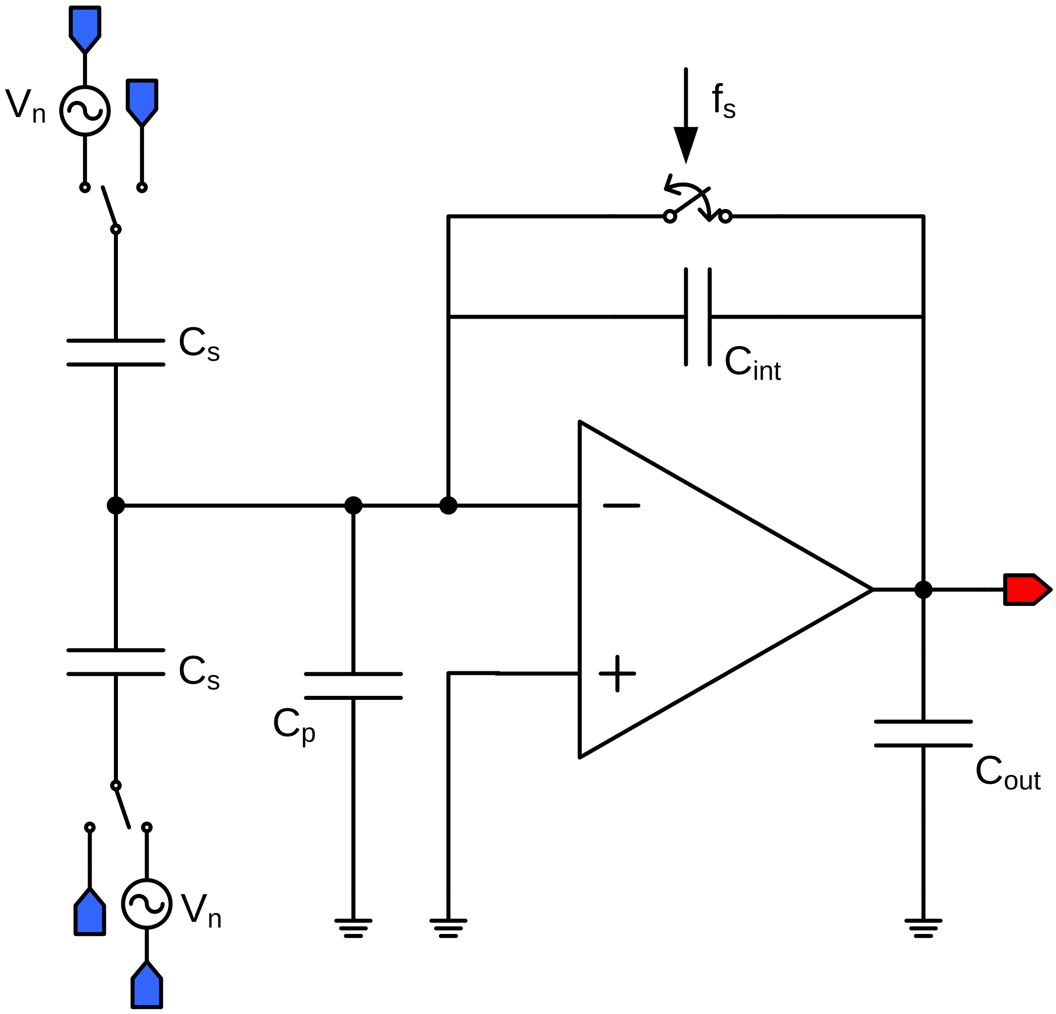

Figure 3.12: Schematic drawing of a charge integrator type front-end amplifier connected to a micromechanical accelerometer modified for sensor charging reference voltage noise detection.

3.3.2 Closed Loop Mode

In closed loop mode all the noise sources described in the open loop mode also have effect on the overall noise performance of the accelerometer system. In addition to these sources due to the force feedback nature of the system and the analog-to-digital conversion, two additional noise sources are added to the overall performance. These two sources are mass residual motion noise and quantization noise. In this section both of these noise sources will be described in detail.

3.3.2.1 Quantization Noise

In closed loop operation the output of the circuit is either a single or multi bit pulse which is fed back to the sensor in order to prevent the proof mass motion of the accelerometer. This single or multi bit pulse output is generated at the final stage of the readout which is actually a comparator. Quantization noise of the accelerometer can be described as the amount of information noise during this analog to digital conversion operation via the comparators at the output stage.

Quantization noise of a second order $\Sigma - \Delta$ type closed loop readout circuit with single bit digital output can be expressed as [82]

$$V_{quantization} = e_{rms} \frac{\pi^2}{\sqrt{5}.M^{2.5}} \qquad \left({}^{g}\!/_{\sqrt{Hz}} \right) \qquad (3.14)$$

where e_{rms} is the rms value of the unshaped quantization noise and M is the oversampling ratio of the closed loop system. For a single bit modulator e_{rms} can be calculated as

$$e_{rms} = \frac{\Delta}{\sqrt{12}} \qquad (3.15)$$

where $\Delta/2$ is the measurement range of the accelerometer system which can be calculated by equation 3.2, and M is the oversampling ratio of the system and is equal to the decimation of the filter at the output of the readout circuit. With increasing decimation ratio, amount of pulses averaged at the output of the system increases and noise decreases consecutively.

Quantization noise increases with increasing operation range of the accelerometers. To decrease the noise of the accelerometers designed to operate for high measurement ranges, output decimation ratio should be increased. But this will decrease the output data rate of the readout circuit. For high bandwidth and high measurement range applications, sampling frequency should be increased in order to increase the output data rate.

For the accelerometer model in closed loop measurement range calculation section, quantization noise can be determined by using the mechanical and electrical parameters. The operation range of the accelerometer in closed loop mode was calculated as ±5.7g and M is the total decimation order used at the cascaded $Sinc^3$ and $Sinc^2$ filters which is 640. Using these values and equation 3.14 and 3.15 quantization noise of the system is calculated as 1.4µg/√Hz.

3.3.2.2 Mass Residual Motion Noise

Mass residual motion noise generates one of the most important contributions to the overall noise performance of the accelerometer system. This noise source is only effective in the closed loop operation mode as a result of force rebalancing. Consecutive high and low feedback pulses applied to the proof mass of the accelerometer creates a random oscillation under the equilibrium condition, even under the zero acceleration. This movement contributes to the overall noise of the system. In order to find the amount of this noise, output of the accelerometer should be observed under constant acceleration state for some duration and the variance of the output signal should be determined. In the literature [4], [82], and [84] a method is described to calculate the mass residual motion of the accelerometer. During these calculations several assumptions are made. First assumption is that the accelerometer proof mass oscillates in $f_s/4$ Hz with fixed amplitude which can be calculated as:

$$\Delta x_{residual} = \frac{range}{\left(2.\pi.{f_s}/_{4}\right)^2} \qquad (m) \qquad (3.16)$$

where range is the measurement range of the accelerometer in closed loop and can be calculated with equation 3.2 and f_s is the sampling frequency of the closed loop circuit. Calculated mass residual displacement can be converted to capacitance change as:

$$\Delta C_{residual} = \left(\frac{N.\varepsilon_0.A}{d_1 - \Delta x_{residual}} + \frac{N.\varepsilon_0.A}{d_2 + \Delta x_{residual}}\right) - \left(\frac{N.\varepsilon_0.A}{d_1} + \frac{N.\varepsilon_0.A}{d_2}\right) \quad (F) \qquad (3.17)$$

where N is the number of fingers, ε_0 is the permittivity of the air, A is the capacitive area of a single finger, d_1 is the small capacitive finger spacing and d_2 is the large capacitive finger spacing. Amount of acceleration required to change the capacitance by $\Delta C_{residual}$ can be calculated using the capacitance change per g value of the system. In order to find capacitance change per g, first deflection of the proof mass should be found for 1g applied acceleration. This deflection can be calculated as:

$$\Delta x_{1g} = \frac{m.9{,}81}{k} \quad (m) \qquad (3.18)$$

where m is the mass of the accelerometer and k is the spring constant of the suspended structures. Using this value capacitance change per g is calculated as:

$$\Delta C_{1g} = \left(\frac{N.\varepsilon_0.A}{d_1 - \Delta x_{1g}} + \frac{N.\varepsilon_0.A}{d_2 + \Delta x_{1g}}\right) - \left(\frac{N.\varepsilon_0.A}{d_1} + \frac{N.\varepsilon_0.A}{d_2}\right) \quad (F) \qquad (3.19)$$

Finally using $\Delta C_{residual}$ and ΔC_{1g} acceleration equivalent total mass residual motion can be calculated as:

$$a_{residual} = {}^{\Delta C_{residual}}\!\big/_{\Delta C_{1g}} \quad (g) \qquad (3.20)$$

This value is the total noise in the whole operation band of the accelerometer. Second assumption is that the overall mass residual motion noise is distributed in the $f_s/2$ band evenly. Therefore total noise density of the system can be calculated as

$$V_{residual} = a_{residual}/\sqrt{f_s/2} \qquad (g/\sqrt{Hz}) \quad (3.21)$$

In order to prove this formulation, results of mass residual noise calculation and MATLAB simulation should be compared. For this purpose mass residual noise of the accelerometer with design parameters given in Table 3.2 is calculated and found as 0.23μg/√Hz.

MATLAB simulations are performed for the same accelerometer model in order to verify the results found with hand calculations. For this purpose MATLAB model given in figure 2.18 is used. Output of the data is recorded to a text file at 0g input acceleration. Figure 3.12 shows the output of the readout circuit at 0g input acceleration and motion of the proof mass. It can be seen from these figures that the output waveform is stuck at 0 and the proof mass of the accelerometer is oscillating at a single frequency. In the optimum operation of the system, proof mass of the accelerometer should be oscillating randomly. This state of the accelerometer is known as the dead zone and in this mode externally applied accelerations around 0g under some certain amount is not enough to disturb the locked state of the accelerometer system and no acceleration can be measured. Dead zone concept is later described in this chapter of the thesis.

In order to find the mass residual motion noise, acceleration larger than the input dead zone range of the accelerometer should be applied. In this case 1g acceleration is applied in order to find the mass residual motion noise. Figure 3.13 shows the simulation results of output of the accelerometer and motion of the proof mass when 1g external acceleration is applied. In order to find the noise density, output data is collected and variance of this data is divided to the square root of the bandwidth. In our case the bandwidth of the accelerometer model can be calculated by dividing the sampling frequency of the readout by the decimation orders of the $Sinc^3$ and $Sinc^2$ filters. Therefore the noise density of the system is found as 1.93μg/√Hz. But this noise density value includes both the quantization noise and mass residual motion noise. Remembering that the quantization noise is 1.4μg/√Hz, mass residual motion noise of the system can be found as

$$\sqrt{1.93^2 - 1.4^2} = 1.32\mu g/\sqrt{Hz}$$

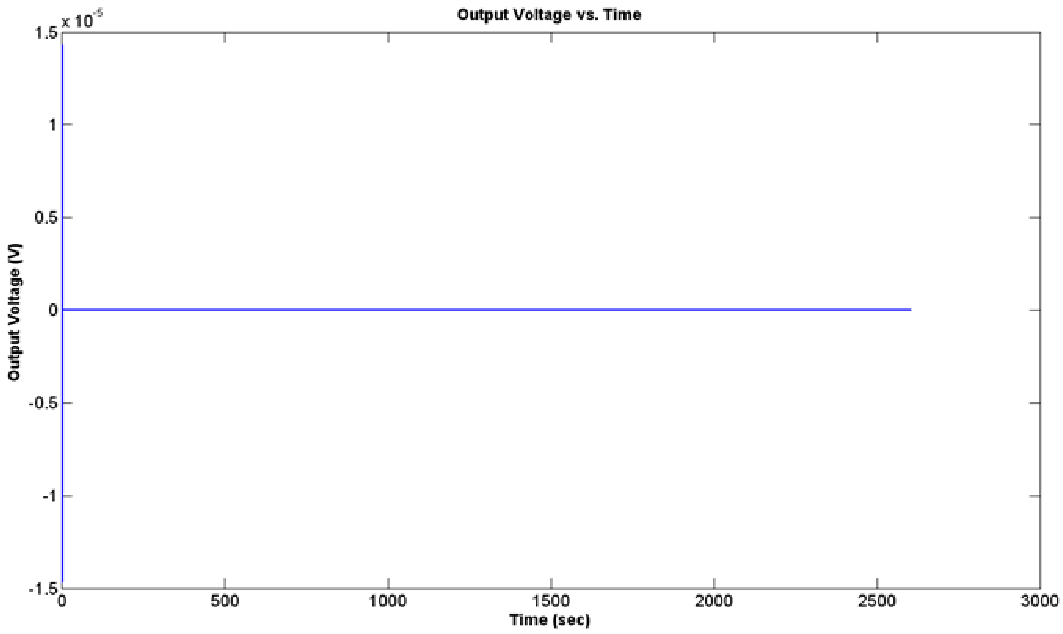

(a)

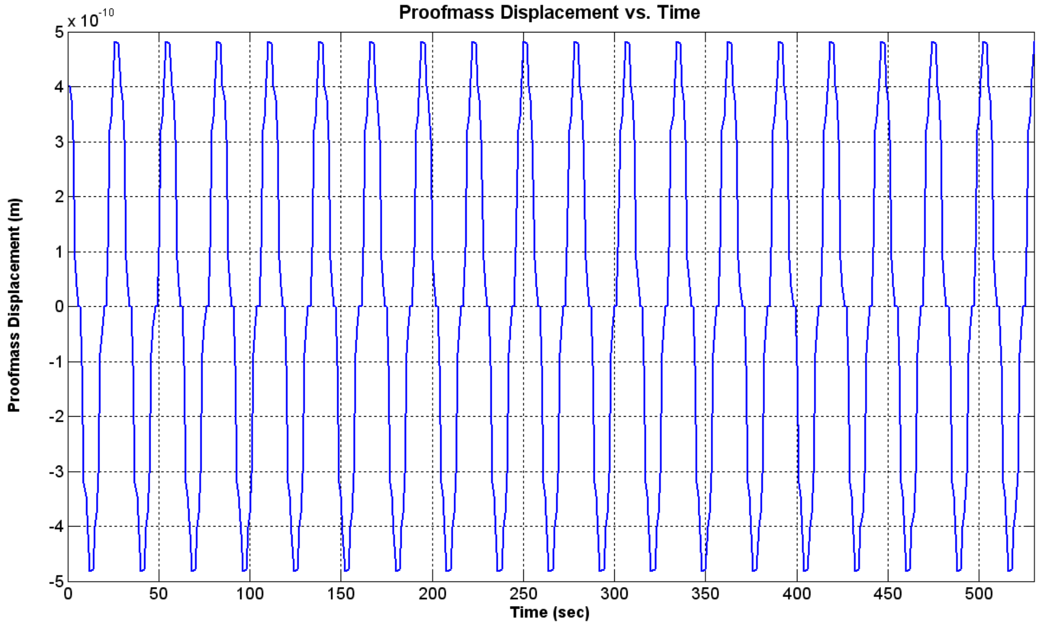

(b)

Figure 3.13: (a) Output of the readout circuit at 0g input acceleration (b) motion of the proof mass at 0g input acceleration.

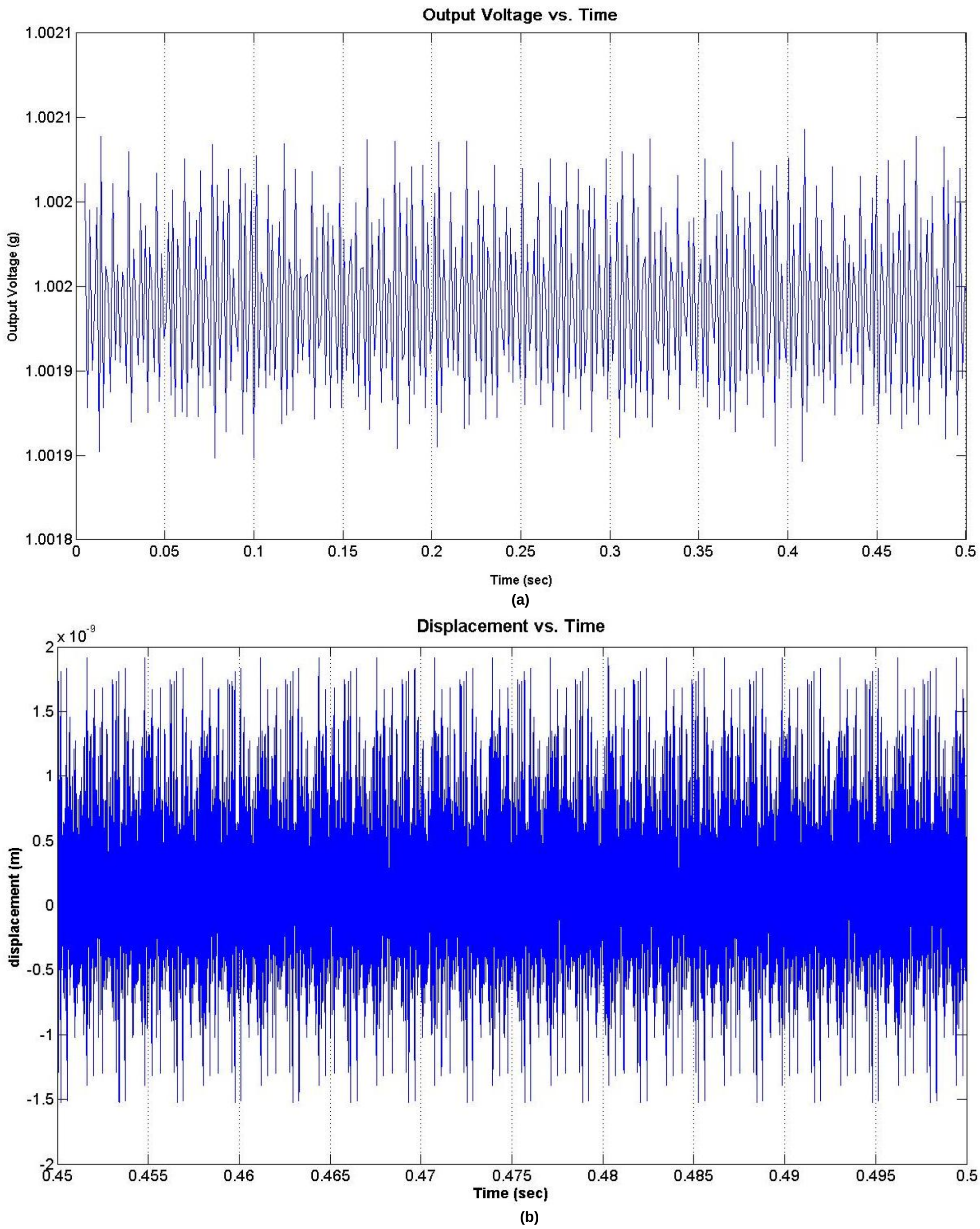

Figure 3.14: (a) Output of the readout circuit at 1g input acceleration (b) Motion of the proof mass at 1g input acceleration.

Although the results of simulation and hand calculation seem to be close, simulation results are 5 times larger than the hand calculations. This problem is reported in several publications through the literature [85], [86]. The difference between these two results is due to the first assumption made during the hand calculations. First assumption of proof mass oscillating at $f_s/4$ frequency does not corresponds with the simulations results in Figure 3.13. Figure 3.14 shows the distribution of the proof mass oscillations in the frequency domain. As it can be seen from this figure, although the magnitude of oscillation is higher at some frequencies it is wrong to assume that the accelerometer proof mass is oscillating at a single frequency. Figure 3.15 shows the distribution of the output waveform in the frequency domain. From this figure it can be said that, second assumption of noise having white characteristic at the output of the readout circuit is a close approximation.

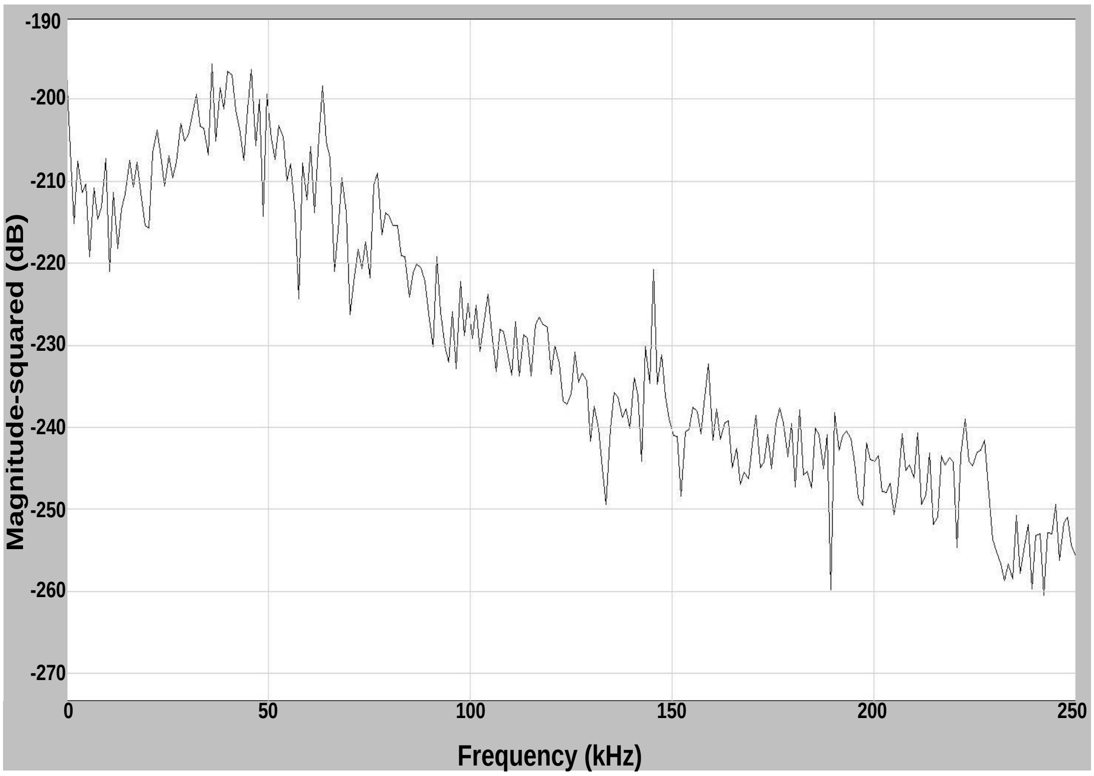

Figure 3.15: Distribution of the proof mass oscillations in the frequency domain

From these results and discussions it can be concluded that although there are some methods in literature which calculates the mass residual motion noise of the accelerometer, assumptions made during these calculations are not very accurate and obtained results are several orders smaller than the actual simulation results. Therefore during accelerometer design, performing system level simulations is crucial for estimating the overall noise performance until more accurate approximations are made.

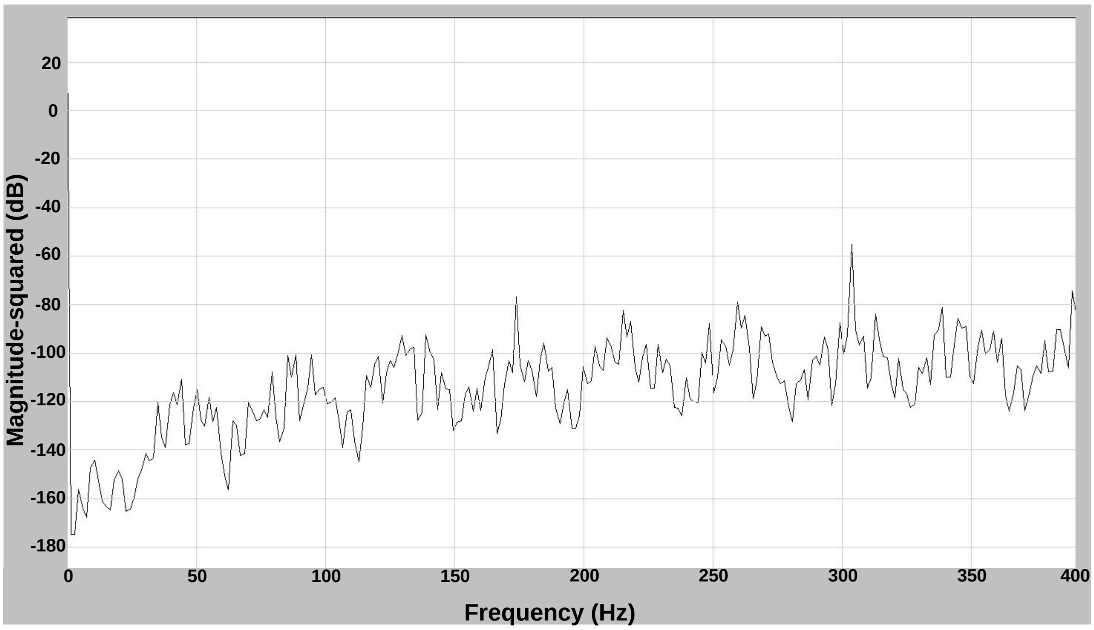

Figure 3.16: Distribution of the output waveform in the frequency domain.

3.4 Non-Linearity

Non-linearity is defined as the deviation of the accelerometer response from the best fit curve for different magnitudes of acceleration signal in its working range. In theory non-linearity source in accelerometer systems originate from the capacitive structure of the sensor. Since varying gap is used as sensing mechanism, capacitance of the accelerometer change is inversely proportional with the square of the mass displacement. If open loop readout architecture is used, this effect will be dominant in the non-linearity of the accelerometer output. Voltage output of the accelerometer with respect to the applied acceleration in an accelerometer system can be calculated as:

$$\frac{\partial V}{\partial a} = \frac{\partial V}{\partial C} . \frac{\partial C}{\partial x} . \frac{\partial x}{\partial a} \qquad (V/g) \qquad (3.22)$$

where $\partial V/\partial C$ is the gain of the charge integrator, $\partial C/\partial x$ is the sensitivity of the accelerometer to the deflection of the proof mass, and $\partial x/\partial a$ is the tendency of the proof mass movement with respect to the externally applied acceleration. Equation 3.22 can be rewritten by replacing all parameters with their equivalents as follows:

$$\frac{\partial V}{\partial a} = \left(\frac{2.V_{DD}}{C_{int}}\right).\left(\frac{N.\varepsilon_0.A}{(d_1 - x)^2} - \frac{N.\varepsilon_0.A}{(d_2 + x)^2}\right).\left(\frac{m}{k}\right) \qquad (V/g) \qquad (3.23)$$

In this equation all parameters are constants except the squares of displacement terms on the denominator which induces non-linearity to the system. To observe the effect of this non-linearity, open-loop simulation is performed for a MEMS capacitive accelerometer with the parameters given in Table 3.1. Figure 3.16 shows the input acceleration vs. output voltage characteristics obtained at the end of the simulations. Non-linearity of this characteristic is found as 17.26% in ±20g input acceleration range and 3.55% in the ±10g range. Although linearity of the open loop characteristic improves with decreasing measurement range, non-linearity requirement for the accelerometers in the market are less than 0.5%. Non-linearity issue in open-loop can be solved with a look-up table implementation at the output of the readout circuit, but this will increase the complexity and area of the circuitry.

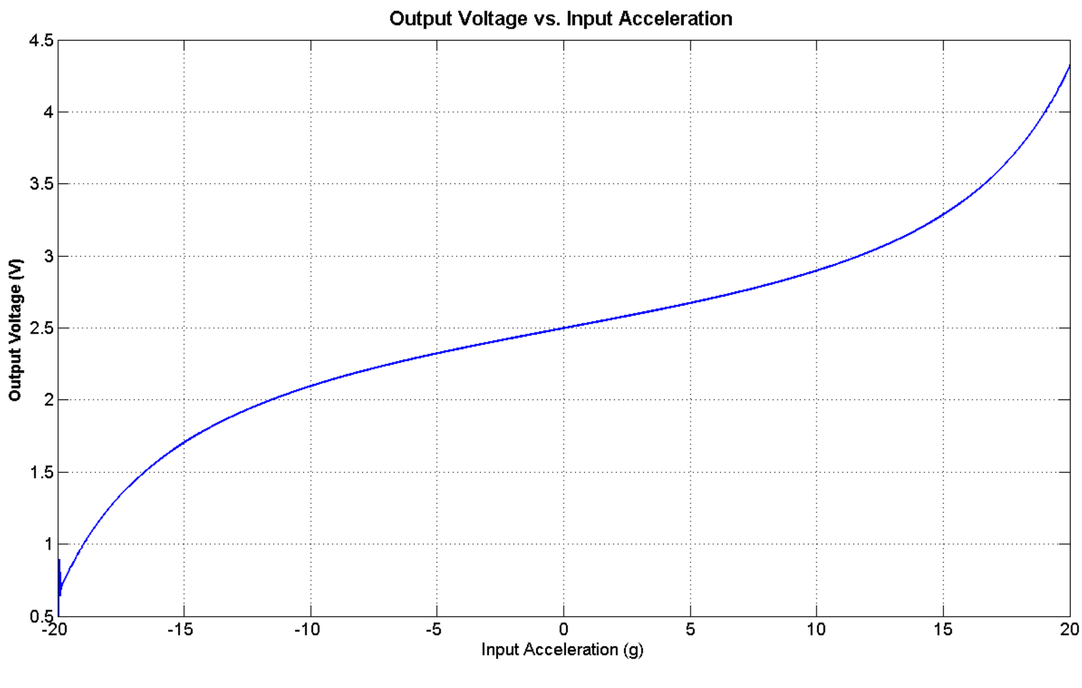

Figure 3.17: Output voltage vs. input acceleration graph of accelerometer in open loop mode operation.

Instead of using open-loop readout architecture, non-linearity problem can be eliminated by using closed-loop readout circuit. The reason of this problem in open loop was the non-linear response of capacitance change with the displacement of proof mass. Closed loop architecture cancels this behavior by preventing the movement of the proof mass. By this way non-linearity from the sensitivity equation does not affect the system anymore and system becomes theoretically linear. In order to prove this statement closed loop non-linearity simulation is performed on the MATLAB model given in Figure 2.18. Figure 3.17 shows the full range acceleration sweep of the accelerometer having properties given in Table 3.2. Previously measurement range of this model was calculated and simulated as ~5.7g's. In this range if the non-linearity of the accelerometer is calculated it is found as 0.15% which is much better when compared with the open loop case. Reason of this small non-linearity is the small dependence of feedback force to the proof mass displacement, which is in acceptable limits.

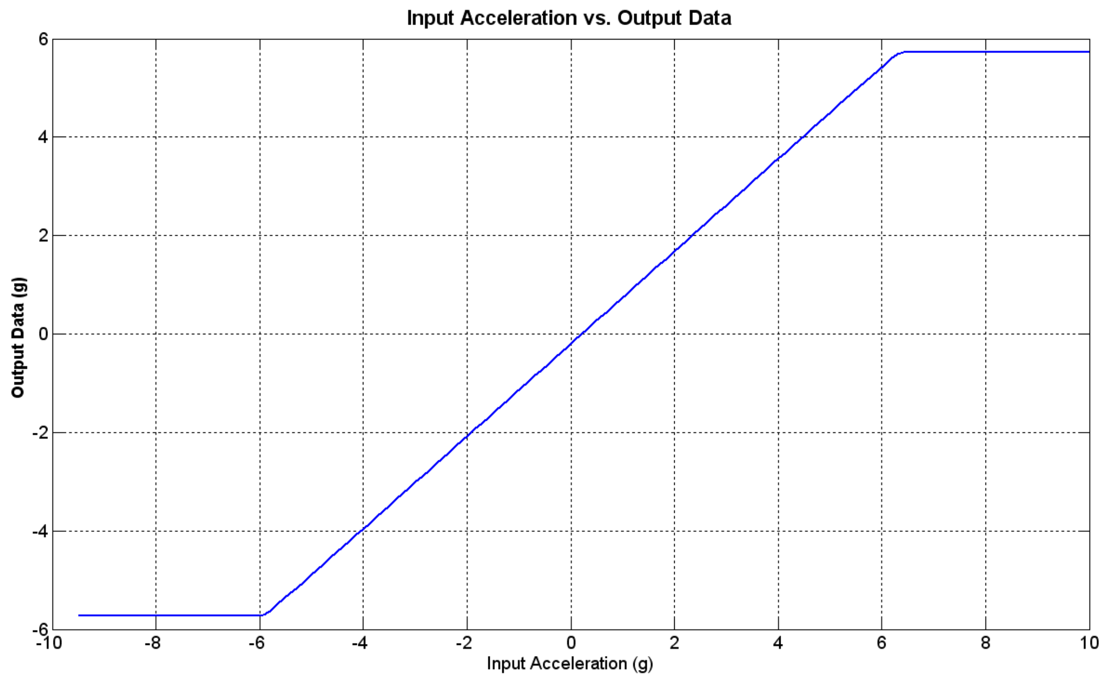

Figure 3.18: Full range acceleration sweep simulations of the model accelerometer in closed loop mode.

Second non-linearity source of the accelerometer is due to fabrication of the accelerometers. Fabrication of the sense capacitances, springs or proof masses does not always conclude with perfect results. Flaws occurred during the fabrication of sensors causes the system response to become non-linear. This non-linearity component can't be predicted or calculated theoretically but it can only be solved by further optimizing the fabrication processes.

3.5 Dead-Zone

Dead-zone is a region where the accelerometer does not respond to the applied accelerations. This phenomenon only exists in the closed loop operation mode and around 0g input acceleration state. Figure 3.18 shows the block diagram of the closed loop accelerometer system showing the origin of dead zone. In this mode mechanical sensor denoted as H(s) in the figure below and readout circuit are in such a state that with no input acceleration the proof mass of the accelerometer is oscillating at a perfect sinusoidal path having a frequency of $f_s/4$ [87]. Magnitude of this oscillation can be calculated from the transfer function of accelerometer as:

$$H(s) = \frac{x(s)}{a(s)} = \frac{1}{{^{w_s}/_4}^2 + {^b/_m}{^{w_s}/_4} + {^k/_m}} \qquad (s^2) \qquad (3.24)$$

where m, b and k are mass, damping and spring constant of the accelerometer respectively. From this equation oscillation magnitude of the accelerometer proof mass can be approximated as:

$$x(s) \approx \frac{^{a_{max}}/_2}{\left(^{w_s}/_4\right)^2} \qquad (m) \qquad (3.25)$$

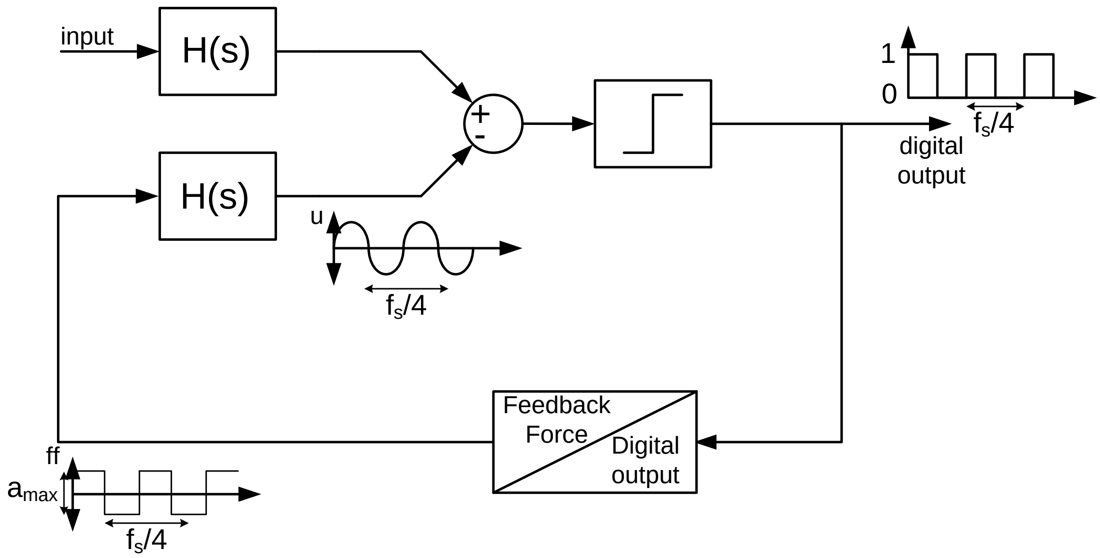

Figure 3.19: Block diagram of the closed loop accelerometer system showing the origin of dead zone

Therefore accelerometer proof mass oscillates with $(8.a_{max}/w_s^2)\sin(w_s)$ and input acceleration should be large enough to disturb this periodic motion of the proof mass of the accelerometer. Deflection of the proof mass having small bandwidths compared with the sampling frequency can be written as:

$$x(s) = \frac{a_{input}}{s^2 + {}^{b}/_{m}\, s + w_r^2} \approx \frac{a_{input}}{w_r^2} \qquad \text{(m)} \qquad (3.26)$$

Width of the dead band of the accelerometer where the sensor is unable to measure the applied acceleration can be found as:

$$\frac{a_{input}}{w_r^2} > \frac{8.a_{max}}{{w_s}^2} \qquad \rightarrow \qquad a_{input} > 8.a_{max}\left(\frac{f_r}{f_s}\right)^2 \qquad (3.27)$$

where f_r is the resonance frequency of the mechanical sensor, f_s is the sampling frequency of the readout circuit and a_{max} is the measurement range of the accelerometer in closed loop mode.

In order to observe this phenomenon MATLAB simulations are performed for the accelerometer with properties given in Table 3.2. In order to observe the small dead-band region, ±10mg ramp signal is applied to the input of the accelerometer and output of the sinc^3 and sinc^2 filters are monitored. For this accelerometer model, dead band region is calculated to be ±1.15mg. Figure 3.19 shows the MATLAB simulation results of the closed loop accelerometer output in ±10mg range. From this figure it can be seen that the width of the dead-zone region is approximately equal to its calculated value and in this region accelerometer is unable to respond to the applied acceleration.

In order to solve this problem, resonance frequency of mass of the accelerometer can be increased, spring constant of the accelerometer can be decreased by placing longer or narrower springs or sampling frequency of the readout circuit can be increased. Although these measures tend to decrease the dead zone band, neither can totally eliminate this problem. In the literature dead zone problem can only be eliminated by either adding a dither circuit to the architecture or by increasing the order of the closed loop system by adding more filters [85].

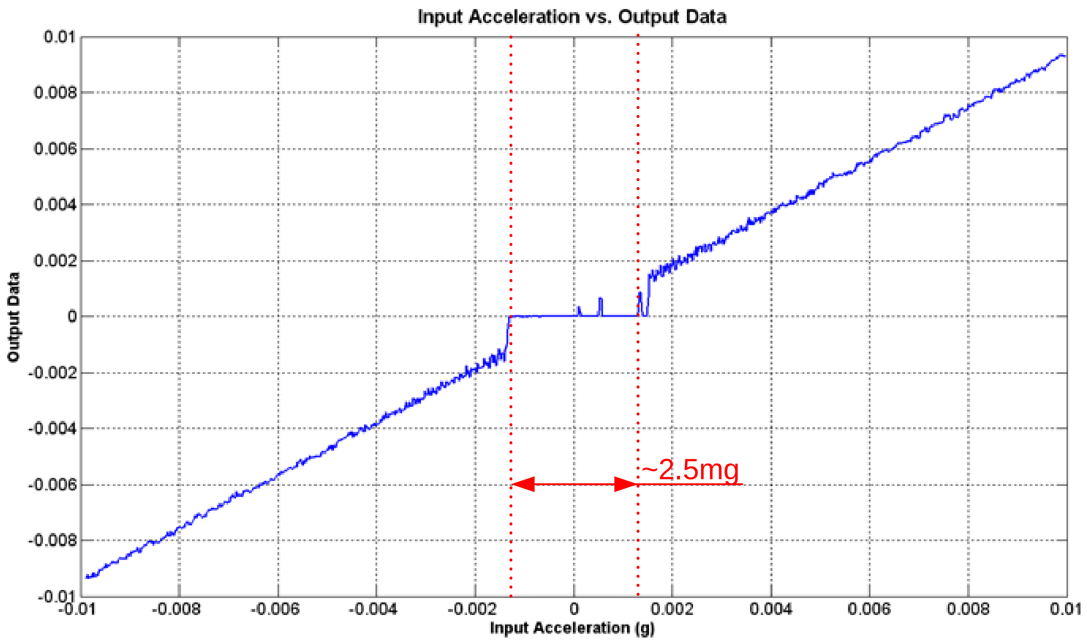

Figure 3.20: MATLAB simulation results of the closed loop accelerometer output in ±10mg range.

3.6 Turn-on Time

Turn-on time of an accelerometer system is very important for some military application since it is the initial duration which the accelerometer starts to properly evaluate the applied external acceleration. A fast response time is a desired property for an accelerometer system.

In an open loop accelerometer system charge integrator and sample and hold stages detects the movement of the accelerometer mass instantaneously, and this movement is immediately converted to a voltage signal. If an Analog-to-Digital converter is used after sample and hold stage, and voltage is converted to digital at the end of integration period than the response time of the overall circuit becomes limited by the analog to digital conversion time. If a low pass filter is placed at the output of the circuit and analog voltage is acquired from the system than the system delay becomes limited with the phase delay of the low pass filter. For the open loop system described in section 2.3.1 response time simulations are performed and a 1g step input is applied at time t=0.1second and output is monitored. Figure 3.20 shows the step input and output graphs of the open loop accelerometer system. From this figure it can be concluded that the settling time for the output voltage is ~5ms with

4th order Butterworth low pass filter which has 500Hz cut-off frequency is connected at the output of the system.

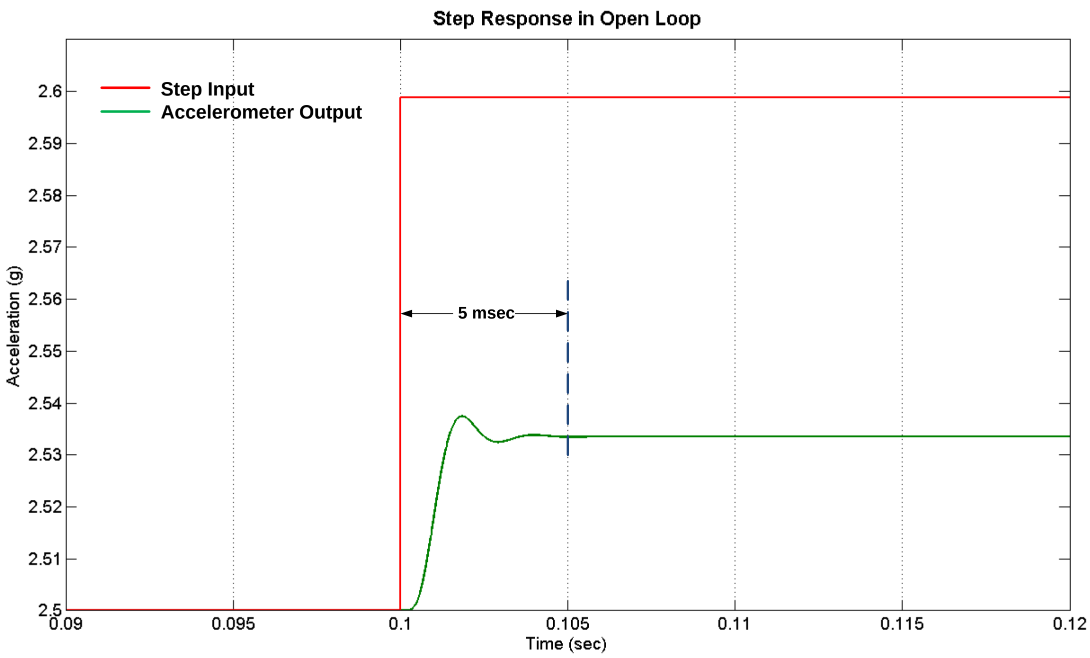

Figure 3.21: MATLAB simulation results of step input and output graphs of the open loop accelerometer system.

In closed loop systems, analog to digital conversion is performed as a property of the system and low pass filtering is done by the decimation filters at the output of the system. Response time of a closed loop system is determined by the decimation order of the filters at the output stage. For the closed loop system described at section 2.3.2, there are two low pass Sinc filters at the output of the accelerometer having 40 and 16 decimation orders and 3 and 2 stages consecutively. For this kind of output stages having cascaded Sinc filters at the output, response time can be calculated as follows:

$$d_{closed-loop} = \frac{\prod_{i=1}^{N} M_i}{fs} \cdot \prod_{i=1}^{N} k_i \qquad (3.27)$$

where N is the number of filters, M_i is the decimation order of each filter, f_s is the sampling frequency of the circuit and k_i is the order of each filtering stage. If the delay time is calculated using equation 3.27 for the closed loop model given in figure 2.18, it is found that output of the accelerometer system should lag the input for

~7.7ms. Figure 3.21 shows the MATLAB simulation results of step input and output graphs of the closed loop accelerometer system. It can be observed from this figure that the simulation results are in agreement with the hand calculations.

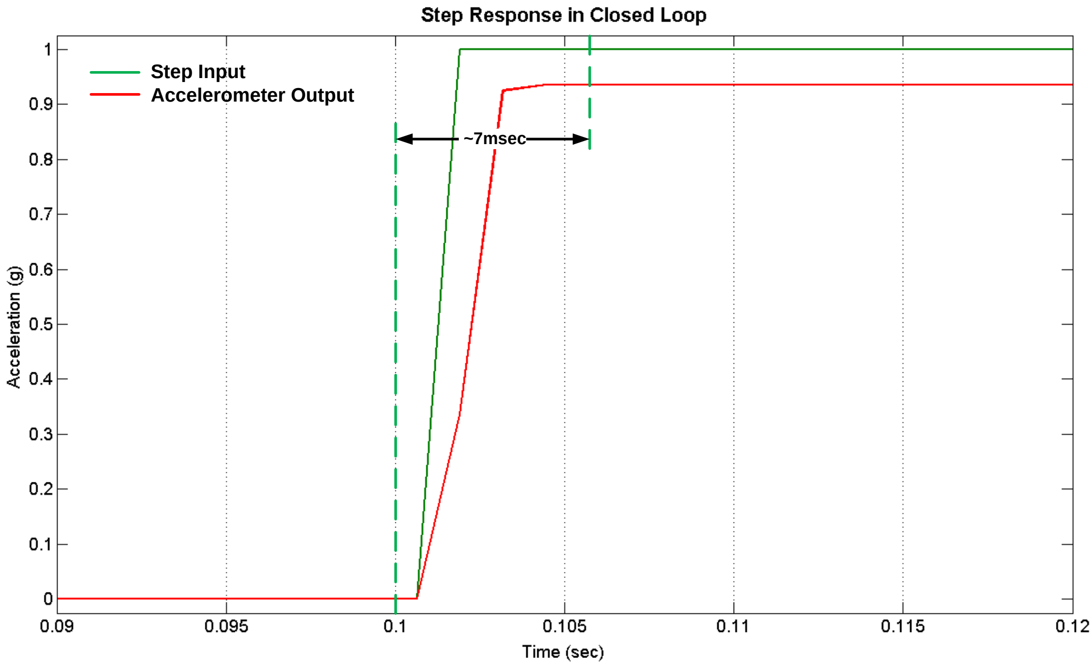

Figure 3.22: MATLAB simulation results of step input and output graphs of the closed loop accelerometer system.

Delay time for a closed loop system can be adjusted by changing the decimation orders and order of the Sinc filters. Increasing sampling frequency also improves the delay time for closed loop systems.

3.7 Summary of the Chapter

In this chapter, important performance parameters of an accelerometer system are introduced one by one and their definitions are given together with the calculation techniques for each parameter including every noise source of the system. Also all parameters are simulated in MATLAB environment together with the models constructed in the second chapter of this thesis. Results of the MATLAB simulations are compared with the theoretical calculations and several interpretations are made for the incompatibilities between the simulation results and hand calculations.

CHAPTER 4

FABRICATION PROCESSES AND PROTOTYPES

MEMS fabrication or micromachining refers to fabrication of devices with dimensions in micrometer range. There are basically two micromachining techniques: bulk and surface micromachining.

In bulk micromachining, wafer is etched such that the bodies of devices are formed from the wafer itself. Generally silicon substrate is used to realize bulk micromachined sensors. There are various methods to etch silicon using wet or dry silicon etching techniques. Wet etching can be done in two ways which are named as isotropic and anisotropic etching. In isotropic etching silicon is etched such that the etch rate is same in all directions, on the other hand in anisotropic etching, etch rates differ according to the crystalline orientation of the wafer. For accelerometers having capacitive finger type structures, vertical comb structures can be realized using Reactive Ion Etching (RIE) or Deep Reactive Ion Etching (DRIE) techniques. Although RIE can open trenches up to a limited depth value, DRIE enables the fabrication of high aspect ratio capacitive fingers.

On the other hand surface micromachining tries to build up structures onto the wafer with deposition techniques. First thin film deposition techniques are used and then by etching sacrificial layers suspended mechanical structures are formed. The process steps of surface micromachining are similar to CMOS circuitry fabrication, and hence the main advantage of surface micromachining is its compatibility with the standard IC processes. In addition to this, the vertical comb fingers can easily be realized with this technique. However, the disadvantage of the surface micromachining is the thin structural layer thicknesses and internal stress issues encountered during film depositions. But processes using high aspect ratio molds like electroplating, remove this disadvantage of the surface micromachining with providing high thickness proof masses.

Accelerometers designed for this study have been fabricated under three different fabrication processes which are Silicon-on-Glass Process (SOG), Dissolved Wafer Process (DWP), and Dissolved Epitaxial Wafer Process (DEWP). All these processes are held in METU MEMS Research and Development Facilities. Sections 4.1, 4.2, and 4.3 present the details of each fabrication process as well as the problems encountered and improvements achieved for each process respectively. Finally section 4.4 gives a brief summary of the chapter.

4.1 Silicon-on-Glass Process (SOGP)

Silicon-on-Glass process is performed by bonding glass and silicon wafers and defining the structures afterwards [88] - [90]. Glass wafers are prepared by opening recesses in the regions where the structures will be suspended and laying the metal lines for inter-structural connections and pads. Structural patterning is done with Deep Reactive Ion Etching (DRIE) technique. Using this technique structures having very high aspect ratios can be fabricated. SOG process is suitable for fabrication of high thickness structures which increases the reliability and repeatability of the fabricated sensors. In addition to this due to large proof mass of the sensors, mechanical noise will be very low. On the other hand since aspect ratio of the DRIE limits the etch depth / etch opening ratio, finger spacings less than ~3.3µm are not possible to fabricate with this process. This is a major limit for high sensitivity accelerometer fabrication. A summary of the Silicon-on-Glass micromachining process is as follows:

4.1.1 Overview of the SOG Process

SOG process requires 4 masks which are anchor mask, structure mask, shield mask and metallization mask.

The process starts with the cleaning of the 500µm thick glass and 100µm thick silicon wafers in piranha solution (1:1 H_2SO_4:H_2O_2). This is a crucial step for all wafers entering the cleanroom for the first time. With this cleaning all organic residues are removed from the surface as well as an additional physical cleaning is applied. After cleaning glass wafers are roughened in buffered HF for 1 minute and they are evaporated with 100Å chromium and 1500Å gold in the evaporator. This metallization layer will be used as the masking layer for the glass etching step. The adhesion of the chromium and gold to the glass surface should be perfect in order to prevent undercut of the glass as much as possible during the etching. Reason of the glass roughening step before the evaporation of Cr / Au is to enhance the adhesion of metal layer to the surface.

Cr / Au evaporated wafers are then coated with SHIPLEY SPR 220-3 photoresist at 4000rpm in order to achieve a masking layer of 3µm's. This photoresist layer is patterned with anchor mask in order to form the glass anchor on which the accelerometer structure will stand suspended. After photoresist is patterned and developed, it is hard baked in IMPERIAL IV Microprocessor Oven for 40 minutes at 120^{o}C. This evaporates the remaining humidity in the photoresist and makes it durable for the further etch processes.

Patterned glass wafer is first etched in TRANSENE commercial gold etchant for 75 seconds, and then etched in TRANSENE commercial chromium etchant for 60 seconds and finally etchant again in gold etchant for 10 seconds. Reason of this second gold etching process is to remove the diffused gold particles in the glass. If they are not removed this may cause many different problems like contamination of wafer or local undesired glass etch masks. After the patterning of metal lines is completed, photoresist is removed in PRS 2000 photoresist stripper chemical at 80^{o}C. After the removal of photoresist, glass wafer is finally etched in 48% HF for ~80seconds. At the end of this process ~10-12µm thick recesses are opened on the glass wafer in order to remove the bottom of the suspended glass devices. Figure 4.1 shows the process steps of glass wafer preparation for SOG fabrication technique.

After the preparation of anchors on the glass wafer, a secondary metallization is coated this time for electrical connections. This secondary metallization is again 100Å chromium and 1500Å gold in thickness and has same lithography, development, hard bake, metal etch and photoresist strip steps with the anchor mask. The only difference between two processes is the photoresist used. Instead of SPR220-3, SPR220-7 is used which is a denser and thicker photoresist. Reason of using a different and denser photoresist is that it can cover the 10-12μm depth recesses which were formed during the glass etching process. Figure 4.2 shows the secondary metallization step of the glass wafer in SOG process. With the final metallization step, glass wafer become ready for the anodic bonding.

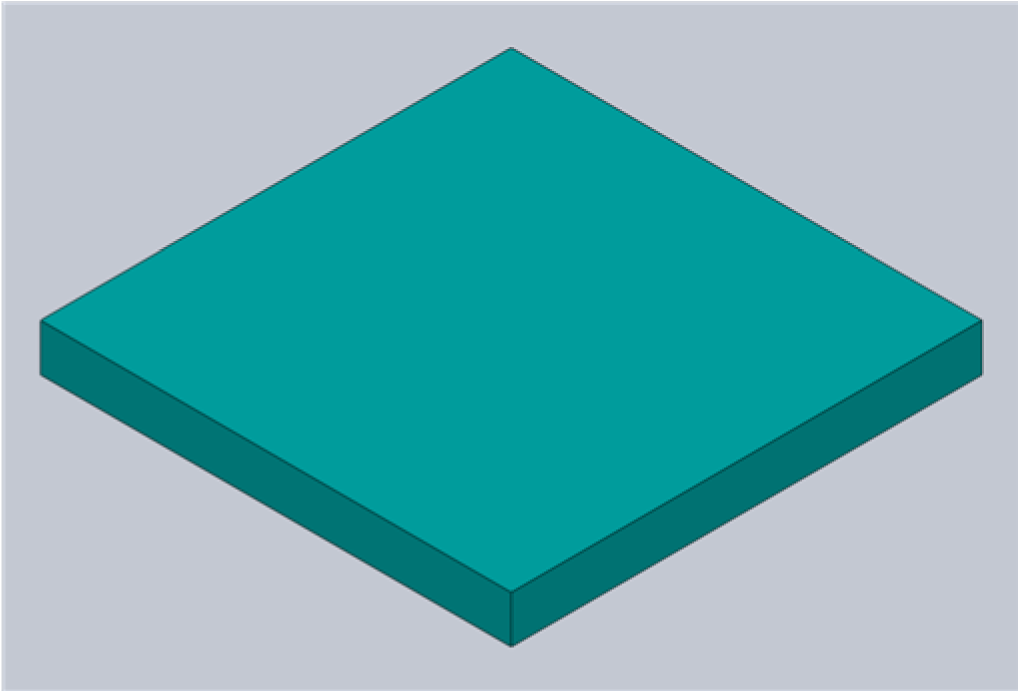

(a)

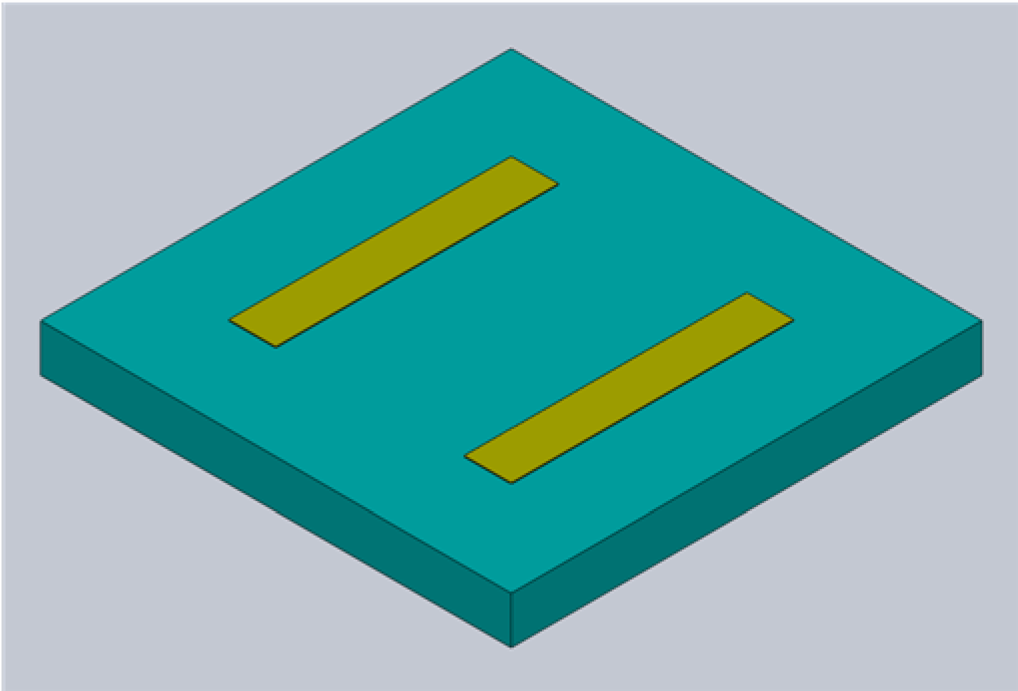

(b)

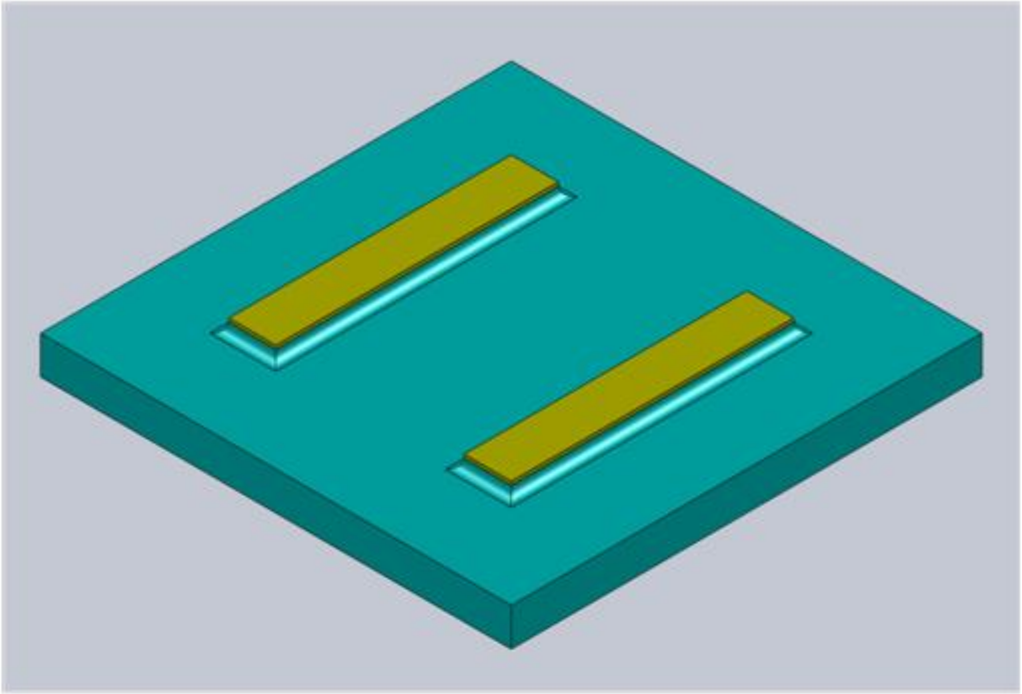

(c)

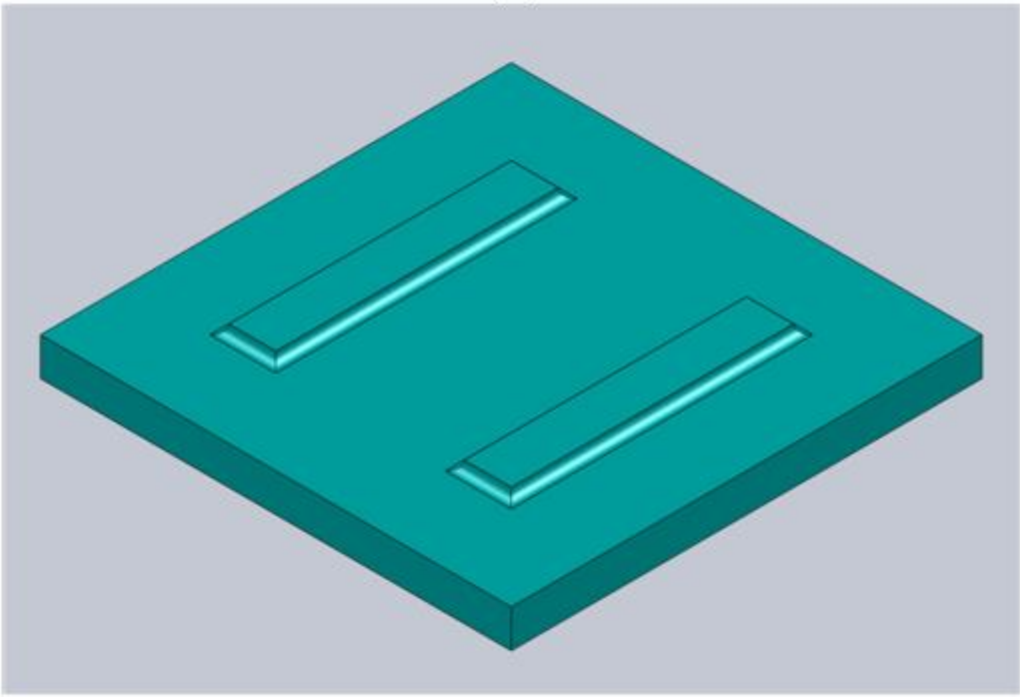

(d)

Figure 4.1: Process steps of glass wafer preparation for SOG fabrication technique (a) Process starts with a 500μm Pyrex glass wafer. (b) 100Å Chromium and 1500Å Gold is used as glass etch mask. (c) Glass wafer is etched in 48% HF for 80 seconds for 10-12μm recess opening. (d) Chromium and gold is stripped from the surface of the glass.

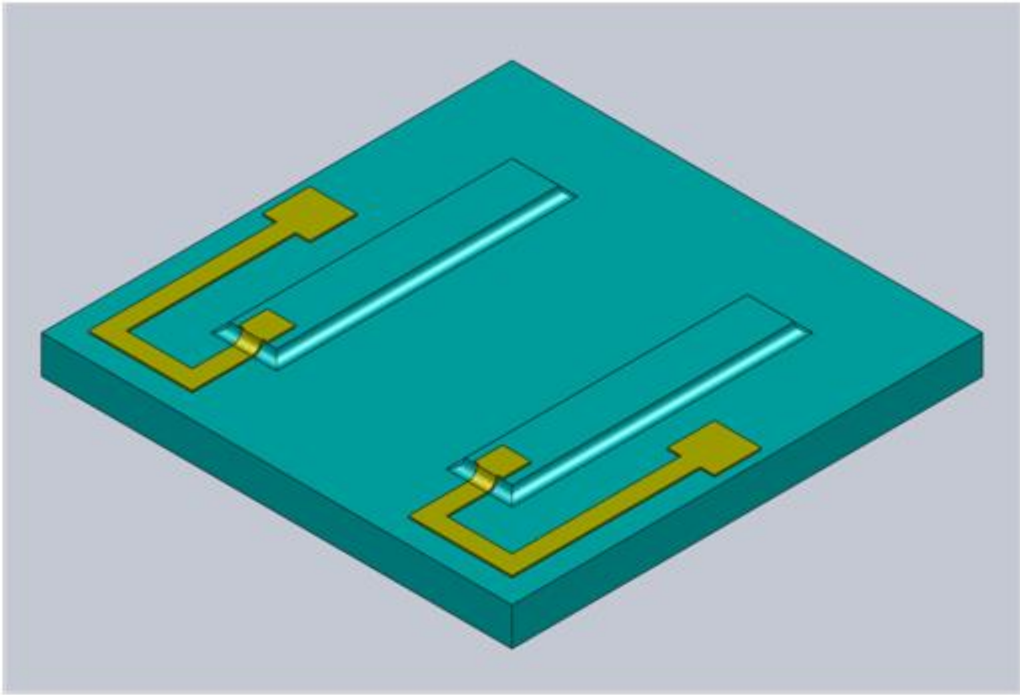

Figure 4.2: Secondary metallization step of the glass wafer in SOG process.

After the preparation of the glass wafer, silicon wafer should also be evaporated with 4000Å aluminum shield before bonding it to the glass wafer. Aluminum layer evaporated on the backside of the silicon wafer will behave as a shield to prevent notching during DRIE and it will distribute the heat uniformly throughout the wafer during etching in order to provide the etch uniformity.

DRIE process is an anisotropic dry etching mechanism that employs charged ions and plasma gases to etch silicon from the surface of the wafer. DRIE is performed in two consecutive cycles which are passivation and etching. In the passivation cycle, whole wafer surface is coated with thin polymer layer with C_4F_8 plasma. In etch cycle ion bombardment with SF_6 plasma starts and accelerated ions etches the passivation layer on the horizontal surfaces and continue etching silicon beneath them, on the other hand polymers coated on the structural side walls could not be completely removed and sidewalls are protected from etching. Figure 4.3 shows the two phases of anisotropic high profile silicon etching with DRIE technique. Notching is the distortion of etch profile during the DRIE process at the bottom of the trenches. This problem usually occurs whenever ions passing through etched cavity come across an insulator surface. As long as the etching continues the insulator surface starts to charge up, and after some certain voltage level, insulating layer starts to push the ions backwards to sidewalls. This causes distortion of the etch profile on the bottom side of the wafer and ions start to etch from the backside of the wafer [91]-[93]. When a conductive shielding layer is used, ions arriving to this layer are discharged from the wafer via the ground connection. Therefore notching effect can be completely eliminated [90]. Figure 4.4 shows the notching mechanism and Figure 4.5 shows how shielding layer prevents notching.

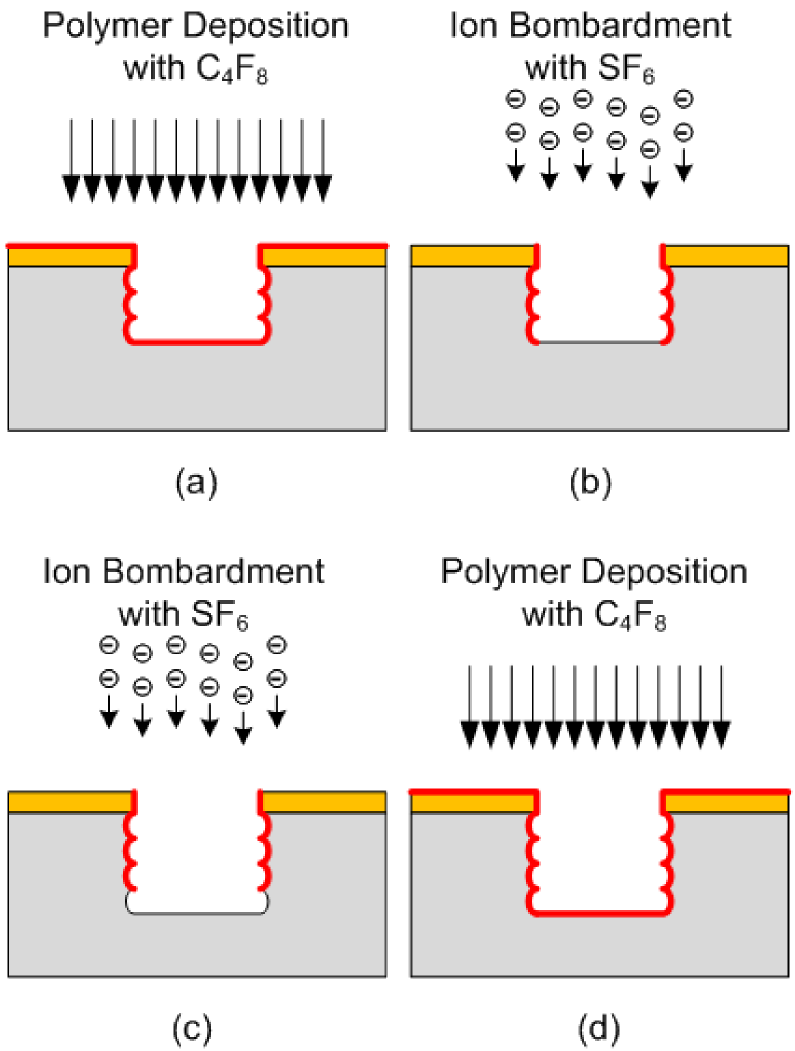

Figure 4.3: Two phases of anisotropic high profile silicon etching with DRIE technique. (a) Polymer deposition with C_4F_8. (b) Ion bombardment with SF_6, first the polymer on the horizontal surfaces are etched. Polymer on the vertical surfaces are protects the sidewalls from etching. (c) As the ion bombardment continues, etching of the silicon takes place. (d) Polymer is again deposited on all surfaces and cycle continues.

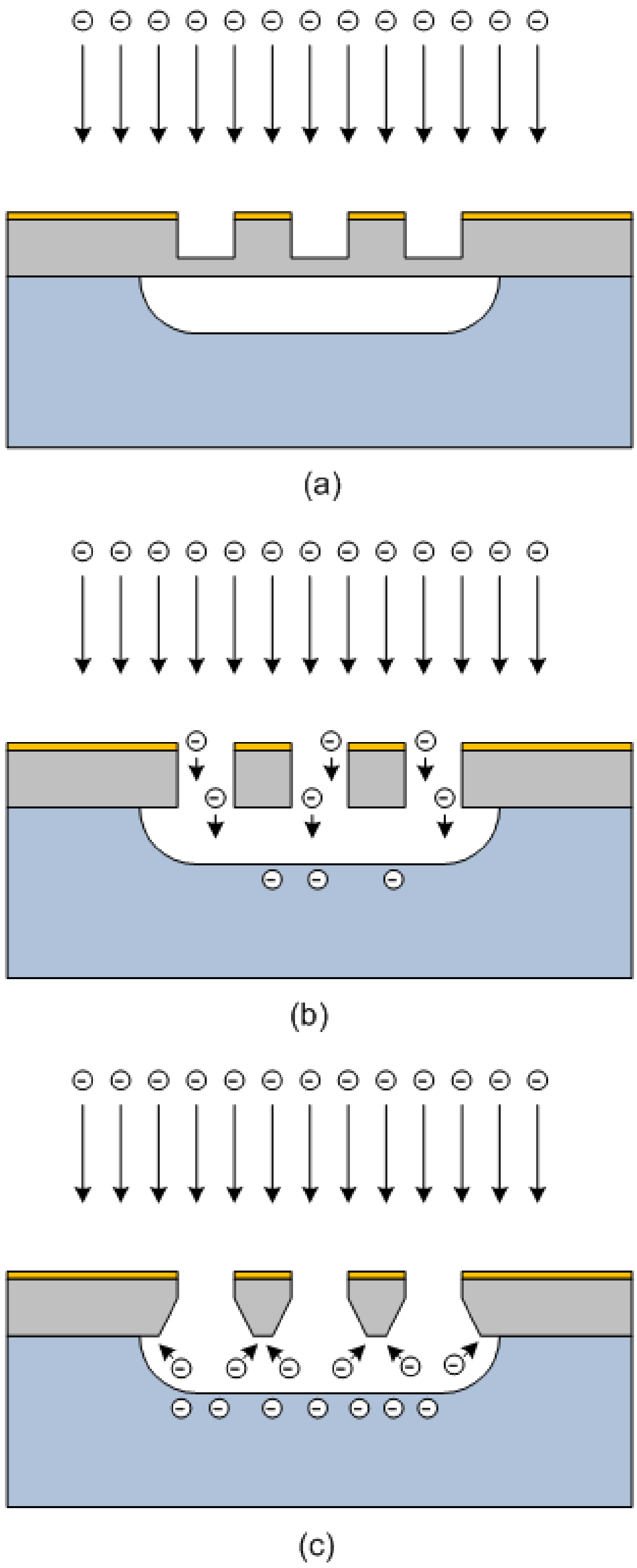

Figure 4.4: Notching mechanism (a) Etching of the silicon continues with the ions in SF_6 plasma. (b) After etching is completed ions start to charge the glass wafer. (c) Charged glass reflects the incoming ions which etches the silicon wafer from backside.

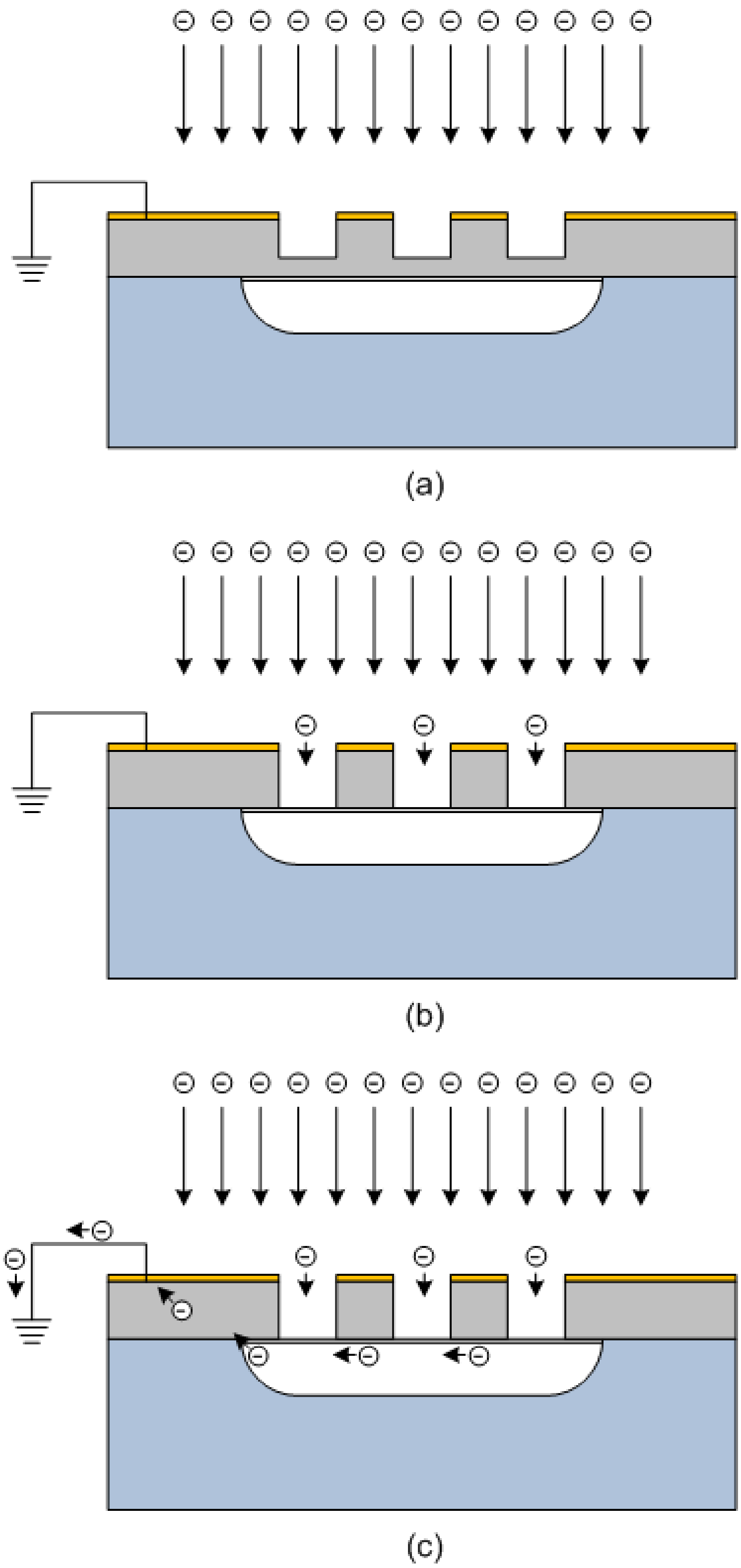

Figure 4.5: Prevention of notching with aluminum shield. (a) Etching of the silicon continues with the ions in SF_6 plasma. (b) When etching completed ions reaches the aluminum layer sputtered beneath the silicon wafer. (c) Charges arriving the shield discharge from the wafer.

Aluminum shielding layer is patterned with shield mask before bonding silicon and glass wafers together. After a lithography step with SPR 220-3 at 4000rpm, aluminum is etched in TRANSENE commercial AL etchant. Aim of this etch step is to open the regions of silicon wafer where the glass and silicon surfaces will be bonded to each other. If this step is skipped or the aluminum in these regions could not be completely removed, bonding quality will decrease significantly. Figure 4.6 shows the silicon wafer with aluminum shield layer etched with shield mask.

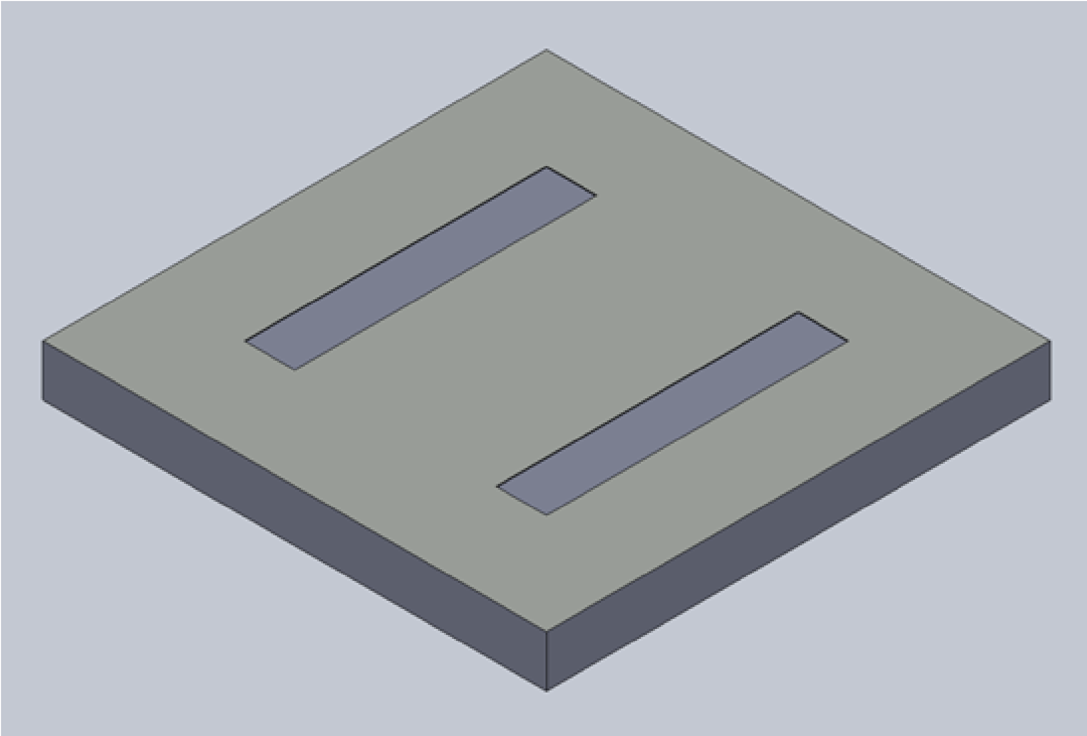

Figure 4.6: Silicon wafer with aluminum shield layer etched with shield mask.

After the silicon wafer is prepared both glass and silicon wafers are anodically bonded to each other at 350^{o}C, with 1000N piston pressure and 1000V bonding voltage. Top surface of the bonded silicon wafer is coated with SPR 220-3 at 2000rpm and patterned with structural mask. Patterned wafer is placed in DRIE for the final etching operation and etched for 10+10+10 minutes. 5 minute intervals are placed between each etching step in order to cool the wafer harder to maintain constant etch rate. Photoresist and polymer deposited during DRIE is removed with O_2 plasma up to some extent. Remaining polymer, photoresist and the aluminum shield beneath the silicon wafer is removed in piranha solution. Figure 4.7 shows the anodic bonding, structural etch with DRIE and final cleaning steps.

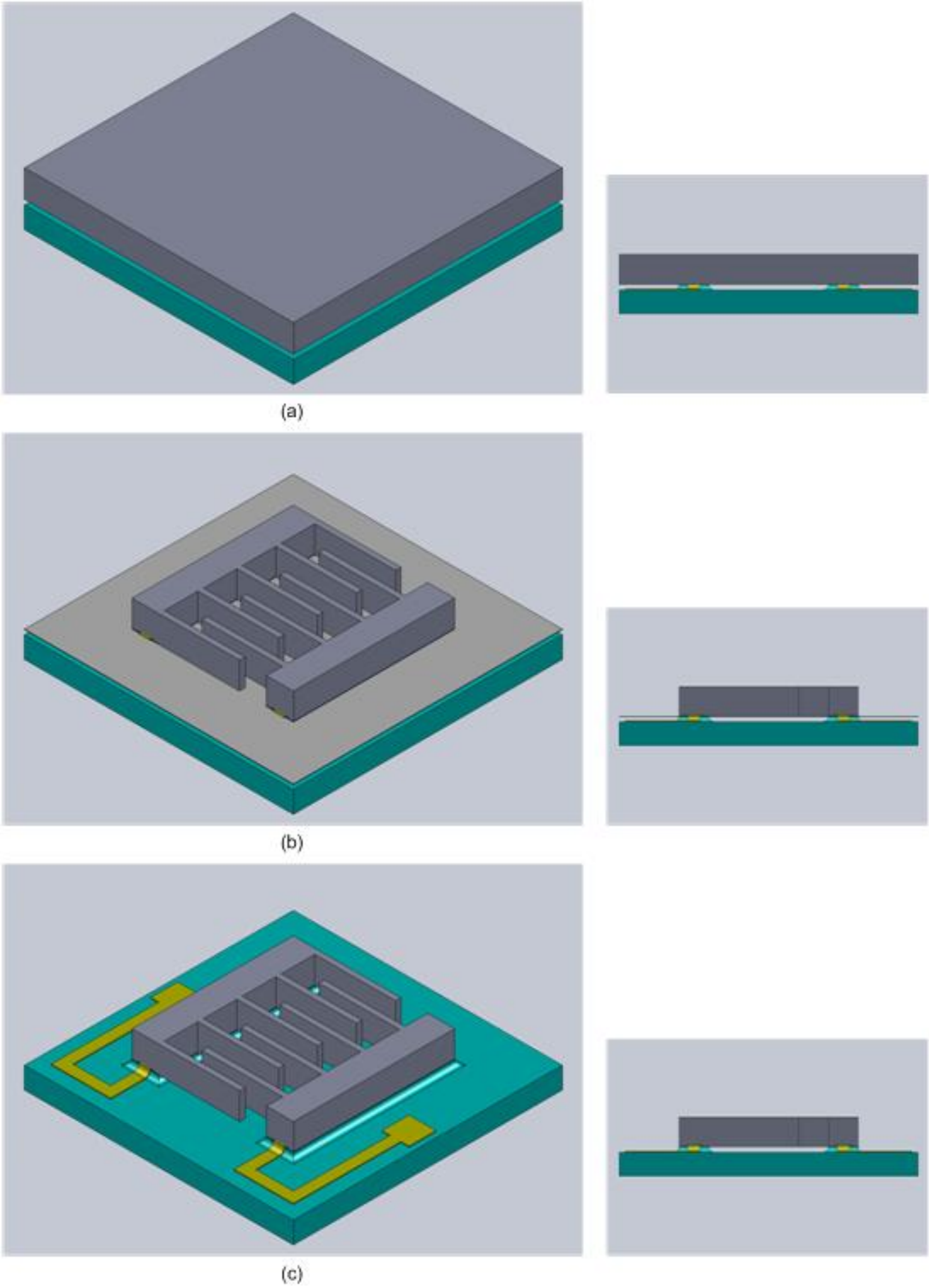

Figure 4.7: (a) Prepared glass and silicon wafers are bonded to each other. (b) After lithography step, structural layer is patterned with DRIE and aluminum shield behaves as an etch stop. (c) Aluminum shield is removed and structures are cleaned and suspended.

4.1.2 Prototypes Designed for SOG Process

A single accelerometer is designed for SOG process. Since the aspect ratio of DRIE process is limited with ~30, 3.5µm finger spacing is drawn for this accelerometer by taking the 100µm structural thickness into account. Although 3.5µm finger spacing is used for the mask layouts these spacings are measured as 4µm after the fabrication is completed. Table 4.1 presents the design and performance parameters for 3.5µm finger spacing and estimated performance parameters for 4µm finger spacing. Performance parameters for the designed accelerometers are calculated using the equations given in chapter 3. Figure 4.8 shows the mask layouts of the Silicon-on-Glass accelerometer.

Table 4.1: Design and performance parameters of SOG accelerometers.

DESIGN PARAMETERS		PERFORMANCE PARAMETERS	
Finger Overlap Length	380µm	Sense Capacitance (drawn / estimated)	17.6pF 16.1pF
Finger Width	7µm	Damping (drawn / estimated)	0.038 0.026
Finger Gap (drawn)	3.5µm	Sensitivity (drawn / estimated)	$4.2x10^{-6}$F/m $3.4x10^{-6}$F/m
Finger Anti gap (drawn)	7.5µm	Operation Range (drawn / estimated)	±2.66g ±2.15g
Spring Constant	221N/m	Brownian Noise (drawn / estimated)	2.13µg/√Hz 1.78µg/√Hz
Number of Fingers per Side	125		
Proof Mass	$12x10^{-7}$kg		

Fabrications of these sensors are made and the performance results are measured. As expected the measurement range of the SOG accelerometers are found to be ~±2g. Measurement range of these sensors was limited with the accelerometer finger spacing. Since the minimum feature of this fabrication process is limited with the aspect ratio of the DRIE, it is not possible to open finger spacings less than 3.5µm on wafers having 100μm structural thicknesses. Figure 4.9 shows the SEM pictures of the fabricated SOG accelerometers.

In order to increase the measurement range of the accelerometers, a process that allows creating narrower gap spacings should be employed to fabricate accelerometers.

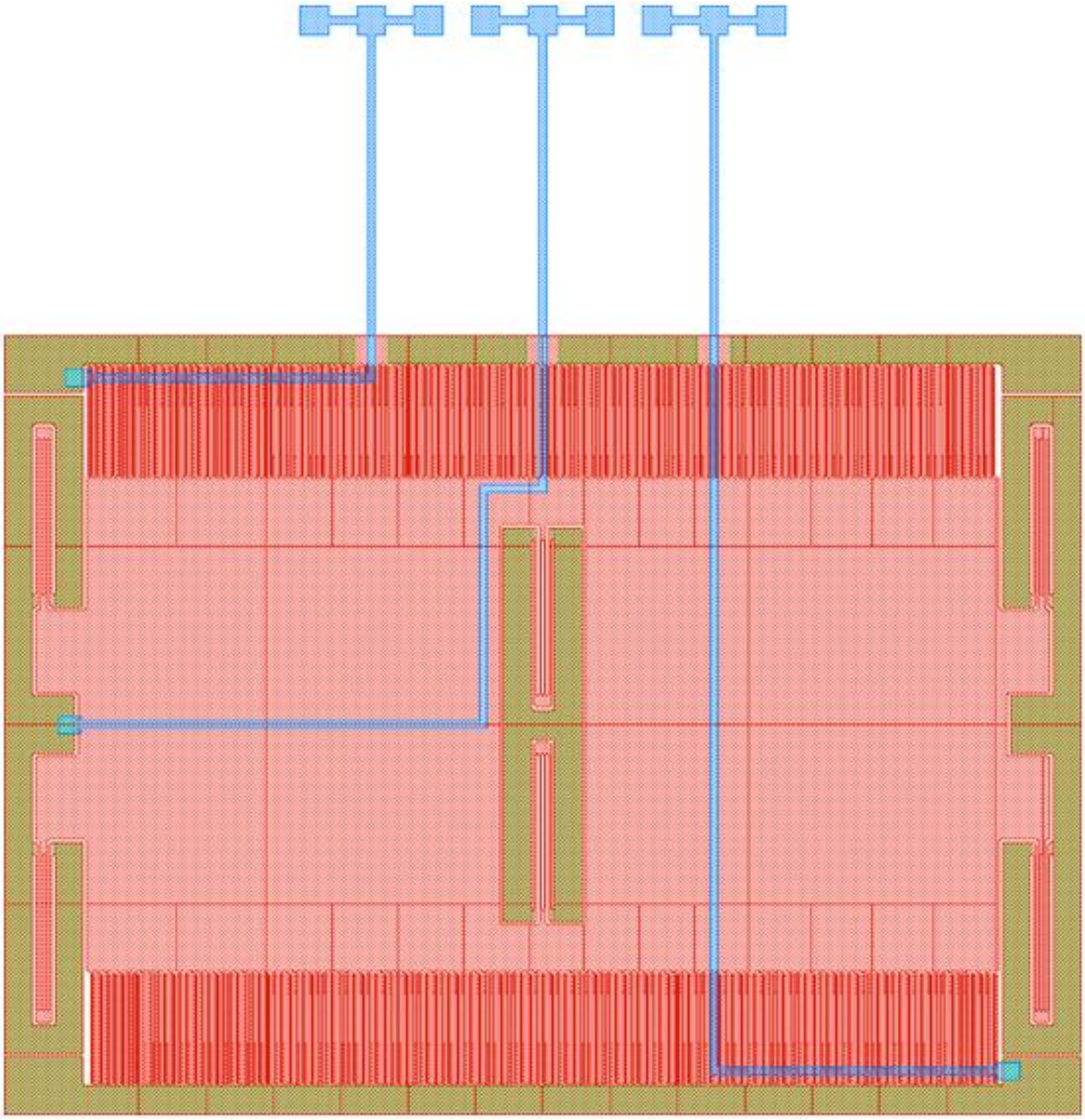

Figure 4.8: Mask layout of the accelerometer designed for Silicon-on-Glass process.

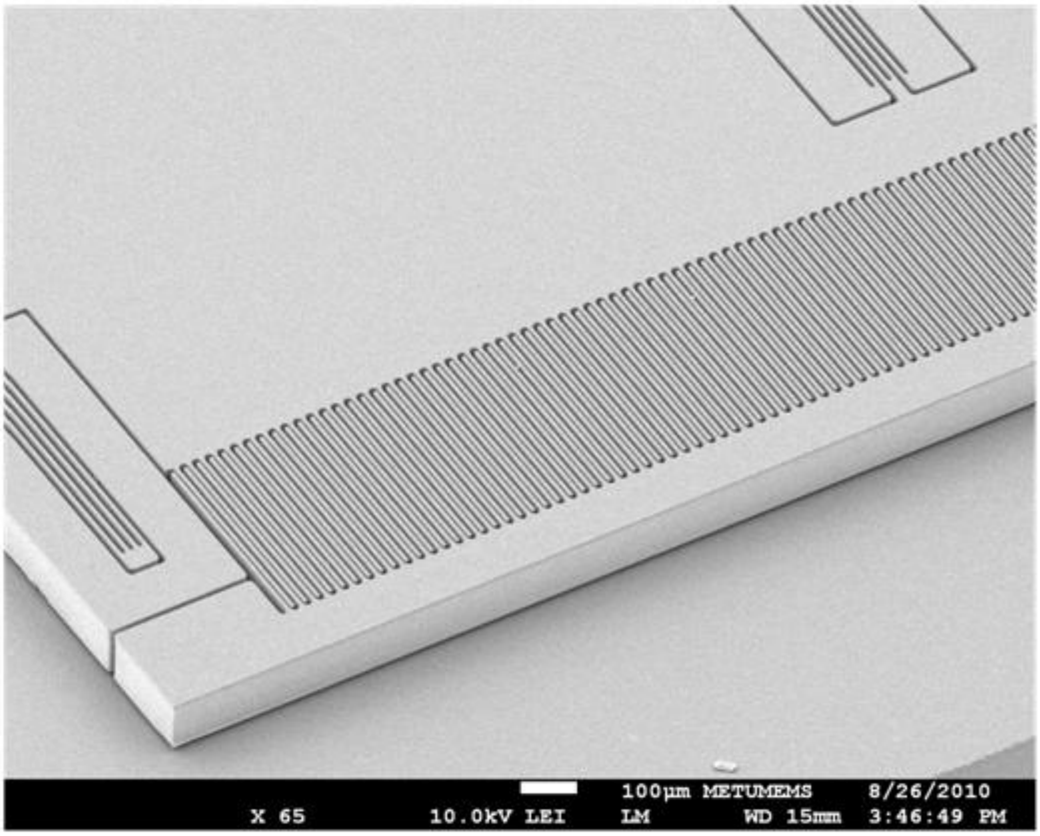
100µm METUMEMS 8/26/2010
X 65 10.0kV LEI LM WD 15mm 3:46:49 PM

(a)

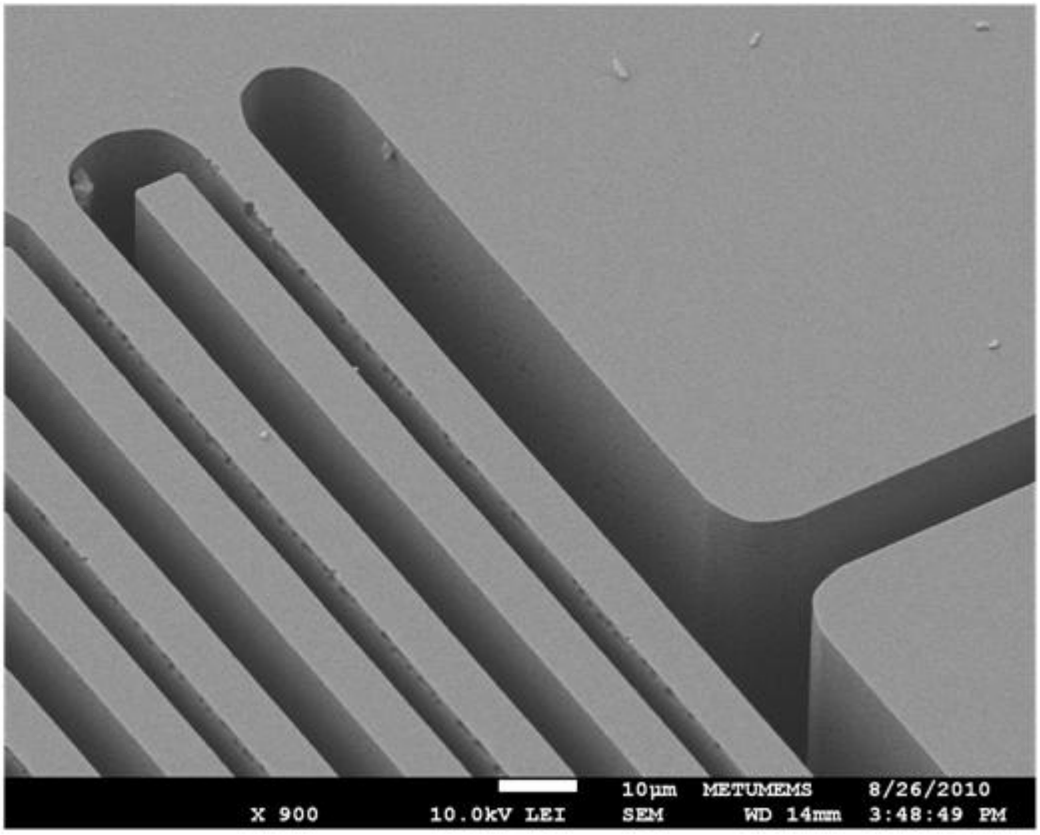
10µm METUMEMS 8/26/2010
X 900 10.0kV LEI SEM WD 14mm 3:48:49 PM

(b)

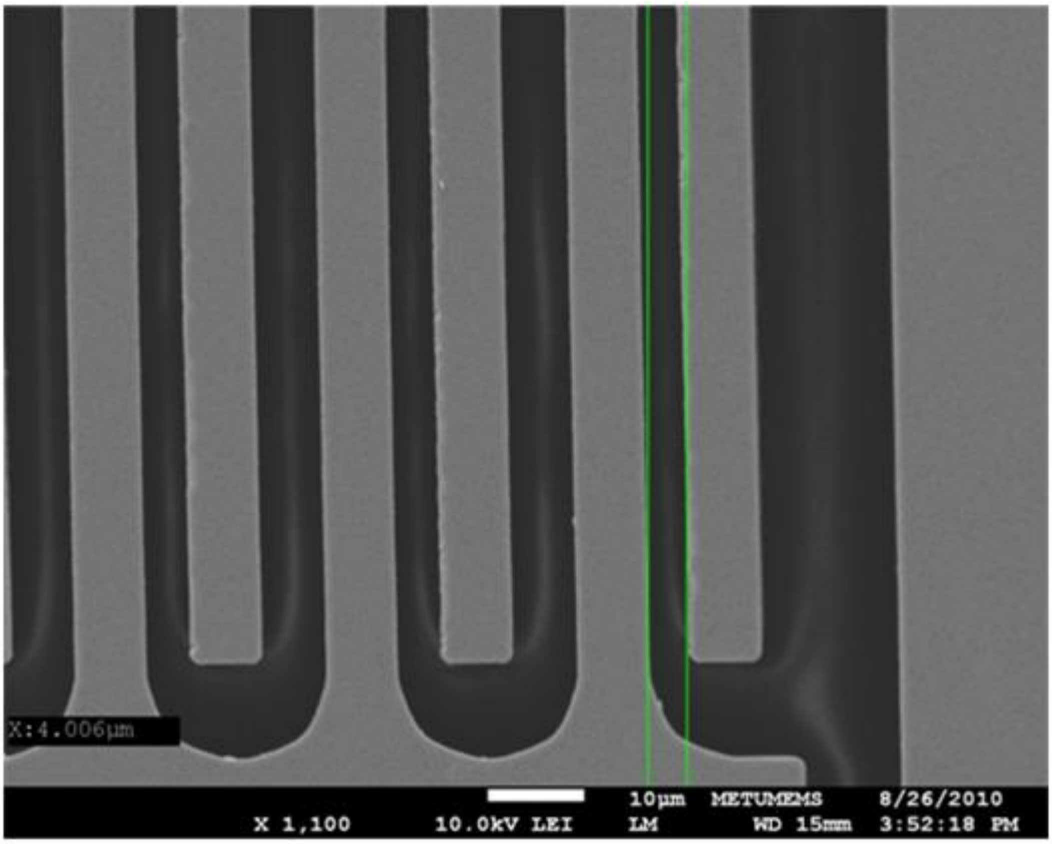

(c)

Figure 4.9: (a), (b), and (c) SEM pictures of the fabricated SOG accelerometers. Fabricated finger spacing is measured as ~4µm.

4.2 Dissolved Wafer Process (DWP)

Result of the SOG process indicated that no matter how much the mass of the accelerometer is decreased; capacitive finger spacing of the sensors should be fabricated narrower in order to reach higher measurement range values. For this purpose a process with lower structural thickness should be employed in order to obtain narrower capacitive gaps.

Dissolved wafer process is fabricating structures with deep trenches on a highly boron doped silicon wafers which are anodic bonded to low-loss insulating substrates. After the bonding of the wafer undoped silicon is chemically removed in order to suspend the structures. This process enables the fabrication of accelerometers with structural thicknesses varying between 10µm and 15µm. Having low structural thicknesses allows the fabrication of submicron finger spacings and lighter proof mass, which provides the fabrication of accelerometers achieving higher measurement ranges. On the other hand having high measurement range and narrower gap spacing with lighter proof mass increases both the electrical and mechanical noise of the system. Therefore fabrication of the accelerometers with DWP requires a careful design and simulation in order to obtain desired performances after fabrication. A summary of the Dissolved wafer process is as follows:

4.2.1 Overview of the Dissolved Wafer Process

Dissolved wafer process requires 3 masks which are anchor, structure and metallization masks. The process starts with deep boron diffusion of the front side of standard <100> oriented silicon wafer. The depth of the highly p++ doped boron diffusion may vary between 10μm to 15μm. Several techniques are developed in the literature to control the depth of the boron diffusion but it is not possible to increase the depth further due to the physical properties of silicon crystal. An additional drive-in step is required after the diffusions step, in order to reach desired boron diffusion depth and obtain a uniform boron diffusion density [94], [95]. After boron doping, surface oxide on the front side of the wafer is removed in HF or buffered HF. If surface oxide is not removed it may hinder the DRIE and may cause grassing. Front side of the wafer is than coated with photoresist and patterned using the structural mask. Using this mask as a protective layer silicon wafer is etched up to a depth of 20μm with DRIE. With the completion of this step highly boron doped silicon wafer becomes ready for anodic bonding process. Figure 4.10 shows the process steps for preparation of highly boron doped structural wafer.

Glass wafer for this process is prepared similar to the fabrication steps used for SOG process. First metallization is used as the glass etch masking layer and glass is etched in order to release the bottom of the suspended structures and with the second metallization electrical connections are formed. Metal lines climb on top of the anchors at some regions and these regions forms the ohmic contacts between the silicon and glass wafers after anodic bonding of the wafers.

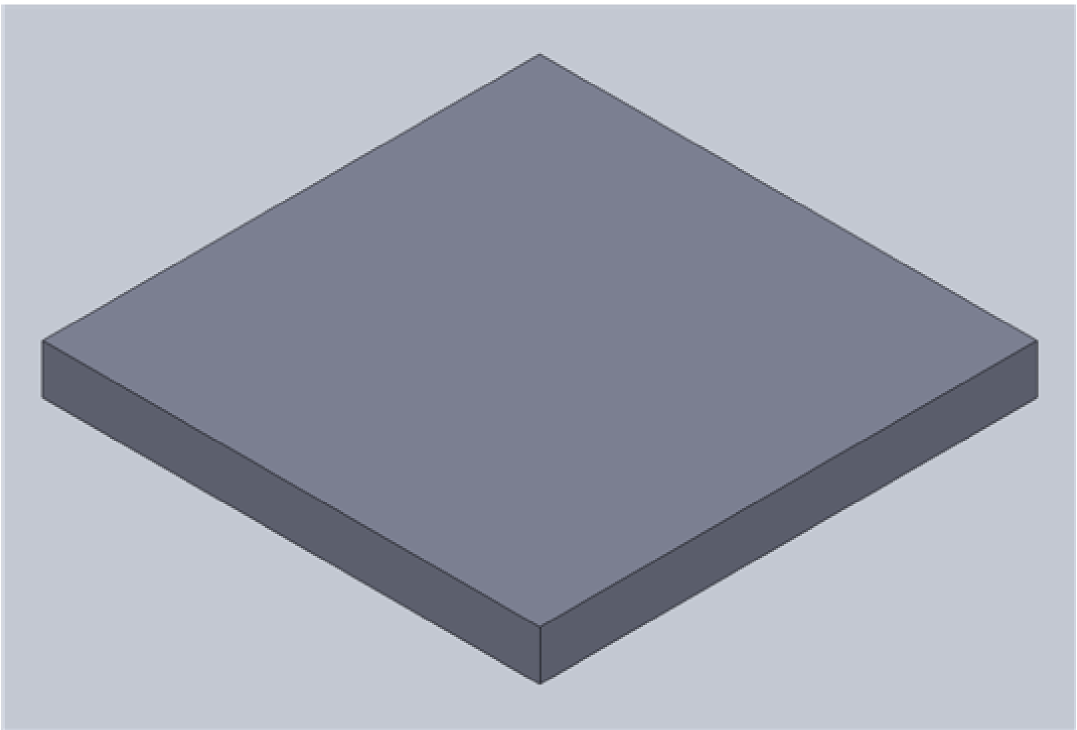

(a)

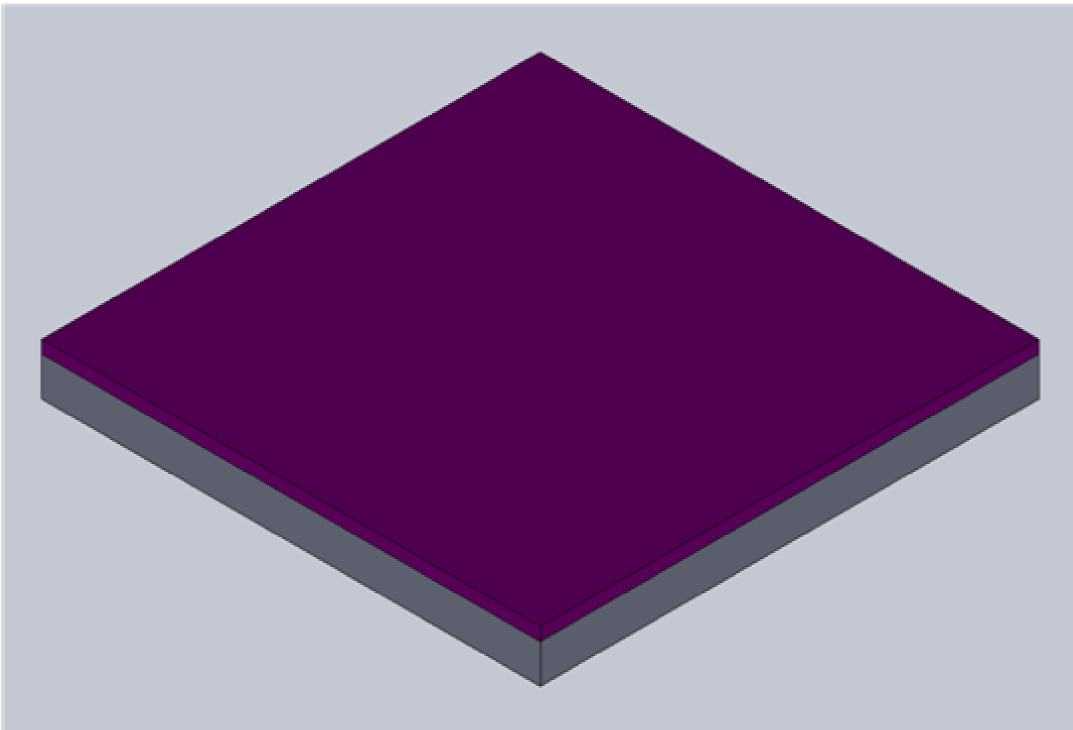

(b)

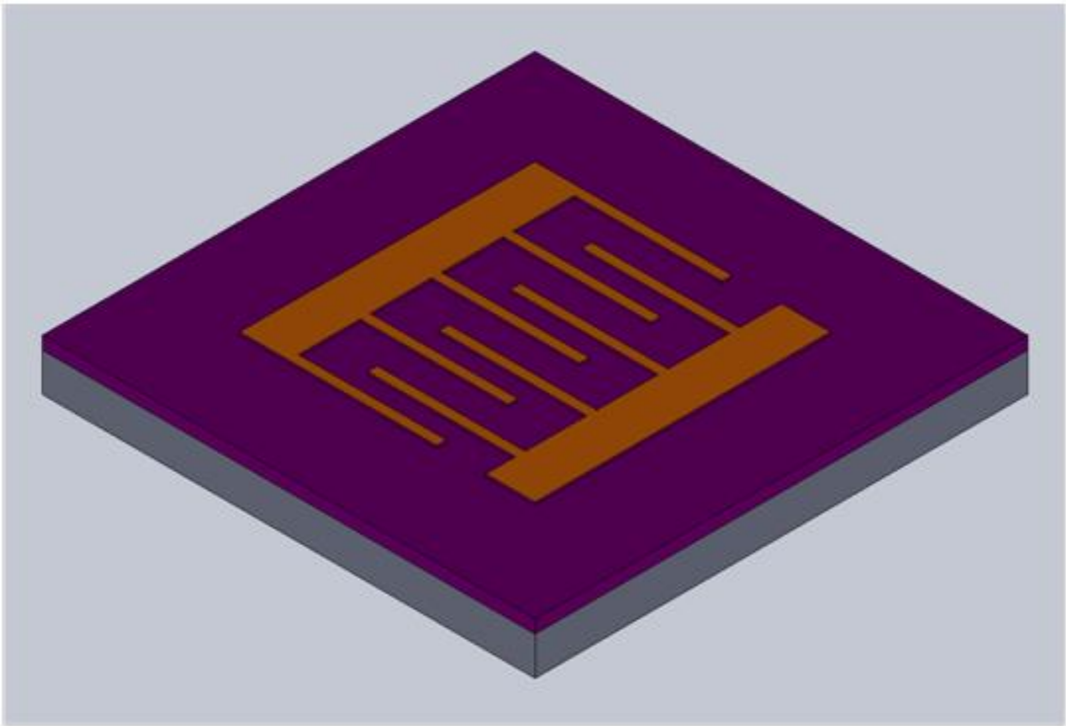

(c)

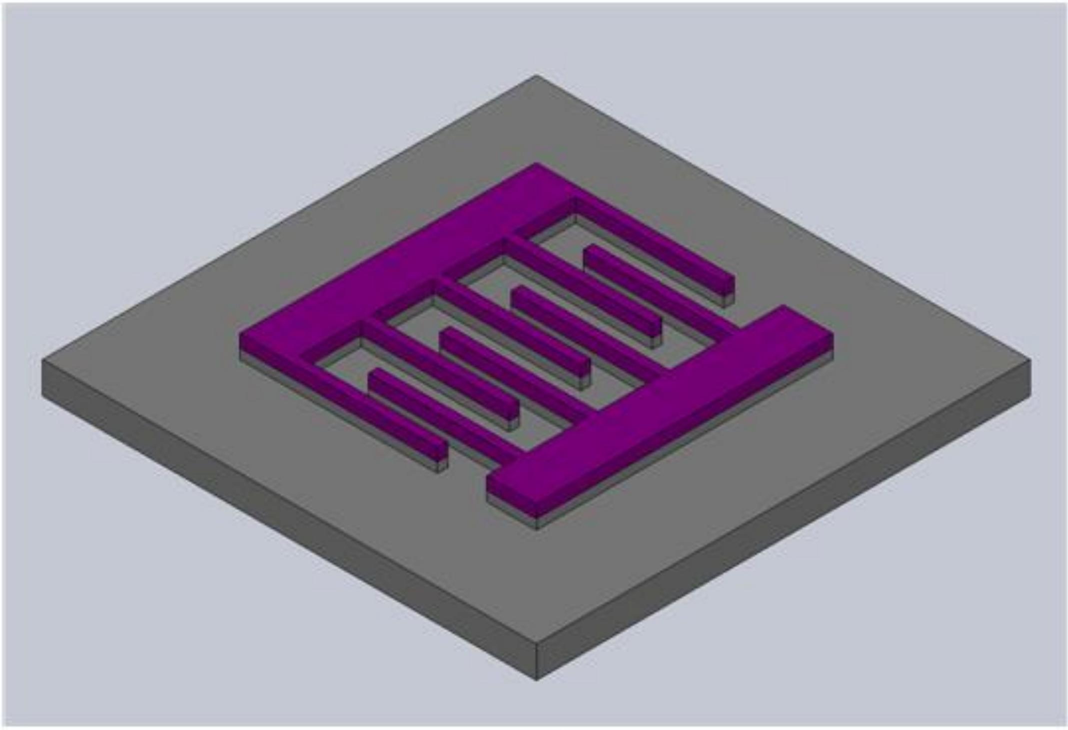

(d)

Figure 4.10: Process steps for preparation of highly boron doped structural layer. (a) Process starts with a <100> silicon wafer. (b) High boron diffusion is performed to obtain concentrations larger than $1x10^{20}$. (c) Lithography defines the structures on the wafer. (d) DRIE is done and photoresist and polymer is strip cleaned.

Both glass and silicon wafers are then cleaned in piranha solution (1:1 H_2SO_4:H_2O_2) and surface oxide of the silicon wafer is removed once more in the HF or buffered HF. This step is very important and compulsory in order to obtain good ohmic contacts between the metal lines on the glass wafer and the silicon substrate. After all wafers are prepared they are anodically bonded together in "EVG 501 Universal Bonder". Finally un-doped silicon is selectively etched in ethylenediamine pyrocathecol (EDP) solution up to highly boron doped layer is reached where the etch rate decreases drastically. If removing the whole undoped silicon wafer is performed in EDP solution it will take around 6-7 hours since the etch rate of the Fast EDP solution is ~80μm/hours [96], [97]. Instead a faster etching method can be used to thin wafer up to 100-150μm's before putting it into EDP solution. Though there are many methods that can be used to thin the wafer, two different methods are employed in this study. First method is to thin wafer chemically in HNA solution (1:8:1 HF: HNO_3: CH_3COOH). Etch rate of the HNA solution is 10μm/minutes. Therefore with a 35-40 minute of etching wafer thickness can be decreased to desired levels. Second method is to thin the wafer physically with Grinder. The wheels designed for grinding, thins the silicon wafer with 0.5 – 3 μm/second etch rates and within several minutes desired wafer thicknesses can be reached. Wafers are cleaned in deionized water and piranha solution after removing the undoped silicon with EDP and sensors are diced and they became ready for testing. Figure 4.11 shows the process steps for anodic bonding, thinning and selective etching of un-doped silicon.

4.2.2 Prototypes Designed for Dissolved Wafer Process

Fabrication of the dissolved wafer process is done in three phases. In the first phase four different types of accelerometers are designed for dissolved wafer process. All accelerometers have different structural properties and aim of having four different designs was to find the optimum accelerometer. From the observations and results obtained at the end of the first phase, a new design is prepared for the second phase of the process which improves the performance and yield of the best design of first phase.

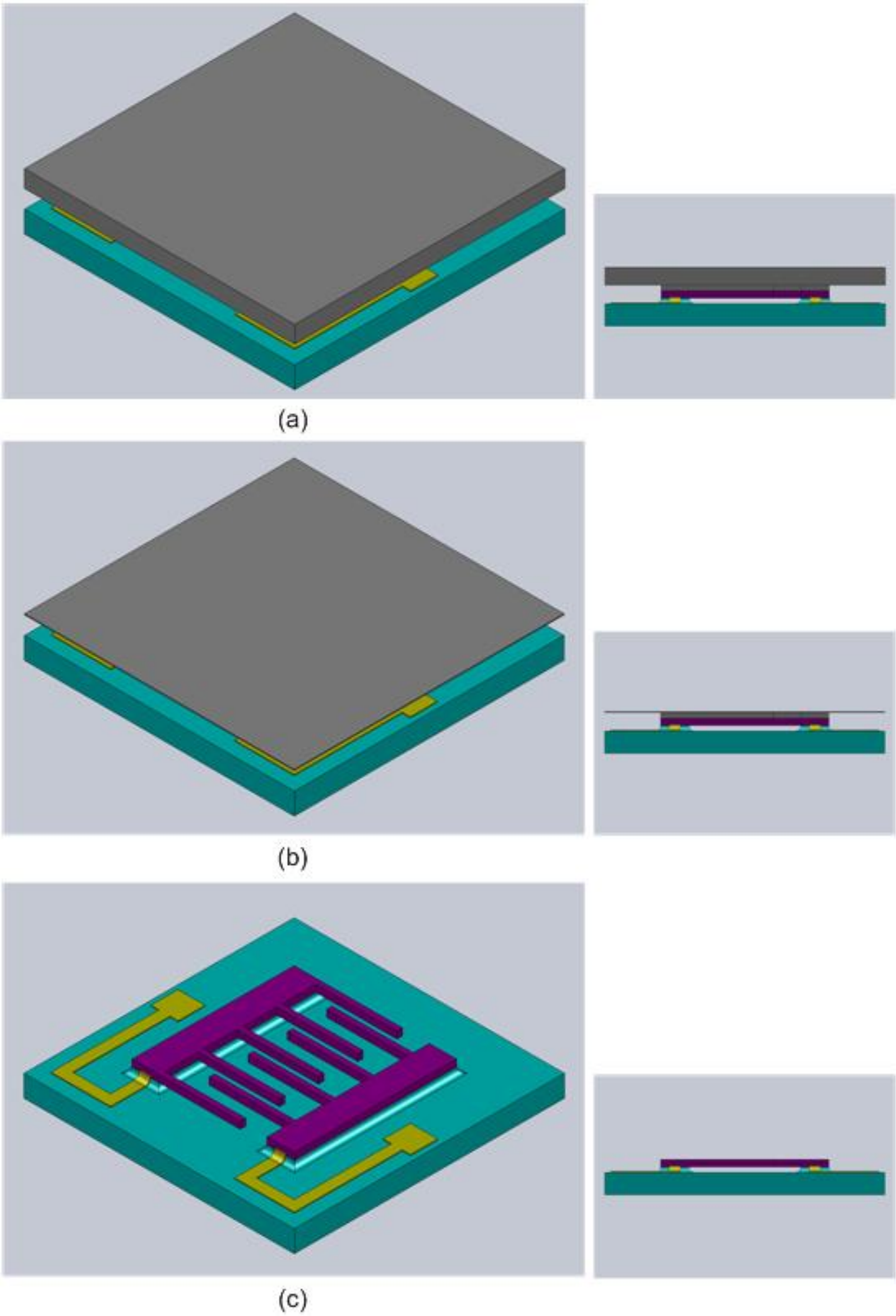

Figure 4.11: Process steps for anodic bonding, thinning and selective etching of undoped silicon. (a) Patterned silicon wafer is bonded to glass wafer using anodic bonding method. (b) Bonded wafer is thinned up to 100-150µm in HNA or with grinder. (c) Rest of the undoped silicon is etched in EDP.

First design of the first phase has two sets of fingers on each side of the accelerometer. By opening a gap at the center of the proof mass and placing capacitive sense fingers, sensitivity of the accelerometer increased significantly. Four doubly clamped beams are used to attach the proof mass to the electrodes on each side of the accelerometer which increase the sensitivity due to its lower spring constant. Table 4.2 summarizes the design and performance parameters of type-I DWP accelerometer and Figure 4.12 shows type-I accelerometer layout designed for dissolved wafer process.

Table 4.2: Design and performance parameters of type-I DWP accelerometer.

DESIGN PARAMETERS		PERFORMANCE PARAMETERS	
Finger Overlap Length	340μm	Sense Capacitance (drawn / estimate)	21.9pF 15.2pF
Finger Width	5.5μm	Damping (drawn / estimate)	0.021 0.005
Finger Gap (drawn/estimate)	0.8/1.3μm	Sensitivity (drawn / estimate)	$2.1x10^{-5}$F/m $6.9x10^{-6}$F/m
Finger Anti-gap	3.2μm	Operation Range (drawn / estimate)	±78g ±26g
Spring Constant	19N/m	Brownian Noise (drawn / estimate)	9.4μg/√Hz 4.7μg/√Hz
Number of Fingers per Side	345		
Proof Mass	$2x10^{-7}$kg		

Second design has same structure with the first design, but the only difference is, instead of doubly clamped springs, doubly folded type springs are used. Doubly folded springs occupy more area compared with doubly clamped springs, but the movement of the proof mass becomes linear with doubly folded springs. With increasing spring size, the number of fingers and sensitivity is decreased. On the other hand maximum stress that will be loaded on each spring decreases with increased safety of the structures. Table 4.3 summarizes the design and performance parameters of type-II DWP accelerometer and Figure 4.13 shows type-II accelerometer layout designed for dissolved wafer process.

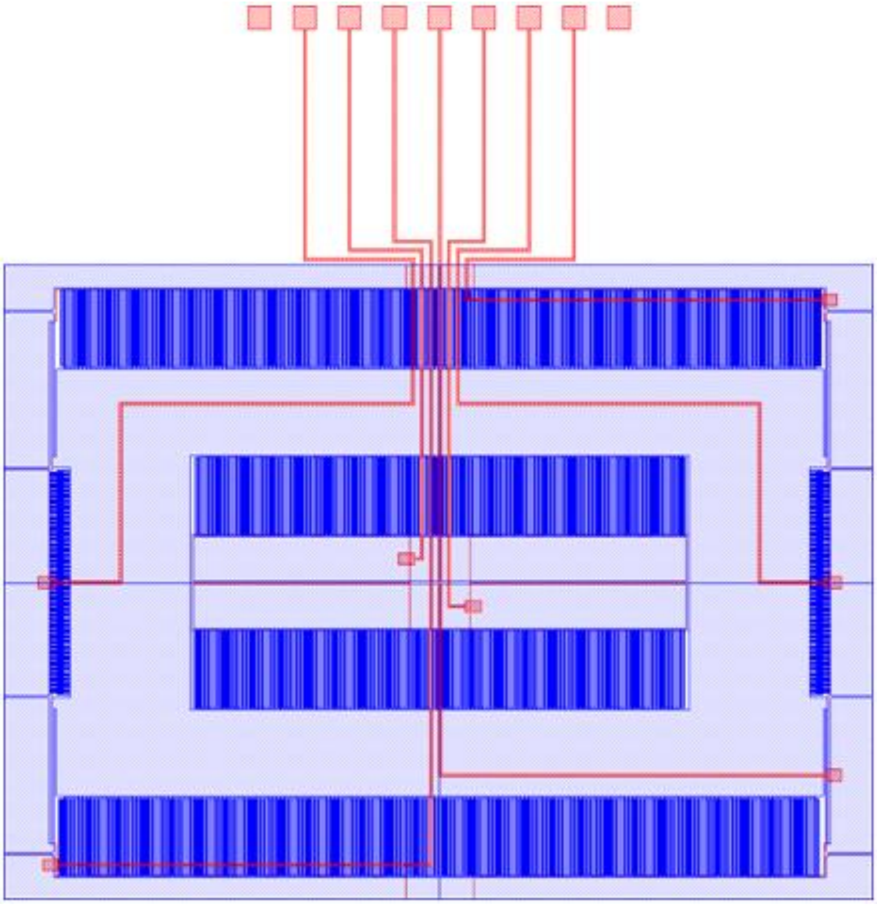

Figure 4.12: Type-I accelerometer layout designed for dissolved wafer process.

Third accelerometer structure does not have any fingers placed at the center of the proof mass and instead of 4 doubly clamped springs, proof mass is attached to the electrodes with 6 doubly clamped springs. Aim of placing additional two springs at the center of the proof mass was to prevent the buckling due to any internal stress. All these properties make third design the safest of all but it is also the least sensitive design with its high spring constant and low number of fingers.

Table 4.4 summarize the design and performance parameters of type-III DWP accelerometers and Figure 4.14 shows type-III accelerometer layout designed for dissolved wafer process.

Table 4.3: Design and performance parameters of type-II DWP accelerometers.

DESIGN PARAMETERS		PERFORMANCE PARAMETERS	
Finger Overlap Length	390 µm / 340 µm	Sense Capacitance	18.5pF 12.8pF
Finger Width	5.5µm	Damping	0.0175 0.0043
Finger Gap (drawn/estimate)	0.8/1.3µm	Sensitivity	1.7 x10^{-5}F/m 5.8x10^{-6}F/m
Finger Anti-gap	3.2µm	Operation Range	±66g ±22g
Spring Constant	26N/m	Brownian Noise	8.7 µg/√Hz 4.3µg/√Hz
Number of Fingers per Side	191 / 72		
Proof Mass	2x10^{-7}kg		

Table 4.4: Design and performance parameters of type-III DWP accelerometers.

DESIGN PARAMETERS		PERFORMANCE PARAMETERS	
Finger Overlap Length	500 µm	Sense Capacitance	15.1pF 10.5 pF
Finger Width	5.5 µm	Damping	0.0144 0.0035
Finger Gap (drawn/estimate)	0.8/1.3 µm	Sensitivity	1.4x10^{-5}F/m 4.8x10^{-6}F/m
Finger Anti-gap	3.2 µm	Operation Range	±54g ±18g
Spring Constant	33 N/m	Brownian Noise	7.9µg/√Hz 3.9µg/√Hz
Number of Fingers per Side	162		
Proof Mass	2x10^{-7} kg		

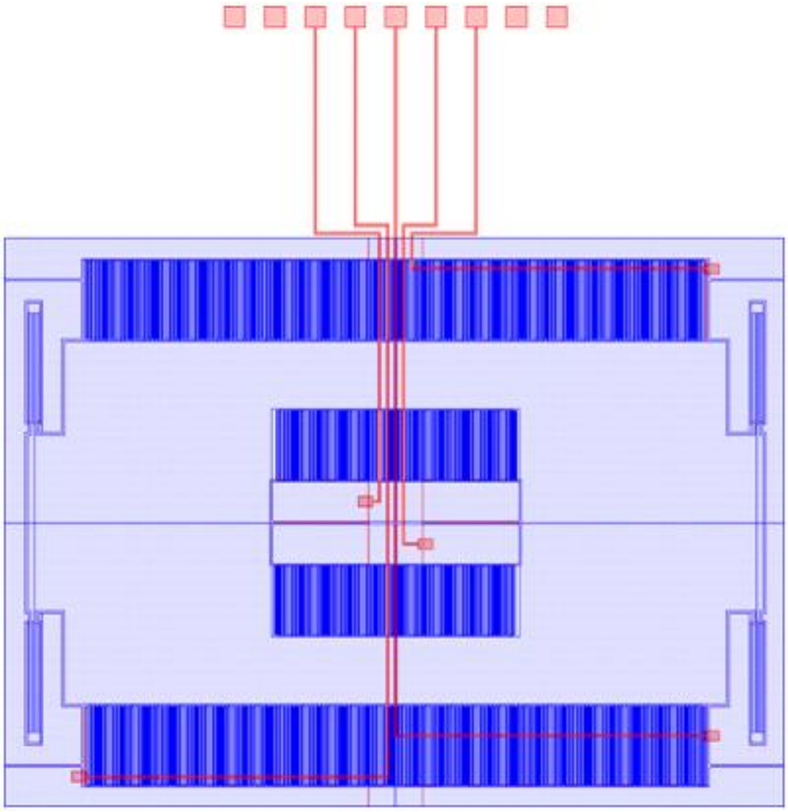

Figure 4.13: Type-II accelerometer layout designed for dissolved wafer process.

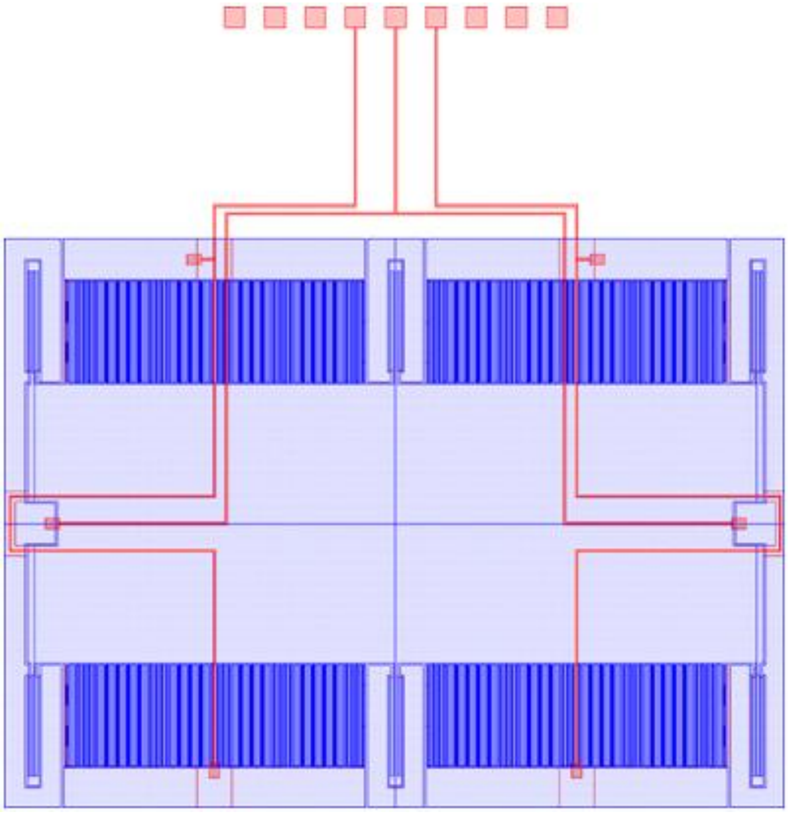

Figure 4.14: Type-III accelerometer layout designed for dissolved wafer process

Fourth accelerometer structure looks similar to the third structure but it has additional fingers at the center of the proof mass. Decreasing mass increases the maximum measurement range of the accelerometer, but it also increases the mass residual motion. To suspend the proof mass, accelerometer has 6 doubly folded beams. Having this many springs decreases the maximum stress loaded on each spring beam and it also prevents the proof mass to buckle. Fourth design can be chosen as the optimum design compared with the previous three designs. Table 4.5 summarize the design and performance parameters of type-IV DWP accelerometer and Figure 4.15 shows type-IV accelerometer layout designed for dissolved wafer process.

Table 4.5: Design and performance parameters of type-IV DWP accelerometer.

DESIGN PARAMETERS		PERFORMANCE PARAMETERS	
Finger Overlap Length	390 µm / 340 µm	Sense Capacitance	21.2pF 14.7 pF
Finger Width	5.5 µm	Damping	0.0201 0.0049
Finger Gap (drawn/estimate)	0.8/1.3 µm	Sensitivity	2.0 x10^{-5}F/m 6.7x10^{-6} F/m
Finger Anti-gap	3.2 µm	Operation Range	±76g ±26 g
Spring Constant	25 N/m	Brownian Noise	9.3µg/√Hz 4.6µg/√Hz
Number of Fingers per Side	182 / 126		
Proof Mass	2x10-7 kg		

First versions of the Dissolved Wafer process accelerometers are fabricated and from the results it is observed that these accelerometers suffer many problems like grassing and buckling during the fabrication. These problems were due to the non uniform boron doping of the silicon wafers used as the structural layer and the high internal stress due to the small atomic size of the boron atoms doped in the silicon crystal. All 4 different types of accelerometer structures were fabricated and tested at the end of the first DWP run. Tests performed on these 4 structures showed that only design #3 could be fabricated with high yield and its test results were very close to the design parameters. Therefore a new accelerometer structure is designed, by taking the structure of design#3 as a reference. This design had same number of springs, but this time two of the springs are placed at the middle of the proof mass instead of the sides of the accelerometer. By moving springs to the middle of the proof mass, mass of the accelerometer is decreased and number of fingers can be increased. Both increasing the number of fingers and decreasing the proof mass enables to design more sensitive accelerometers having higher measurement ranges.

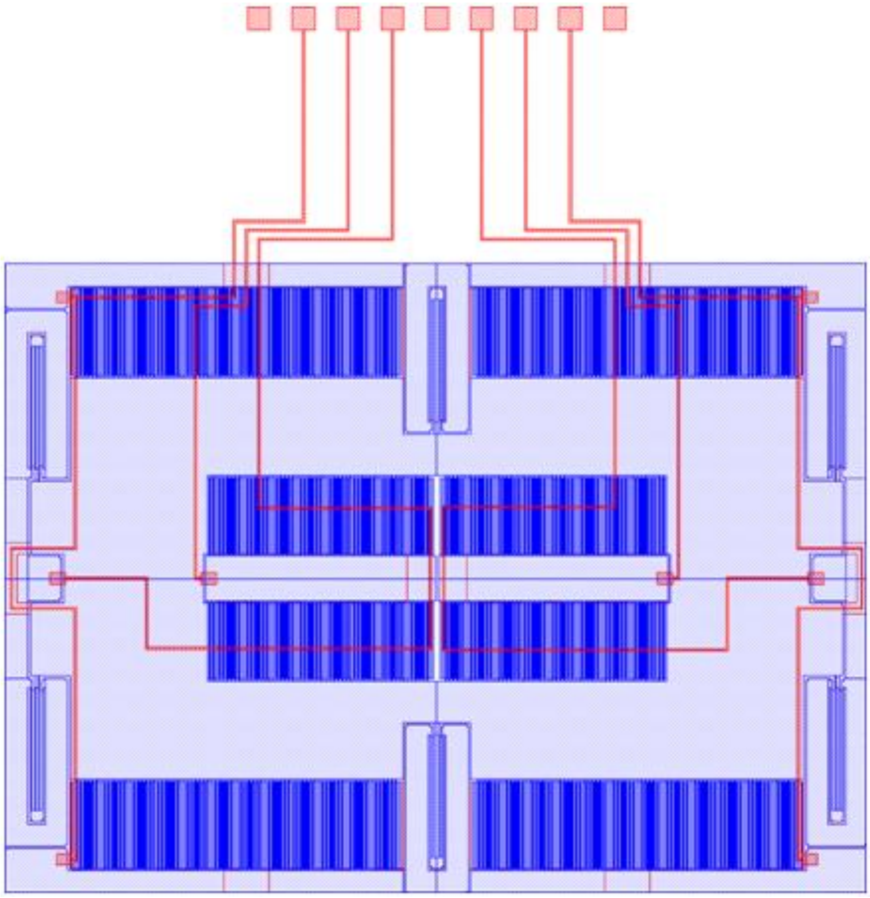

Figure 4.15: Accelerometer type-IV layout designed for dissolved wafer process.

The accelerometer designed in the second phase of the DWP process has 6 doubly folded spring structure, 3 on each side of the accelerometer. Reason of placing 3 folded springs is to fix the accelerometer proof mass from two ends and from the middle to prevent accelerometer from buckling and oscillating in the undesired directions. Instead of placing the middle springs to the sides of the accelerometer middle part of the proof mass is removed and springs are placed at that place. By this way both finger number, operation range and sensitivity of the accelerometer are increased. In the first stage of the design it was also observed that most of the accelerometers were not working in all types due to the broken capacitive fingers and small capacitive spacings. For this purpose in this second phase of the design finger widths are increased to 7μm's from 5.5μm's and spacing of the finger are drawn as 1μm. Figure 4.16 shows the layout of the accelerometer designed for the second phase of the Dissolved Wafer Process. Table 4.6 shows the design and performance parameters of second phase DWP accelerometer.

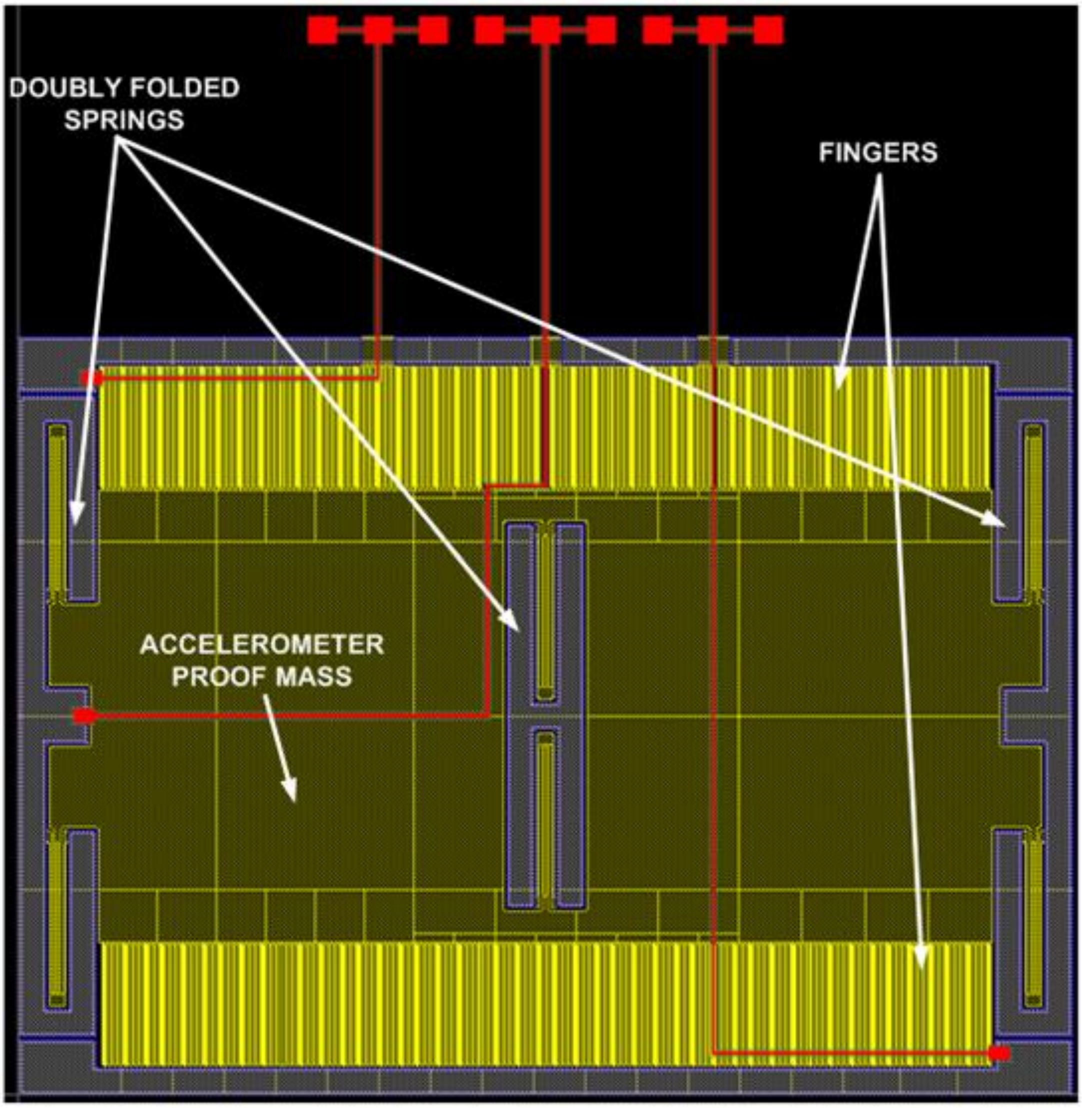

Figure 4.16: Layout of the accelerometer designed for the second phase of the Dissolved Wafer Process.

Table 4.6: Design and performance parameters of second phase DWP accelerometer

DESIGN PARAMETERS		PERFORMANCE PARAMETERS	
Finger Overlap Length	440µm	Sense Capacitance	11.0pF 9.6pF
Finger Width	7 µm	Damping	0.0067 0.0039
Finger Gap (drawn/estimate)	1µm / 1.2µm	Sensitivity	8.3×10^{-6}F/m 5.6×10^{-6}F/m
Finger Anti-gap	4 µm	Operation Range	±28g ±19g
Spring Constant	54 N/m	Brownian Noise	4.7µg/√Hz 3.6µg/√Hz
Number of Fingers per Side	168		
Proof Mass	2×10^{-7} kg		

6 DWP runs are completed for the second phase of the dissolved wafer process. Among these 6 runs there were still many problems, but number of working accelerometers increased significantly compared with the first phase. In order to evaluate the process and design, many fabricated accelerometers are tested and their performance results are compared with the design values. Accelerometers having ±18.5g operation range and 10.8pF rest capacitances were found during these tests but most of the accelerometers were still very far from the expected performances. Main reason of this performance lost is the internal stress of the boron doped wafers, which causes buckling of the sensors at die level after the fabrication. Due to the high buckling, overlapping capacitive areas of the sensors were not close to design and the rest capacitance, sensitivity and operation range values were lower than the design parameters. Figure 4.17 shows the SEM pictures of the accelerometers fabricated in the second phase of the dissolved wafer process. Test results of these accelerometers are presented in chapter 4 of this thesis. These test results showed that a new design is required to further improve the performance of the fabricated DWP accelerometers and for this purpose a new optimization study is performed.

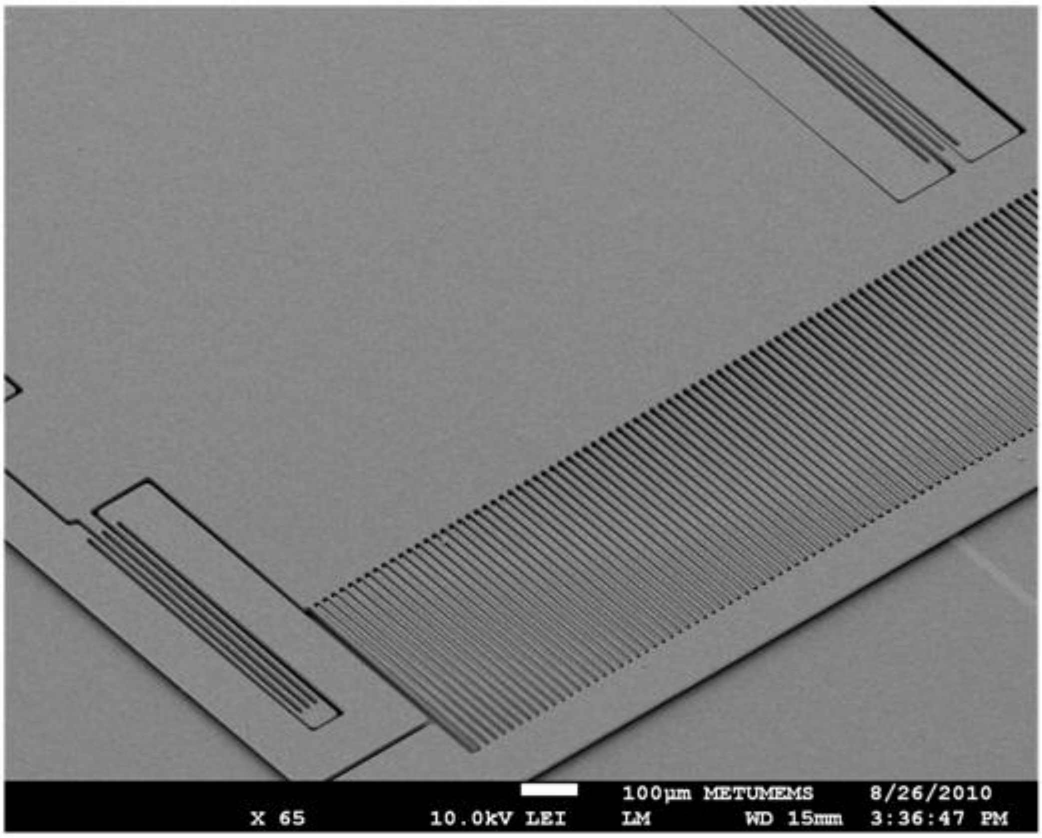
100µm METUMEMS 8/26/2010
X 65 10.0kV LEI LM WD 15mm 3:36:47 PM

(a)

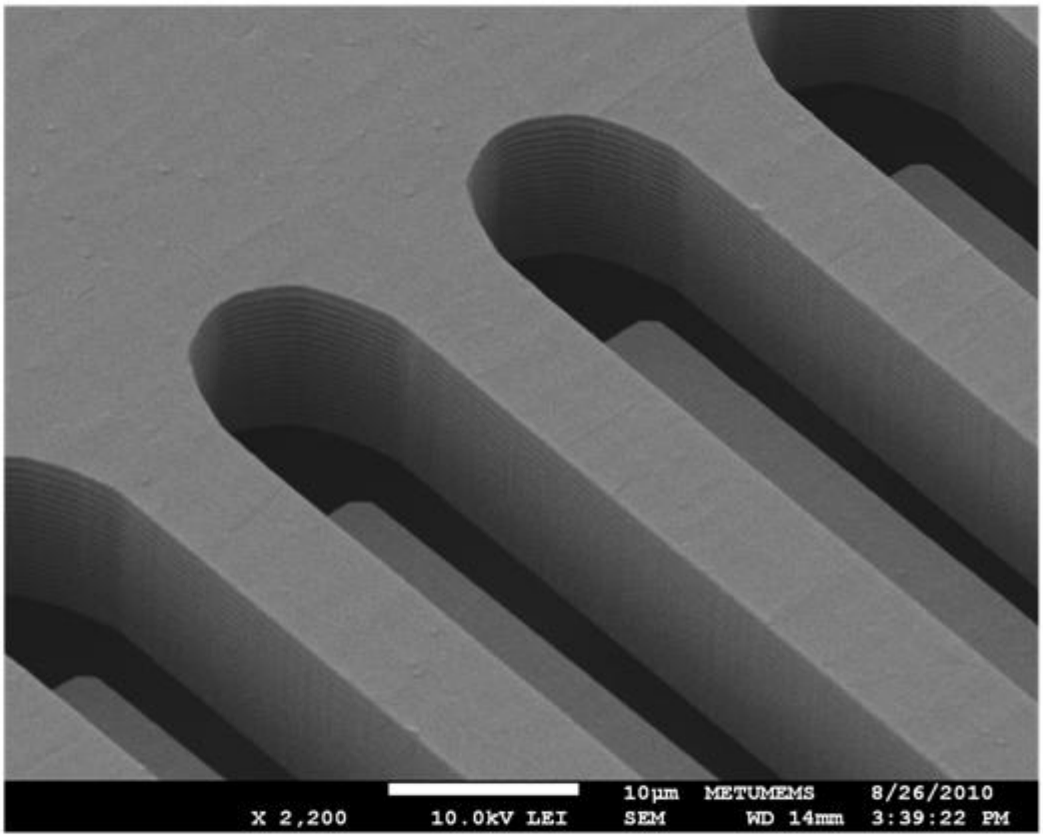
10µm METUMEMS 8/26/2010
X 2,200 10.0kV LEI SEM WD 14mm 3:39:22 PM

(b)

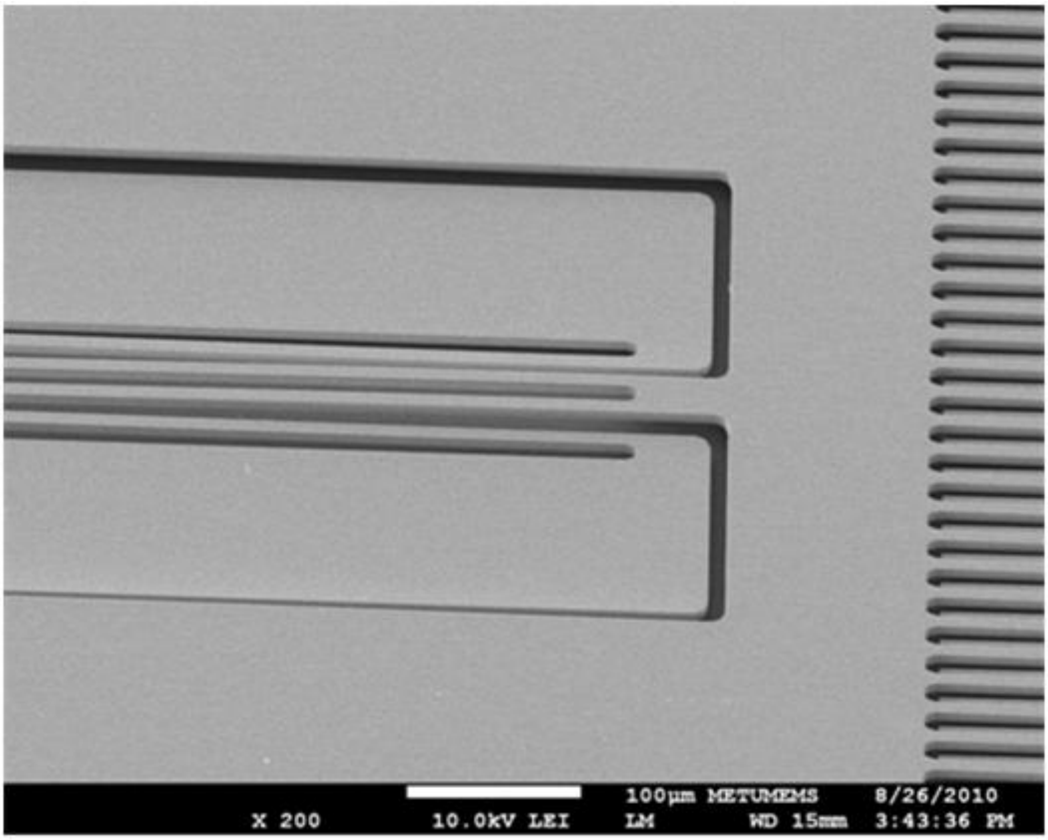

(c)

Figure 4.17: (a), (b), and (c) SEM pictures of the accelerometers fabricated in the second phase of the Dissolved Wafer Process.

4.2.3 Design optimization of Dissolved Wafer Process

The reason of designing new accelerometers in the third phase of the DWP was the unexpected behavior of the accelerometers fabricated in the second phase, like output voltage jumps observed during the system level tests. The reason of these jumps was predicted as the long capacitive fingers around 440μm's. Due to internal stresses and electrostatic forces during the operation, capacitive fingers on the proof mass bend and touch to the opposing fingers on the electrodes which cause disturbances at the output voltage of the accelerometer readout. These results bring out the need for the new accelerometer designs having shorter finger lengths. New dimensions of the accelerometer are chosen same as the previous designs since cap wafers for the accelerometers were already fabricated which are suitable for the already existing die dimensions. Since the length of the capacitive fingers is planned to be decreased more than their half length, their number should be increased accordingly. Therefore the first limitations that should be taken into account during the accelerometer design were:

1. Die sizes should be same with the original DWP accelerometers (3776μm x 2722μm)
2. When decreasing the finger length, number of fingers should be increased proportionally to satisfy the same sensitivity value.

Since the finger length will be decreased and an additional space is required to place more fingers to obtain the same sensitivity value, rectangular regions are opened in the proof mass area. Figure 4.18 shows the initial accelerometer template that the new DWP accelerometer design is started from. After deciding on the template, the remaining job was to determine the dimensions of entities such as finger length, number of fingers and dimensions of the holes on the proof mass. To optimize these values some set of mathematical equations are derived to modal the dimensions of the accelerometer in terms of performance parameters given in chapter 3. Modeling is started by writing each dimension in horizontal and vertical axes and calculating the proof mass parametrically. Table 4.7 lists the constants used in the equations which model the mechanical dimensions of the accelerometer and Table 4.8 lists the equations to calculate the important parameters of accelerometer in terms of physical dimensions and other constants. During these calculations constants related with the readout circuit like decimation order and ripple on reference voltage are taken as 640 and 400nV respectively.

Most important quantities that has to be considered during accelerometer design is the operation range, noise performance and second order mechanical model parameters which are mass, spring constant and damping. With the equations given in Table 4.8 all of these parameters are calculated except the noise performance of the accelerometer. Noise performance of the system can be estimated with the formulations given in chapter 3 of this thesis. Table 4.9 summarizes major noise sources that are used to estimate the overall noise performance of an accelerometer system.

The optimization process is performed with a code written in MATLAB which sweeps all performance parameters and find optimum values for each parameter.

Table 4.7: Constants used in the equations which model the mechanical dimensions of the accelerometer

MECHANICAL CONSTANTS					
CW	Cell Width	2722µm	FS1	Finger Spacing	variable
CH	Cell Height	3772µm	FS2	Finger Anti-spacing	variable
AW	Anchor Width without Contact	100µm	SL	Spring Length	variable
AWC	Anchor Width with Contact	200µm	SW	Spring Width	7µm
PMOW	Proof Mass Opening Width	variable	NOS	Number of Springs	6
FL	Finger Length	variable	ST	Structural Thickness	~13.5µm
FW	Finger Width	7µm	CF	Clock Frequency	variable
OTHER CONSTANTS					
ε_0	Permittivity	$8.85\text{x}10^{-12}$	k_b	Boltzmann's Constant	$1.38\text{x}10^{-23}$
E	Young's Modulus	130MPa	µ	viscosity of air	$1.85\text{x}10^{-5}$

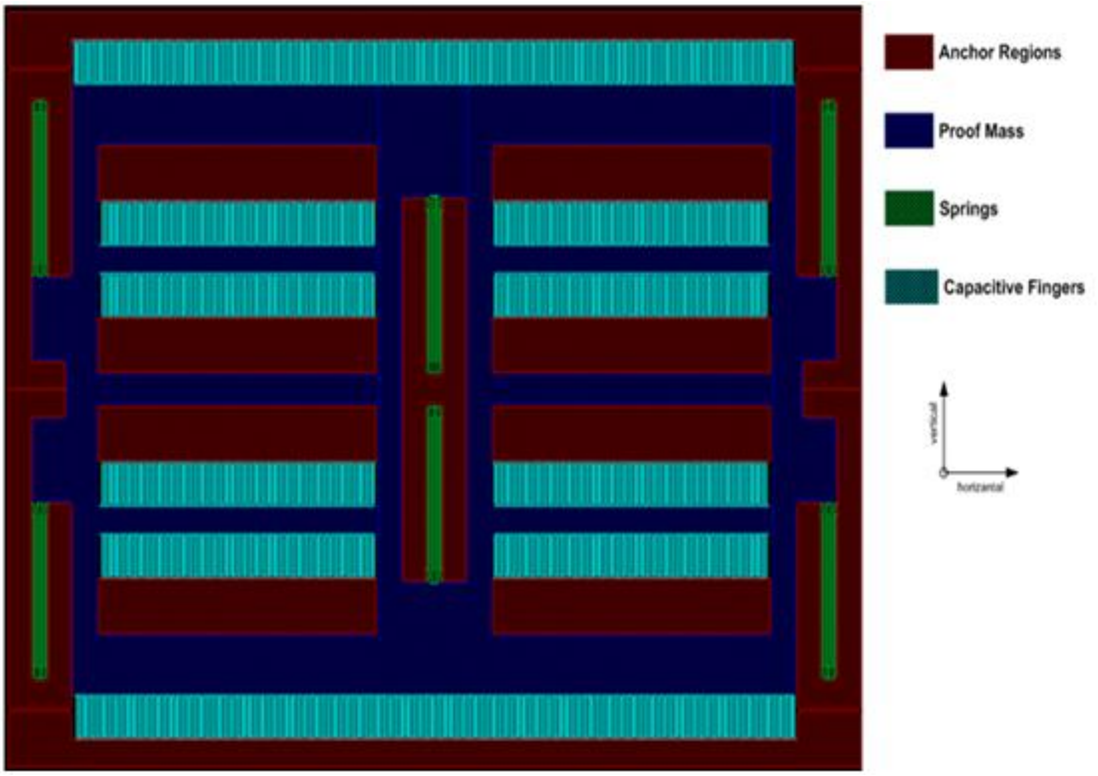

Figure 4.18: Initial accelerometer template that the third phase DWP accelerometer design started from.

Table 4.8: Equations to calculate the important parameters of accelerometer in terms of physical dimensions and other constants

Identity	Equation
Proof Mass Area	$[(CW - 2 \times AW - 2 \times FL - 20\mu m) \times (CH - 4 \times AW - 8 \times SW - 120\mu m$ $-[8 \times (PMOW + 20\mu m) \times (AWC + FL + 20\mu m)]$ $-[(2 \times SL + 200\mu m + AW) \times (2 \times AW + 4 \times SW + 70\mu m)]$ $+[4 \times (450 \times 180\mu m^2) - (110 \times 150 \times \mu m^2)]$
NoOfFingers	$2 \times floor\left(\frac{CH - 4 \times AW - 8 \times SW - 120 \times 10^{-6}}{2 \times FW + FS1 + FS2}\right)$ $+8 \times floor\left(\frac{PMOW}{2 \times FW + FS1 + FS2}\right)$
Volume	$(ProofMassArea + (NoOfFingers \times FW \times FL)) \times ST$
Mass	$Volume \times Density$
Spring Constant	$\frac{NOS \times E \times ST \times SW^2}{SL^3}$
Resonance Frequency	$\frac{1}{2\pi} \times \sqrt{\frac{Spring\ Constant}{Mass}}$
$\mu_{effective}$	$\mu \times (1 - \frac{0.6 \times ST}{FL - 10 \times 10^{-6}})$
Damping	$\mu_{effective} \times ST^3 \times (FL - 10\mu m) \times NoOfFingers \times \left(\frac{1}{FS1^3} + \frac{1}{FS2^3}\right)$
Rest Capacitance	$\epsilon_0 \times (FL - 10\mu m) \times ST \times NoOfFingers \times \left(\frac{1}{2 \times FS1} + \frac{1}{2 \times FS2}\right)$
Sensitivity @0g	$NoOfFingers \times \epsilon_0 \times (FL - 10\mu m) \times ST \times \left(\frac{1}{2 \times FS1^2} - \frac{1}{2 \times FS2^2}\right)$
Deflection @1g	$\frac{Mass \times 9{,}81}{Spring\ Constant}$
Sensitivity @1g	$NoOfFingers \times \epsilon_0 \times (FL - 10\mu m) \times ST$ $\times \left(\frac{1}{2 \times (FS1 - Deflection@1g)^2} - \frac{1}{2 \times (FS2 + Deflection@1g)^2}\right)$
Capacitance Change @1g	$Sensitivity@1g \times Deflection@1g$
Range	$\frac{Sensitivity\ @0g}{Mass \times 9{,}81} \times {V_{DD}}^2 \times (1 - (CF \times 8 \times 10^{-7}))$

Table 4.9: Major noise sources that are used to estimate the overall noise performance of an accelerometer system

Noise Source	Equation
Mechanical Noise	$\frac{1}{\mathrm{g}} \times \sqrt{\frac{4 \times k \times T \times Damping}{m^2}}\ (g/\sqrt{Hz})$
kT/C Noise	$\frac{\mathrm{a_{max}}}{2.5} \times \sqrt{\frac{4 \times k \times T}{\mathrm{C_{int}} \times \mathrm{f_s}}}\ (g/\sqrt{Hz})$
Front-End Thermal Noise	$\frac{\mathrm{a_{max}}}{2.5} \times \sqrt{\frac{16}{3} \times \frac{\mathrm{C_s} + \mathrm{C_p}}{\mathrm{C_{int}}} \times \frac{\mathrm{k} \times \mathrm{T}}{\mathrm{C_{out}}} \times \frac{1}{\mathrm{f_s}}}\ (g/\sqrt{Hz})$
Quantization Noise	$\frac{2 \times \mathrm{a_{max}}}{\sqrt{60}} \times \frac{\pi^2}{M^{2.5}}\ (g/\sqrt{Hz})$
Mass Residual Motion Noise	$\sqrt{\frac{4}{f_s}} \times \frac{SpringConstant}{m} \times \frac{4 \times a_{max}}{\pi^2 \times {f_s}^2}\ \ (g/\sqrt{Hz})$
(*) a_{max} is the operation range of the accelerometer divided by 9.81m/s^2.	

After defining all noise and performance parameters of an accelerometer system in terms of feature sizes and other quantities, mechanical dimensions of the accelerometer can be determined by optimizing these performance parameters. Dimensions that have to be determined to design the accelerometer are finger length (FL), finger spacing (FS_1), finger anti-spacing (FS_2), spring length (SL) and proof mass opening width (PMOW). By knowing the values of these dimensions, number of fingers (NOS), mass (m), spring constant (k), damping (b), rest capacitance (C_{rest}), sensitivity ($\partial C/\partial x$), range and total noise can be calculated. Optimization of each parameter is presented in the following sections.

4.2.3.1 Finger Spacing 1 (FS_1)

Finger spacing is the displacement between the opposing fingers of proof mass and electrodes. This is the main parameter determining the rest capacitance, sensitivity and measurement range. In other words this is the most important parameter in an accelerometer design. The lower limit of this parameter is defined by the DRIE capability which is ~1µm in our case. Although the parameter does not have an upper limit, range will be a determining factor. Figure 4.19 shows the change of range and total noise with respect to varying finger spacing.

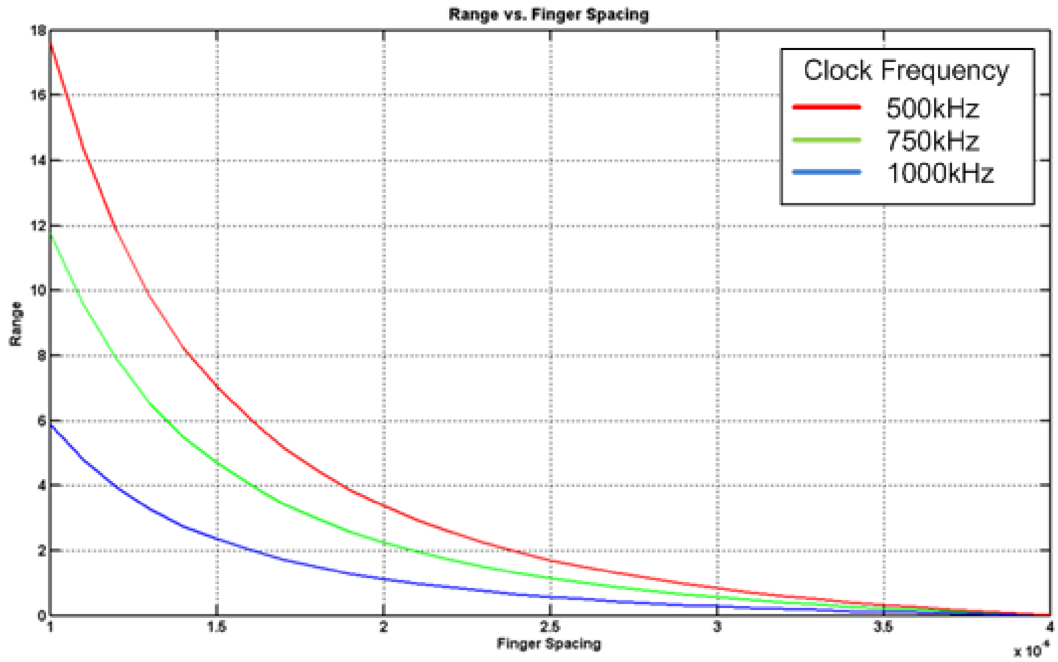

(a)

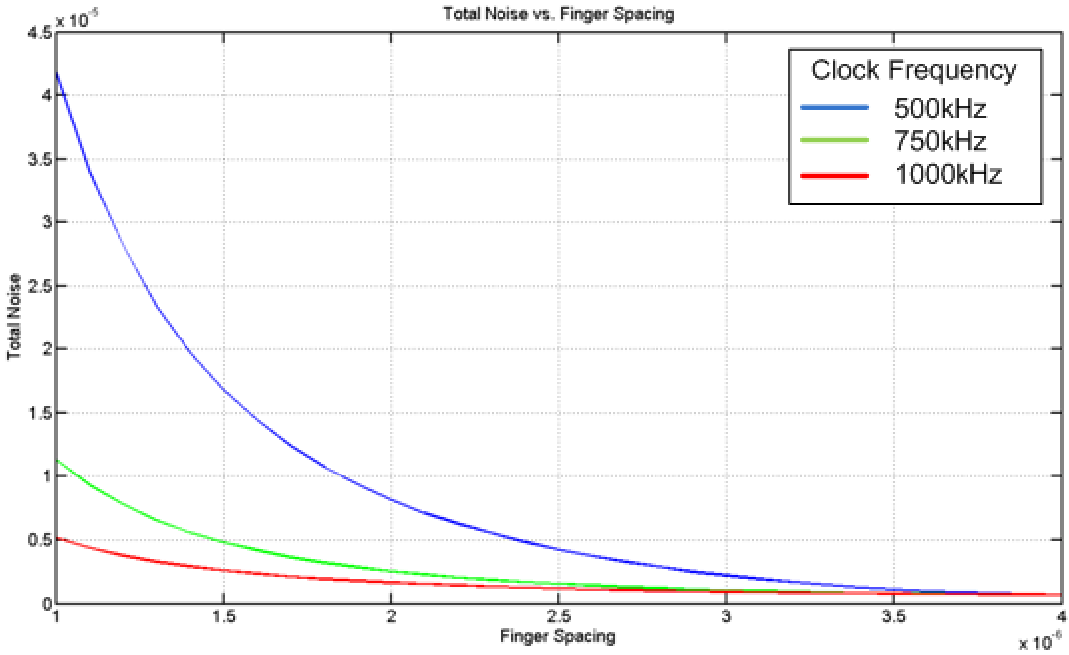

(b)

Figure 4.19: (a) Change of range with respect to finger spacing (b) Change of total noise with respect to finger spacing. (Other parameters are taken as: FL=100µm, FS_2=4 µm, SL=350 µm, PMOW=1000µm, swept with 0.1µm steps)

Although the total noise of the system decreases with the increasing finger spacing; in order to increase the operation range of the accelerometer, finger spacing should be as low as possible. In this analysis with the default values of other parameters and at 500 kHz, clock frequency operation range of the accelerometer could not exceed ±18g. With increasing clock frequency operation range decreases further. Therefore the finger spacing of the accelerometer is chosen as 1μm to achieve highest operation range possible.

$$FS_1 = 1\mu m$$

4.2.3.2 Finger Anti-Spacing (FS_2)

Finger anti-spacing is the larger displacement between the opposing fingers of proof mass and electrodes which affects the sensitivity of the accelerometer in a negative way. The lower limit of finger anti-spacing is defined by FS_1 and it does not have an upper limit. Although the parameter does not have an upper limit, by increasing the FS_2 sensitivity per finger pair is increased, but the number of fingers on each side of the accelerometer is decreased. Therefore the performance peaks at some certain value which is the optimum design value. Figure 4.20 shows the change of range and total noise with respect to varying finger anti-spacing. Both the maximum operation range and total noise parameters reached an optimum point around 3.8-4μm. Therefore finger anti-spacing of the accelerometer is chosen as 4μm.

$$FS_2 = 4\mu m$$

4.2.3.3 Proof Mass Opening Width (PMOW)

Previous accelerometer designs had around 450μm capacitive fingers which had lots of fabrication or contamination problems. Even some of the fingers may break during the sensor level testing after fabrication. To overcome these problems which decrease the yield of the fabrication, shorter fingers are intended to be placed. In order to achieve the same sensitivity and measurement range the number of fingers should be increased accordingly. Therefore the accelerometer proof mass is designed such that additional capacitive fingers can be placed in the proof mass openings. Range of the accelerometer is also increased by decreasing the mass of the accelerometer. The lower limit of the PMOW is actually 0μm's, meaning that there is no proof mass opening. The upper limit of the PMOW is 1231µm's which is the maximum width allowed by the dimensions of the cell height. Figure 4.21 shows the change of range and total noise of the closed loop system with respect to changing proof mass opening width. As it is expected the range and noise of the system both increases by increasing PMOW, since both the number of fingers increase and mass of the accelerometer decreases. Therefore the PMOW is chosen as its maximum value.

$$PMOW = 1231\mu m$$

4.2.3.4 Finger Length (FL)

Finger length is like finger spacing, one of the other important parameters in determining the sensitivity and range of the accelerometer. By increasing the finger length the sensitivity of the accelerometer increases and the mass decreases. These all cause the range and noise of the accelerometer to increase. One important aim of this design was to decrease the length of the fingers. Therefore they should be at least smaller than half of the previous finger lengths. Figure 4.22 shows the change of range and total noise of the system with respect to varying finger length. A finger length value should be chosen such that the range should be sufficiently large and noise should be as low as possible. In this case choosing the finger length as 150µm's should be wise since the measurement range of the accelerometer is at least 20g at both 500 and 750kHz with a safety margin of at least 5g's and noise is below 200µg in both clock frequencies. Unfortunately measurement range drops below ±20g for 1MHz clock frequency. Therefore finger length of the accelerometer is selected as 150µm.

$$FL = 150\mu m$$

4.2.3.5 Spring Length (SL)

Springs are the structures connecting the solid proof mass of the accelerometer to the fixed substrate anchors. Length and width of the springs determine the spring constant of the structure and the stiffness of the spring constant is a measure of withstanding force opposed to the proof mass movement. Spring constant of the accelerometer affects sensitivity, operation range and resolution in open loop mode of readout circuit operation. But in close loop mode spring constant slightly affects the operation range of the accelerometer by changing the proof mass area. Its major affect is on the total noise of the system. Therefore since this is the only parameter that can change the noise value without changing operation range too much, noise can be fine tuned by adjusting spring length after all other parameters are determined. Figure 4.23 shows the change of operation range and total noise with respect to the length of the springs attached to the accelerometer proof mass. The noise of the system is related to the spring length and below 350µm's systems total noise exceeds 200µg's. To be on the safe side spring length is chosen to be 550µm's where the total noise value saturates around 30µg/√Hz at 500 kHz clock frequency.

$$SL = 550\mu m$$

With the determination of all five important dimensions, design of the new DWP accelerometer is completed. Table 4.10 shows the expected performance parameters of the DWP accelerometer together with the design dimensions.

Table 4.10: Expected performance parameters and design dimensions for the third phase of the DWP accelerometer fabrication.

PERFORMANCE PARAMETERS					
Parameter	Value	Parameter	500kHz	750kHz	1MHz
Proof Mass	127×10^{-9}kg	Range	39 g	26 g	13 g
Spring Constant	22N/M	Mechanical Noise	7µg/√Hz	7µg/√Hz	7µg/√Hz
Damping	0.52×10^{-2}kg/m	Quantization Noise	10µg/√Hz	7µg/√Hz	3µg/√Hz
Resonance Frequency	2073kHz	Mass Residual Noise	31µg/√Hz	7µg/√Hz	2µg/√Hz
Rest Capacitance	9.47×10^{-12}F	Front-end Amp. Noise	7µg/√Hz	4µg/√Hz	2µg/√Hz
Sensitivity	437fF/g	Switching Noise	2µg/√Hz	1µg/√Hz	0.5µg/√Hz
No. of Fingers	424	Total Noise	32µg/√Hz	13µg/√Hz	8µg/√Hz

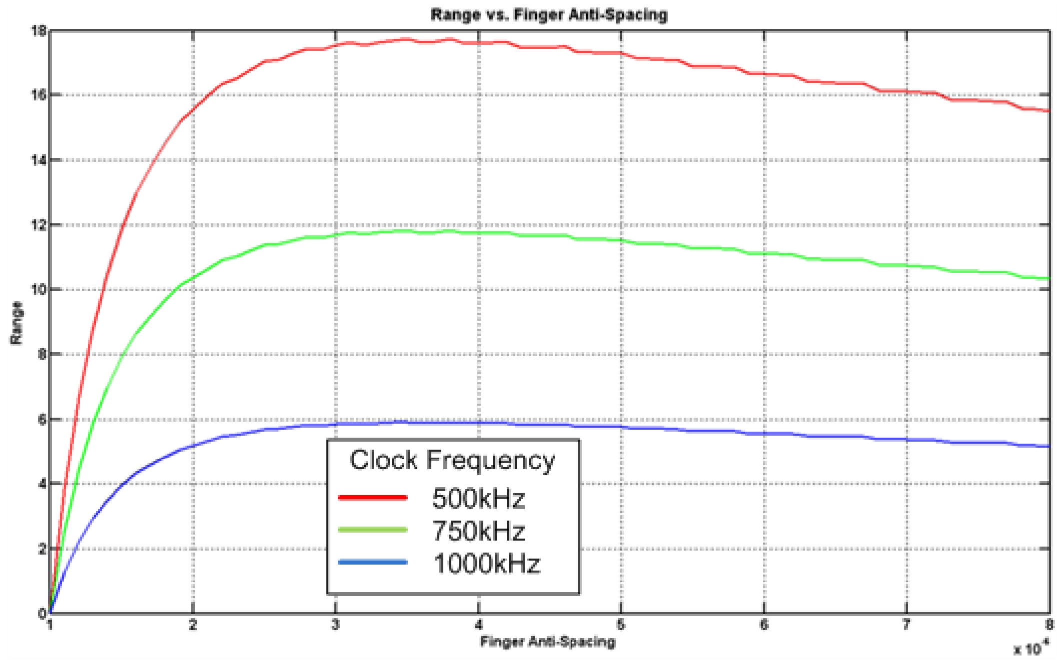

(a)

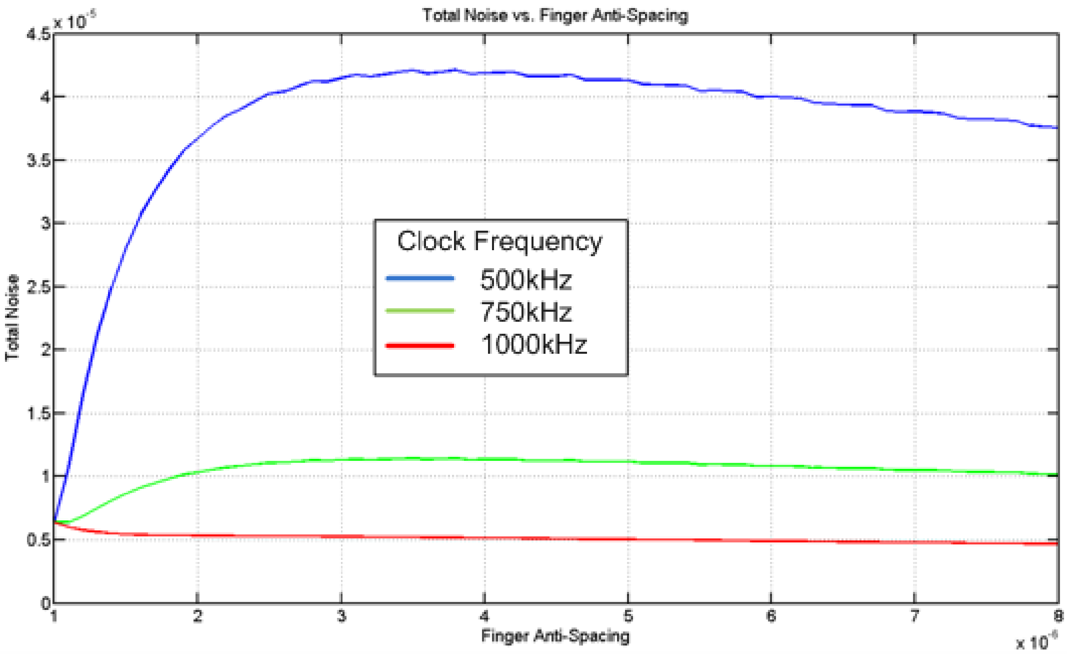

(b)

Figure 4.20: (a) Change of range with respect to finger anti-spacing (b) Change of total noise with respect to finger anti-spacing. (Other parameters are taken as: FL=100µm, FS_1=1µm, SL=350µm, PMOW=1000µm, swept with 0.1µm steps)

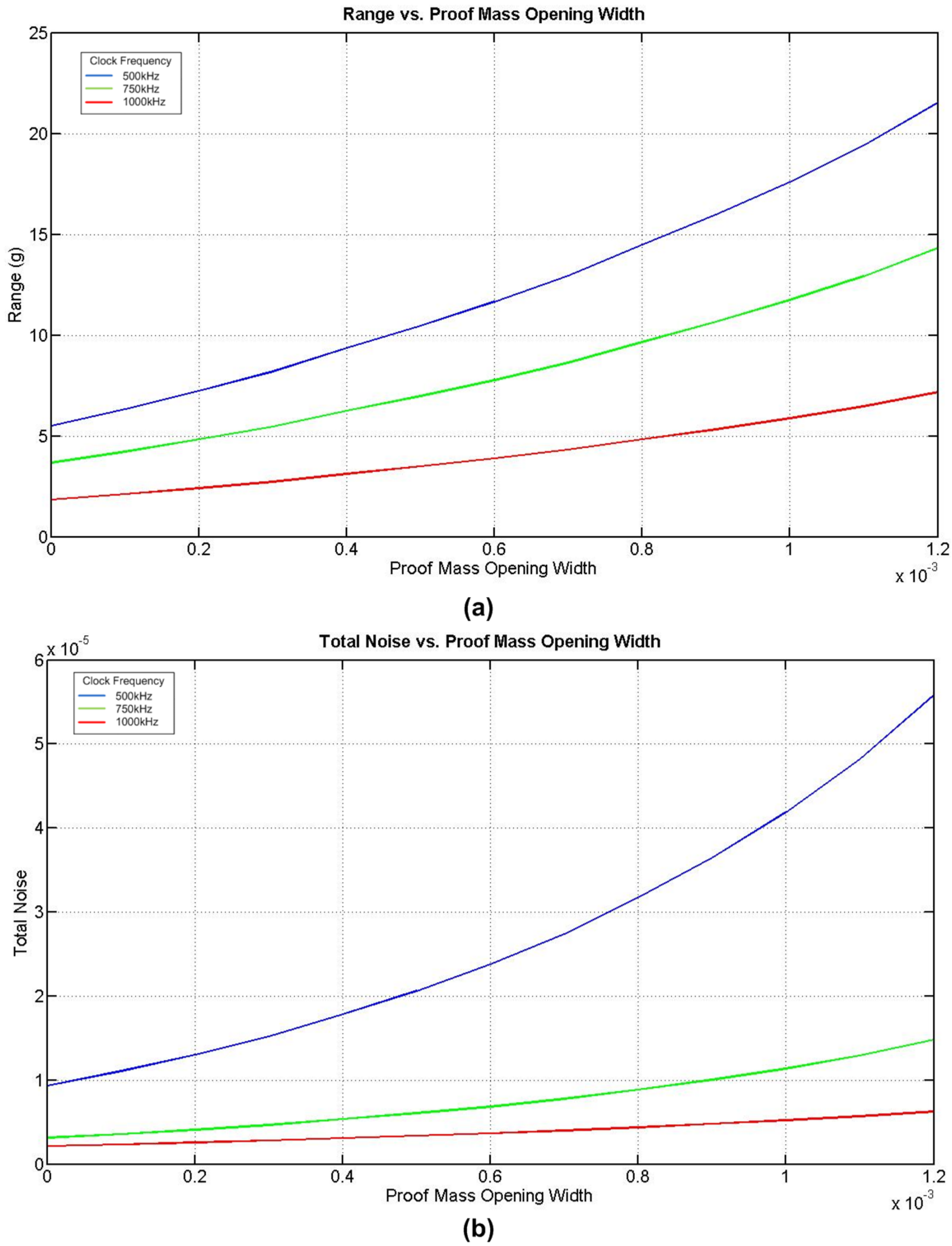

Figure 4.21: (a) Change of range with respect to proof mass opening width (b) Change of total noise with respect to proof mass opening width (Other parameters are taken as: FL=100µm, FS_1=1µm, FS_2=4µm, SL=350µm, swept with 100µm steps)

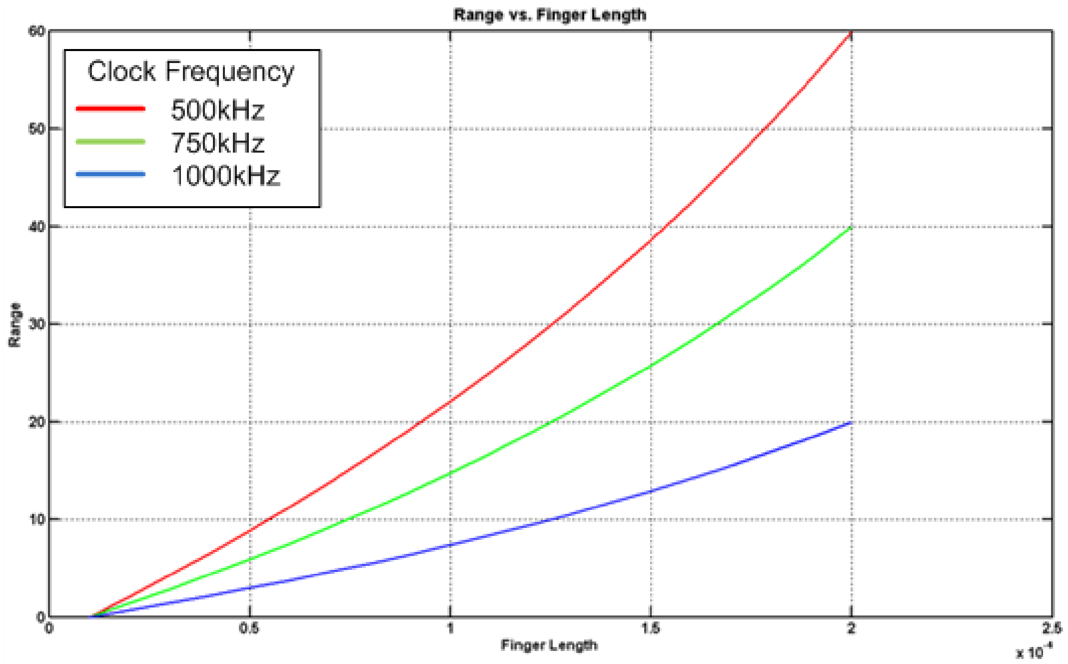

(a)

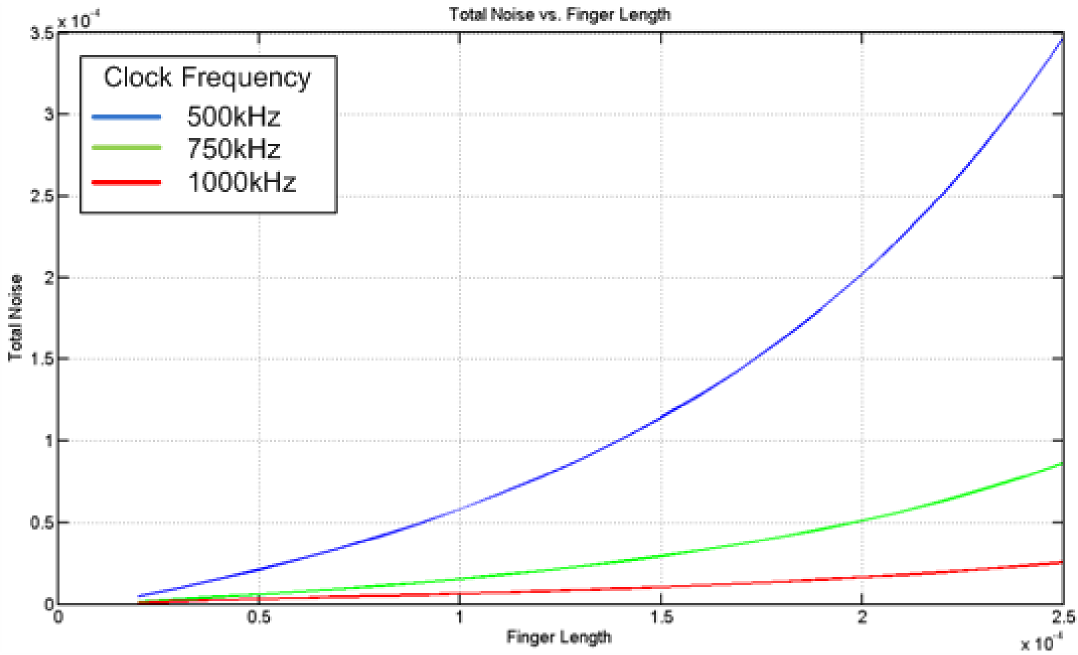

(b)

Figure 4.22: (a) Change of range with respect to finger length. (b) Change of total noise with respect to finger length. (Other parameters are taken as: PMOW=1231µm, FS1=1µm, FS2=4µm, SL=350µm, swept with 10µm steps)

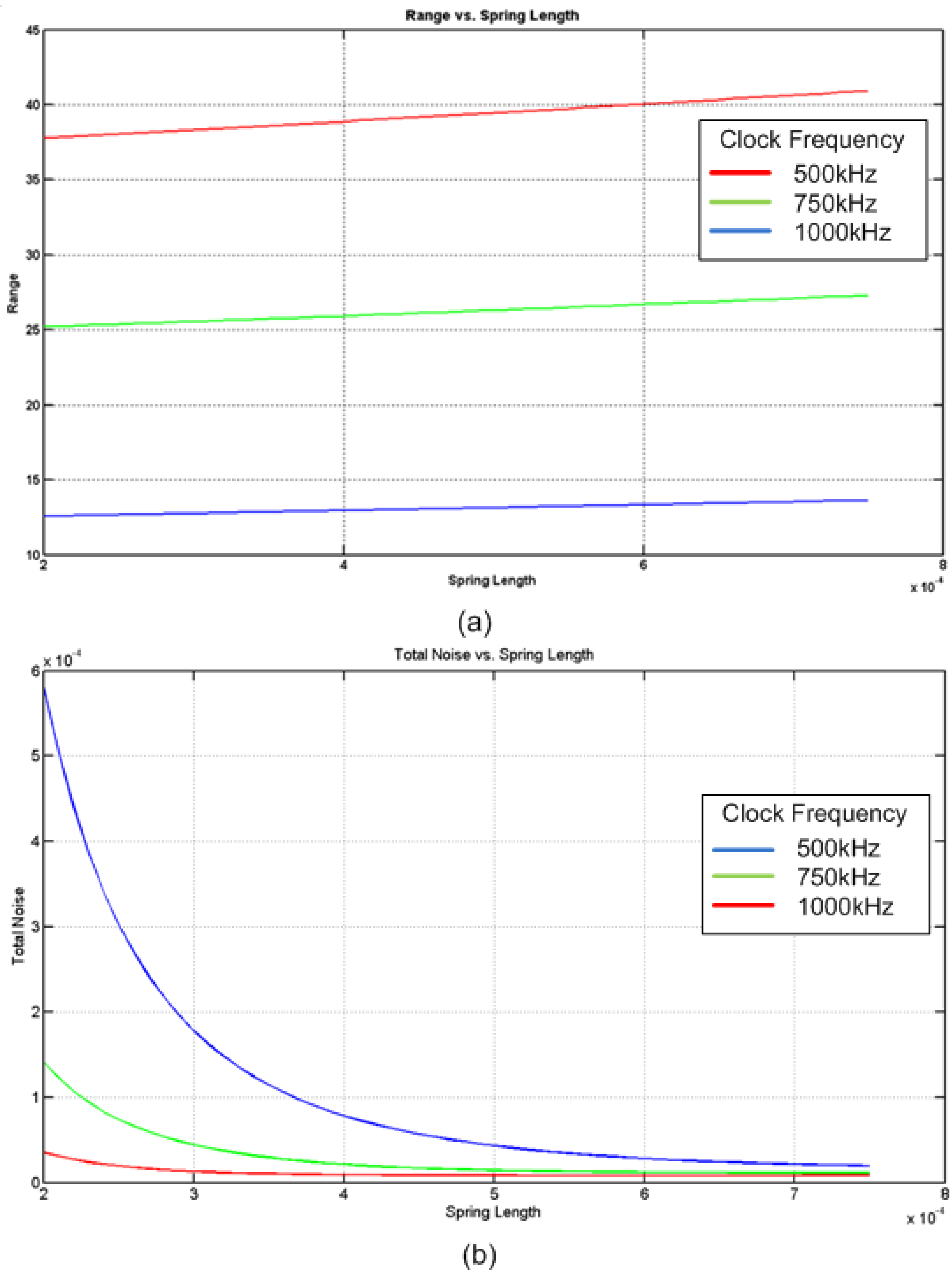

Figure 4.23: (a) Change of range with respect to spring length. (b) Change of total noise with respect to spring length. (Other parameters are taken as: PMOW=1231µm, FS_1=1µm, FS_2=4µm, FL=150µm, swept with 10µm steps)

By using MATLAB, all possible accelerometer designs can also be plotted in range vs. total noise chart. Figure 4.24, Figure 4.25 and Figure 4.26 shows range and total noise of all possible DWP designs for 500, 750 and 1000 kHz respectively. Blue dot in each plot shows the optimized design accelerometer for DWP process.

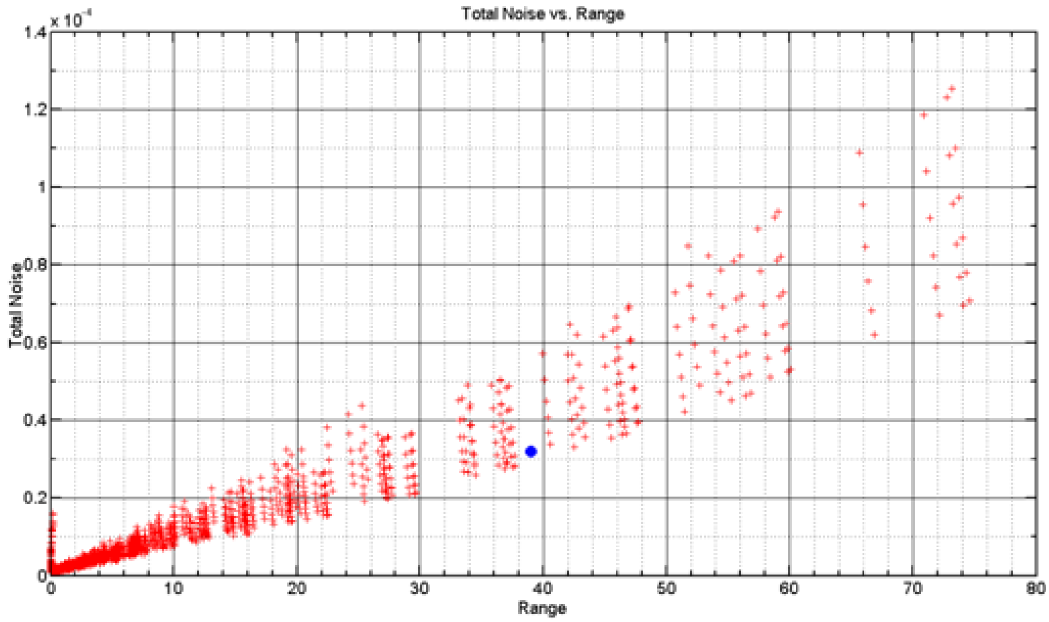

Figure 4.24: Possible DWP designs for 500 kHz clock frequency. (Blue point indicates the current design)

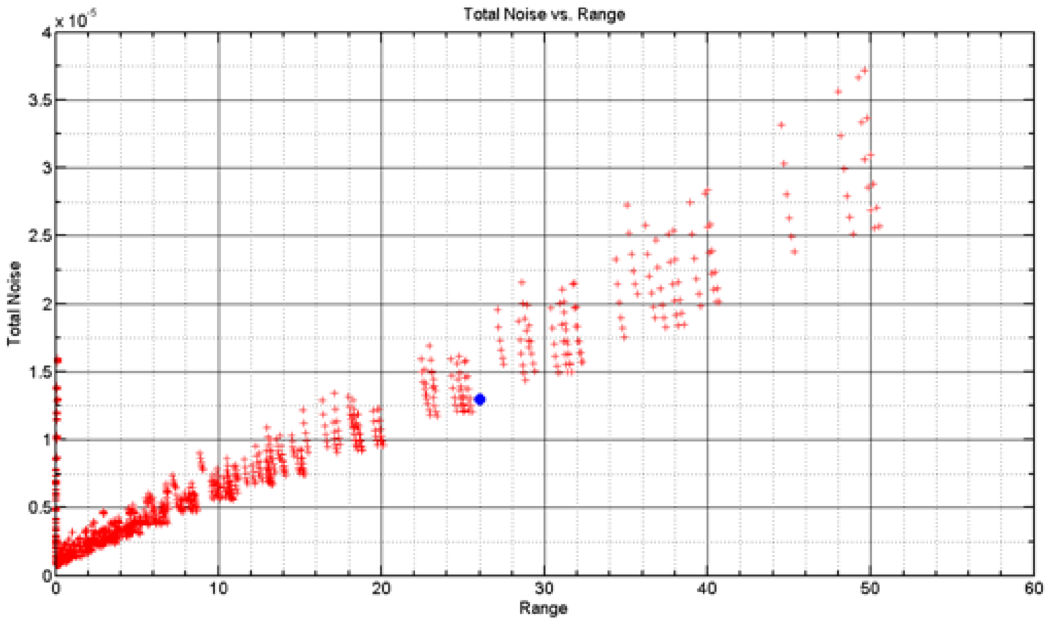

Figure 4.25: Possible DWP designs for 750 kHz clock frequency. (Blue point indicates the current design)

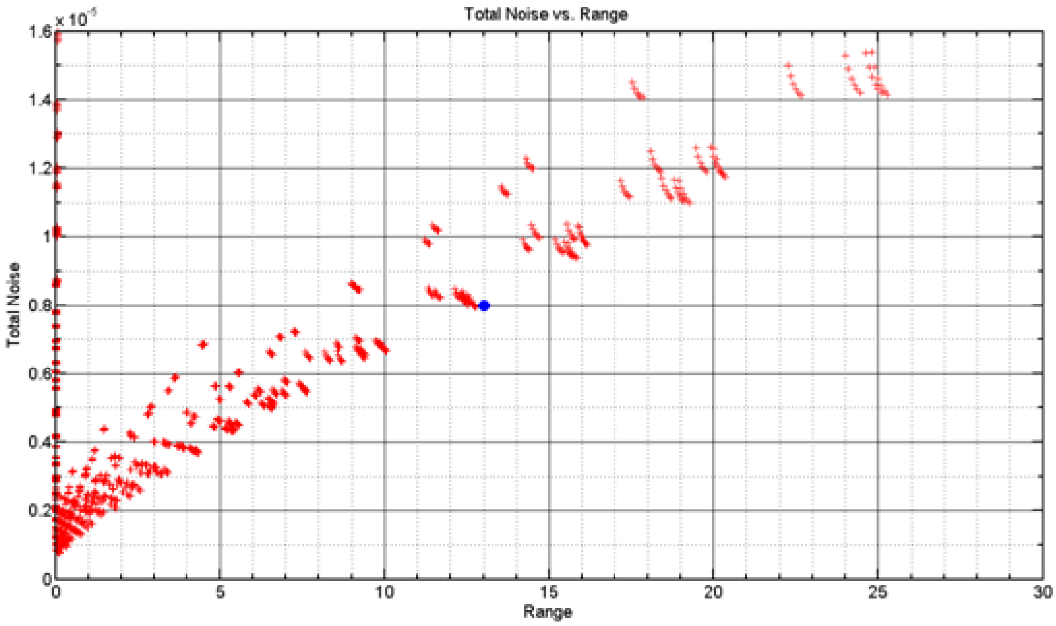

Figure 4.26: Possible DWP designs for 1 MHz clock frequency. (Blue point indicates the current design)

4.2.4 Verification of the Accelerometer Design

Designed accelerometer is modeled with Coventorware for verification. With the Coventorware analysis mass and resonance frequency of the accelerometer could be simulated and results are compared with the hand calculations. For the sake of the simplicity during the modal analysis the total mass of the fingers are calculated and uniformly distributed to the edges where they are attached to. Figure 4.27 shows the Coventorware model of the third phase DWP accelerometer.

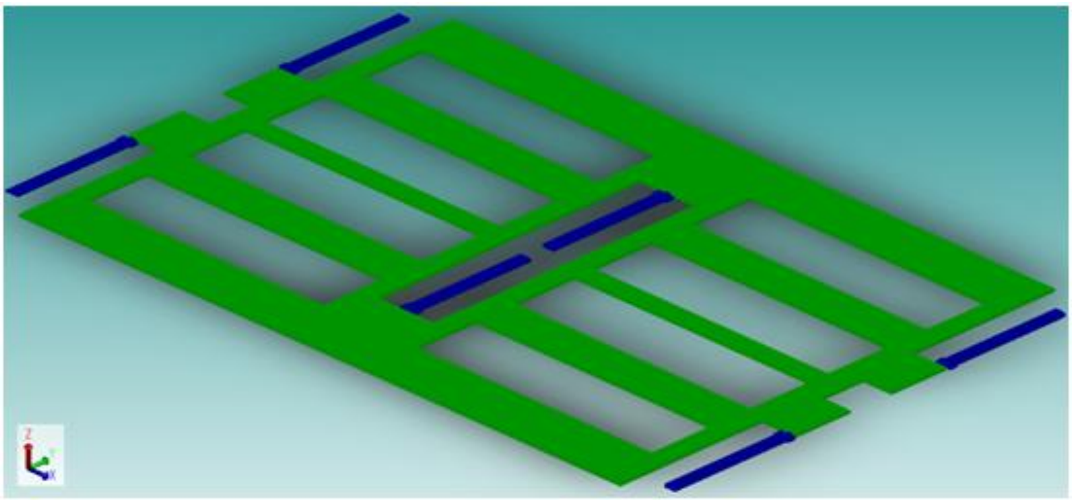

Figure 4.27: Coventorware model of the third phase DWP accelerometer.

Springs and proof mass of the accelerometer are separately modeled than connected with linkage boundary conditions. Figure 4.28 shows the masher settings to divide the model into its finite elements. These mesh sizes are optimized such that by choosing element sizes smaller, analysis results will not change more than 1%.

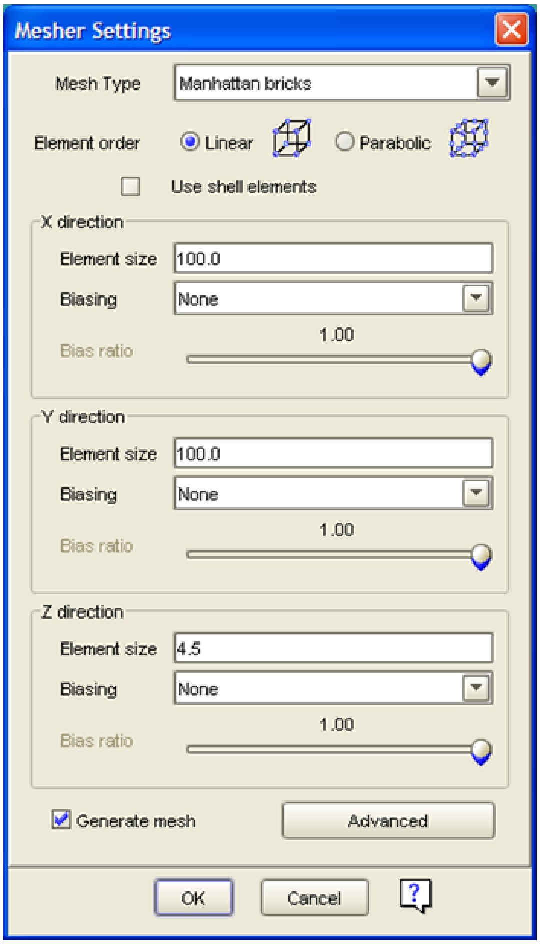

(a)

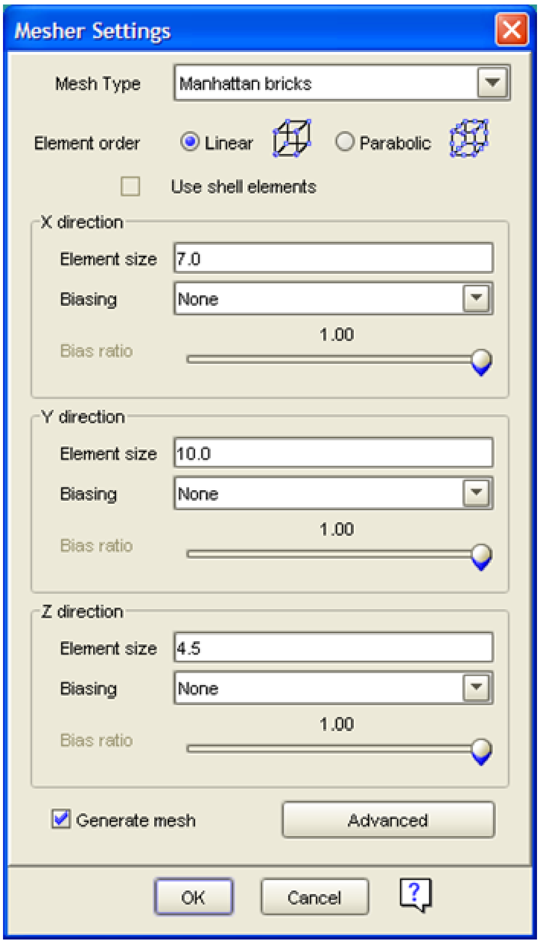

(b)

Figure 4.28: Mesher settings used to divide the model into its finite elements. (a) Mesher settings for proof mass (b) Mesher setting for springs.

With the settings given above modal analysis is performed on the accelerometer to find the first 10 modes of the accelerometer. Figure 4.29 shows the modal analysis results of the DWP accelerometer. Among these results first one is the desired mode of operation and the resonance frequency and proof mass are in agreement with the design values. Unfortunately resonance frequencies of the second and third modes which are in z-axis direction are very close to the first mode. The only way to separate these modes is to increase (Structural Thickness/Spring Width) ratio.

Increasing "Structural Thickness" is not a possible solution. On the other hand decreasing "spring width" will make the spring structures very brittle. Therefore current placements of resonance frequencies could not be changed so easily. Figure 4.30 shows the deflection of the accelerometer proof mass in its first mode of operation.

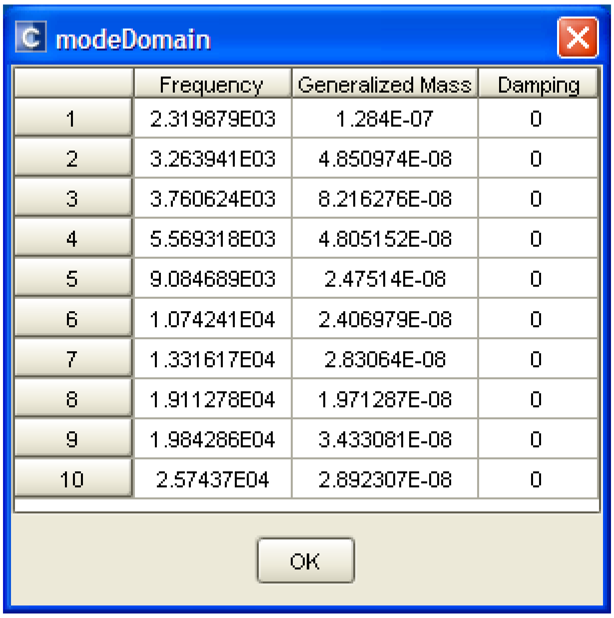
modeDomain

	Frequency	Generalized Mass	Damping
1	2.319879E03	1.284E-07	0
2	3.263941E03	4.850974E-08	0
3	3.760624E03	8.216276E-08	0
4	5.569318E03	4.805152E-08	0
5	9.084689E03	2.47514E-08	0
6	1.074241E04	2.406979E-08	0
7	1.331617E04	2.83064E-08	0
8	1.911278E04	1.971287E-08	0
9	1.984286E04	3.433081E-08	0
10	2.57437E04	2.892307E-08	0

OK

Figure 4.29: Modal analysis results of the DWP accelerometer

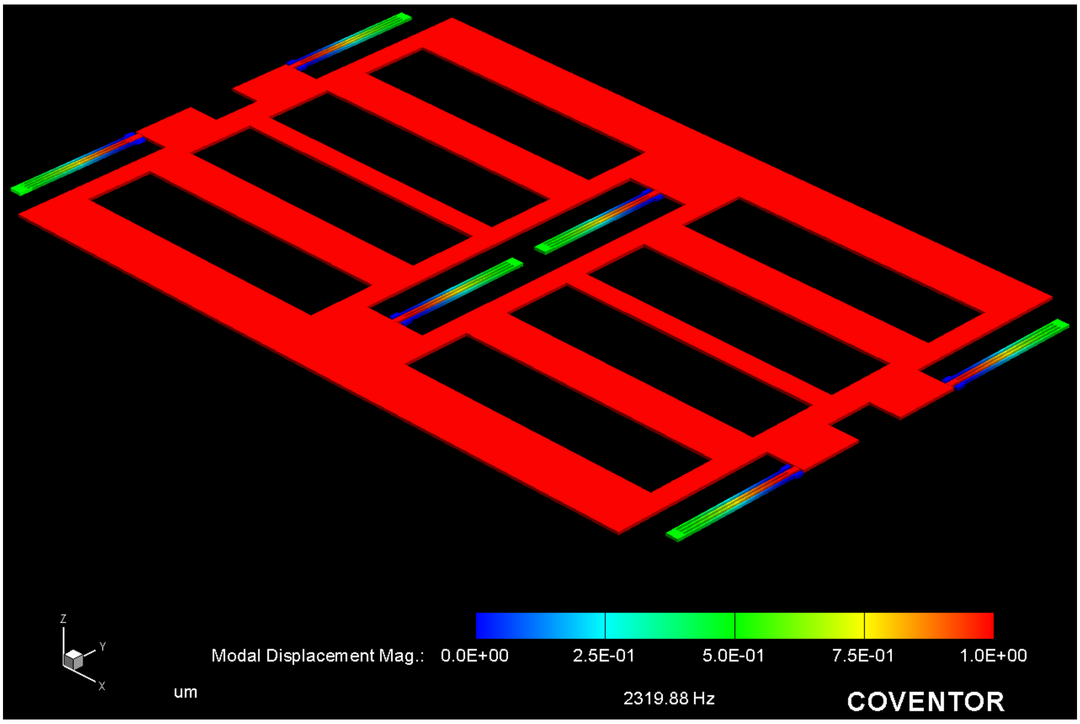

Figure 4.30: Deflection of the accelerometer proof mass in its first mode of operation

Capacitive analysis of the latest accelerometer design was also made with Coventorware. Aim of this analysis was to verify rest capacitance of the accelerometer and if the metal lines passing beneath the accelerometer proof mass have any effect on the operation of the sensor. First the entire accelerometer model is constructed in Coventorware, and whole model is meshed and simulations are tried to be performed on this model. Unfortunately this simulation gave no outcome due to the huge number of finite elements. Therefore capacitive fingers and proof mass are separated from each other and analyses are performed.

Fingers are modeled separately in two different blocks and simulated for their capacitance values. First capacitive electrode has 64 fingers and there are 4 of these electrodes on each side of the accelerometer. Second and larger capacitive block has 168 capacitive fingers and together with the 4 small electrodes there are a total of 424 fingers on each side. Each of these blocks is simulated separately and results given in Figure 4.31 are obtained. When these results are added a total of 11.81pF capacitance is found on each side of the accelerometer including the fringing fields. This value is calculated as 9.47pF with hand calculation without considering fringing fields. In literature up to 40% capacitance difference between the hand calculations and FEM results are acceptable due to fringing effects.

Proof mass and metal lines of the accelerometer are modeled in a separate file and simulated to find the parasitic capacitances in between. Figure 4.32 shows the model prepared for the parasitic capacitance analyses and simulation results. In the results matrix "conductor 0" is the proof mass, "conductor 1" and "conductor 2"are the electrodes. Parasitic capacitances on both sides of the accelerometer are measured as 473fF and 479fF. These results are very close to each other and due to their symmetry they would not affect the balance of the operation.

Model prepared in Coventorware is also simulated by applying 5 Volt DC on the proof mass and analyze the capacitive force between the proof mass and electrode. The resulting attraction force was found as 1.47nN's which is very small to deflect the proof mass in any direction which can also be neglected.

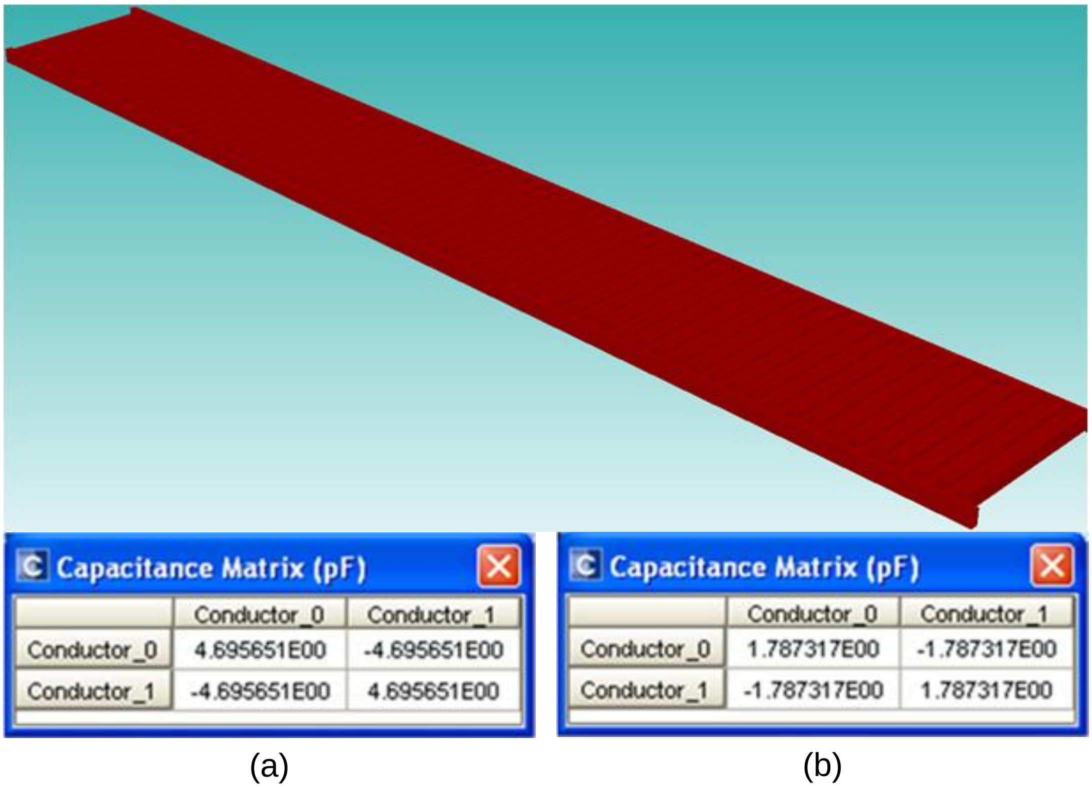

Capacitance Matrix (pF)

	Conductor_0	Conductor_1
Conductor_0	4.695651E00	-4.695651E00
Conductor_1	-4.695651E00	4.695651E00

Capacitance Matrix (pF)

	Conductor_0	Conductor_1
Conductor_0	1.787317E00	-1.787317E00
Conductor_1	-1.787317E00	1.787317E00

Figure 4.31: (a) Capacitance measurement result for the large electrode having 168 fingers. (b) Capacitance measurement result for the narrow electrode having 64 fingers.

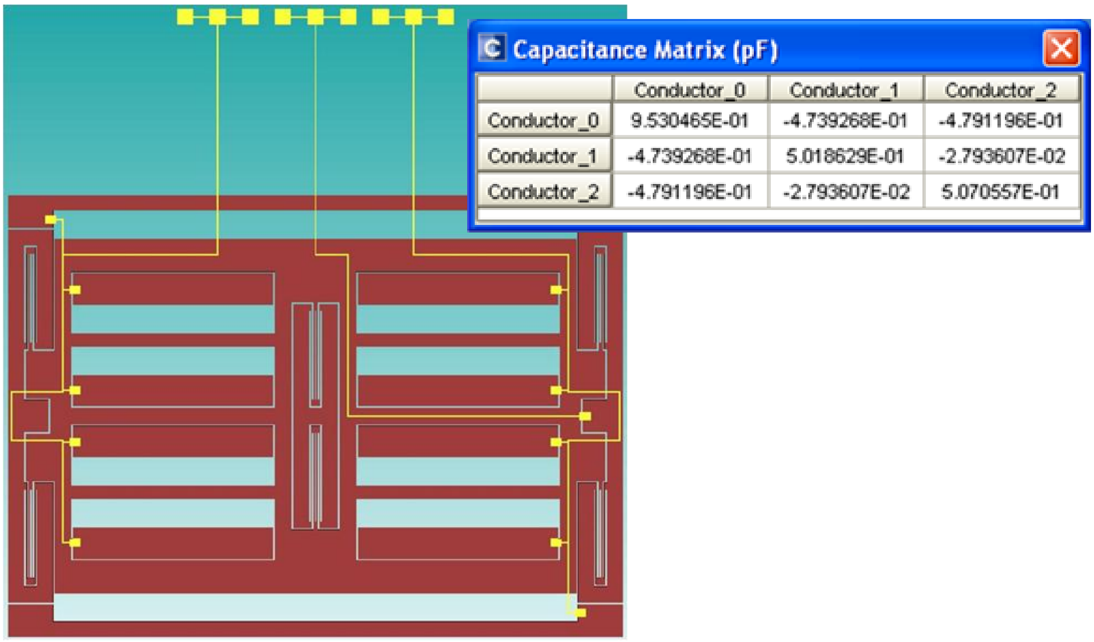

Capacitance Matrix (pF)

	Conductor_0	Conductor_1	Conductor_2
Conductor_0	9.530465E-01	-4.739268E-01	-4.791196E-01
Conductor_1	-4.739268E-01	5.018629E-01	-2.793607E-02
Conductor_2	-4.791196E-01	-2.793607E-02	5.070557E-01

Figure 4.32: Model constructed for parasitic capacitance analysis and the simulation results.

4.2.5 Closed Loop Accelerometer and Readout Circuit Simulations

In order to verify the operation of accelerometer and readout circuit together, MATLAB model of the second order Sigma Delta readout circuit is built. In this MATLAB model accelerometer is modeled in Laplace domain with the parameters found in the previous parts of this thesis. Readout circuit is divided into blocks and each block is modeled separately. Figure 2.18 shows the overall model for the closed loop accelerometer and readout system.

In this model accelerometer is composed of two building blocks which convert the input acceleration to proof mass displacement and proof mass displacement to capacitance difference. Readout circuit is composed of 3 sub blocks which are the front-end amplifier which corresponds to the charge integrator in real circuit, compensator which provides the accelerometer to operate in a more stable way and the comparator which gives a digital "1" or "0" output by comparing the output of the compensator with "0" volt. Feedback block is actually a voltage to acceleration converter by taking the nonlinearities into account caused by the movement of the accelerometer proof mass. Since the output of the closed loop readout circuit is consisting of a bit stream which is composed of 1's and 0's, it should be filtered in order to extract the meaningful acceleration data. For this purpose a third order low pass $sinc^3$ filter and a second order low pass $sinc^2$ filter is implemented at the digital output of the readout circuit.

To understand whether the model reflects the exact behavior of the readout circuit, open loop tests are performed. For the open loop tests an acceleration of 1g amplitude and 100 Hz frequency is applied. Figure 4.33 shows the input output characteristic of the open loop mode of the readout circuit. From this figure it is seen that the differential open loop gain of the system is ~2.04Volt/g which is as expected. To see the open loop operation range of the accelerometer a ramp signal is applied sweeping input from 0g to 3g's and the output is saturated at 2.5Volts which corresponds to the 1.2g input acceleration. Figure 4.34 shows the saturation of the output voltage to the applied acceleration having 1.5g magnitude and 100Hz frequency.

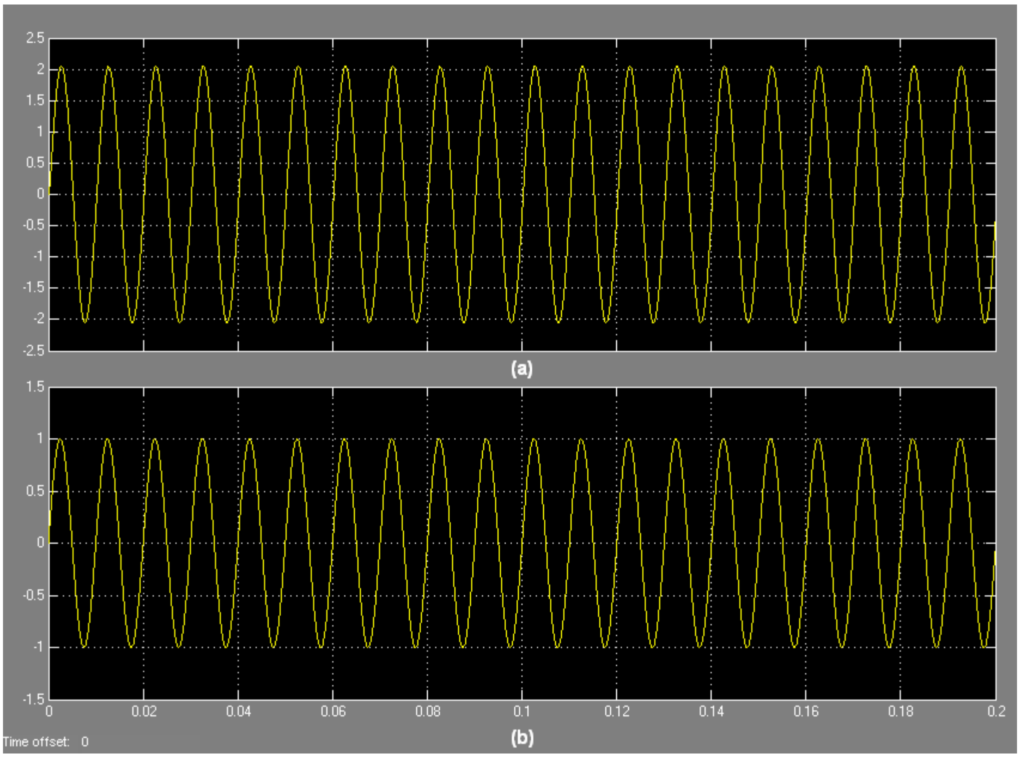

Figure 4.33: Input-output characteristic of the open loop mode of the readout circuit. (a) Output of the readout circuit (b) Applied acceleration.

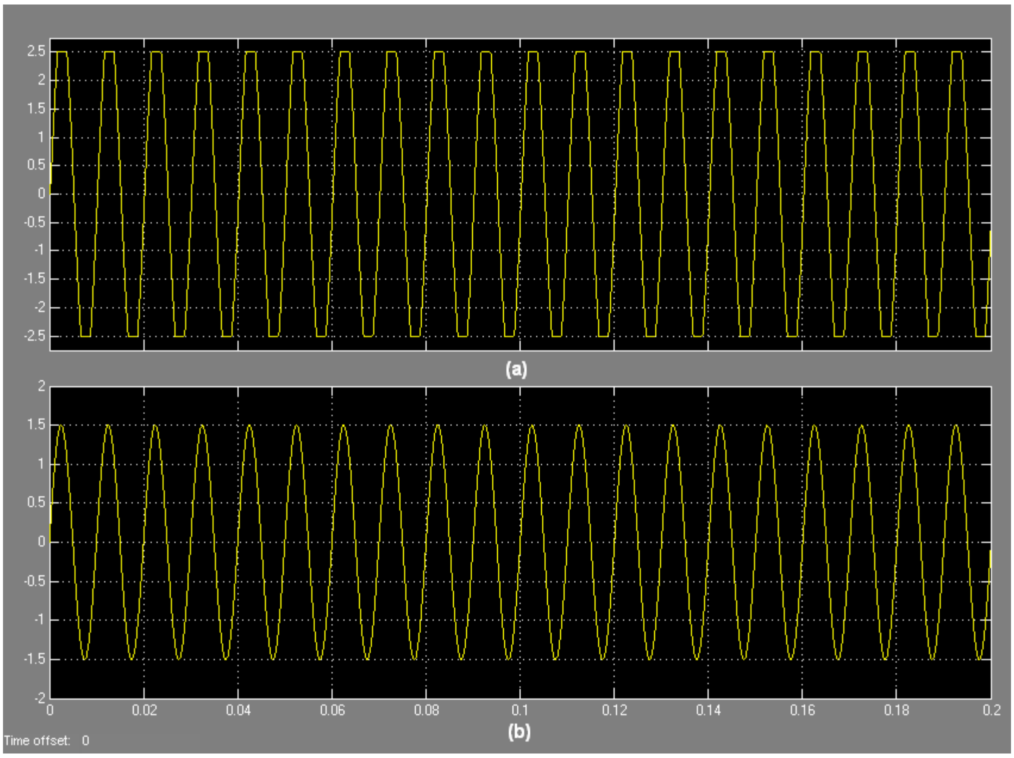

Figure 4.34: Saturation of the output voltage to the applied acceleration having 1.5g magnitude and 100Hz frequency. (a) Output of the circuit (b) Applied acceleration.

After demonstrating the operation of the open-loop mode, closed loop simulations are performed. Again acceleration having 5g amplitude, and 100Hz frequency is applied and it is observed that the $sinc^3$ filter output is following the input acceleration. Figure 4.35 shows the normalized output of the readout circuit in closed loop mode for 5g amplitude, and 100Hz frequency acceleration.

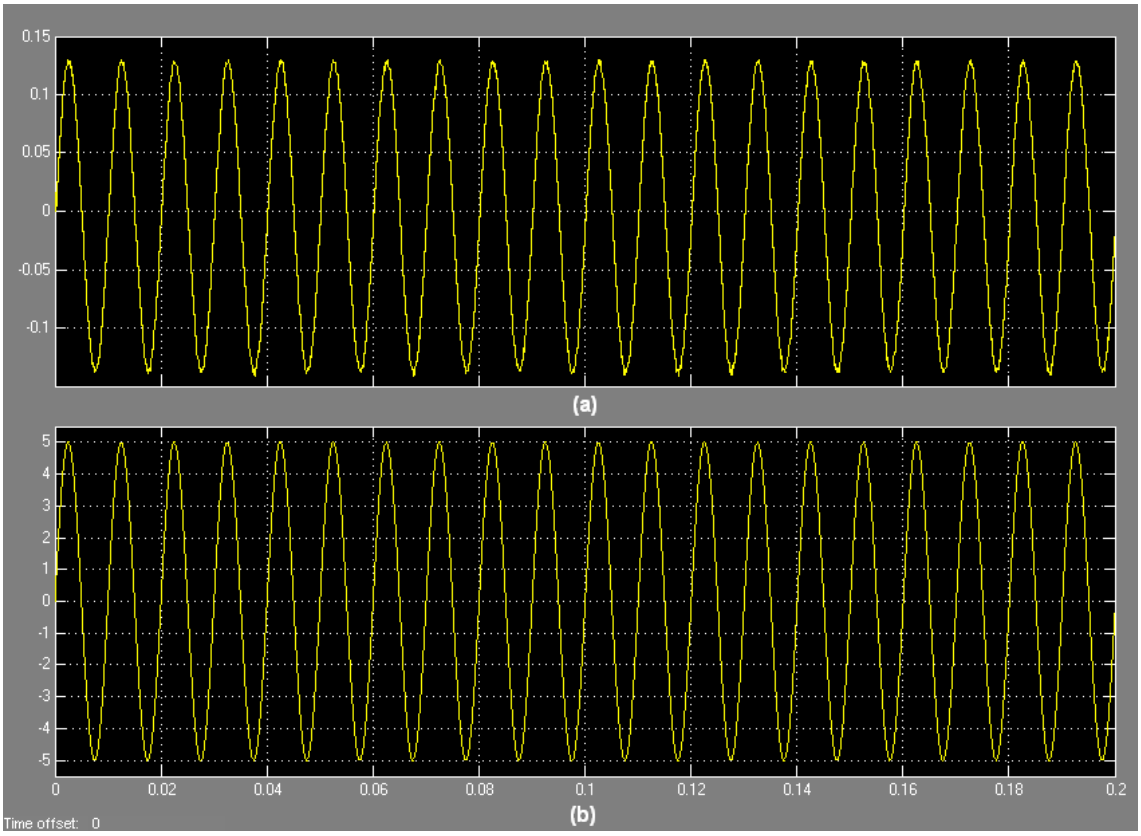

Figure 4.35: Normalized output of the readout circuit in closed loop mode for 5g amplitude, and 100Hz frequency acceleration.

To detect the operation range of the accelerometer at closed loop again a ramp signal is applied starting from 0g up to 40g and the output is observed. When the input acceleration reaches ~35g value the output saturates at "1". The operation range was calculated as 39g in the previous sections but MATLAB detects the operation range of the accelerometer as 35g by taking all the nonlinearities coming from the deflection of the accelerometer into account. Figure 4.36 shows the simulation results to detect the operation range of the accelerometer. One other important result obtained from this simulation is the highly distorted regions at the output of the $sinc^3$ filter for accelerations over 27g which is because the readout feedback could not effectively suppress the motion caused by the high accelerations. This phenomenon is exactly observed at the output of the tested accelerometers which are presented in chapter 5. With these simulation results basic operation of the accelerometer system is verified.

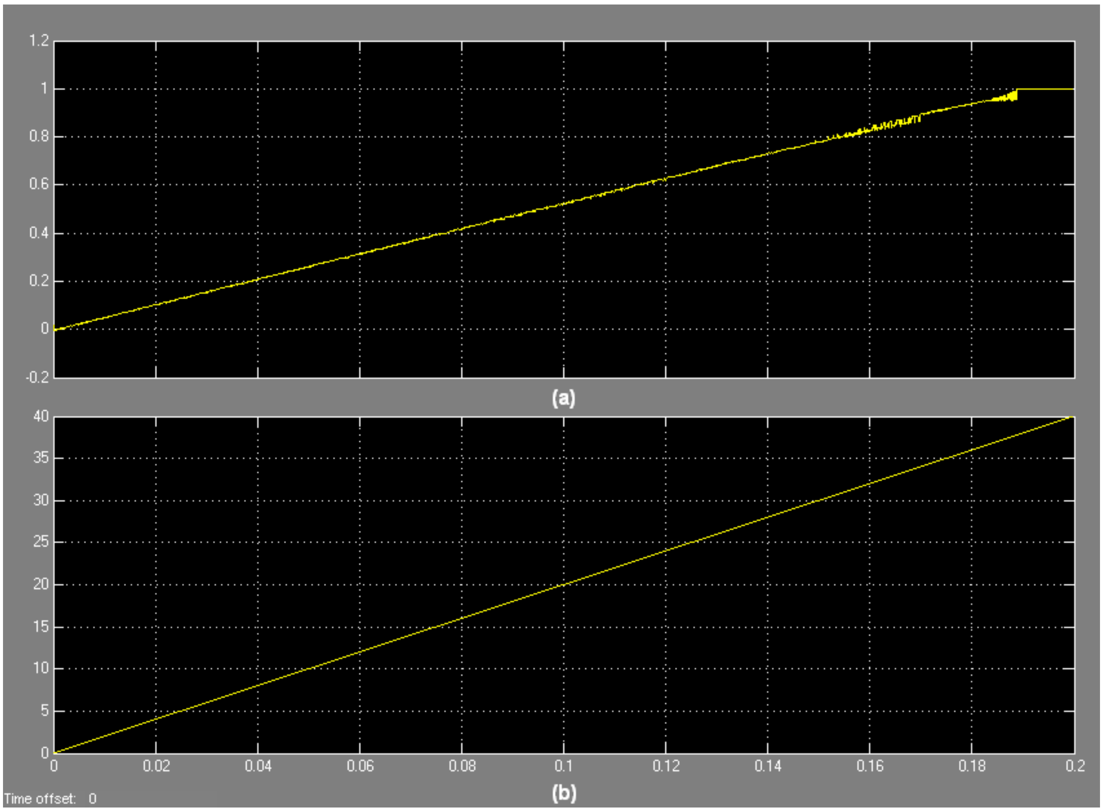

Figure 4.36: Simulation results to detect the operation range of the accelerometer. (a) Output of the sinc^3 filter (b) Applied 0 to 40g ramp input.

After the design and simulations are completed and the basic operation of the designed accelerometer is verified, dissolved wafer process proceeded with the fabrication of the sensors. 5 wafers are fabricated with DWP process and several functionally working accelerometers are connected to closed loop second order $\Sigma-\Delta$ readout circuits and tested at system level. These test results are presented in chapter 5 of this thesis. Although working accelerometers are found from the fabricated wafers, yield of the fabrications were still very low. In addition to this working accelerometers had severe problems during the operation. Most important reason of these problems was the buckling of sensors. Although the sensitivities of the accelerometers are increased with the new design and other measures are taken to decrease the buckling of the sensors, this problem could not be completely solved.

Figure 4.37 shows the buckling problem related with the new designed accelerometers fabricated using DWP.

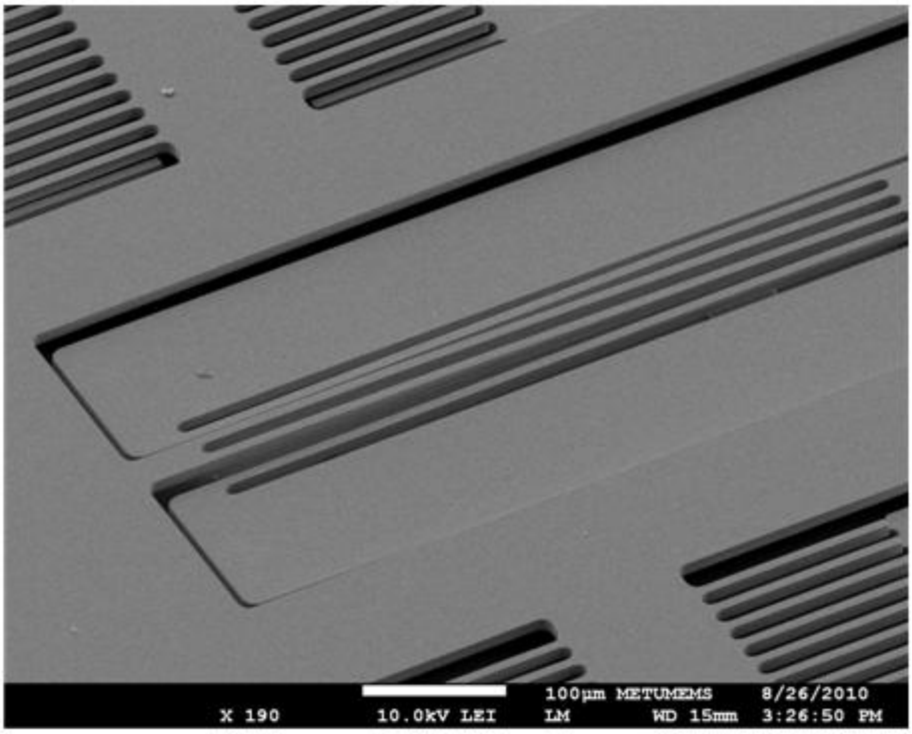

(a)

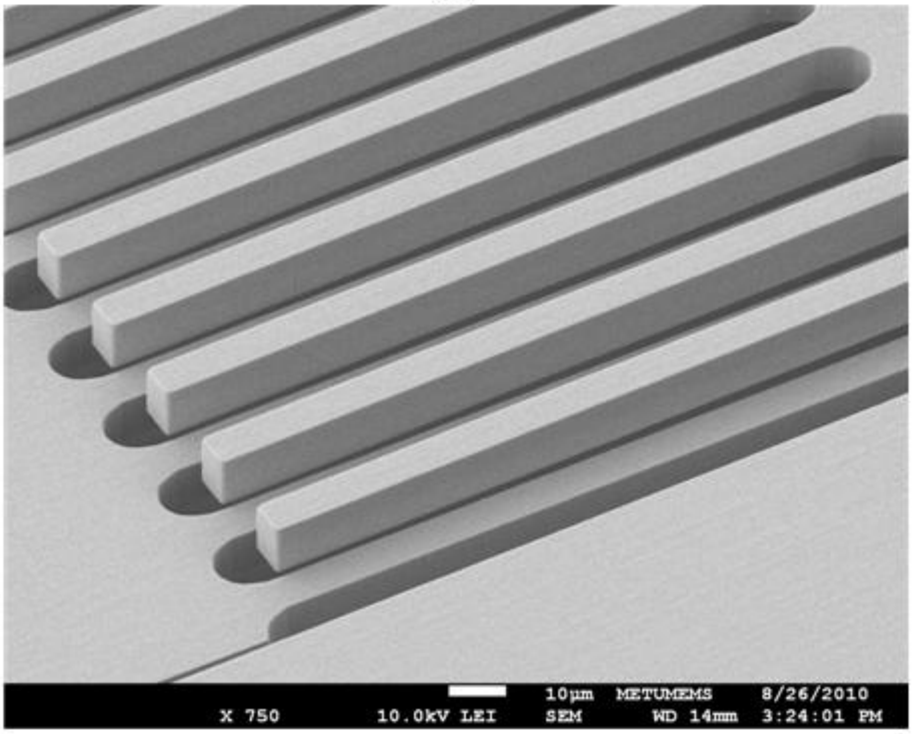

(b)

Figure 4.37: Buckling problem related with the new designed accelerometers fabricated using DWP.

4.3 Dissolved Epitaxial Wafer Process (DEWP)

Accelerometers fabricated with DWP demonstrated performance results very close to their design expectations described in the previous part of this chapter. Unfortunately there were several problems which were originating from the fabrication of the accelerometers. The structural thicknesses of the DWP accelerometers were very thin due to the maximum diffusion depth of boron atoms in the silicon. In addition to the thickness problem, crystal defects occurred during the diffusion process, causing internal stress which bends the proof mass of the accelerometer. Bending of the proof mass decreases the capacitive finger overlap area which reduces the sensitivity and rest capacitance of accelerometers.

Dissolved epitaxial wafer process has a completely similar fabrication procedure with the dissolved wafer process as described in the previous section and they are both done based on the etch selectivity of EDP between high and low doped silicon regions. The only difference between these two processes is the wafer used as the structural layer. In regular DWP process a silicon wafer with high boron doped p++ region is used. Unfortunately high boron doped region thickness does not exceed 12-14μm. In epitaxial wafers, device layer behaves as the structural layer and its thickness can be selected as the required structural thickness. Unlike normal silicon wafers with high boron doping, these wafers may have device layers up to few hundred μm's. Another important property of these wafers is the 1-2% Germanium doping during the epitaxial growth procedure. Large radius of Germanium atoms compensate the internal stress formed by the small atomic radius of Boron atoms [98]. For the inertial sensor applications, in order to obtain higher sensitivities, finger spacing must be decreased; on the other hand structural thickness must be increased as much as possible as shown in sensitivity equation given below:

$$\frac{\partial C}{\partial x} = \frac{N \times \epsilon_0 \times FL \times h}{{d_1}^2} - \frac{(N-1) \times \varepsilon_0 \times FL \times h}{{d_2}^2} \tag{4.1}$$

where N is the number of fingers on each side of the accelerometer, ε_0 is the permittivity of the air, FL is the finger overlap length of the two consecutive fingers, h is the structural thickness of the accelerometers, d_1 is the small finger spacing and d_2 is the large finger spacing between two consecutive fingers. The minimum value that the finger spacing d_1 can take in this equation is limited with the mask aligners resolution and it is ~1µm. If some other advance technology like stepper is used finger spacing can further decrease under 0.5µm. While keeping the finger spacing as low as possible, maximum structural thickness of the accelerometers is determined with the aspect ratio of the DRIE in order to open finger spacing. Normally DRIE aspect ratio is around 25-30 but for our applications, when the silicon wafer is directly placed on the DRIE chuck without bonding to a glass wafer and using the stepped etching technique, aspect ratio can increase up to ~40-50 [99]. But selecting the structural thickness of an accelerometer too high will also increase the mechanical noise of the system. Therefore the epitaxial layer thickness should be selected by taking all these factors into account. For this process the structural thicknesses of the device layers are chosen as 35µm's.

4.3.1 Overview of the Dissolved Epitaxial Wafer Process (DEWP)

Fabrication steps of the DEWP one-to-one matches with the DWP with a single difference which is the wafer used for this process. In DEWP instead of a highly boron doped silicon wafer, epitaxial wafers having 35µm device layers are used. As a summary for the process, it starts with the formation of the structures on the device layer of the epitaxial wafer. Anchors are also formed on the glass wafer by wet etching with hydrofluoric acid. After glass recess formation, chromium and gold is evaporated on the glass wafer and metal lines are formed. Prepared silicon and glass wafers are bonded to each other and most of the bulk silicon is removed by thinning with HNA or grinder. Than rest of the high resistive silicon is removed in EDP solution where the low resistive device layer behaves as an etch stop.

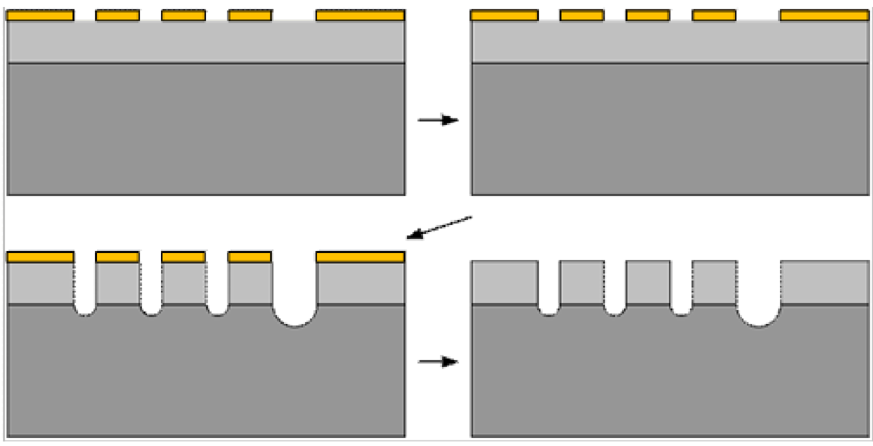

(a)

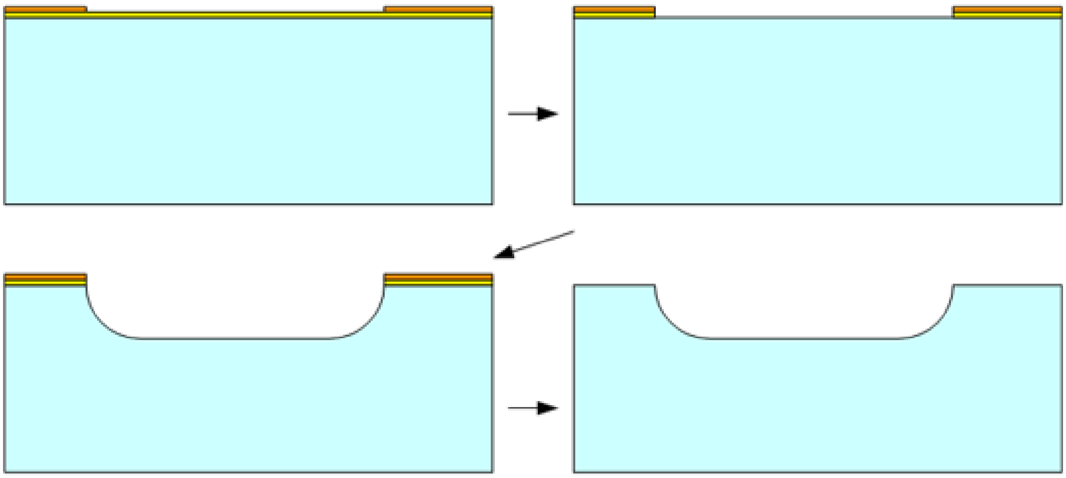

(b)

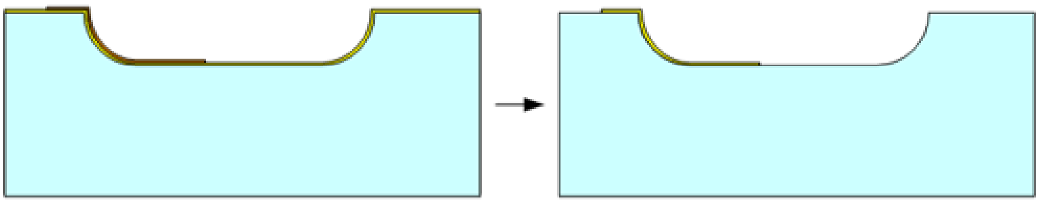

(c)

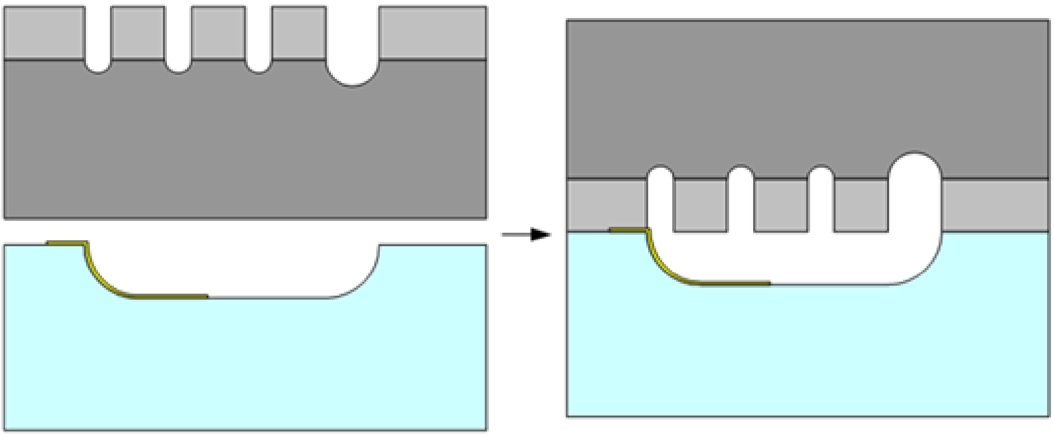

(d)

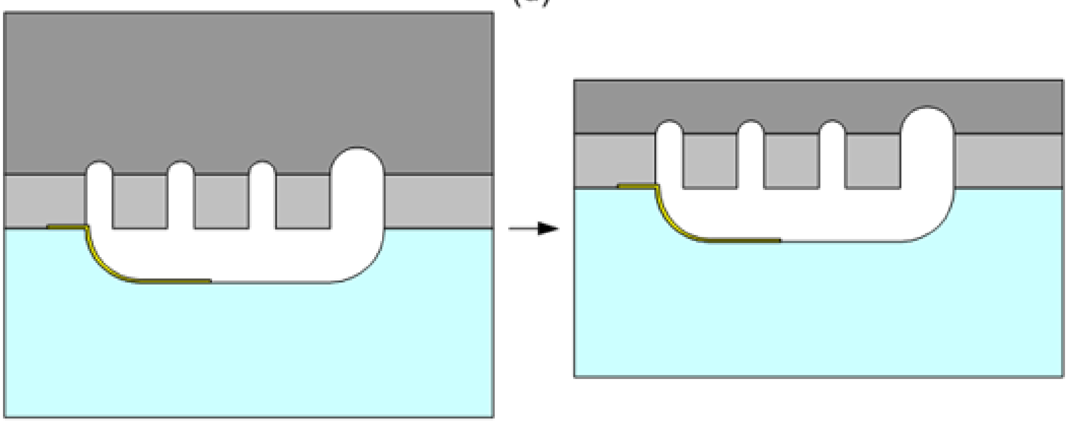

(e)

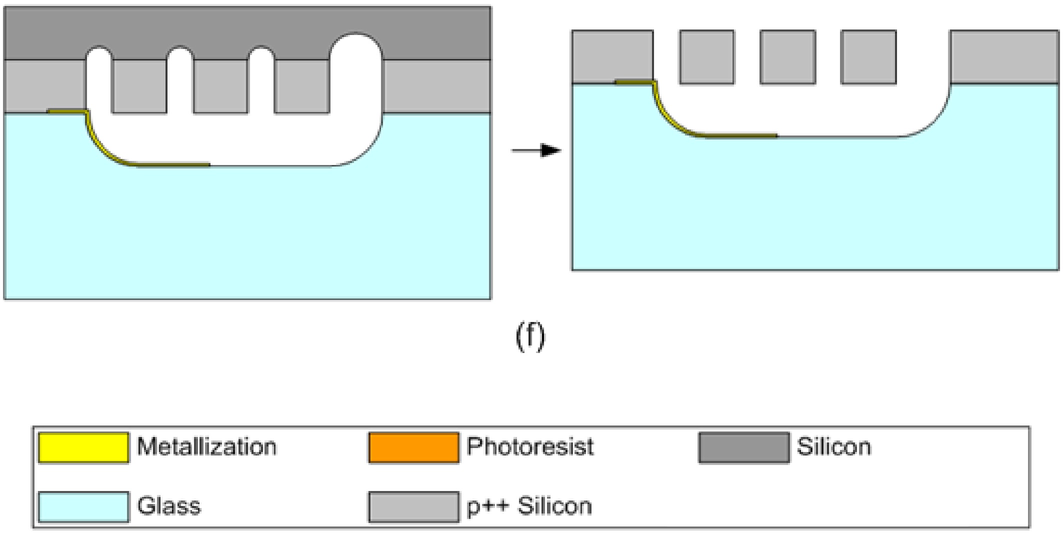

Figure 4.38: Dissolved epitaxial wafer process flow. (a) Epitaxial wafer is patterned and etched with DRIE. (b) Anchor recess formation is done on the glass wafer. (c) Chromium and gold is sputtered and patterned as the metal lines of the devices. (d) Prepared glass and epitaxial wafers are anodically bonded. (e) Epitaxial wafer is thinned with HNA or grinder. (f) Rest of the undoped silicon is removed in EDP.

This process has several drawbacks like DWP, in spite of its easy fabrication technique. First drawback is the utilization of Ethylene Diamine Pyrocathecol (EDP) etching in the final release step. EDP is a highly polluting and carcinogenic material which is very harmful against the human health and nature. Second and most important drawback is the low doping level of the device layer of the epitaxial wafers. Fast EDP etches low doped silicon with 80µm/ hour etching rate. But for p concentrations exceeding ~$5x10^{19}$, etch rate decreases drastically to its 1/100 speed [100]. This phenomenon is used to etch the substrate selectively. Commercial wafer dealers generally do not have epitaxial wafers with device layer resistivities lower than 0.001-0.003 Ω.cm in their inventories. In order to satisfy the doping requirements for EDP etching, resistivity of the device layer should be lower than 0.0012 Ω.cm. Therefore instead of commercial wafers, specially prepared wafers are needed to be used in order to meet the high doping requirements of this fabrication technique.

4.3.2 Performance Estimation for DEWP accelerometers

For the dissolved epitaxial wafer process, a new accelerometer design was not made since the current design for the dissolved wafer process was already optimized to increase the measurement range and decrease the overall noise of the system. Therefore same mask is directly used in DEWP. The only issue that has to be considered during the design is the change of important performance parameters with the structural thickness.

Figure 4.39 shows the MATLAB analyzes results for important performance parameters with changing structural thickness like mass, spring constant, damping, operation range, rest capacitance, sensitivity, and mechanical noise. From these simulation results we can conclude that the operation range of the accelerometer system remains constant while the mechanical noise of the sensor increases slightly with increasing structural thickness. This increase in the mechanical noise is not very important since electrical noise is still dominant in the system and mechanical noise is negligible when compared with the electrical noise. Sensitivity and rest capacitance of the accelerometer also increases with increasing structural thickness which is a desired behavior.

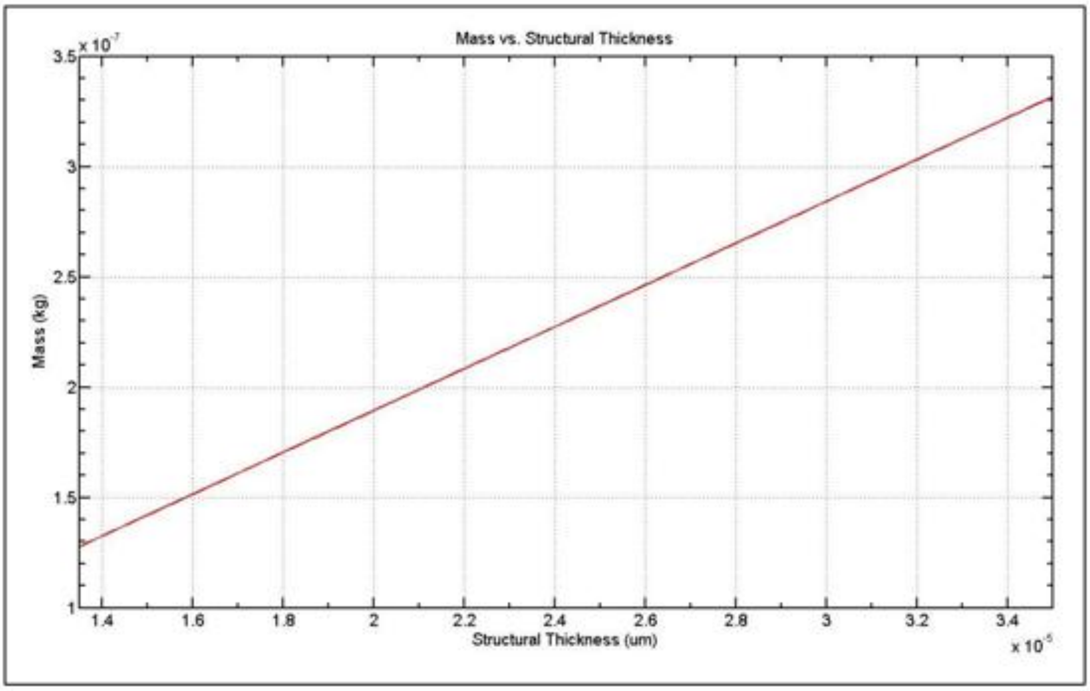

(a)

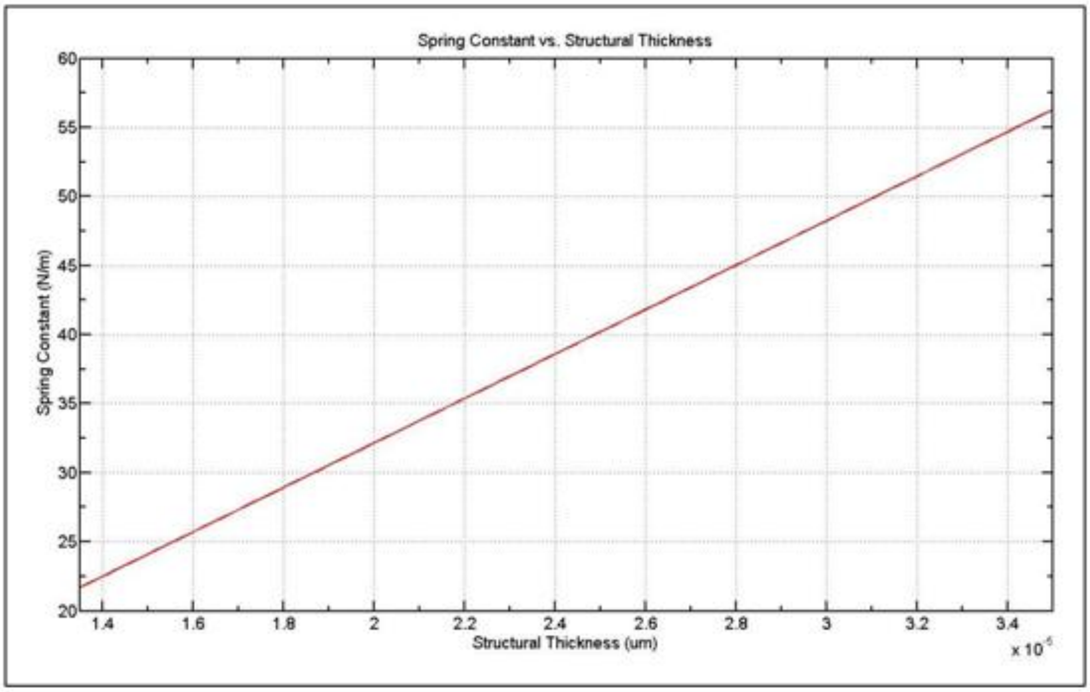
Spring Constant vs. Structural Thickness
Spring Constant (N/m)
60
55
50
45
40
35
30
25
20
1.4
1.6
1.8
2
2.2
2.4
2.6
2.8
3
3.2
3.4
Structural Thickness (um)
x 10^-5

(b)

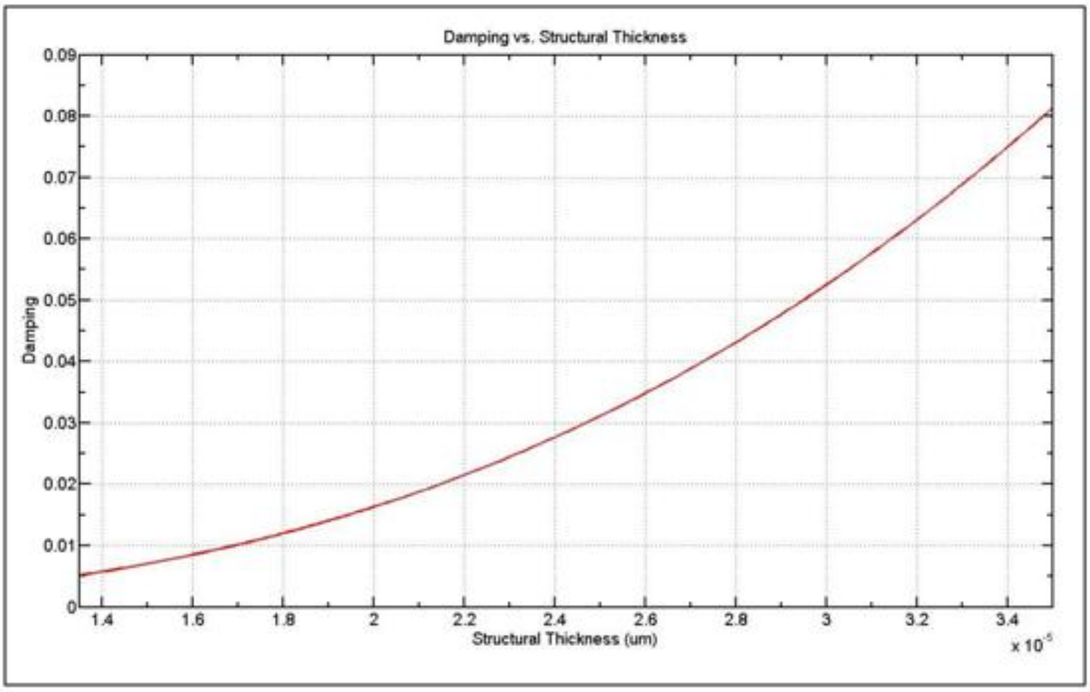
Damping vs. Structural Thickness
Damping
0.09
0.08
0.07
0.06
0.05
0.04
0.03
0.02
0.01
0
1.4
1.6
1.8
2
2.2
2.4
2.6
2.8
3
3.2
3.4
Structural Thickness (um)
x 10^-5

(c)

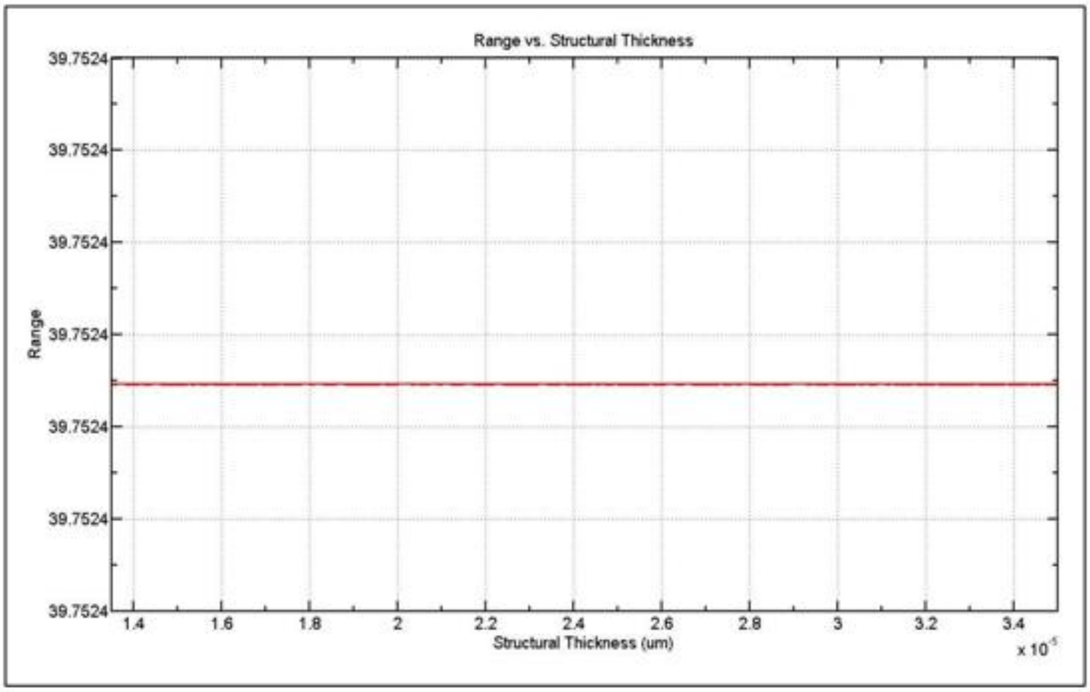
Range vs. Structural Thickness
Range
39.7524
39.7524
39.7524
39.7524
39.7524
39.7524
39.7524
1.4
1.6
1.8
2
2.2
2.4
2.6
2.8
3
3.2
3.4
Structural Thickness (um)
x 10^-5

(d)

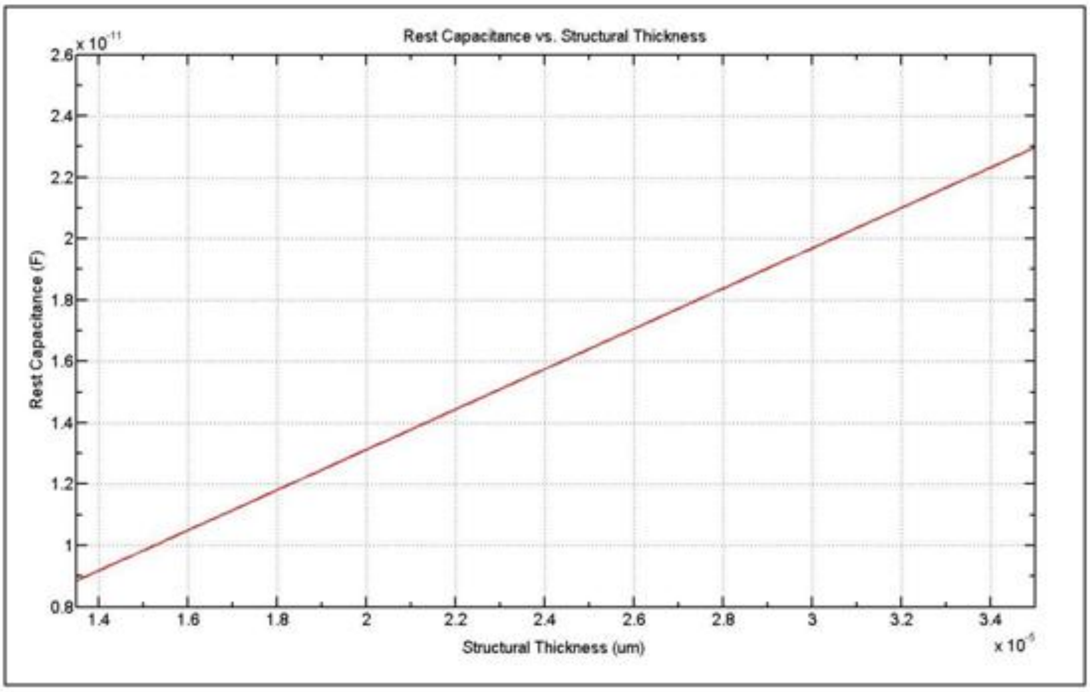
Rest Capacitance vs. Structural Thickness
x 10^-11
Rest Capacitance (F)
2.6
2.4
2.2
2
1.8
1.6
1.4
1.2
1
0.8
1.4
1.6
1.8
2
2.2
2.4
2.6
2.8
3
3.2
3.4
Structural Thickness (um)
x 10^-5

(e)

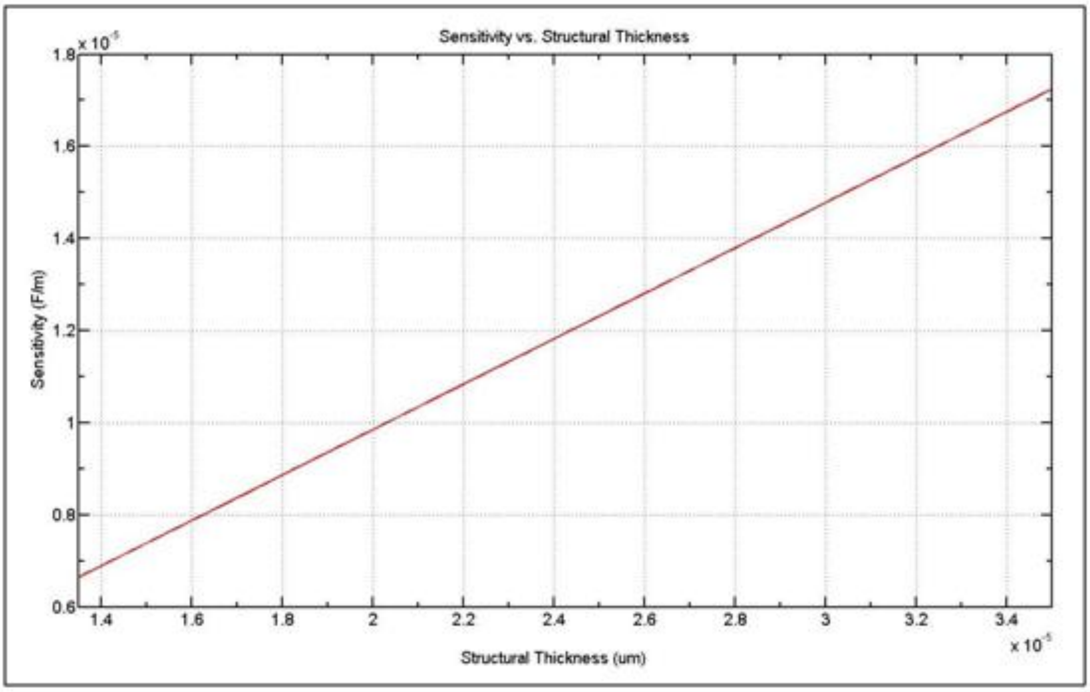

(f)

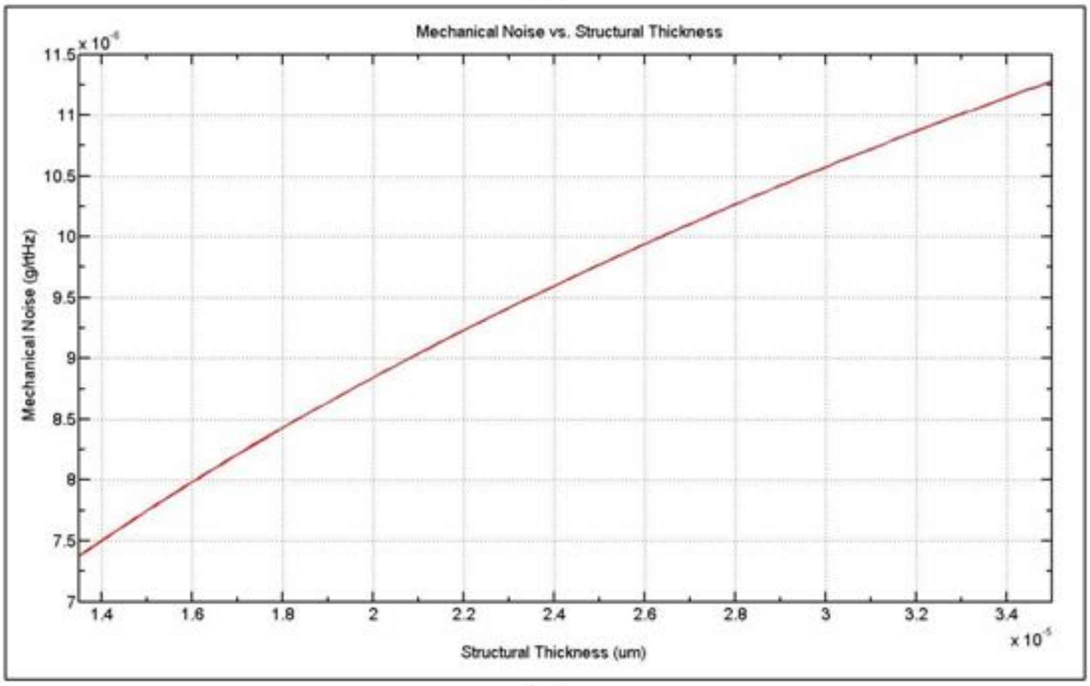

(g)

Figure 4.39: MATLAB analyzes results for important performance parameters with changing structural thickness. (a) Mass vs. structural thickness. (b) Spring constant vs. structural thickness. (c) Damping vs. structural thickness. (d) Operation range vs. structural thickness. (e) Rest capacitance vs. structural thickness. (f) Sensitivity vs. structural thickness. (g) Mechanical noise vs. structural thickness.

By looking at these graphs one can expect that the performance of the accelerometer doesn't deteriorate too much. But stability of the closed loop system is also another important issue and it should also be checked if the sensor works in harmony together with the closed loop readout circuitry. For the system to be stable, three different solutions can be applied to the system, which are; over-damped proof mass response, limiting the loop bandwidth electrically, and compensation with a lead filter [87]. When the structural thickness of the accelerometer is 13.5μm, transfer function of the sensor is as given below:

$$Accelerometer(s) = \frac{1}{s^2 + 40429\, s + 169745330} \tag{4.2}$$

This accelerometer model is totally stable with its two complex poles on the real axis at -35670 and -4758. Figure 4.40 shows the bode diagram and pole-zero map of the transfer function for 13.5μm thick DWP accelerometer. From this transfer function η of the system can be calculated as 1.55 which indicates an over damped system. (η>1)

System operates in stable mode in this configuration with a compensator circuit connected at the output of the front-end readout circuitry with a transfer function given as follows:

$$Compensator(z) = \frac{2z - 1}{2z} \tag{4.3}$$

When the structural thickness of the accelerometer is increased up to 35μm, mass, spring constant and damping of the system become $3.32\text{x}10^{-7}$kg, 56.28N/m and 0.0813 respectively. With these structural properties, transfer function of the accelerometer is changed to the one given in equation 4.4. Figure 4.40 shows the bode diagram and pole-zero map of the transfer function for 35μm thick DEWP accelerometer.

$$Accelerometer(s) = \frac{1}{s^2 + 245168s + 169745330} \tag{4.4}$$

Poles of this system move apart from each other on the real axis by increasing the structural thickness and their new places become -694 and -244474. η of this system increases to 9.41 which also increases the over-damping of the system and also enhances the stability as described previously. The only disadvantage of this increase in the thickness is that mechanical 3dB bandwidth of the structure decreases to 105 Hz from 890Hz. But this doesn't constitute a problem since the bandwidth of the system greatly increases when it's operated in the closed loop mode.

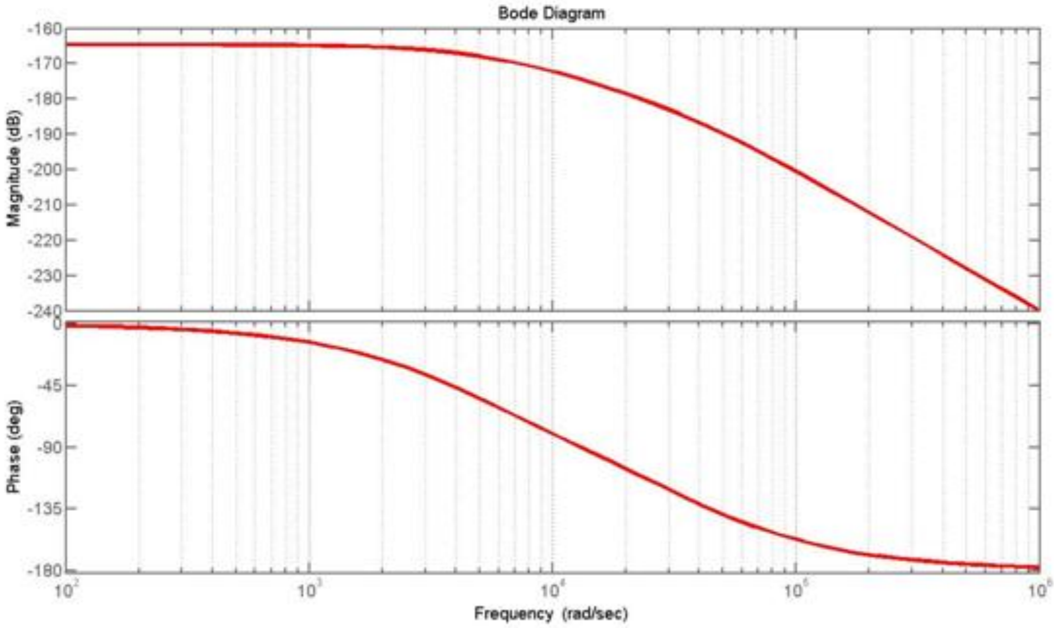

(a)

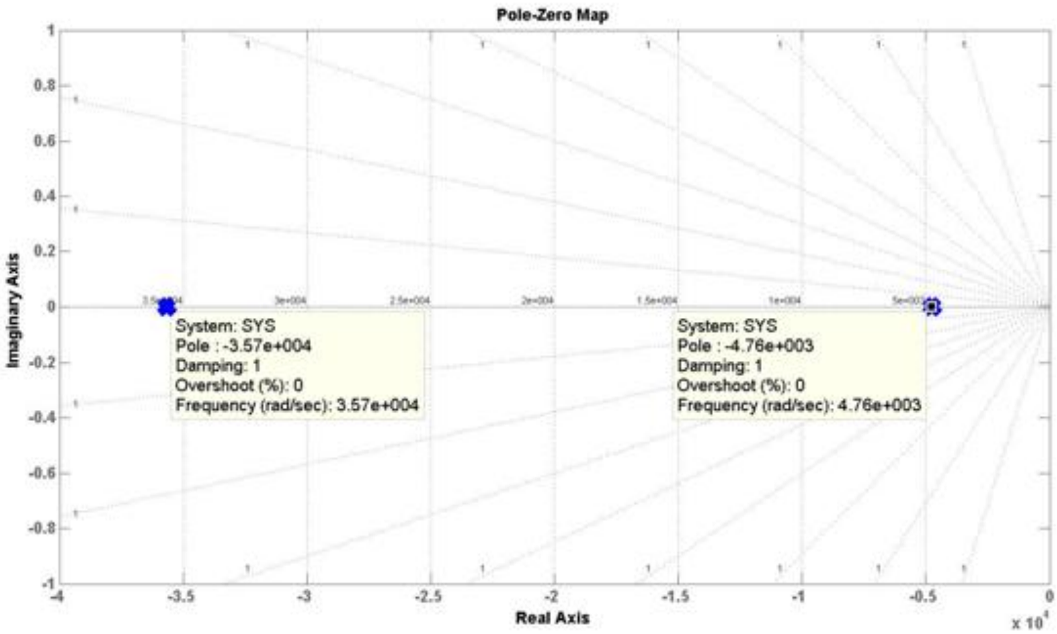

(b)

Figure 4.40: Bode diagram and pole-zero map of the transfer function for 13.5µm thick DWP accelerometer. (a) Bode Plot of the 13.5µm thick sensor. (b) Pole-Zero Map of the 13.5µm thick sensor.

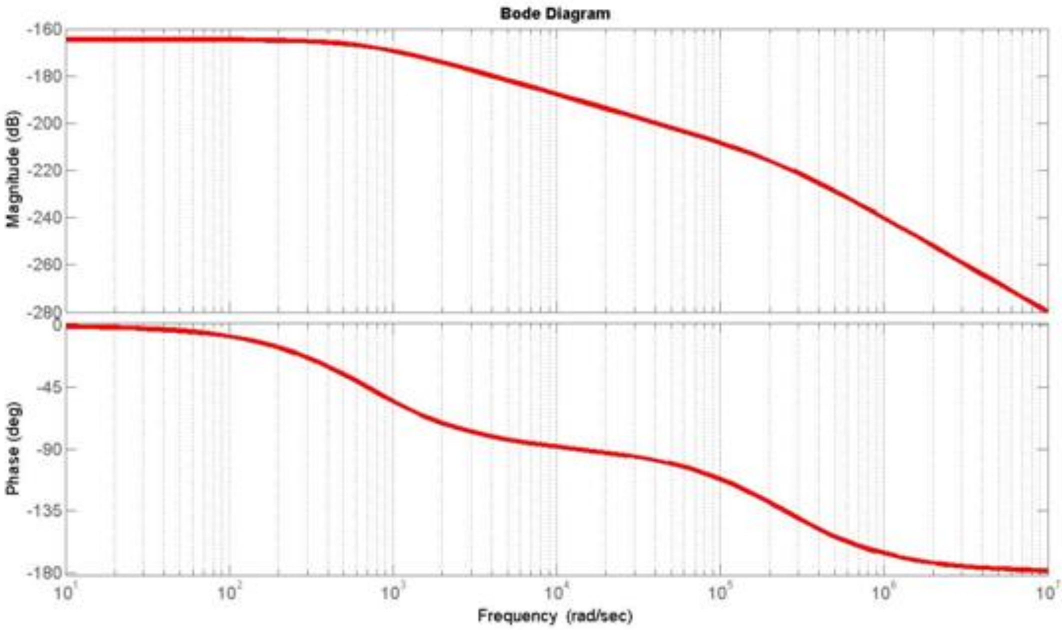

(a)

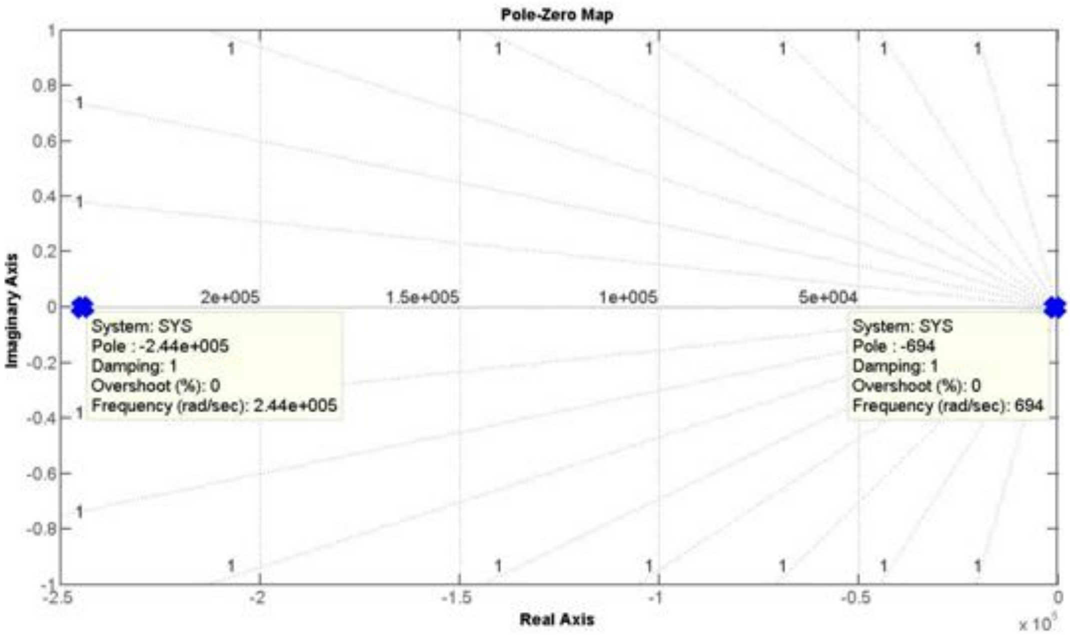

(b)

Figure 4.41: Bode diagram and pole-zero map of the transfer function for 35µm thick DEWP accelerometer. (a) Bode Plot of the 35µm thick sensor. (b) Pole-Zero Map of the 35µm thick sensor.

Using the epitaxial growth wafers having 35µm epi-layers, several fabrication trials are done and working accelerometers are obtained from these fabrications. Sensor and system level tests of these sensors are presented in chapter 5 of this thesis. From the fabrication trials few accelerometers could be found for testing. There are two major reasons for low yield of DEWP fabrication technique. First reason is the narrow capacitive finger spacing of fabricated accelerometers. During DRIE of the epitaxial wafer, polymer is deposited in the passivation phase of the etching process. Deposited polymer on the vertical walls should be removed in the cleaning step for the accelerometer to operate properly. Since 1µm spacing is too narrow, it becomes very difficult to remove the polymer and other contamination between the fingers and this problem becomes more obvious with the accelerometers having 440µm finger lengths. Also glass anchors do not have any spacing for the cleaning chemicals to access bottom of the suspended structures. This theory is proved by observing several sensors which are not working properly; started to work after cleaning for an additional cycle and working sensors stops their operation after an additional cleaning cycle. Second reason is the spike like shapes formed after the DRIE at the tip of rectangular fingers. These spikes touch to the opposing fingers during the operation which distorts the sensor characteristics. Figure 4.42 shows successfully fabricated 35µm thick DEWP accelerometers having fine structures and Figure 4.43 shows the devices having faults in their structures.

In order to solve these problems a new accelerometer design is made to increase the yield of the DEWP process. In this new design following changes are made:

- Finger spacing is increased from 1µm to 2µm's.
- In order to increase the measurement range of the devices, etch holes having 30µm radius are opened for each 100µmx100µm region on the suspended structures.
- Tip of the fingers are drawn rounded instead of sharp rectangular edges.
- Anchors are divided into smaller regions in order to provide access for the cleaning chemicals to the bottom of the suspended structures.

As it was mentioned in chapter 3 the most important parameter for an accelerometer in order to determine its performance is the capacitive finger spacing and with the increase of this spacing performance of the accelerometer also changes. In order to increase the yield of the fabrication, number of capacitive fingers and measurement range of the accelerometer is decreased together with the expected overall system noise. Additional etch holes are opened to decrease the mass of the accelerometer to increase the measurement range and this also enhances the access of the chemicals to the bottom of the suspended structures. Table 4.11 summarizes the performance expectations of the DEWP accelerometers having both 1μm and 2μm finger spacing.

Table 4.11: Performance expectations of the DEWP accelerometers having both 1μm and 2μm finger spacing

PERFORMANCE PARAMETERS					
Parameter	Finger Spacing		Parameter	Expected Performance	
	1μm	2μm		1μm	2μm
Proof Mass	331×10^{-9}kg	246×10^{-9}kg	Range	39.8g	10.8g
Spring Constant	56N/m	56N/m	Mechanical Noise	11μg/√Hz	5μg/√Hz
Damping	81×10^{-3}kg/s	8×10^{-3}kg/s	Quantization Noise	9μg/√Hz	2μg/√Hz
Resonance Frequency	2073Hz	2409Hz	Mass Residual Noise	31μg/√Hz	11μg/√Hz
Rest Capacitance	23pF	9.75pF	Front-end Amp. Noise	11μg/√Hz	2μg/√Hz
Sensitivity	172×10^{-7}F/m	35×10^{-7}F/m	Switching Noise	2μg/√Hz	0.5μg/√Hz
			Total Noise	36μg/√Hz	12μg/√Hz

4 fabrication trials are done with this new design and it is observed that the overall yield of the wafer is increased to 45-50% from 2-3%. Yield of the accelerometers having 440μm fingers is increased to %50-55 from 0% and yield of the accelerometers having 150μm fingers is increased to 45-50% from 5%. These test results prove that the changes made to improve the yield of the wafer succeeded. Figure 4.44 shows the SEM pictures of fabricated DEWP accelerometers having 2μm finger spacing, rounded finger tips and etch holes. SEM pictures prove that rounding the tip of the capacitive fingers solves the spike formation at the edges. Test results of these devices in sensor and system level are presented in fifth chapter of this thesis.

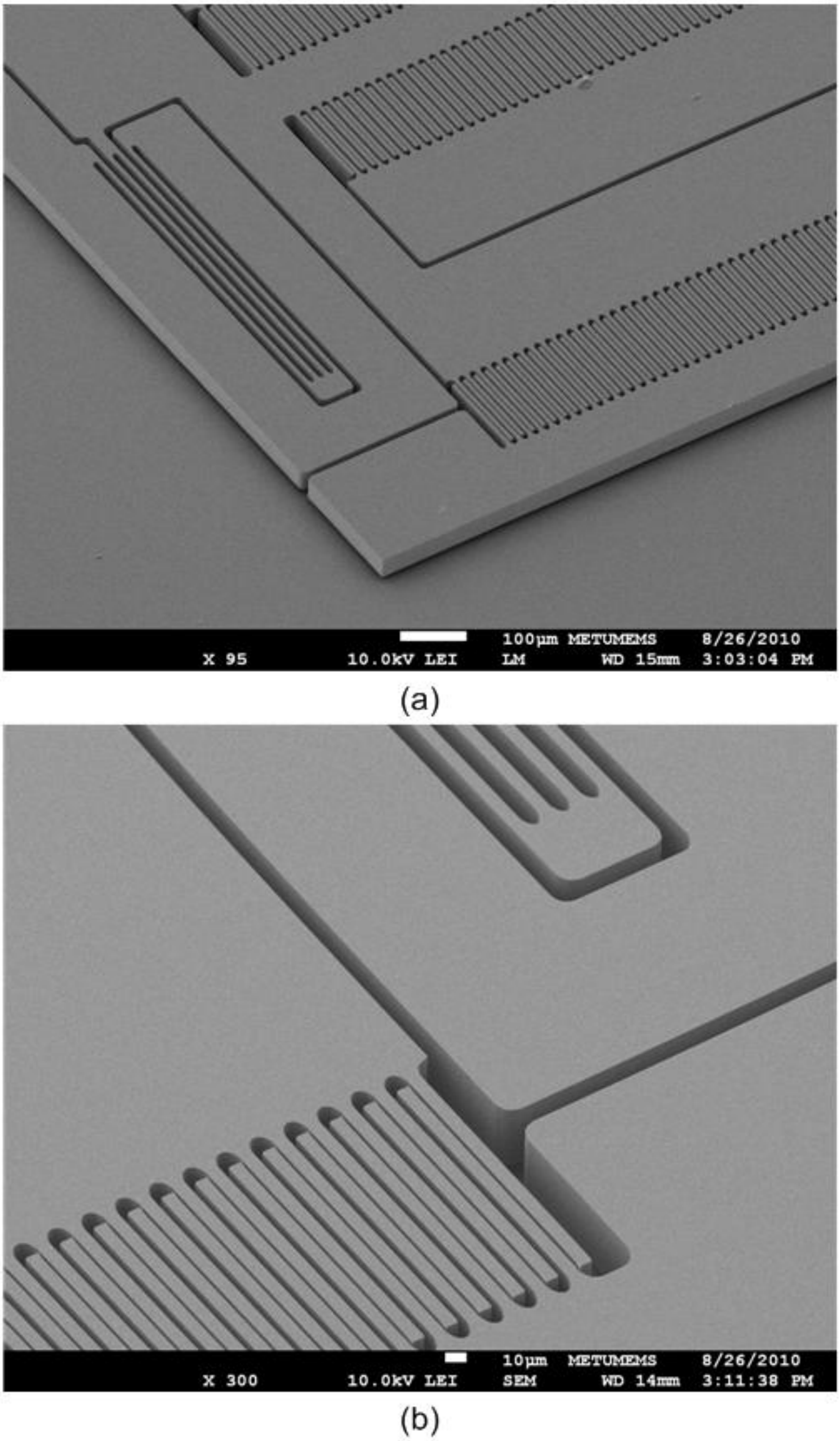

Figure 4.42: Successfully fabricated 35μm thick DEWP accelerometers with fine structures.

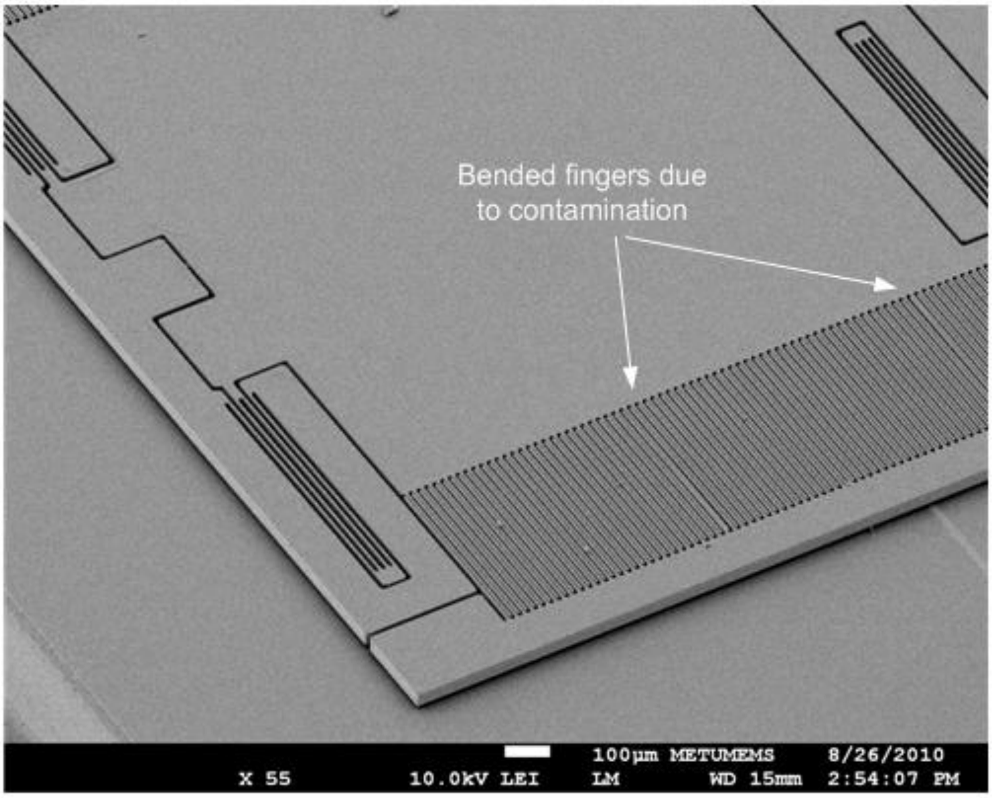

(a)

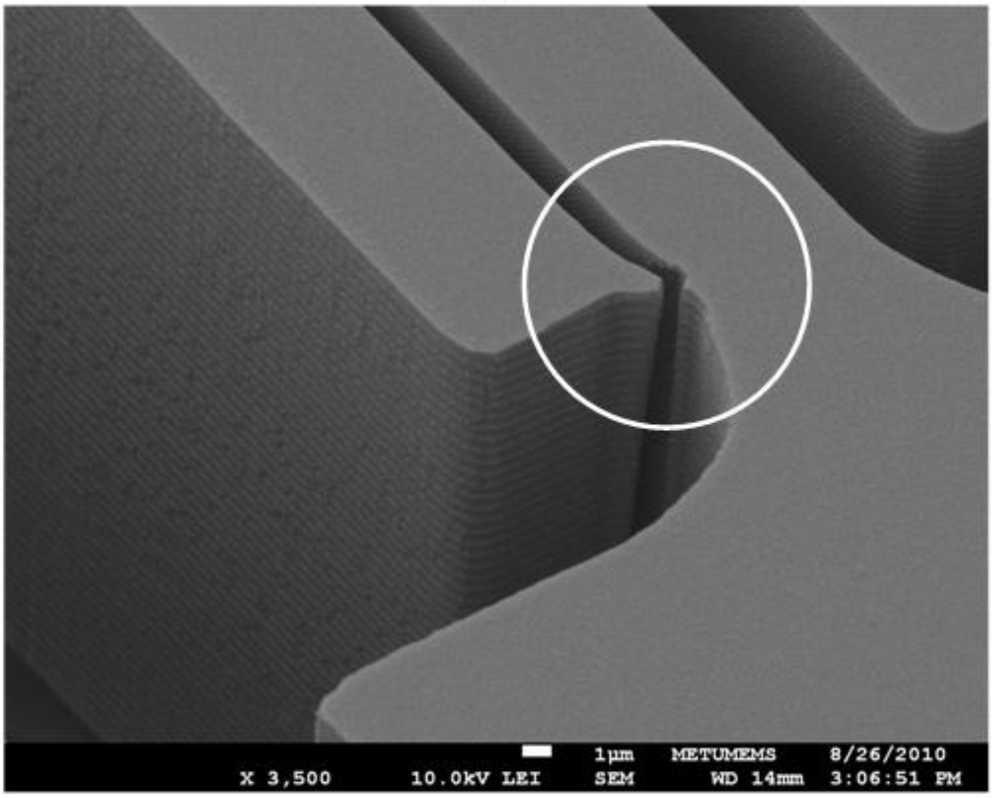

(b)

Figure 4.43: SEM pictures of the devices having faulty structures. (a) Opposing fingers stick each other due to contamination (b) Spikes formed at the fingers tips.

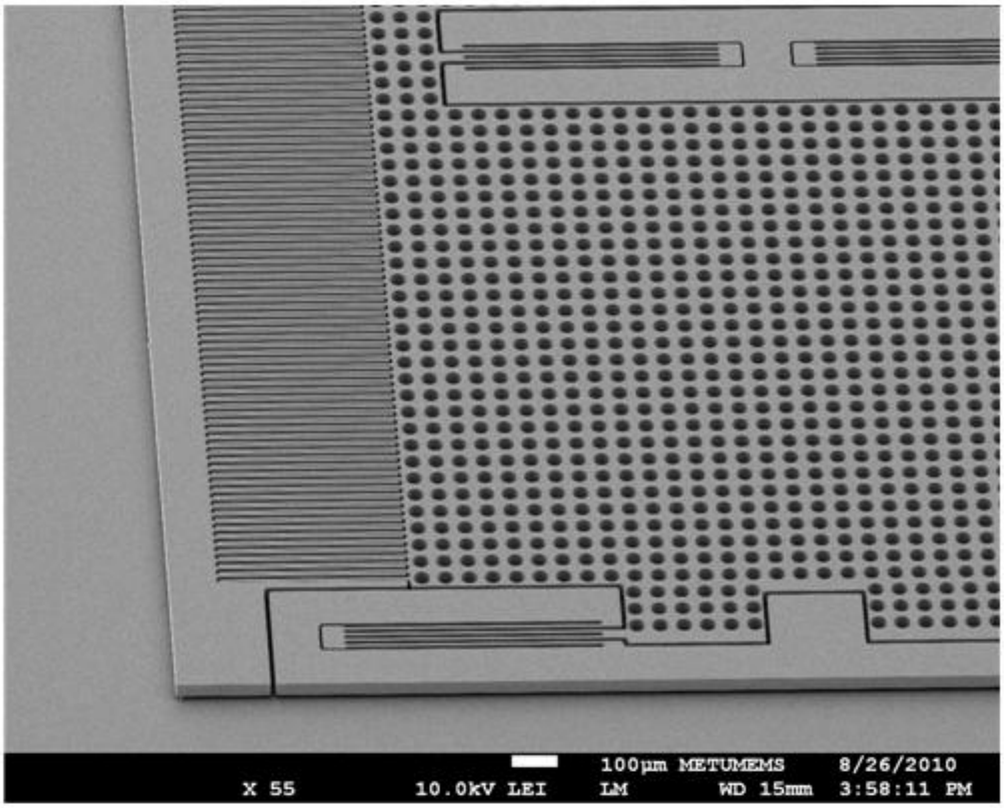
100µm METUMEMS 8/26/2010
X 55 10.0kV LEI LM WD 15mm 3:58:11 PM

(a)

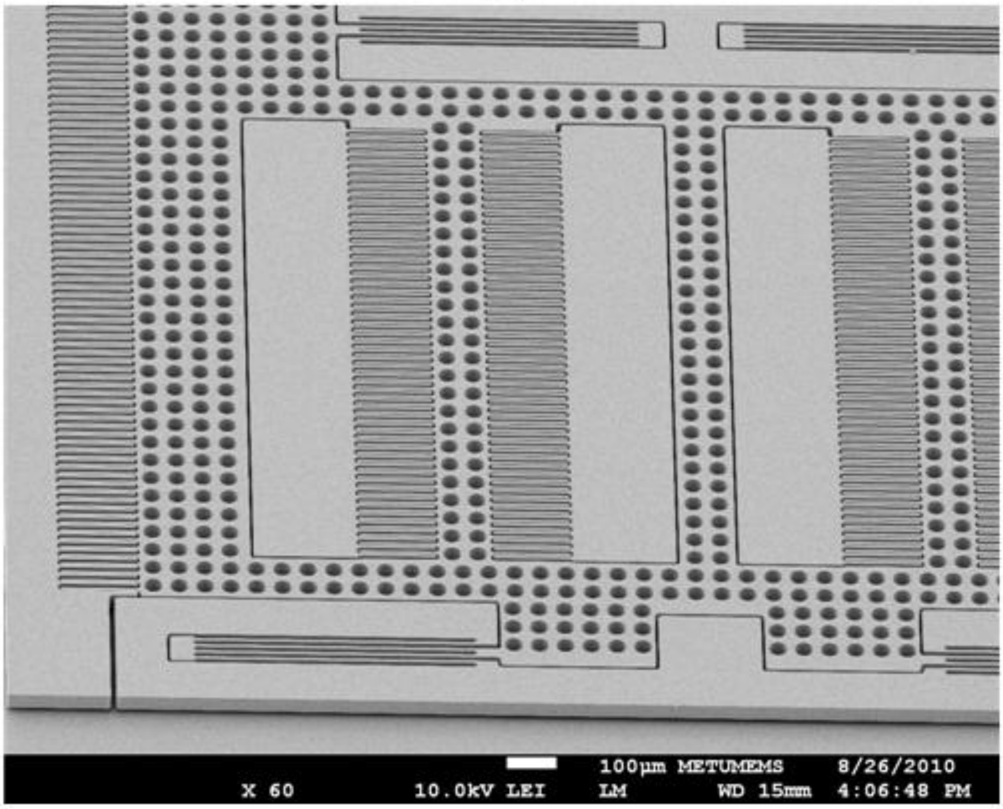
100µm METUMEMS 8/26/2010
X 60 10.0kV LEI LM WD 15mm 4:06:48 PM

(b)

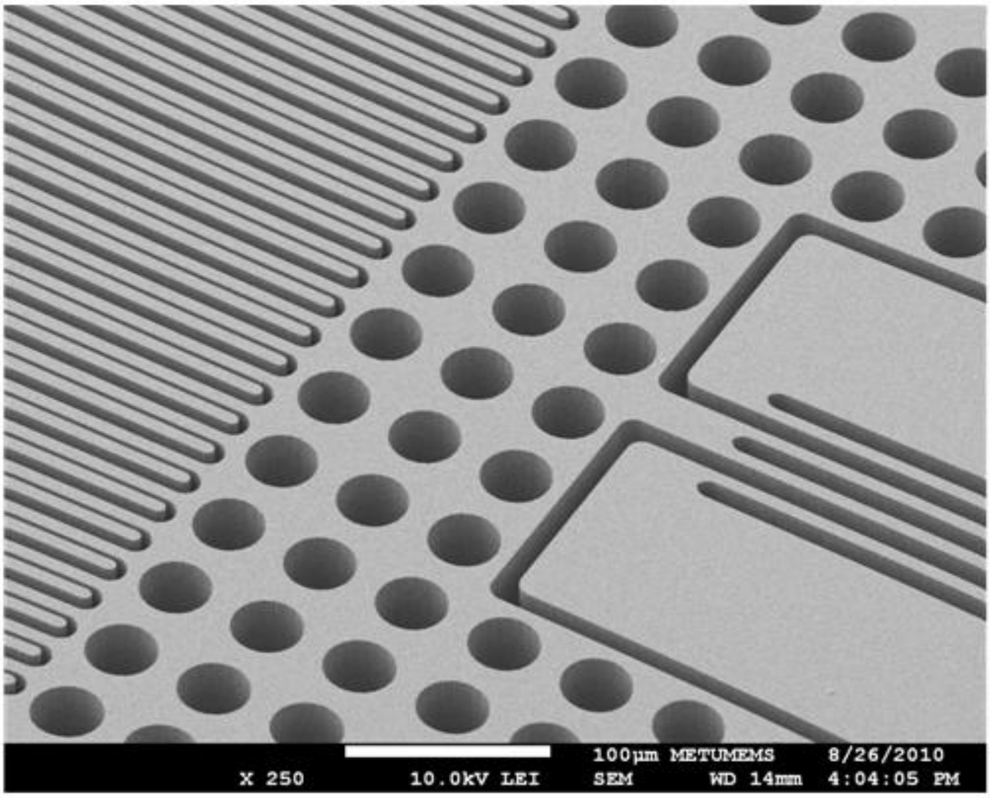

(c)

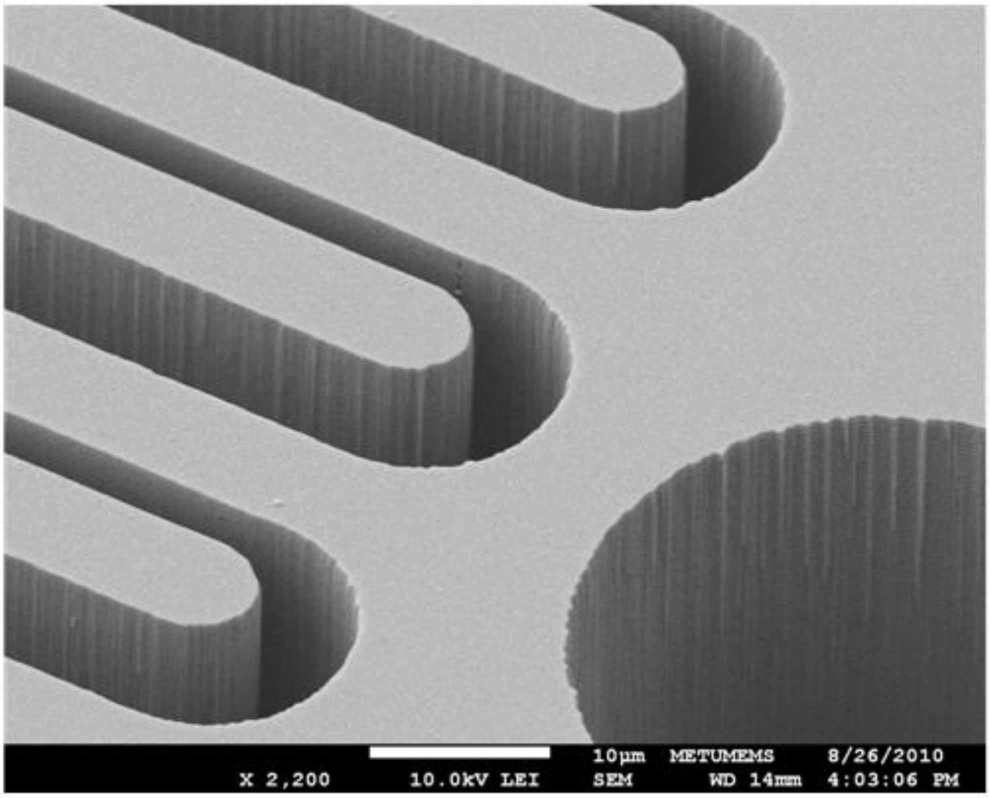

(d)

Figure 4.44: SEM pictures of fabricated DEWP accelerometers having 2µm finger spacing, rounded finger tips and etch holes.

4.4 Summary of the Chapter

In this chapter various fabrication techniques used to fabricate accelerometers are discussed and the designed accelerometers for each fabrication technique are described.

In chronological order accelerometers are initially fabricated with SOG process. In this process whole 100µm thick wafers are used as structural layers and accelerometers are fabricated by anodic bonding of this 100µm silicon wafers to glass wafers. Unfortunately with this process, accelerometers having measurement ranges more than 2g's could not be fabricated since the narrowest finger spacing that can be achieved with this process was 3.5µm's.

Secondly dissolved wafer process is employed in order to fabricate accelerometers having 1µm finger spacing. Fabrications are made in two phases. In the first phase several different designs are tried and the best design qualifies for the second phase of the fabrication. In the second phase a detailed design optimization procedure is used for obtaining high performance accelerometers. Accelerometers are also fabricated with this process but this time buckling of the boron doped 13.5µm layer limited the performance of these devices. Performance measurements of some fabricated devices were matching with the expected design parameters but the yield of the wafers was very low.

Finally dissolved epitaxial wafer process is employed for the fabrication of designed accelerometers. In this process structural thicknesses are increased to 35µm's and with the doping of 1-2% Germanium into Boron doped silicon, internal stress of the device layers could be decreased below 20MPa level. In the first fabrication trials working accelerometers were obtained having performance parameters very close to design values, but the yield of the wafers were still very low. Therefore some measures are taken to increase the yield of the accelerometers in expanse of measurement range. A new design is made by increasing finger spacing from 1µm to 2µm's and decreasing the mass of the accelerometer by opening etch holes. These changes increased the overall wafer yield from 2-3% to 45-50%.

CHAPTER 5

TEST RESULTS OF THE FABRICATED ACCELEROMETERS

In the scope of this thesis tactical grade accelerometers are fabricated with Silicon-on-Glass (SOG) fabrication process, Dissolved Wafer Process (DWP), and Dissolved Epitaxial Wafer Process (DEWP) which are described in detail in the fourth chapter of this thesis. In order to find the performance of accelerometers first they are tested at sensor level. Sensor level tests of the accelerometer are performed in order to understand if the fabricated accelerometer performances are close to the design values. During the sensor level tests accelerometer rest capacitance and sensitivity values are measured. The results are compared with the expected performances. If the test results are close to the expected values then the accelerometers are wire bonded to a proper readout circuit and tested at system level. System level tests are for finding more important performance parameters like the noise level, measurement range, bias drift and non-linearity.

In this chapter first the tests and the equipments are explained in detail in section 5.1. In sections 5.2, 5.3 and 5.4 sensors fabricated in SOG, DWP and DEWP are presented and the test results are given for each sensor. In section 5.5, three axes accelerometer package and the test results related with this package is presented. Finally in section 5.6 this chapter is concluded with a brief summary.

5.1 Accelerometer Tests

Fabricated accelerometers are first tested under the probe station at sensor level in order to find the sensor characteristic. With these tests rest capacitance and sensitivity change with voltage values are measured and results are compared with the design values. Satisfactory sensors are wire bonded to readout circuits and extensive system level tests are performed.

5.1.1 Sensor Level Tests

Sensor level tests are performed in two stages. These are C-V Measurement test performed under the probe station and sensitivity test performed after bonding accelerometer sensors to appropriate package.

5.1.1.1 C-V Measurement Test

Dried sensors are placed under the probe station and fixed to their places by turning on the vacuum of the chuck. This way any damage that can be done by the uncontrolled movement of the sensor or the probes are prevented. C-V measurement tests are performed with Agilent 4294A Precision Impedance Analyzer. Figure 5.1 shows the Agilent 4294A Precision Impedance Analyzer used for C-V measurement tests of the fabricated accelerometers. In these tests, left and right rest capacitances of accelerometers are measured separately. Between the proof mass and each electrode a voltage sweep is applied starting from negative voltage levels up to positive voltages and during this time measured capacitance values are recorded for each voltage value. Before the tests are started calibration of the test equipment is done in order to be sure to obtain proper results. At the end of these tests accelerometers having symmetric and close to expected capacitance values are qualified for the next tests and wire bonded to a package for sensitivity tests.

5.1.1.2 Sensitivity (C-g) Measurement Tests

After the sensors are tested at die level, symmetrical sensors are detected and wire bonded to a package for the C-g measurement tests. In this test, accelerometers are mounted on a rotating head and the left and right rest capacitances are connected to a LCR meter for capacitance measurement. Figure 5.2 shows the rotating head on which the accelerometer is mounted during the sensitivity tests and Figure 5.3 shows Agilent E4980A LCR meter used to measure capacitance changes on both sides of the accelerometer. Accelerometer is rotated with 30^0 angles in order to apply accelerations between ±1g range and the output is recorded. With this test sensitivity of the accelerometers per g value is detected for both right and left capacitances.

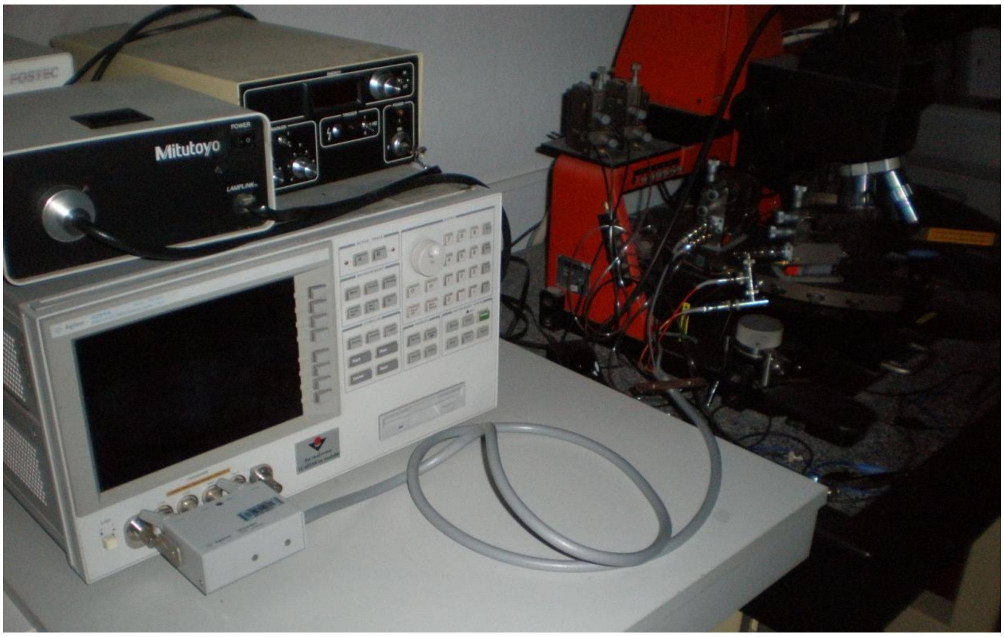

Figure 5.1: Agilent 4294A Precision Impedance Analyzer used for C-V measurement tests of the fabricated accelerometers.

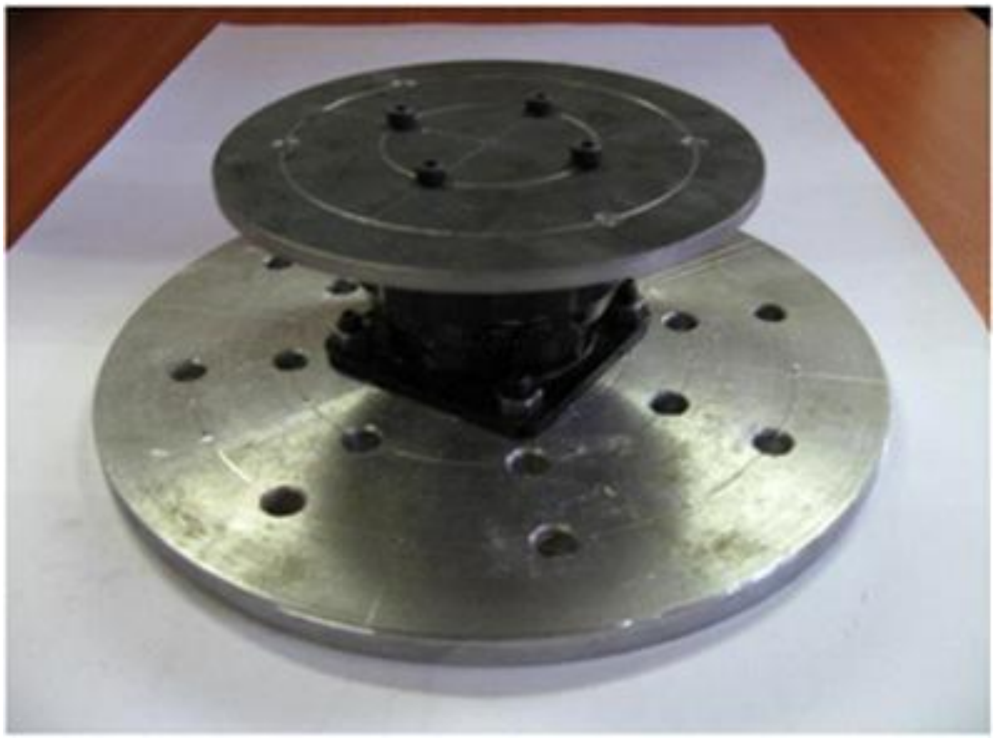

Figure 5.2: Rotating head on which the accelerometer is mounted during the sensitivity tests

Figure 5.3: Agilent E4980A LCR meter used to measure capacitance changes on both sides of the accelerometer during sensitivity measurements.

5.1.2 System Level Tests

After sensor level tests are completed and the capacitive performances of the accelerometers are detected, they are mounted on an alumina substrate and wire bonded to a readout circuit. These components are then placed in a 16 pin package for system level testing. Figure 5.4 shows the alumina substrate designed and fabricated for the accelerometers that will be tested at system level, Figure 5.5 shows a picture of the wire bonded readout circuit and accelerometer pair and Figure 5.6 shows the 16 pin package where the accelerometer and readout circuit are placed into after wire bonded to each other on alumina substrate.

16-pins are used for testing the accelerometers since initially the alumina substrate is designed for three axes accelerometer packaging. Therefore using this substrate and package a single axis or three orthogonal axis accelerometers can be packed. Table 5.1 shows the distribution and function of each pin on 16-pin accelerometer package. With this package, system level tests are performed in three stages which are noise and bias drift measurement with Allan-Variance method, maximum measurement range detection and non-linearity measurement.

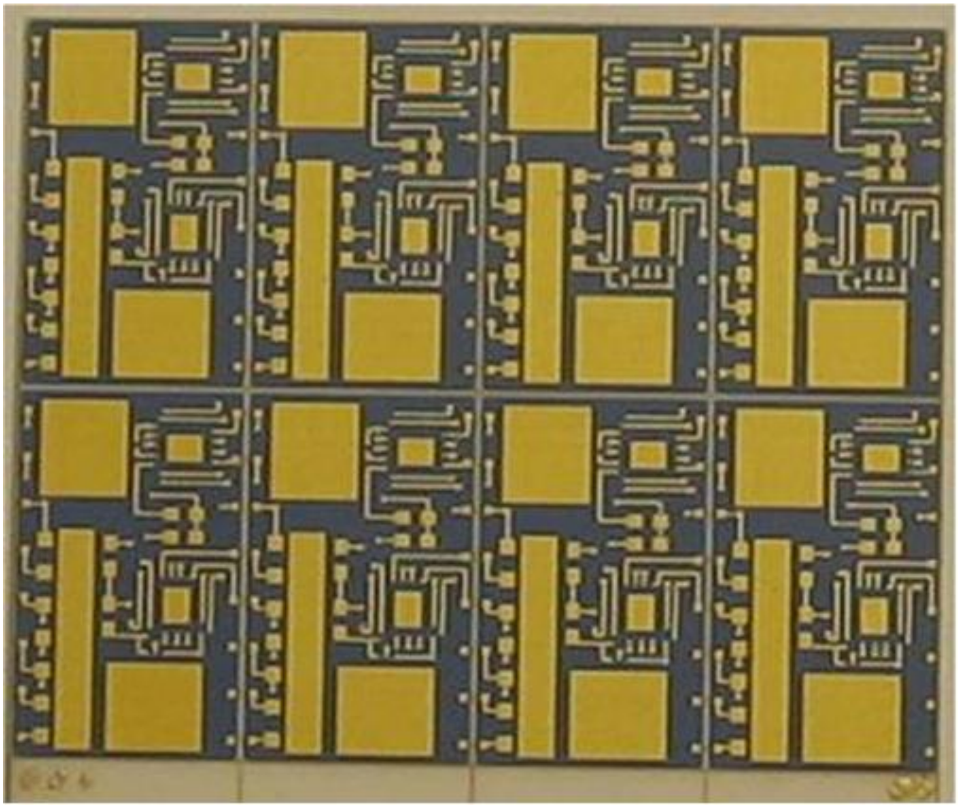

Figure 5.4: Alumina substrate designed and fabricated for the accelerometers that will be tested at system level

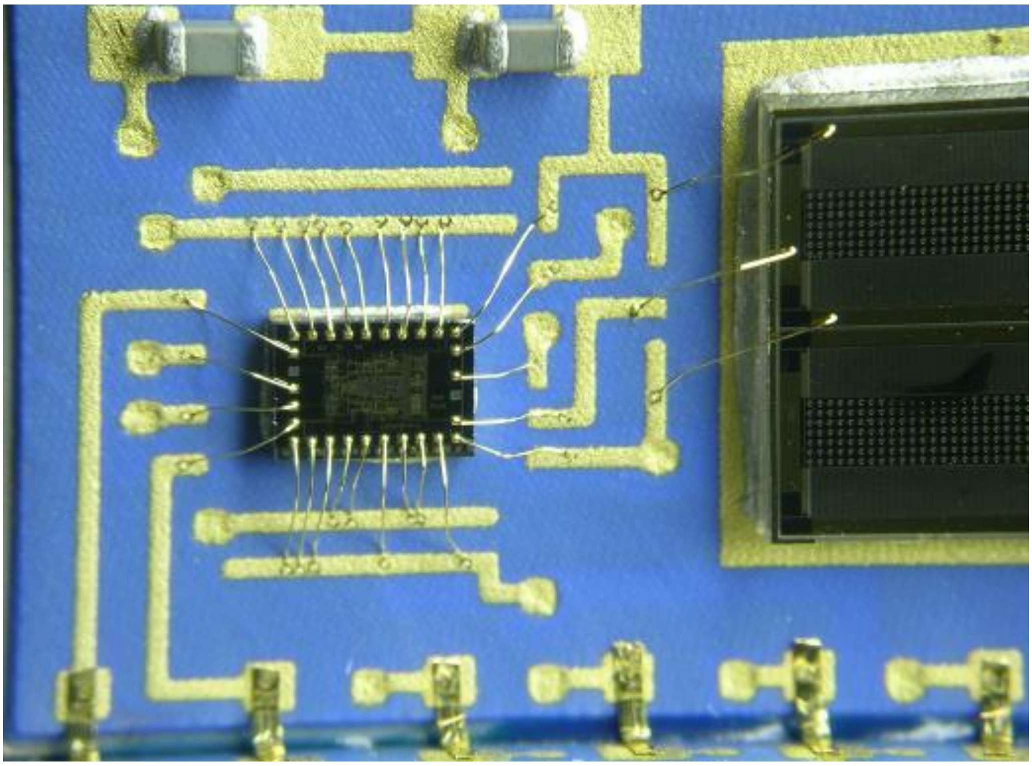

Figure 5.5: Picture of the wire bonded readout circuit and accelerometer pair

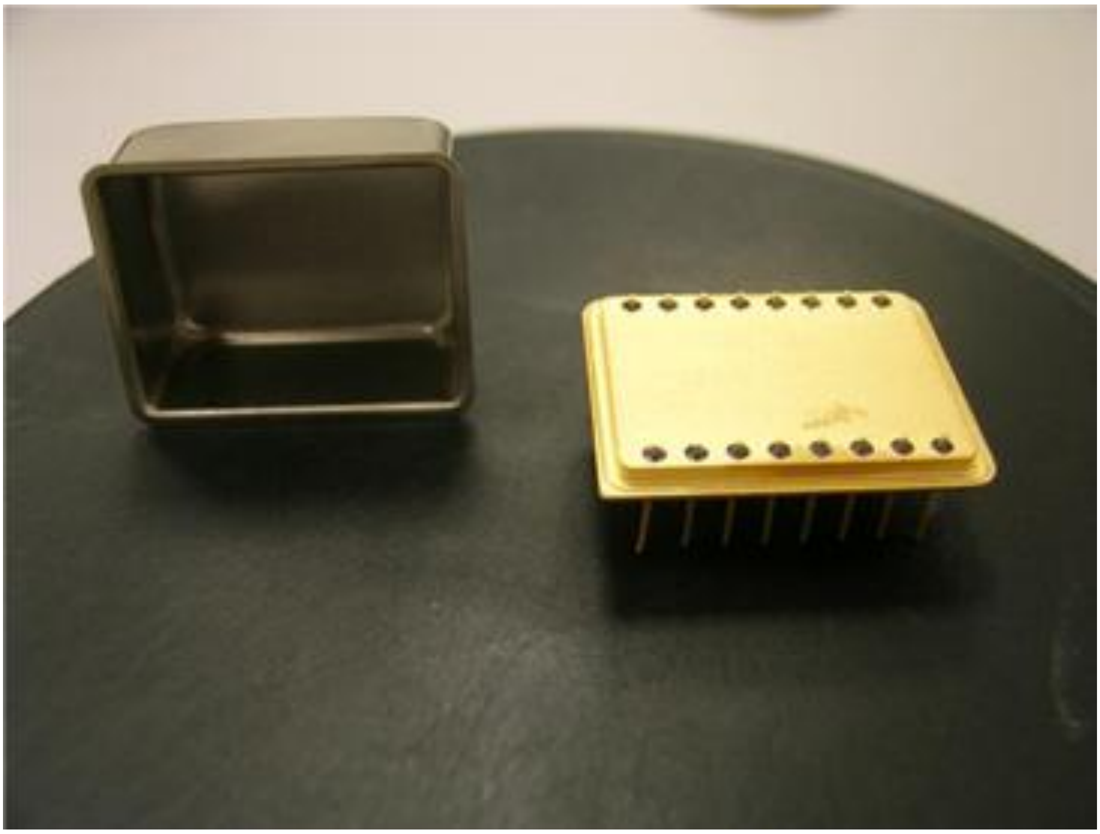

Figure 5.6: 16 pin package where the accelerometer and readout circuit are placed into after wire bonded to each other on alumina substrate.

Table 5.1: Distribution and function of each pin on 16-pin accelerometer package

PIN #	PIN Name	PIN Function	PIN #	PIN Name	PIN Function
1	Aoutx_p	Analog Pos. Output x-axis	9	Aoutz_p	Analog Pos. Output z-axis
2	Aoutx_n	Analog Neg. Output x-axis	10	Aoutz_n	Analog Neg. Output z-axis
3	GND	Ground	11	VSS	2.5V reference voltage
4	Aouty_p	Analog Pos. Output y-axis	12	VDD	5V supply voltage
5	Aouty_n	Analog Neg. Output y-axis	13	Doutx	Digital Stream Out x-axis
6	Toutx	Temperature Out x-axis	14	Clock	Clock Input
7	Touty	Temperature Out y-axis	15	Douty	Digital Stream Out y-axis
8	Toutz	Temperature Out z-axis	16	Doutz	Digital Stream Out z-axis

5.1.2.1 Allan-Variance Noise and Bias Drift Measurement Technique

Allan-variance method is used to extract the noise and bias drift values of an inertial measurement sensor. In this method accelerometer is placed on a rigid plane and the output voltage of the system is collected for more than 2 hours. With less data, Allan Variance technique can also be used to find noise and bias drift of a sensor but for more accurate results, longer data is better. Figure 5.7 shows the setup used to gather the output of the system at its rest position for noise and bias drift measurement. After the data acquisition is completed, it is processed and Allen-variance graph is plotted. From this graph bias drift and noise of the accelerometer can be found. Figure 5.8 shows a sample plot of Allan variance analysis graph.

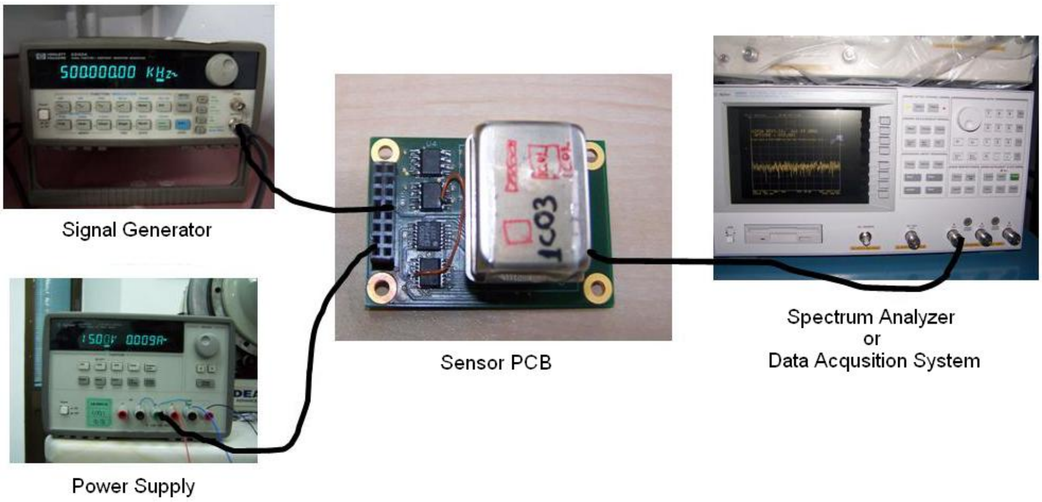

Figure 5.7: Setup used to gather the output of the system at its rest position for noise and bias drift measurement

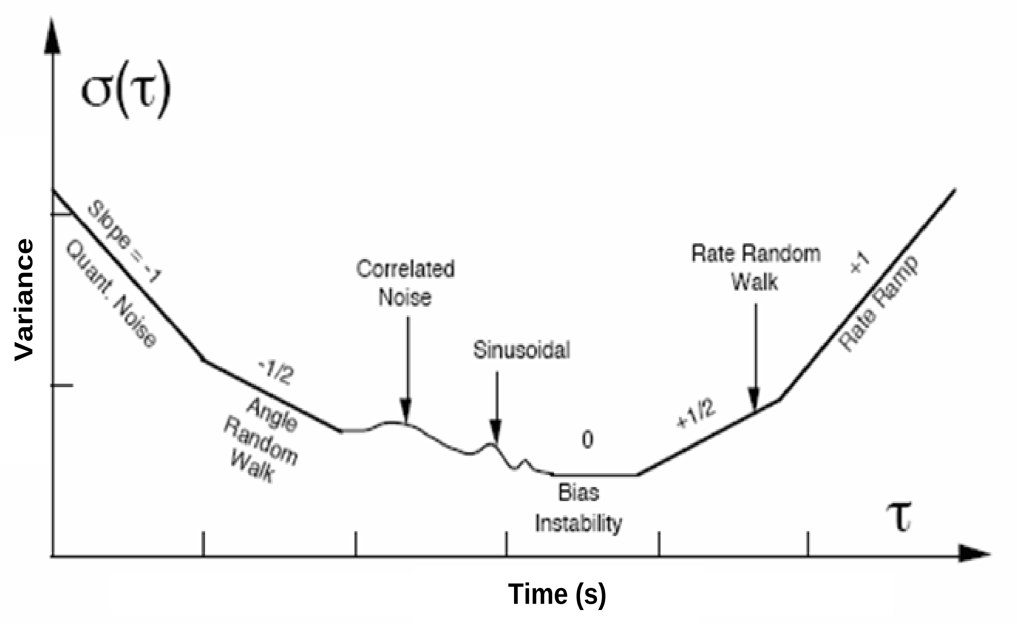

Figure 5.8: A sample plot of Allen-variance analysis graph.

In order to draw Allan variance graph, collected data should be processed properly. For sampling rate of f_S and sampling time of T, a total of N data is collected where

$$N = T \times f_s \times 3600 \tag{5.1}$$

Using these N samples standard deviations are calculated by decreasing the sampling frequency at each step. For example, if the output of the system is sampled at 1 kHz frequency for 2 hours, a total of N= 7,200,000 samples would be acquired. These samples are grouped as shown in the Figure 5.9 where numbers of consecutive data's are doubled at each step of the grouping and average of each level is calculated. After finding averages at each step, equation 5.2 is used to calculate the variance of each sampling frequency:

$$\sigma(\tau)^2 = \frac{1}{2(\frac{N}{f_s \times \tau} - 1)} \sum_{k=1}^{\frac{N}{f_s \times \tau}} (a_{k+1} - a_k)^2 \tag{5.2}$$

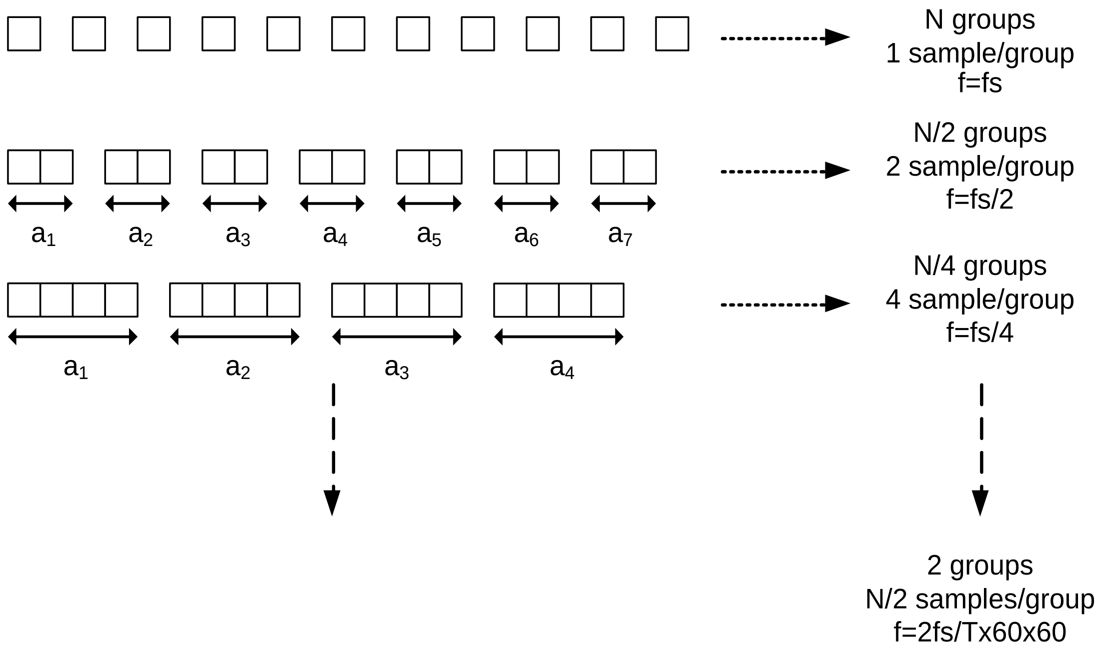

Figure 5.9: Data groups generated during the calculation of Allen-Variance method.

By drawing τ vs. σ graph using the formula given in equation 5.2 Allen variance graph can be plotted. There are also commercial programs like Alavar 5.2 a free software program distributed through the internet to plot Allen variance graph of any collected data.

In this graph there are 6 main regions that determine the performance of an accelerometer. Table 5.2 lists the regions in Allan-Variance graph and their meanings. From the graph given in Figure 5.8, one can determine σ and τvalues for any point in any region and by using the equation given for that region the parameter of interest can be calculated easily. Figure 5.10 shows a sample Allan-Variance graph obtained from a 2 hour accelerometer output using Alavar 5.2 software. Bias instability of the sensor can be calculated by dividing the lowest y axis value of this graph to 0.6648 and noise (angle random walk) can be calculated by finding the y-value of the line having -1/2 slope and tangent to curve where x is equal to 1.

In Figure 5.10, bias instability of the tested system can be calculated by dividing the minima of the Allen Variance curve by 0.6648 which is $y_1/0.6648$ and noise equals the y-axis value at which the fitted -1/2 slope crosses the x=1 axis. y_2 is the overall noise density value of this given sample system.

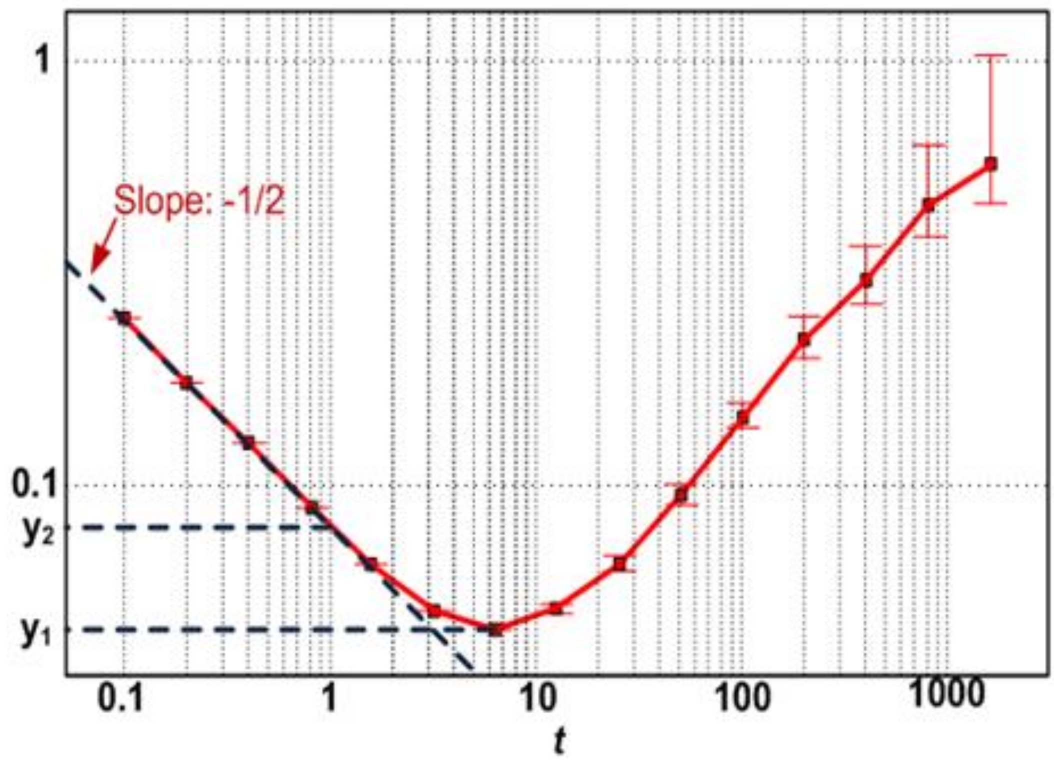

Figure 5.10: Sample Allan-Variance graph obtained from a 2 hour accelerometer output using Alavar 5.2 software

Table 5.2: Regions in Allan variance graph and their meanings.

Region Name	Symbol	Equation	Region Slope
Quantization Noise	Q	$\partial_a = \sqrt{3} \times Q/\tau$	-1
Angle Random Walk	N	$\partial_{WN} = N/\sqrt{\tau}$	-1/2
Sinusoidal	W_0	$\partial_S = (w_0/\pi f_0 \tau) \times sin^2(\pi f_0 \tau)$	sinusoidal
Bias Instability	B	$\partial_B = 0.6648 \times B$	0
Random Walk	K	$\partial_{RW} = K\sqrt{\tau/3}$	1/2
Ramp	R	$\partial_R = R \times \tau/\sqrt{2}$	1

5.1.2.2 Measurement Range Detection

Maximum operation range of the accelerometer is done by mounting the system on a centrifuge table and rotating the table. During this rotation accelerometer measures the centripetal acceleration applied on its sensitive axis. Amount of the applied acceleration can be expressed as follows:

$$a = -w^2 \times r \tag{5.3}$$

where "w" is the angular velocity of the rotating able and r is the distance between the accelerometer and center of rotation. The output of the system is stored on a flash memory card which is embedded on the accelerometer PCB which is then carried to a computer for further processing. Figure 5.11 shows the accelerometer test PCB with flash memory on the same card. Power for both test cards and accelerometer is carried from the slip ring to the test chamber. Measurement range detection tests are performed in the centrifugal test cabin at Tübitak SAGE facilities. Figure 5.12 shows the centrifugal test cabin and the exterior test setup for the measurement range detection tests.

Accelerometer is centered on the centrifugal arm of the rotation table inside the chamber. In order to keep the accelerometer in balance a balancing mass is placed on the symmetric opposite of the centrifugal arm. Figure 5.13 shows the placement of the accelerometer sensor on the centrifugal arm.

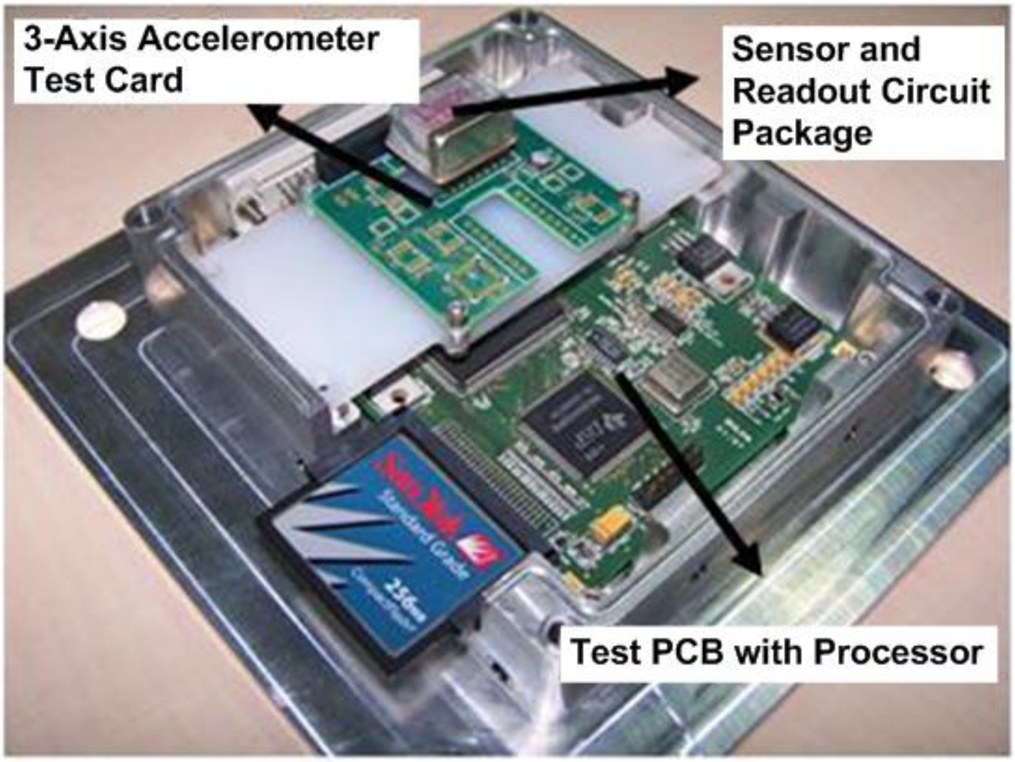

Figure 5.11: Accelerometer test PCB with flash memory on the same card

Figure 5.12: Centrifugal test cabin and the exterior test setup for the measurement range detection tests

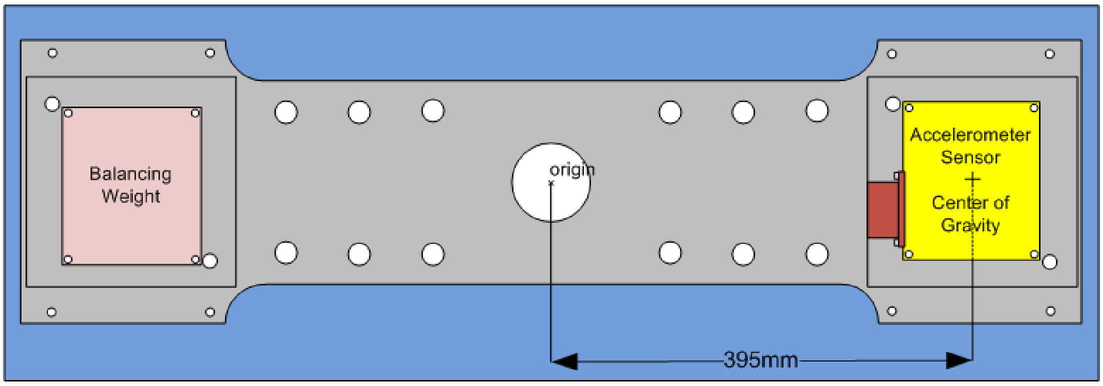

Figure 5.13: Placement of the accelerometer sensor on the centrifugal arm.

After the accelerometer is placed on the centrifuge table, acceleration larger than the expected measurement range of the accelerometer is applied to the sensitive axis of the sensor. For the negative measurement range, accelerometer's sensitive axis is reversed to apply accelerations in the negative axis, since the centripetal acceleration can only be applied in a single direction. For an ideal accelerometer, when input acceleration is increased, output signal follows input up to its maximum measurement range. When the maximum measurement range is reached output of the accelerometer system saturates.

If the non-linearity of the overall measurement range of the accelerometer system is also wanted to be extracted, applied acceleration is increased with fixed step sizes and output data is collected at each step of the input. Extraction of the non-linearity is described in section 5.1.2.3.

5.1.2.3 Non-Linearity Measurement

The accelerometer system described previously is mounted on a rotating table which has 1 degree rotation accuracy. Figure 5.14 shows the rotating table installed at Tübitak SAGE facilities used for the non-linearity, bias and scale factor detection tests. The output of the system is connected to a real time data acquisition card to collect the data from the computer. Rotating table on which the accelerometer system is mounted is rotated by 30 degree steps and 1 minute of data is collected at each step. A total of 12 different test data is collected at different positions until the full cycle completes to 360 degrees. Figure 5.15 shows a sample 12 position test results. Data collected at each position is averaged and input versus output graph of the accelerometer system is plotted. Half of the difference between the maximum and minimum values of this graph equals to the scale factor of the accelerometer. Half of the summation of maximum and minimum values of this graph equals to the bias of the accelerometer. Using the bias and scale factor, data collected during the tests are normalized between ±1g range. Normalized data is plotted against the input acceleration and non-linearity is calculated by fitting a first order line to this plot. Non-linearity is calculated by dividing the maximum difference between each output average and the best fit line by the input acceleration range. Table 5.3 shows sample input acceleration vs. normalized output data collected from an accelerometer system and Figure 5.16 is the input acceleration versus normalized output graph of this data.

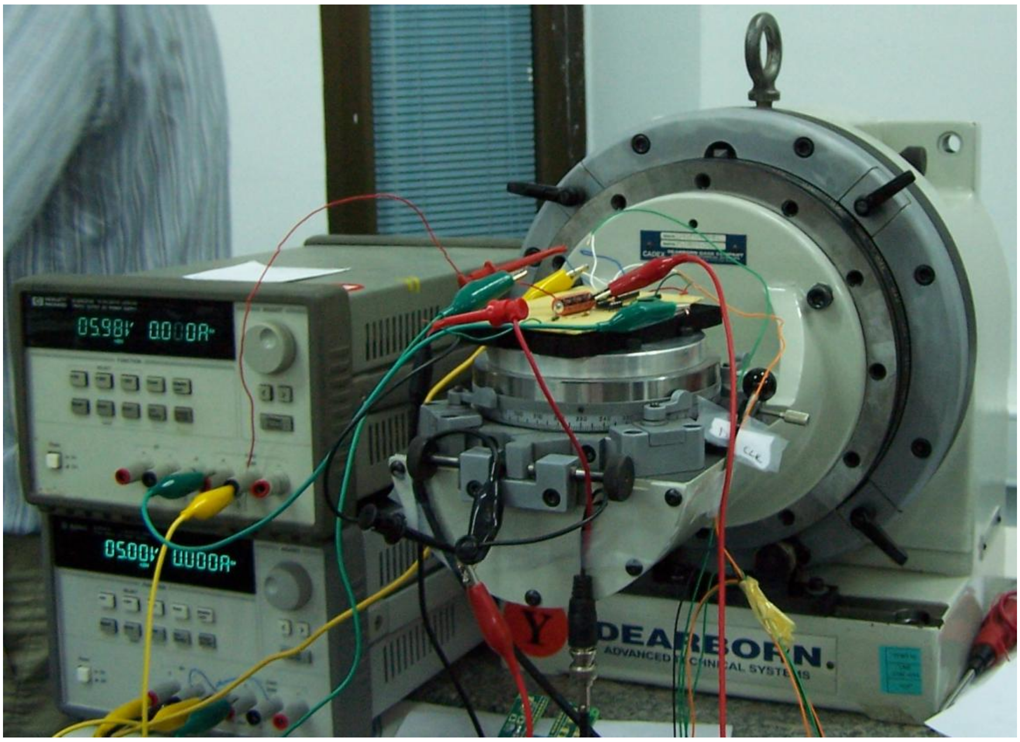

Figure 5.14: Rotating table installed at Tübitak SAGE facilities used for the non-linearity, bias and scale factor detection tests.

Difference between the “normalized output data” and “corresponding data on the best fit line” are divided by range span for each input acceleration and non-linearity of the accelerometer system is the maximum among these values. Non-linearity of the accelerometer system is found as 1.29% for the input-output example given in Table 5.3.

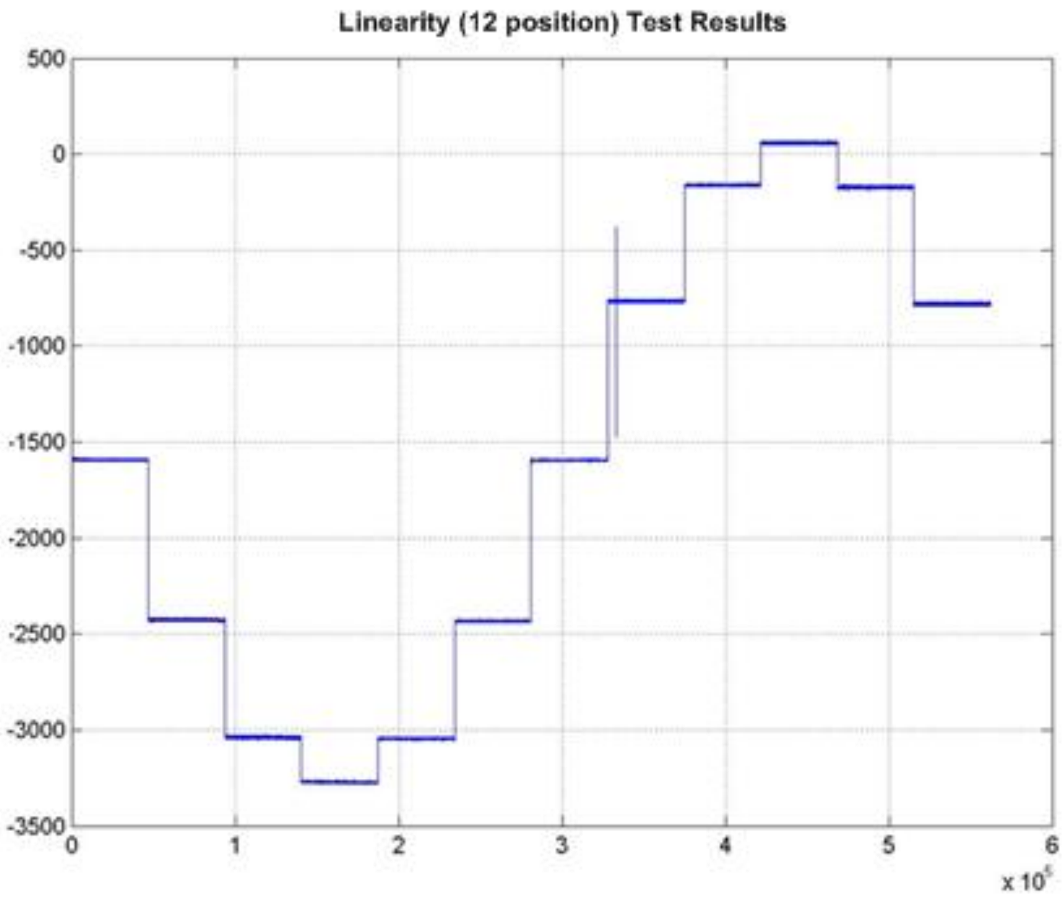

Figure 5.15: Sample 12 position test results.

Table 5.3: Sample input acceleration vs. normalized output data collected from an accelerometer system.

Input Acceleration	Normalized Output Data	Point on the Best Fit Line	Non-Linearity Percentage (%)
-1.00	-1,020	-1,003	0,86
-0,87	-0,850	-0,868	0,90
-0,50	-0,510	-0,501	0,46
0,00	0,010	0,001	0,43
0,50	0,510	0,504	0,32
0,87	0,890	0,871	0,96
1,00	0,980	1,006	1,29

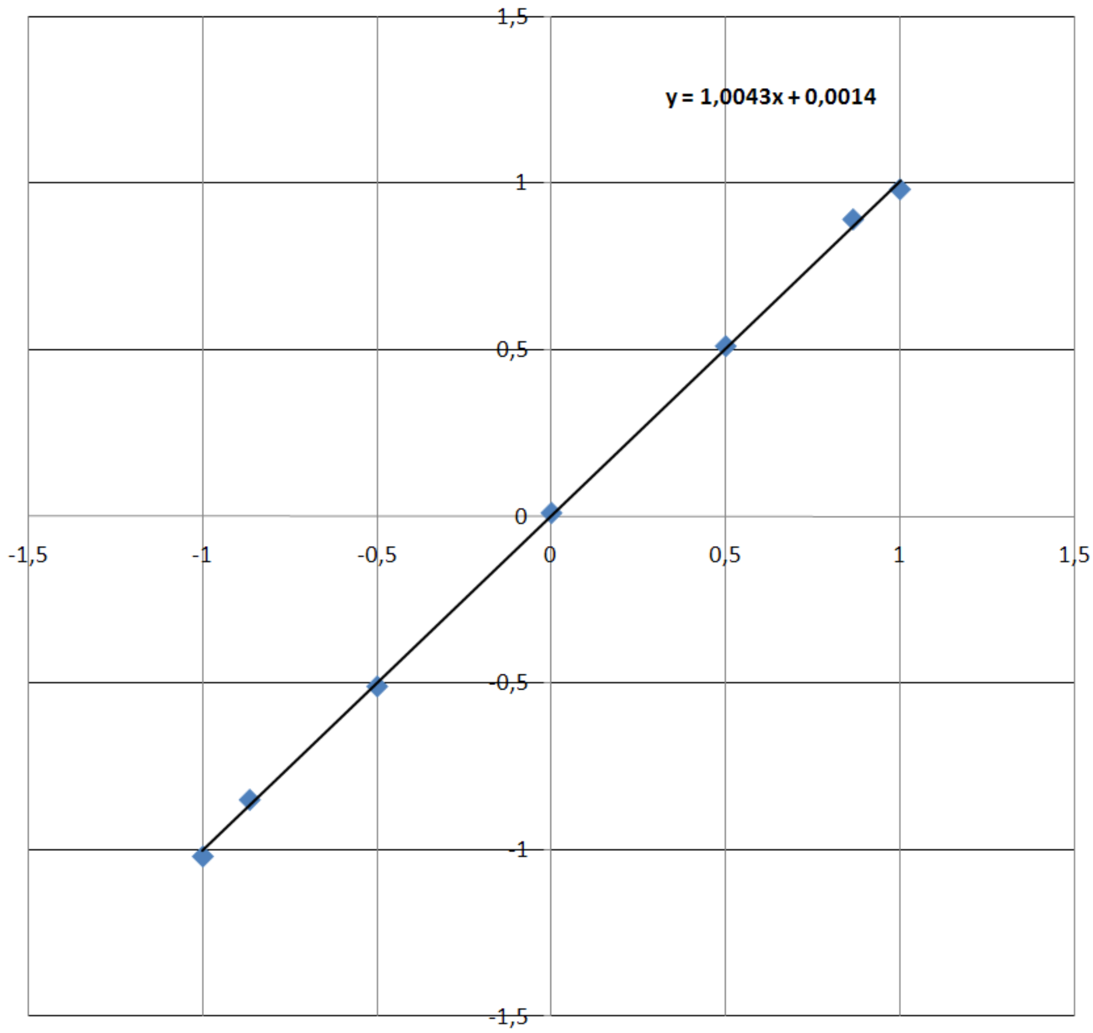

Figure 5.16: Input acceleration versus normalized output graph of the data given in Table 5.3

5.2 Tests Performed on SOG Accelerometers

Many accelerometers fabricated with SOG process had repeatable test results. Since the structural thickness was 100µm and expected finger spacing was 3.5µm, accelerometers could be fabricated reliably. A sample SOG accelerometer is connected to a 2nd order sigma-delta readout circuit and tested at both sensor and system levels.

These test results revealed that the expected measurement range values one-to-one corresponds with the hand calculation results given in the design chapter of this thesis. Since the finger spacing of the accelerometers enlarged to 3.8µm's after fabrication, performances were worse than expectations.

5.2.1 Sensor Level Tests

5.2.1.1 C-V Measurement

Table 5.4 shows the expected and measures rest capacitance values for accelerometer SOG1O02. Figure 5.17 shows the measured C-V curve of left electrode and Figure 5.18 shows the measured C-V curve of right electrode of accelerometer SOG1O02.

Table 5.4: Expected and measured rest capacitance values for accelerometer SOG1O02.

C-V Test of SOG1O02	Expected Value	Measured Value
Left Capacitance	16.1pF< x <17.6pF	16.7pF
Right Capacitance	16.1pF< x <17.6pF	16.3pF

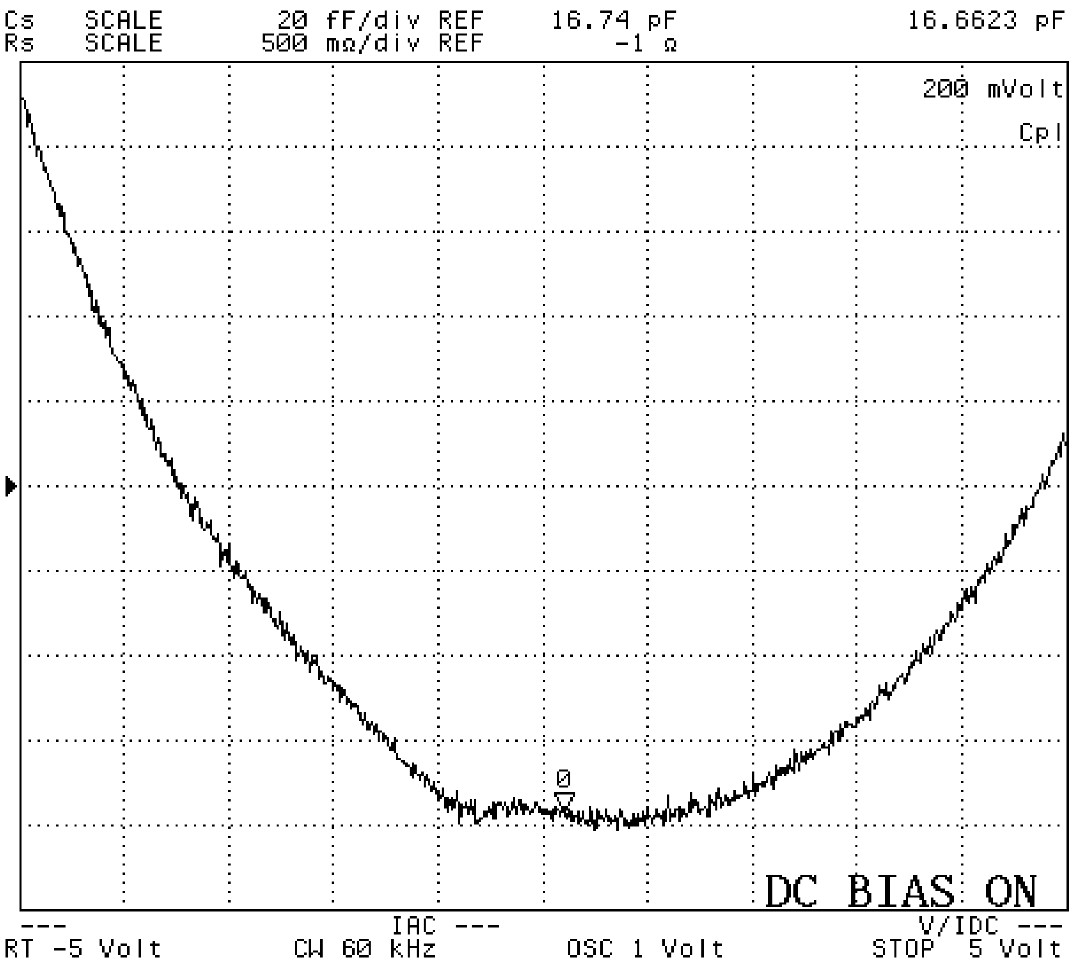

Figure 5.17: Measured C-V curve of left electrode of accelerometer SOG1O02.

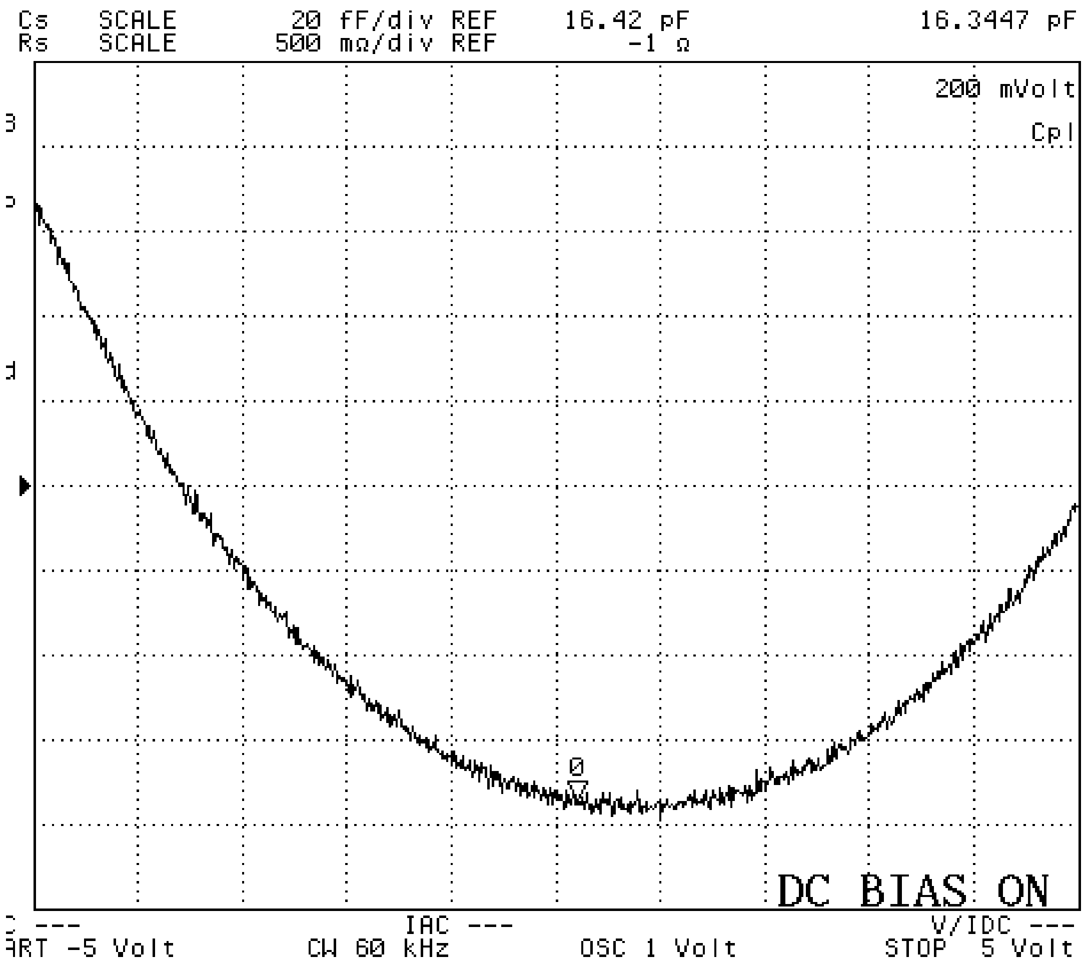

Figure 5.18: Measured C-V curve of right electrode of accelerometer SOG1O02.

5.2.1.2 Sensitivity Measurement

Table 5.5 lists the expected and measured sensitivity values for accelerometer SOG1O02 and Figure 5.19 shows the graphical representation of the 12 position data collected during the sensitivity (C-g) test of accelerometer SOG1O02 for both left and right electrodes.

Table 5.5: Expected and measured sensitivity values for accelerometer SOG1O02

Sensitivity Test of SOG1O02	Expected Value	Measured Value
Left Capacitance	102fF < x < 146fF	127fF
Right Capacitance	102fF < x < 146fF	107fF

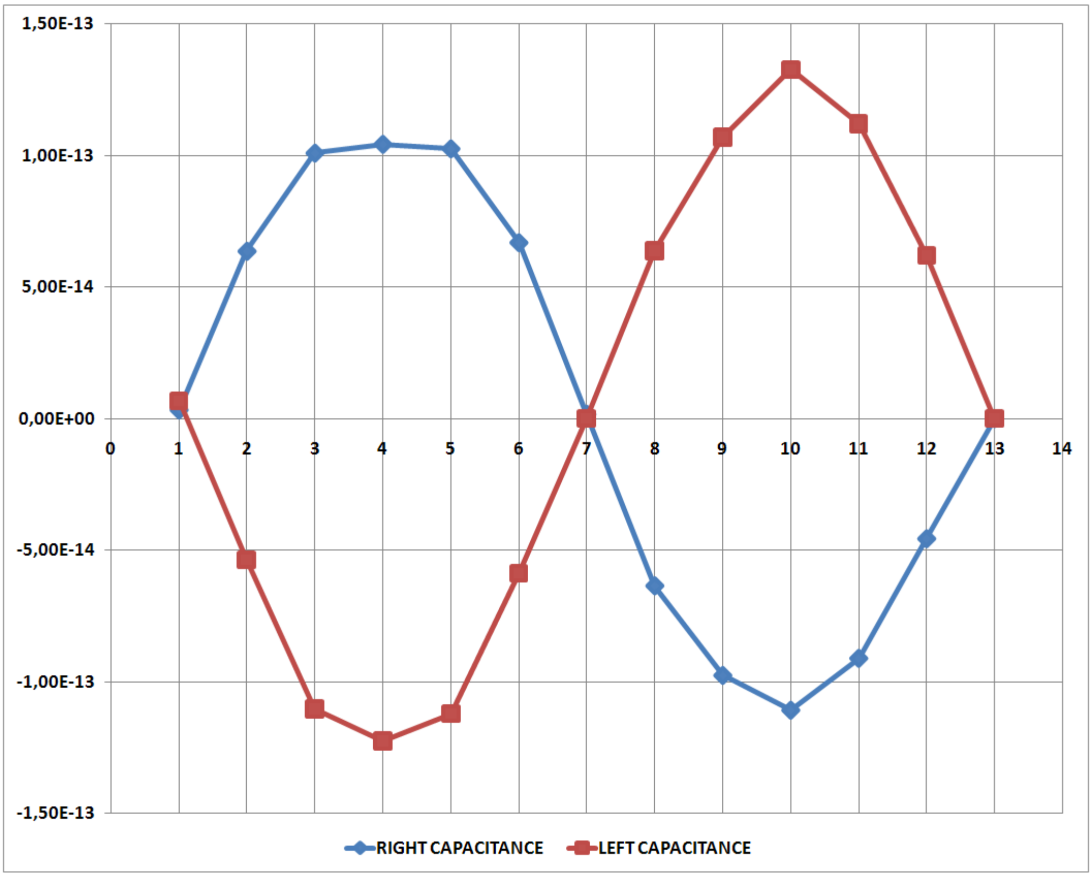

Figure 5.19: Graphical representation of the 12 position data collected during the sensitivity (C-g) test of accelerometer SOG1O02 for both left and right electrodes

5.2.2 System Level Tests

Sensor is wire bonded to a second order sigma-delta readout circuit for system level tests after its sensor performance and capacitive characteristics are extracted.

5.2.2.1 Allan-Variance Noise and Bias Drift Measurement

Table 5.6 lists the noise density and bias drift measurement results of SOG1O02. Figure 5.20 shows the data collected from SOG1O02 for 1 hour at 20Hz sampling frequency and Figure 5.21 shows the drawn Allan-Variance graph using the collected data.

Table 5.6: Noise density and bias drift measurement results of SOG1O02.

Noise Density and Bias Drift Measurement Results			
Noise Density	17µg/√Hz	Bias Drift	29µg

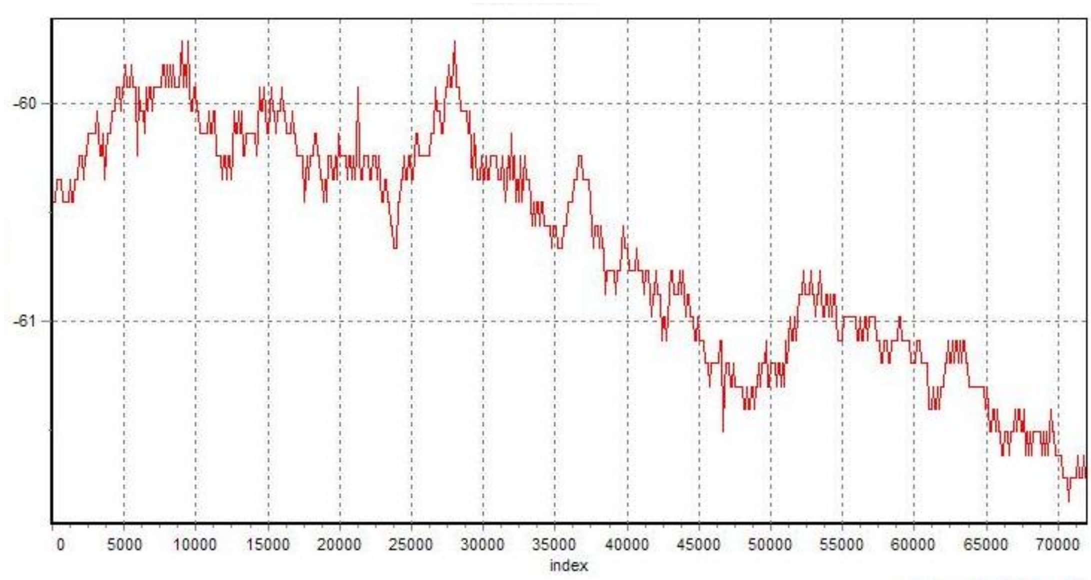

Figure 5.20: Data collected from SOG1O02 for 1 hour at 20Hz sampling frequency.

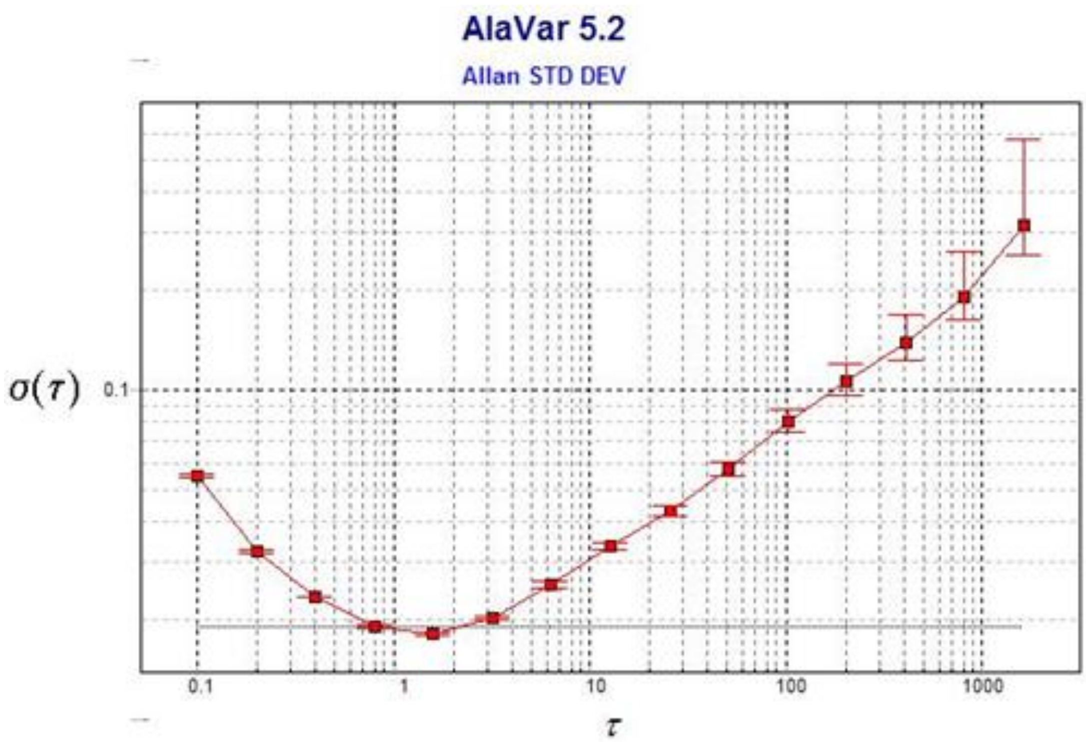

Figure 5.21: Allan-Variance graph drawn using the 1 hour data collected from SOG1O02.

5.2.2.2 Non-Linearity Measurement

Figure 5.22 shows the 12 position test results of accelerometer SOG1O02 and Figure 5.23 shows the averages of the collected data drawn versus the input acceleration in ±1g range and the best fit line. Using the data collected during the 12 position tests and the best fit line, nonlinearity of the system is calculated as %0.90.

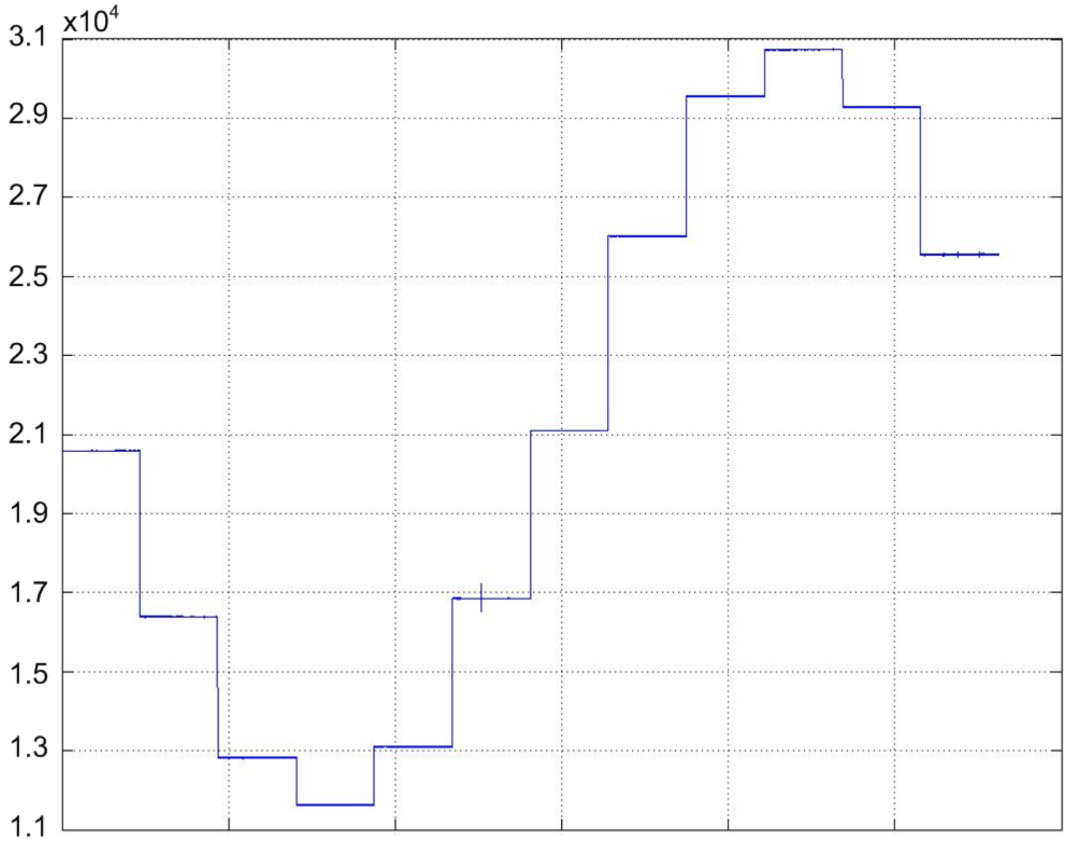

Figure 5.22: 12 position test results of accelerometer SOG1O02

5.2.2.3 Measurement Range Detection

During the tests of this accelerometer, there wasn't a suitable centrifuge system that the accelerometer could be tested for its maximum operation range. But from the 12 position test results of the accelerometer system, maximum operation range estimation can be made using the following equation:

$$Estimate\ Range = \frac{2 \times OffsetBias}{DataAverage@1g - DataAverage@-1g} \tag{5.4}$$

Using this equation and the graph given in Figure 5.23 measurement range of SOG1O02 can be estimated as ±2.22g. Table 5.7 lists the overall performance evaluation of test data for accelerometer SOG1O02.

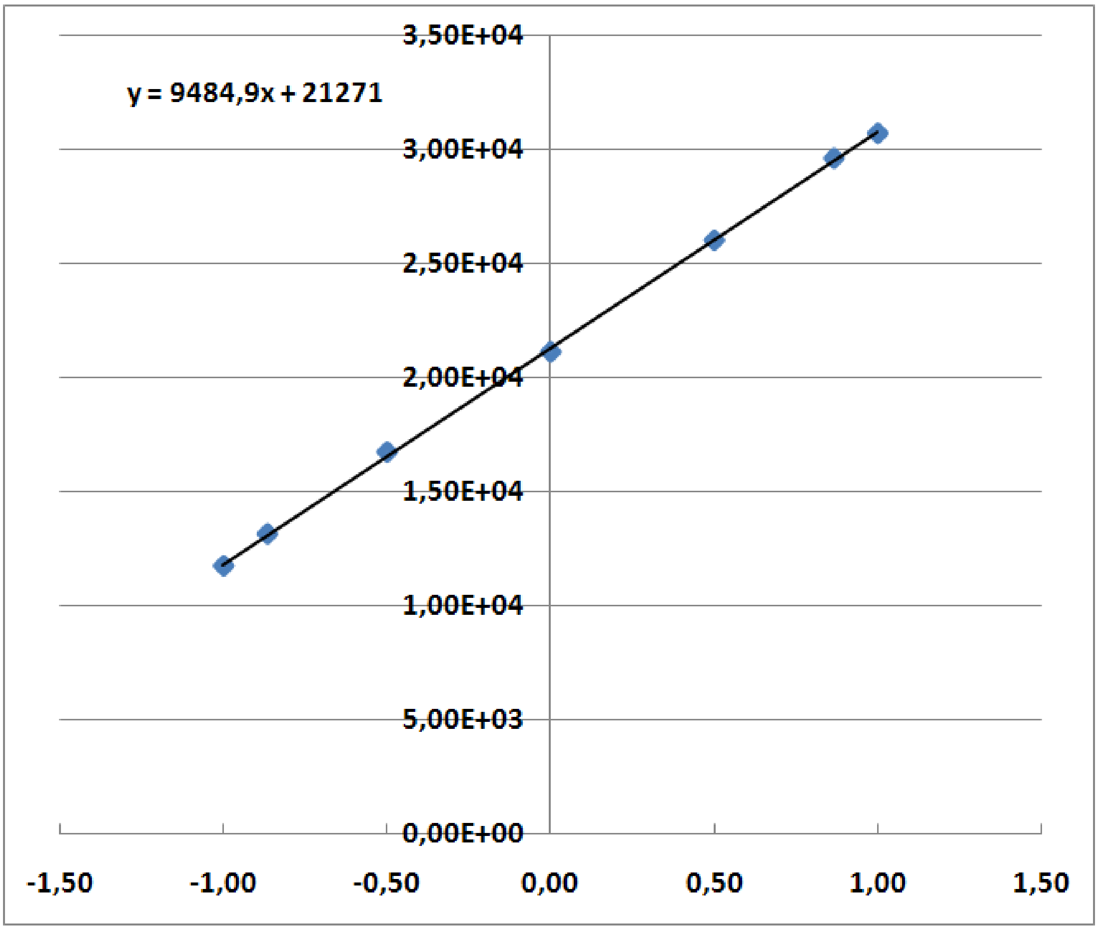

Figure 5.23: Averages of the collected data drawn versus the input acceleration in ±1g range and the best fit line.

Table 5.7: Overall performance evaluation of test data for accelerometer SOG1O02.

Test Results of SOG1O02	Expected	Measured	
		Left	Right
Rest Capacitance	16.1pF< x <17.6pF	16.7pF	16.3pF
Sensitivity	102fF < x < 146fF	127fF	107fF
Noise Density	-	17µg/√Hz	
Bias Drift	-	29µg	
Non-Linearity	-	0.9%	
Measurement Range	±2.15g < x < ±2.66g	±2.22g	

5.3 Tests Performed on DWP Accelerometers

In the first phase of DWP, 4 different accelerometer types were designed and fabricated. Only one of those designs worked properly but with a very low yield. In the second phase of the dissolved wafer process, the working design from the previous phase is improved in order to increase the yield of the fabrication and with this new design 6 different wafer fabrications were made. During these fabrications the mask set was shared with the gyroscopes, therefore number of accelerometers per wafer was too low. In order to increase this number a new mask set is designed by using the optimized accelerometers with shorter fingers. With this full accelerometer mask set 5 more fabrications are made. Among these 11 fabrication trials, 9 sensors could be connected to a readout circuit and tested at both sensor and system levels. In this section, graphical test results for accelerometer DWPx5J06 is given and test results of the other sensors are presented in table form.

5.3.1 Sensor Level Tests

5.3.1.1 C-V Measurement

During this study, DWPx5J06 and various other sensors are measured and the ones with symmetrical capacitive characteristics qualified for the next stage. Figure 5.24 shows the C-V measurement curves of DWPx5J06 for left and right capacitances and Table 5.8 lists the C-V measurement results of fabricated DWP accelerometers.

Table 5.8: C-V measurement results of fabricated DWP accelerometers.

Sensor ID	Expected Rest Capacitance	Left Capacitance	Right Capacitance
DWP4F03	9.47pF	7.8pF	8.0pF
DWP4I10	9.47pF	9.9pF	9.1pF
DWP6C03	9.47pF	11.2pF	9.8pF
DWPx5G01	9.47pF	10.3pF	10.8pF
DWPx5G13	9.47pF	9.2pF	9.5pF
DWPx5K06	9.47pF	9.0pF	8.9pF
DWPx5J06	9.47pF	9.2pF	9.2pF
DWPx5I08	9.47pF	8.5pF	8.8pF
DWPx5O06	9.47pF	8.9pF	8.9pF

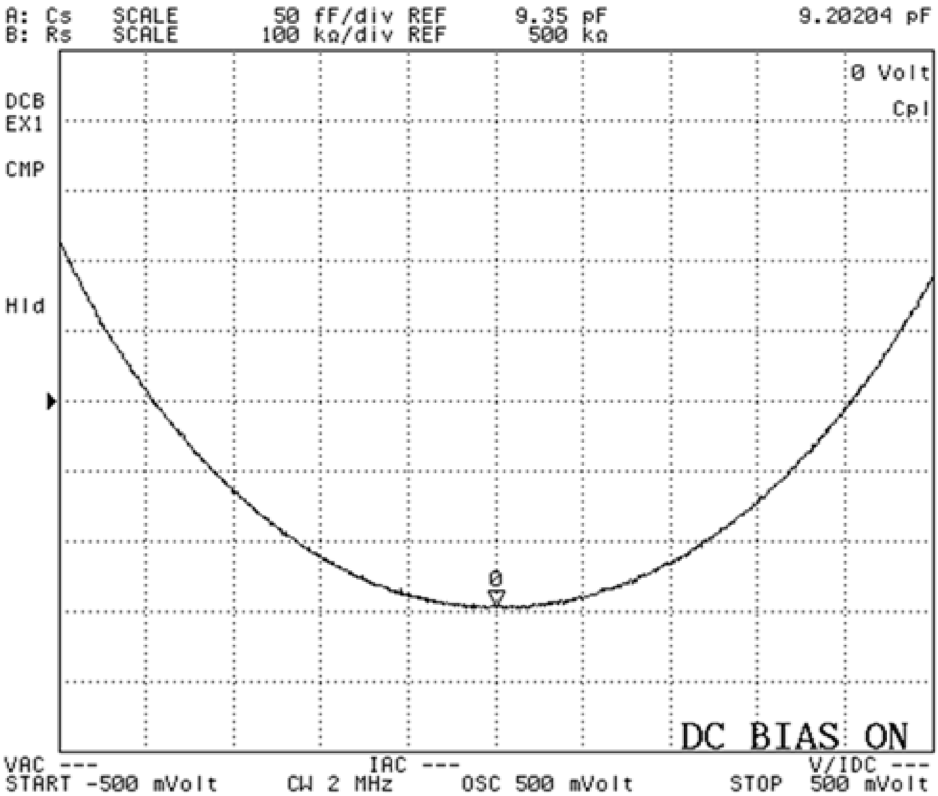

(a)

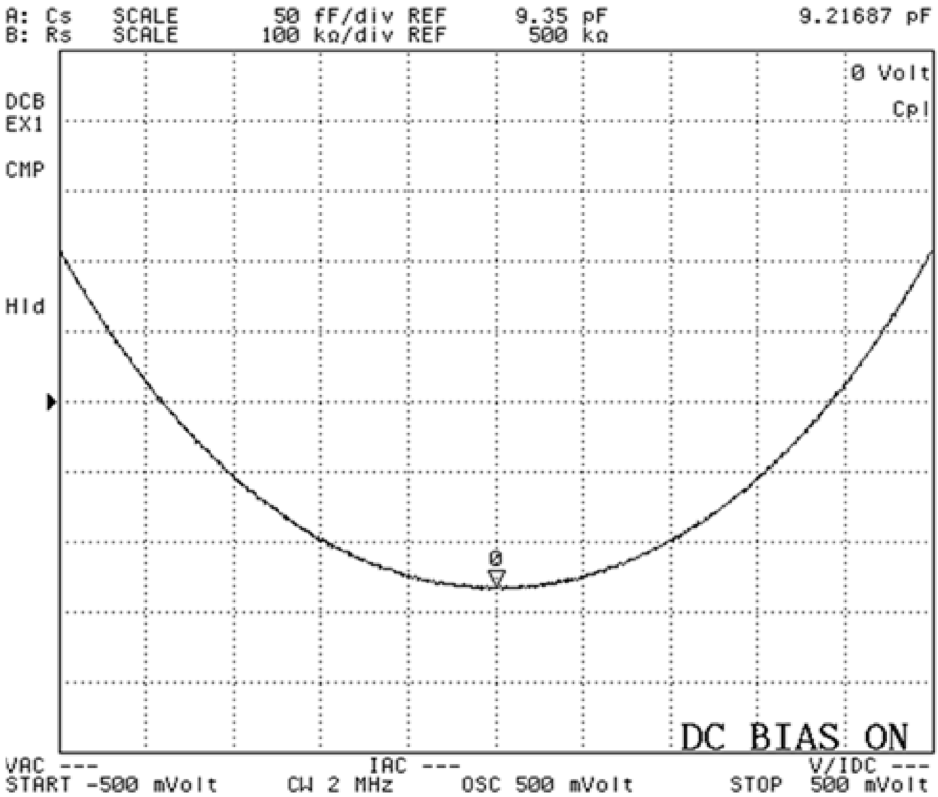

(b)

Figure 5.24: C-V measurement curves of DWPx5J06 for left and right capacitances. (a) Left Capacitance (b) Right Capacitance

5.3.1.2 Sensitivity Measurement

Figure 5.25 shows graphical representation of the 12 position data collected during the sensitivity (C-g) test of accelerometer DWPx5J06 for both left and right electrodes and Table 5.9 lists the C-g measurement results of fabricated DWP accelerometers.

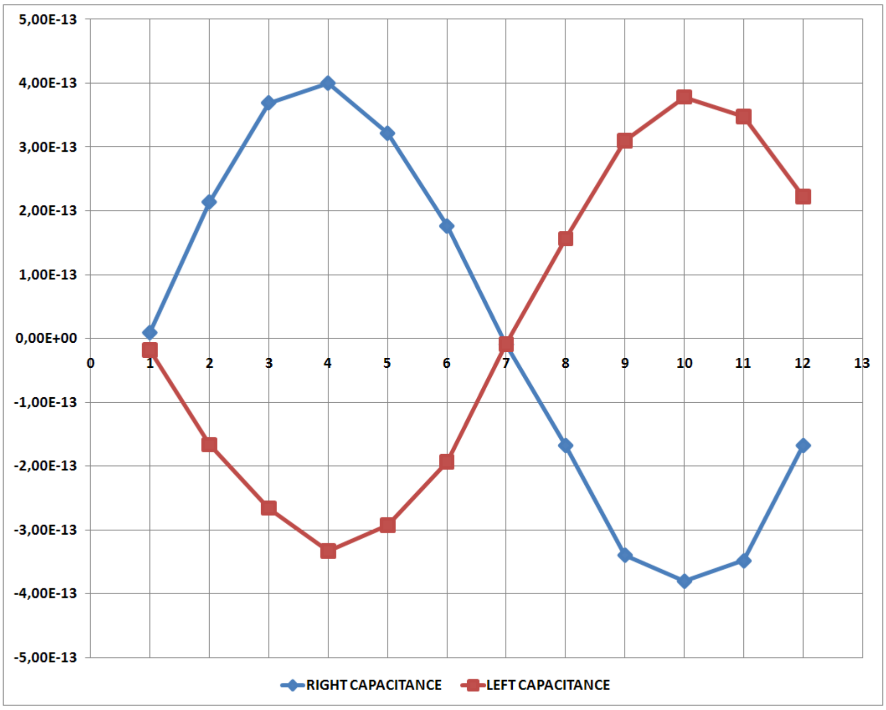

Figure 5.25: Graphical representation of the 12 position data collected during the sensitivity (C-g) test of accelerometer DWPx5J06 for both left and right electrodes

Table 5.9: C-g measurement results of fabricated DWP accelerometers.

Sensor ID	Expected Sensitivity / g	Left Sensitivity /g	Right Sensitivity / g
DWP4F03	446fF/g > x > 268fF/g	323fF/g	385fF/g
DWP4I10	446fF/g > x > 268fF/g	372fF/g	375fF/g
DWP6C03	446fF/g > x > 268fF/g	420fF/g	310fF/g
DWPx5G01	348fF/g > x > 210fF/g	320fF/g	265fF/g
DWPx5G13	348fF/g > x > 210fF/g	305fF/g	296fF/g
DWPx5K06	446fF/g > x > 268fF/g	285fF/g	298fF/g
DWPx5J06	446fF/g > x > 268fF/g	356fF/g	390fF/g
DWPx5I08	446fF/g > x > 268fF/g	305fF/g	312fF/g
DWPx5O06	446fF/g > x > 268fF/g	395fF/g	362fF/g

5.3.2 System Level Tests

5.3.2.1 Allan-Variance Noise and Bias Drift Measurement

Figure 5.26 shows the 1 hour data collected from DWPx5J06 at 500kHz and the Allan-Variance graph drawn using this data. Table 5.10 lists the measured noise density and bias drift values for DWP accelerometers.

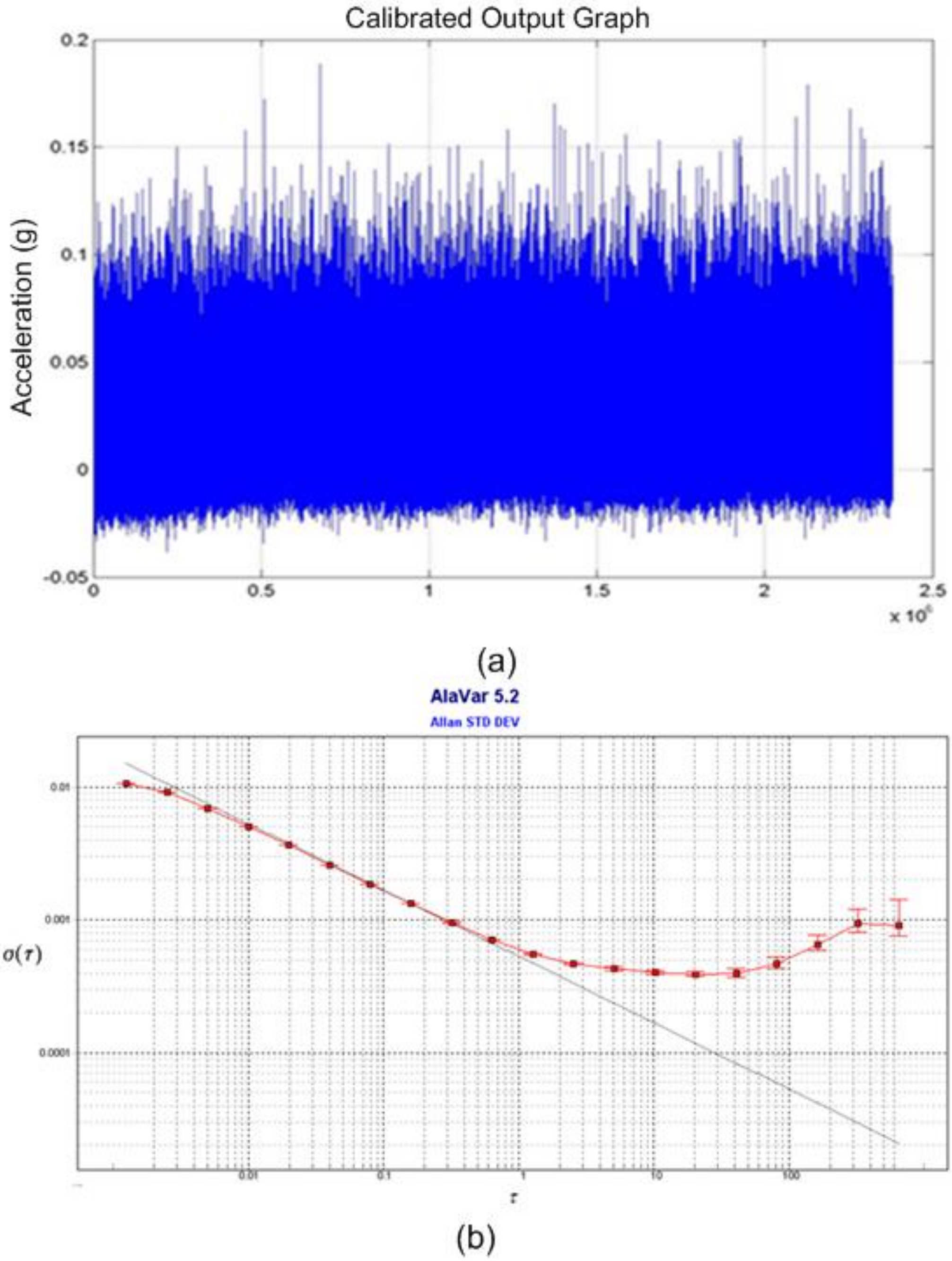

Figure 5.26: (a) 1 hour data collected from DWPx5J06 at 500kHz (b) Allan-Variance graph drawn for DWPx5J06

Table 5.10: Measured noise density and bias drift values for DWP accelerometers

Sensor ID	Measured Bias Drift	Measured Noise Density
DWP4F03	812 µg	353 µg/√Hz
DWP4I10	NA µg	NA µg/√Hz
DWP6C03	406 µg	342 µg/√Hz
DWPx5G01	NA µg	NA µg/√Hz
DWPx5G13	NA µg	NA µg/√Hz
DWPx5K06	588 µg	532 µg/√Hz
DWPx5J06	50 µg	153 µg/√Hz
DWPx5I08	449 µg	279 µg/√Hz
DWPx5O06	714 µg	880 µg/√Hz

Some of the entries in Table 5.10 indicate that bias drift and noise density could not be measured for those sensors. Reason of this is the distorted characteristics collected from the output of the sensors. Figure 5.27 and Figure 5.28 shows the 1 hour long distorted output graphs of DWPx5G01 and DWPx5G13 respectively.

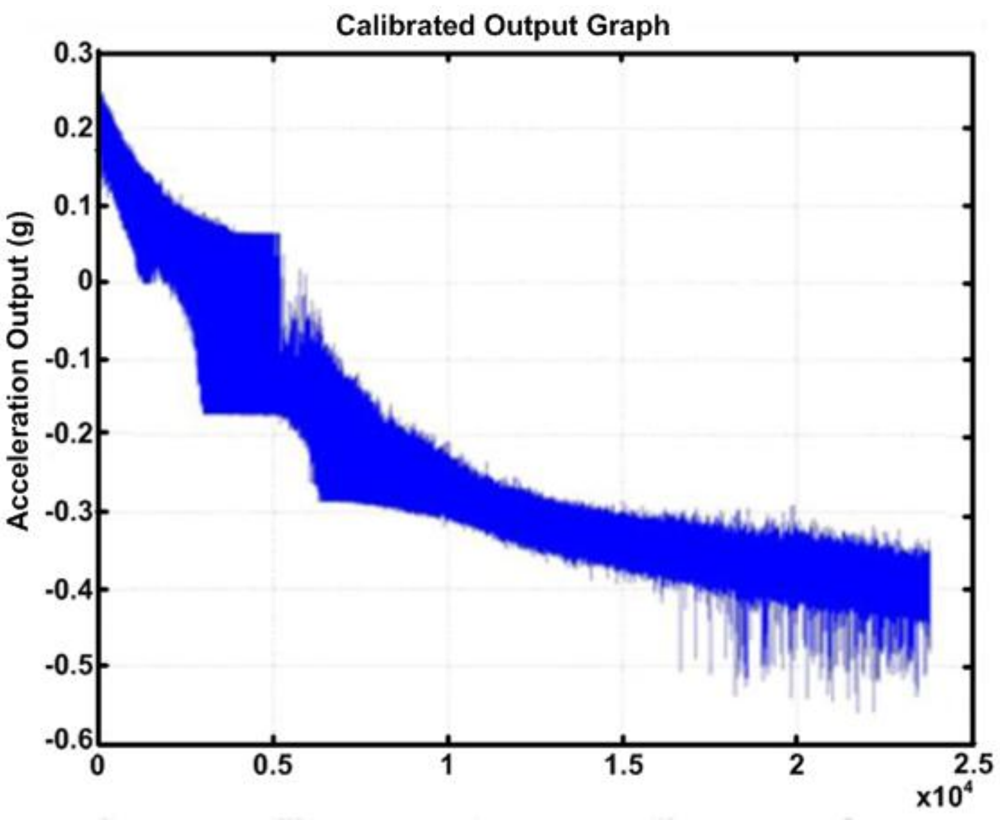

Figure 5.27: 1 hour long distorted drift data of accelerometer DWPx5G01.

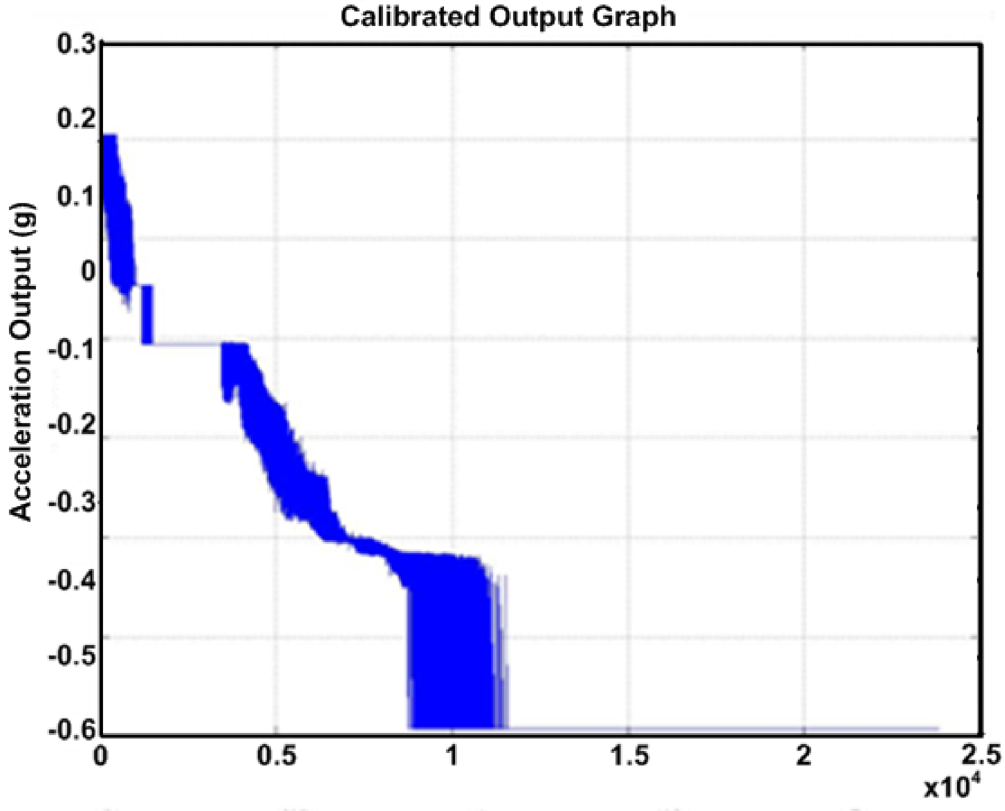

Figure 5.28: 1 hour long distorted drift data of accelerometer DWPx5G13.

5.3.2.2 Non-Linearity Measurement

Figure 5.29 shows the DWPx5J06 output in ±20g range with 2g steps and Figure 5.30 shows linearity graph of DWPx5J06 in ±20g range. Table 5.11 lists all the measured non-linearity values for tested DWP accelerometers. Non-linearity of DWPx5G13 could not be calculated properly, because of the distorted 12 position characteristics of the sensor. Figure 5.31 shows the data collected during the 12 position tests of accelerometer DWPx5G13.

Table 5.11: All measured non-linearity values for tested DWP accelerometers.

Sensor ID	Calculated Non-Linearity (%)	Sensor ID	Calculated Non-Linearity (%)
DWP4F03	1.10 %	DWPx5K06	1.11 %
DWP4I10	2.62 %	DWPx5J06	0.38 %
DWP6C03	0.25 %	DWPx5I08	0.38 %
DWPx5G01	1.03 %	DWPx5O06	0.34 %
DWPx5G13	NA		

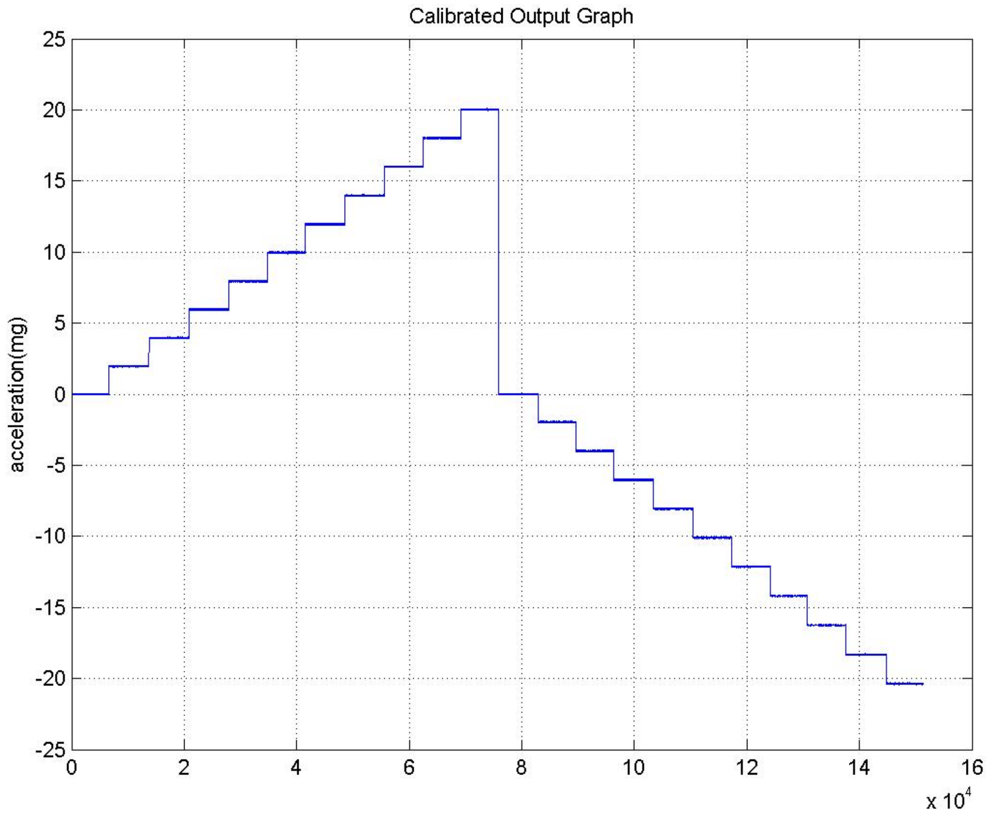

Figure 5.29: DWPx5J06 output in ±20g range with 2g steps.

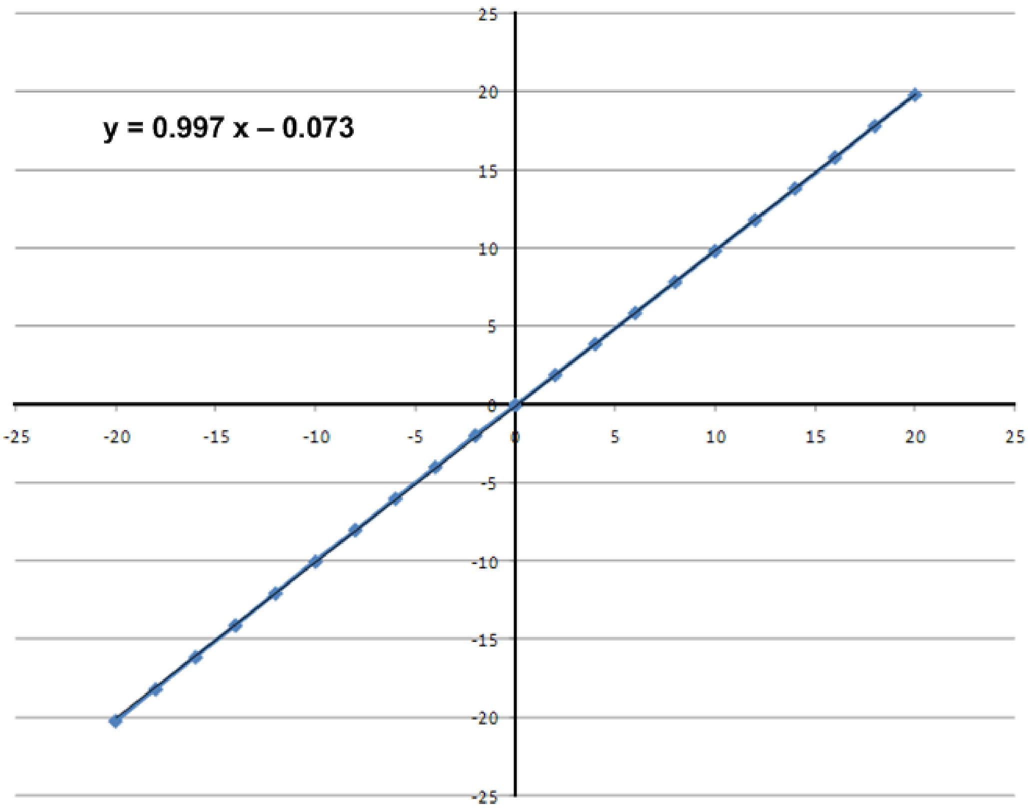

Figure 5.30: Linearity graph of DWPx5J06 in ±20g range.

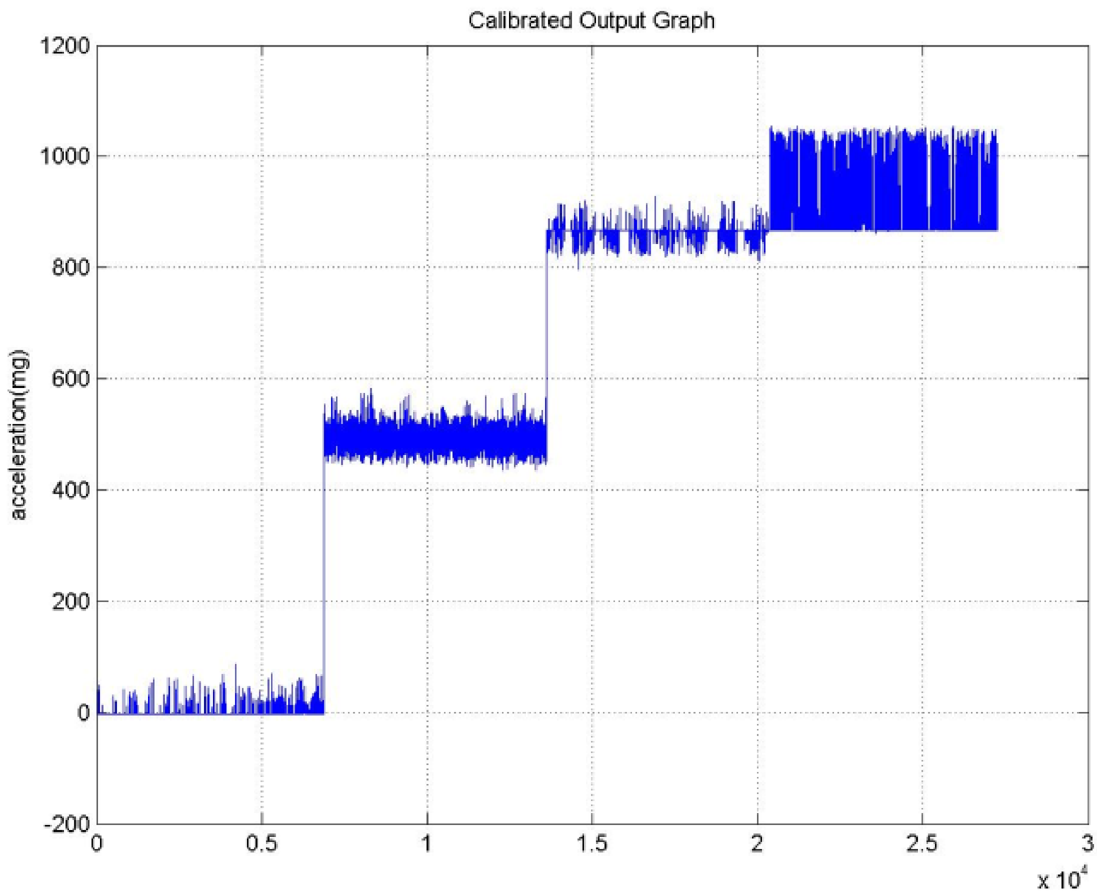

Figure 5.31: Data collected during the 12 position tests of accelerometer DWPx5G13

5.3.2.3 Measurement Range Detection

Figure 5.32 shows the measurement range test result of accelerometer DWPx5J06 and Table 5.12 shows all the measured operation range values for tested DWP accelerometers. The measurement range tests of the earlier accelerometers could not be performed due to the lack of the necessary centrifuge table.

Table 5.12: All measured operation range values for tested DWP accelerometers.

Sensor ID	Measurement Range (g)	Sensor ID	Measurement Range (g)
DWP4F03	NA	DWPx5K06	32
DWP4I10	NA	DWPx5J06	33.5
DWP6C03	NA	DWPx5I08	28
DWPx5G01	NA	DWPx5O06	33
DWPx5G13	35		

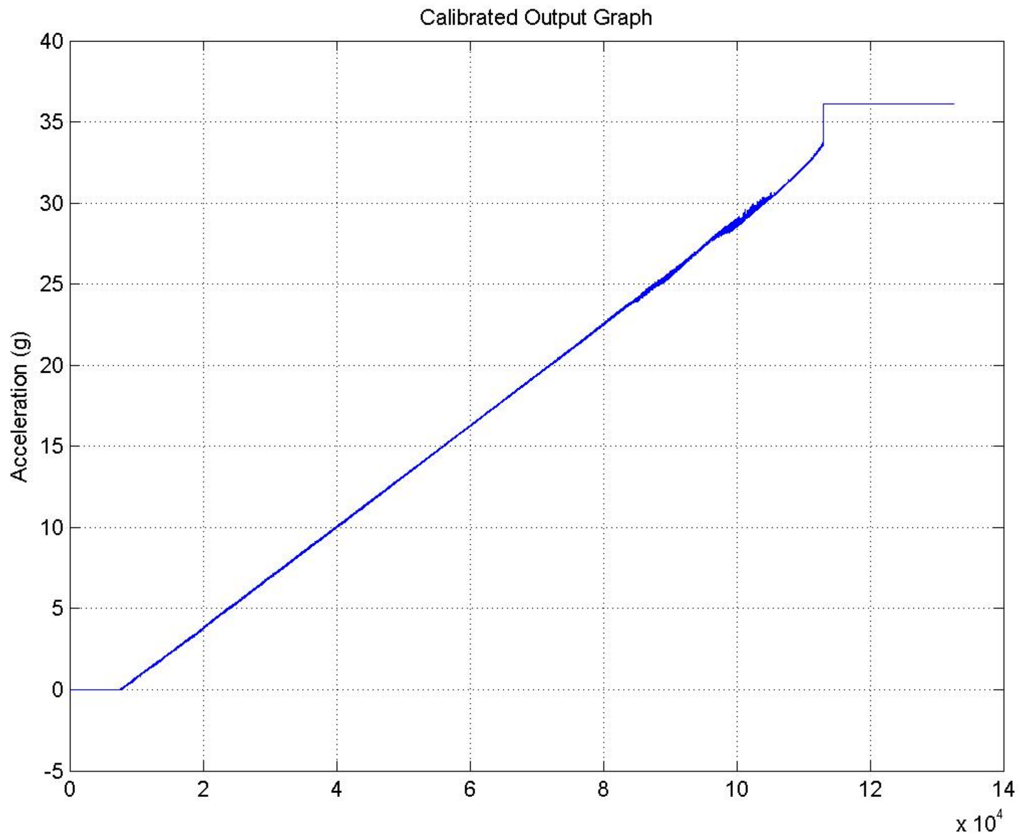

Figure 5.32: Measurement range test result of accelerometer DWPx5J06.

Table 5.13 lists test results of all DWP accelerometers tested in the scope of this study. Although 11 dissolved wafer process runs are conducted, very low number of accelerometers could be tested at system level. The reason for this low yield is the buckling of the accelerometers as described previously in section 4.2 of this thesis. Because of the buckling, accelerometer proof masses can behave strangely during the operation and spikes at the output of the accelerometer like given in Figure 5.27, Figure 5.28, and Figure 5.31 can be observed.

Table 5.13: Test results of all DWP accelerometers tested in the scope of this study

	4F03	4I10	6C03	5G01	5G13	5K06	5J06	5I08	5O06
Left Cap.(pF)	7.8	9.9	11.2	10.3	9.2	9.0	9.2	8.5	8.9
Right Cap. (pF)	8.0	9.1	9.8	10.8	9.5	8.9	9.2	8.8	8.9
Bias Drift (µg)	812	NA	406	NA	NA	588	50	449	714
Noise (µg/√Hz)	353	NA	342	NA	NA	532	153	279	880
Range (g)	NA	NA	NA	NA	35	32	33.5	28	33
Non-Linear. (%)	1.10	2.60	0.25	1.03	NA	1.11	0.38	0.38	0.34

5.4 Tests Performed on DEWP Accelerometers

As stated in section 4.3 of this thesis dissolved epitaxial wafer process replaced dissolved wafer process in order to eliminate the buckling problem which was distorting the performance of tested accelerometers. Structural thickness of the accelerometers were increased therefore an increase in the reliability of the fabricated accelerometers were expected. Unfortunately these expectations did not reflect themselves to the test results. Among 9 DEWP fabrication trials with sensors having 1μm finger spacing, very few accelerometers could be fabricated. The yield of the fabrication was in the range of 2-3%.

5.4.1 System Level Tests

In this section of the thesis test results of 4 different DEWP accelerometers, DEWP#E_I08, DEWP#H_B06, DEWP#H_F01, and DEWP#K_J08 are presented at system level.

5.4.1.1 Allan-Variance Noise and Bias Drift Measurement

Among the four tested accelerometers DEWP#K_J08 has acceptable bias drift performances. The reason of high bias drift of other three accelerometers is the temperature dependency of the readout circuit used during the tests of these sensors. For DEWP#K_J08 a readout circuit specifically designed to be temperature independent is used and the overshoot characteristic during the start-up of the circuit is decreased considerably. Figure 5.33 shows the Allan-Variance graphs of DEWP#B_B06 and DEWP#K_J08. Table 5.14 lists the noise density and bias drift results of all tested DEWP accelerometers

Table 5.14: Noise density and bias drift test results of DEWP accelerometers.

Sensor ID	Bias Drift	Noise Density
DEWP#E_I08	700μg	160μg/√Hz
DEWP#H_B06	720μg	973μg/√Hz
DEWP#H_F01	910μg	210μg/√Hz
DEWP#K_J08	112μg	255μg/√Hz

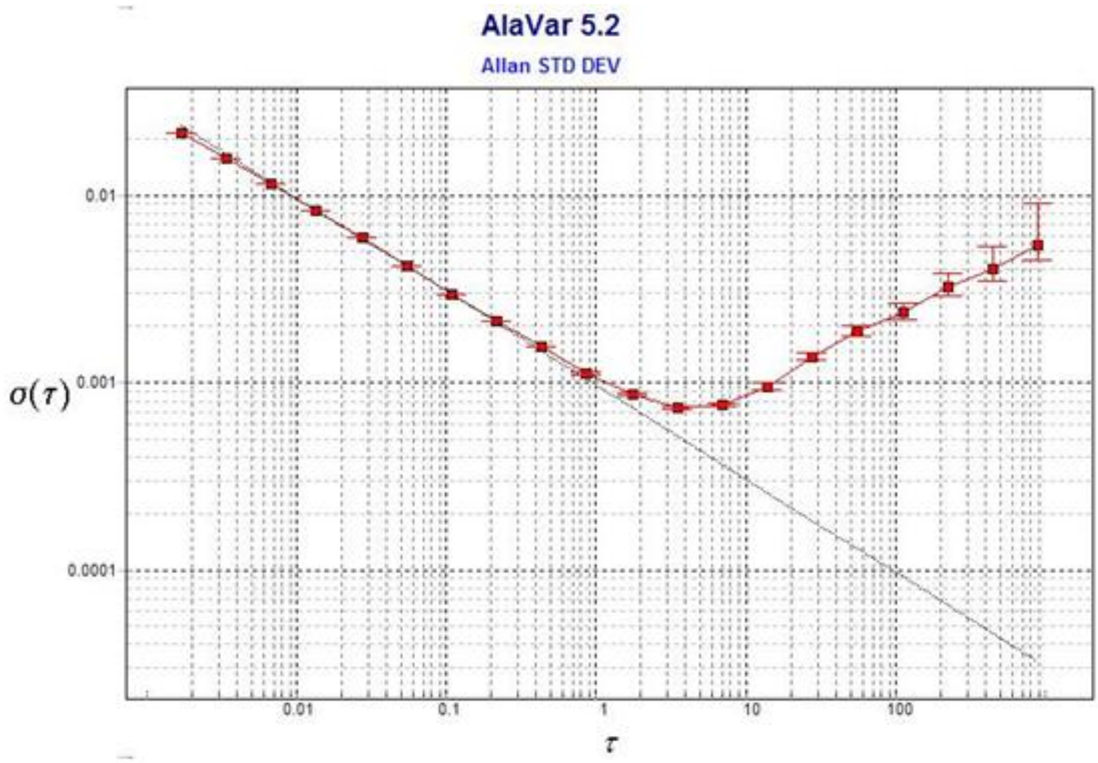

(a)

(b)

Figure 5.33: (a) Allan-Variance graph of DEWP#H_B06 (b) Allan-Variance graph of DEWP#K_J08.

5.4.1.2 Non-Linearity Measurement

Figure 5.34 shows 12 position test result of DEWP#H_B06. When the procedure is applied and the non-linearity of this accelerometer is calculated it is found as 0.34%. Table 5.15 lists calculated non-linearity results for all DEWP accelerometers. Figure 5.35 presents the input output characteristics of DEWP#K_J08 and DEWP#H_B06 with in ±1g range.

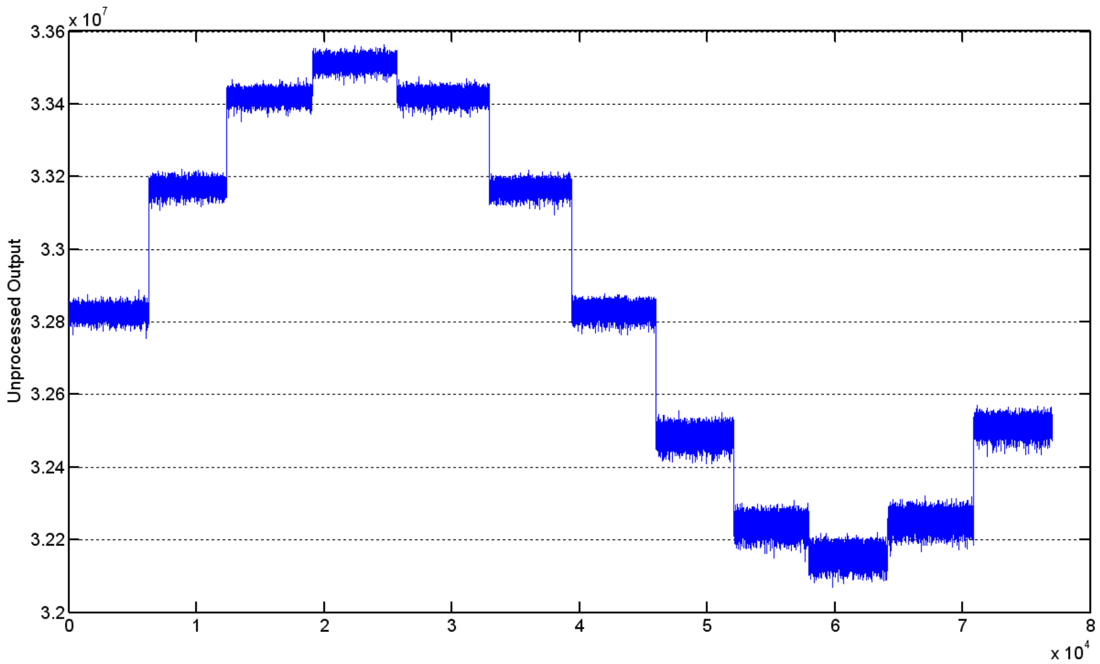

Figure 5.34: 12 position test result of DEWP#H_B06.

Table 5.15: Calculated non-linearity results for all DEWP accelerometers

Sensor ID	Non-Linearity (%)
DEWP#E_I08	0.56
DEWP#H_B06	0.34
DEWP#H_F01	0.42
DEWP#K_J08	0.66

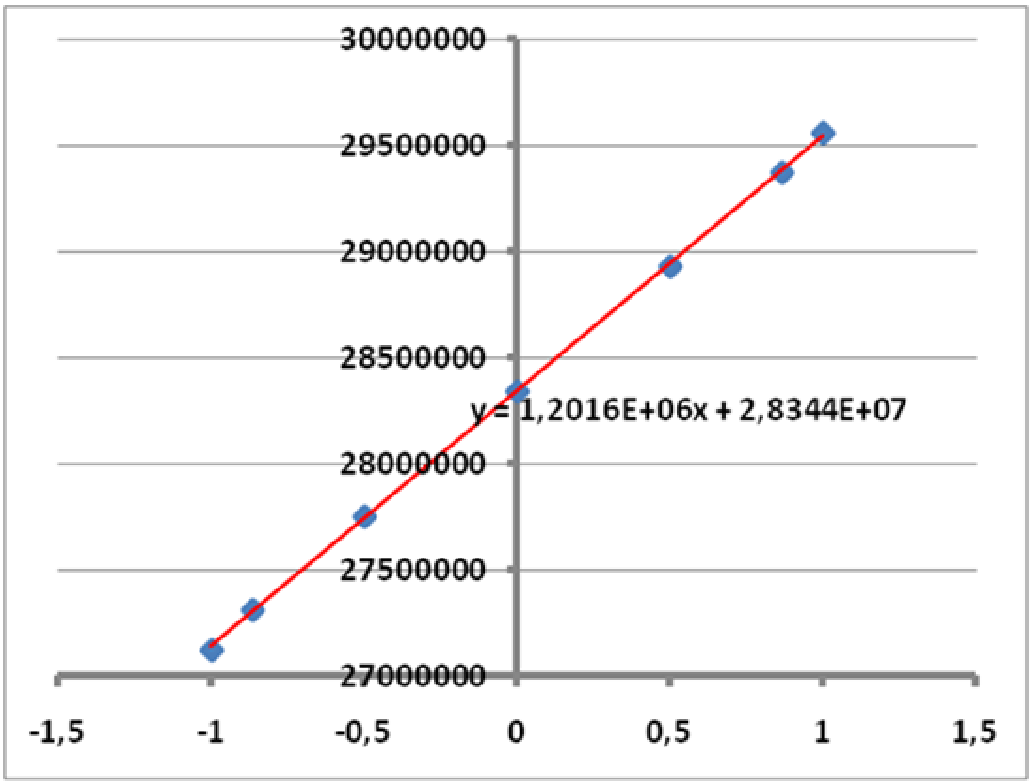

(a)

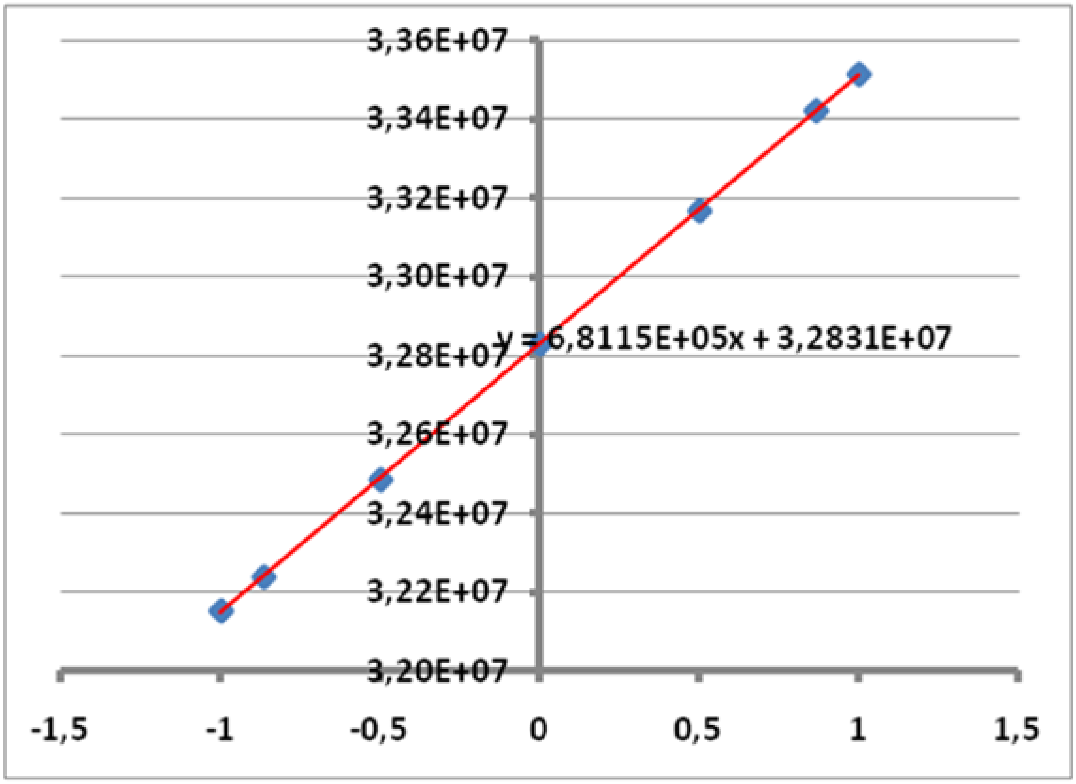

(b)

Figure 5.35: (a) Non-Linearity graph of accelerometer DEWP#K_J08 (b) Non-Linearity graph of accelerometer DEWP#H_B06.

5.4.1.3 Measurement Range Detection

Figure 5.36 shows the operation range measurement results of DEWP#K_J08 and DEWP#H_B06. It can be seen from this graph that DEWP#K_J08 is tested up to 20g and sensor was working fine within this region. Therefore it can be called that the operation range of accelerometer DEWP#K_J08 is larger than 20g. On the other hand DEWP#H_B06 reveals that during the operation range tests there is a jump from -6.5g to -14.5g during the measurement range tests. Similar characteristics are observed in DEWP#E_I08 and DEWP#H_F01. The reason of this behavior is the contamination between the narrow finger spacing of the accelerometers. In SOG accelerometers finger spacing was at least 4µm's and in DWP due to buckling of the sensors cleaning chemicals could access every vertical surface. But in DEWP narrow finger spacing does not allow the chemicals clean those regions.

In order to solve this problem changes described in chapter 4.3.2 is made on the design of the DEWP accelerometers. Finger spacing is increased from 1µm to 2µm's and anchor mask is replaced with a new one to allow the passage of cleaning chemicals beneath the sensors.

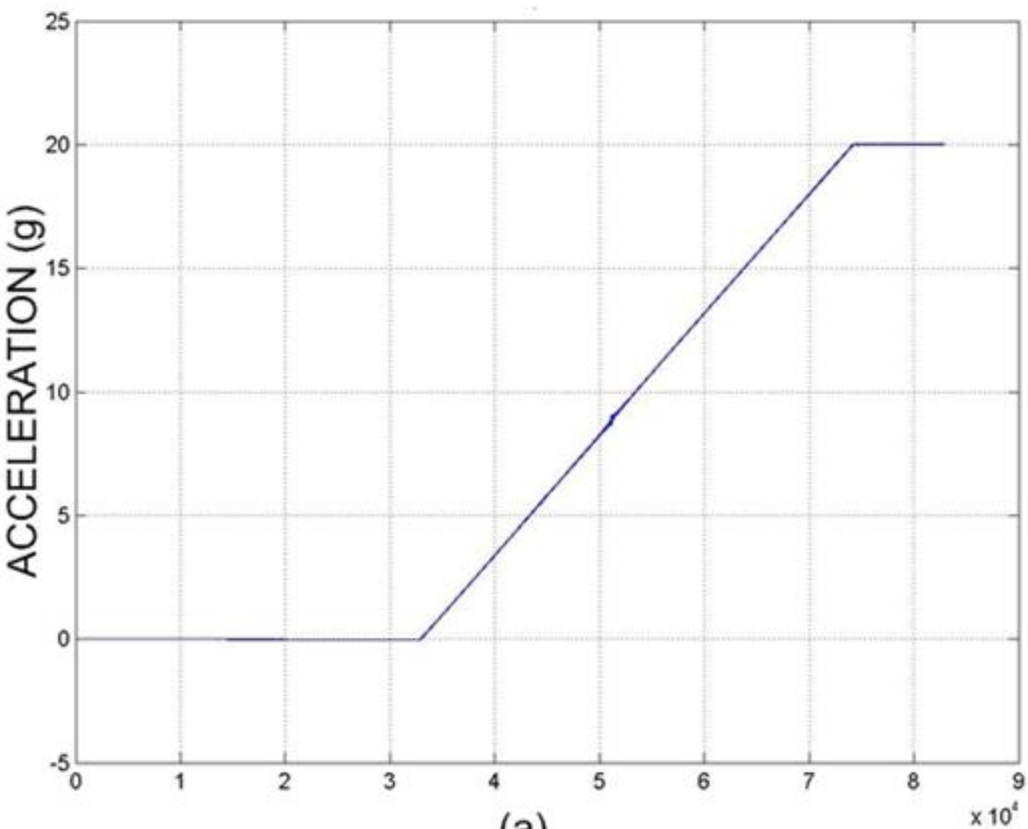

(a)

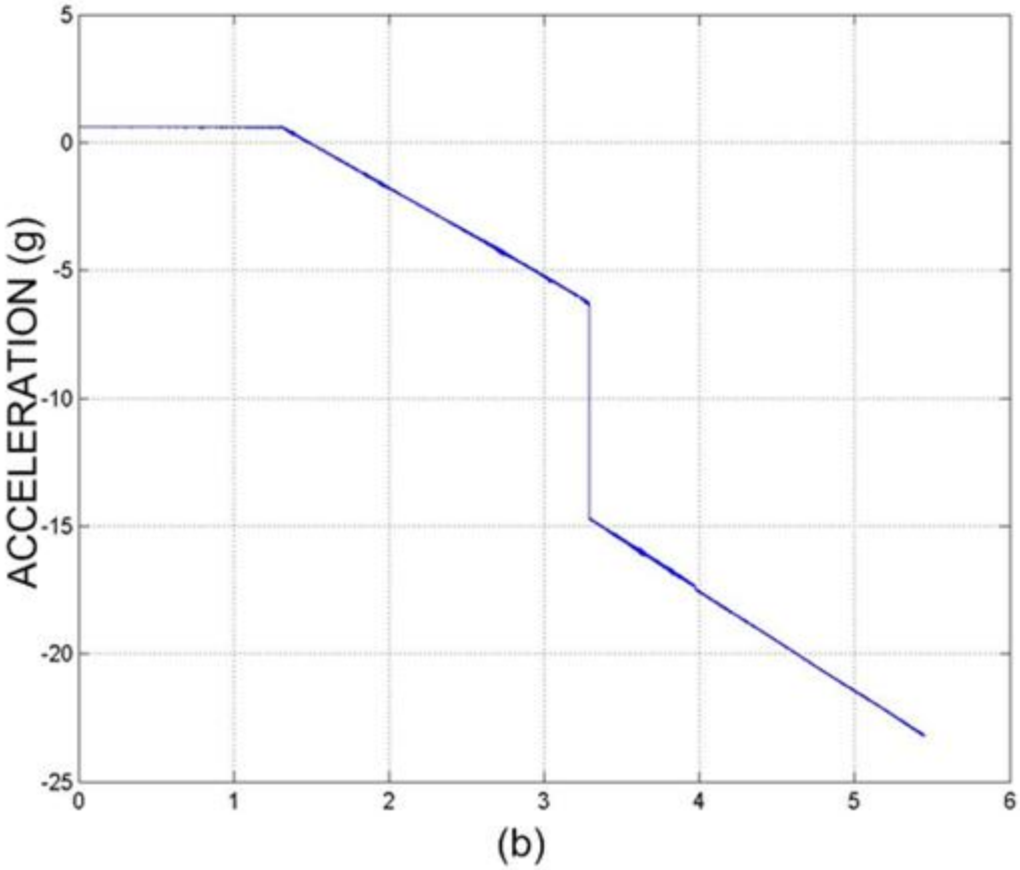

Figure 5.36: (a) Operation range measurement results of DEWP#K_J08. (b) Operation range measurement results of DEWP#H_B06.

After the mask set is renewed and sensors with 2µm finger spacing's are started to be fabricated, 3 more DEWP runs are completed with this mask set. It is observed from the results of this runs that the yield of the fabrications increased from 2-3% up to 45-50%. In expense of increasing the yield of the fabrication, measurement range of the accelerometer design given in Figure 4.16 decreased to ±8.5g and accelerometer design given in Figure 4.18 decreased to ±12.5g.

From the first fabricated wafer with 2µm finger spacing, an accelerometer having long fingered architecture, DEWP#N_J12, is tested at system level. Figure 5.37 shows the 1 hour long drift data collected from the output of DEWP#N_J12 at 600Hz data rate. Figure 5.38 shows the Allan-Variance graph plotted from the data collected during 1 hour long drift test. From these results the noise density and bias drift of the system is found as 214µg/√Hz and 286µg respectively. Figure 5.39 shows the stepped output characteristics of the sensor in 0 – 4g range and Figure 5.40

shows the input output characteristics of DEWP#N_J12 in 0- -4g range and the non-linearity of the system is calculated as 0.36% from this data.

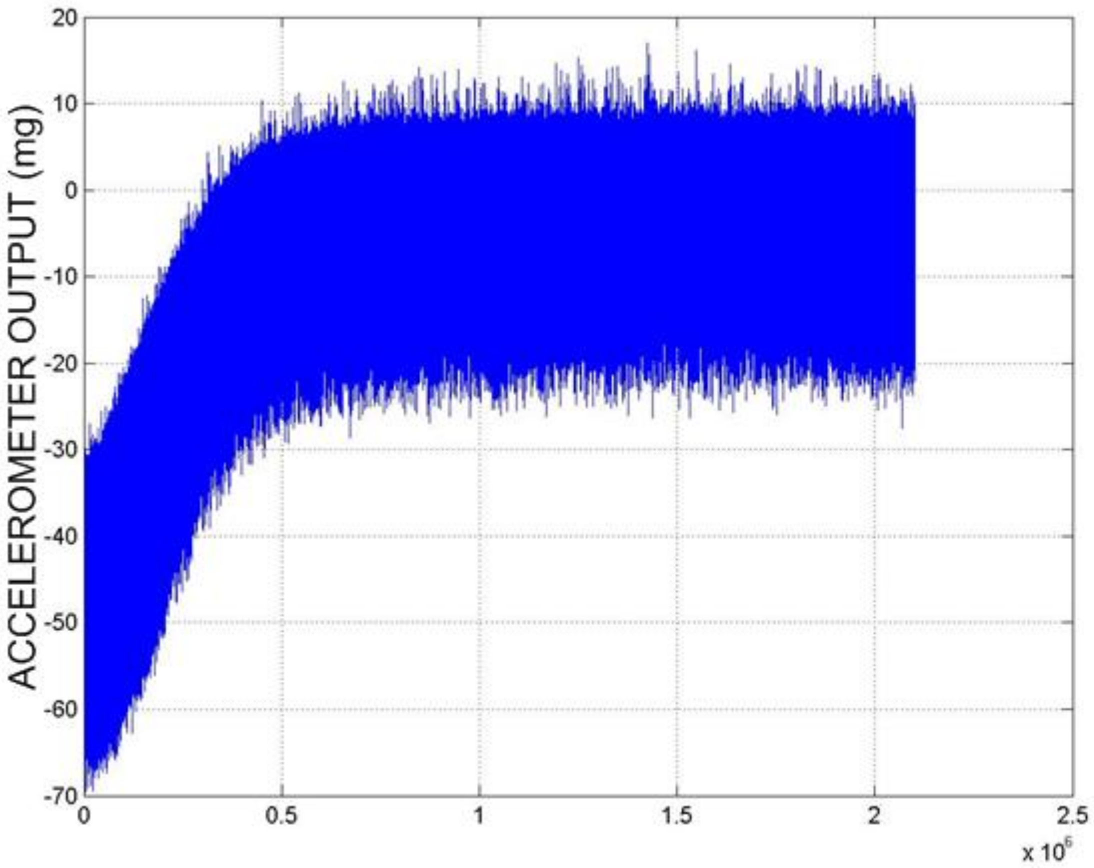

Figure 5.37: 1 hour long drift data collected from the output of DEWP#N_J12 at 600Hz data rate.

Figure 5.41 presents the measurement range test result of DEWP#N_J12 accelerometer. The expected operation range of this accelerometer was ±7.5g but the measured operation range of the sensor was ±4.5g. The major reason for this problem is the widening of the 2µm wide finger spacing to 2.5µm during DRIE. In the later processes this problem is solved and DRIE is optimized for 2µm etching of the finger spacing. With the increase in the yield of the accelerometer, number of identical accelerometers found from the sensor level tests increased. Using these accelerometers a three axes accelerometer system is built. For the z-axis accelerometer another alumina substrate is designed and this alumina substrate is placed vertically on the base alumina substrate for lateral axis accelerometers. Test results of the 3-axes accelerometer is given in the next section of this chapter.

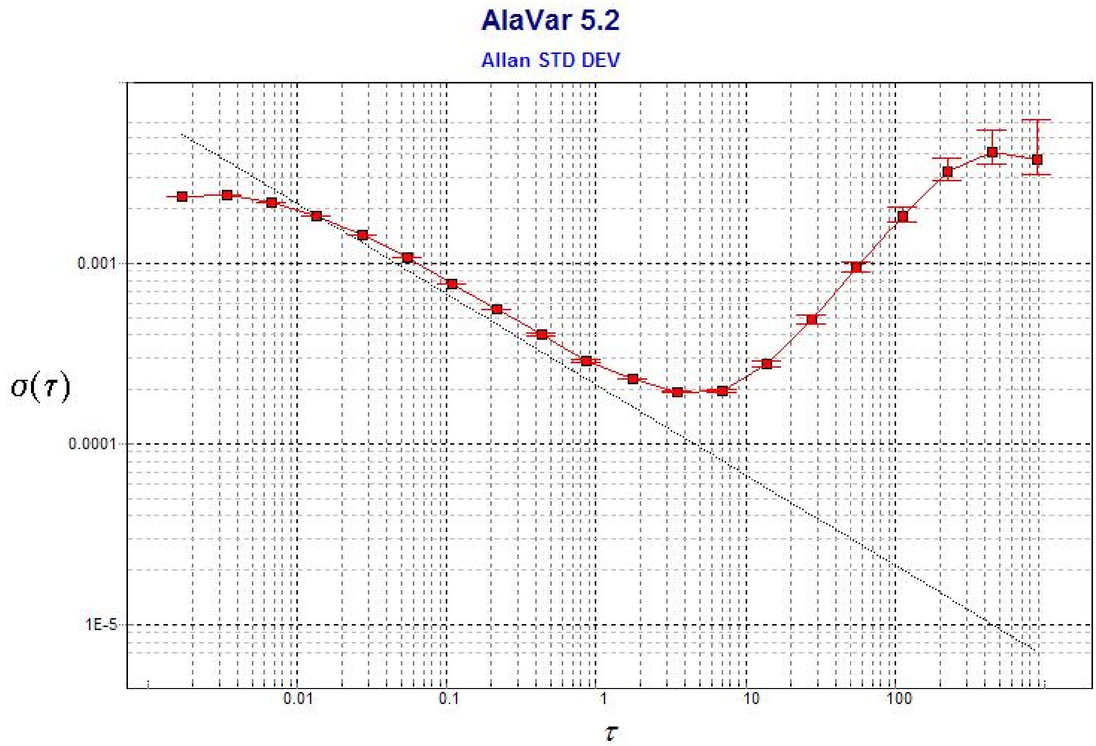

Figure 5.38: Allan-Variance graph plotted from the data collected during 1 hour long drift test

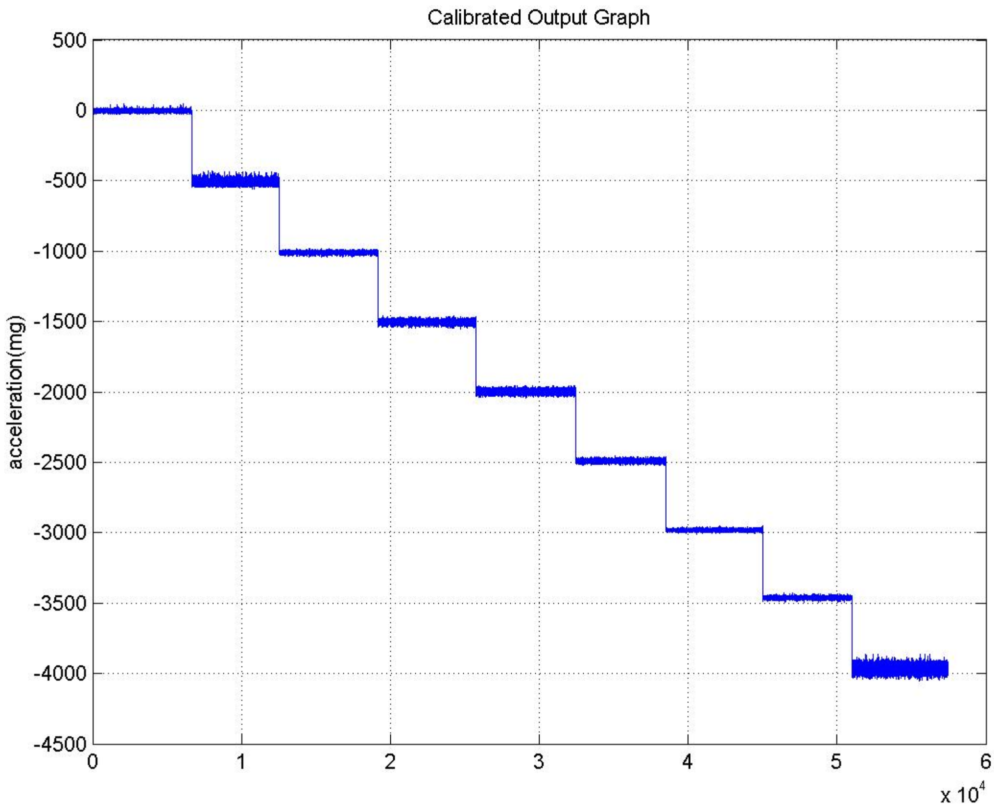

Figure 5.39: Stepped output characteristics of the sensor in 0 – -4g range.

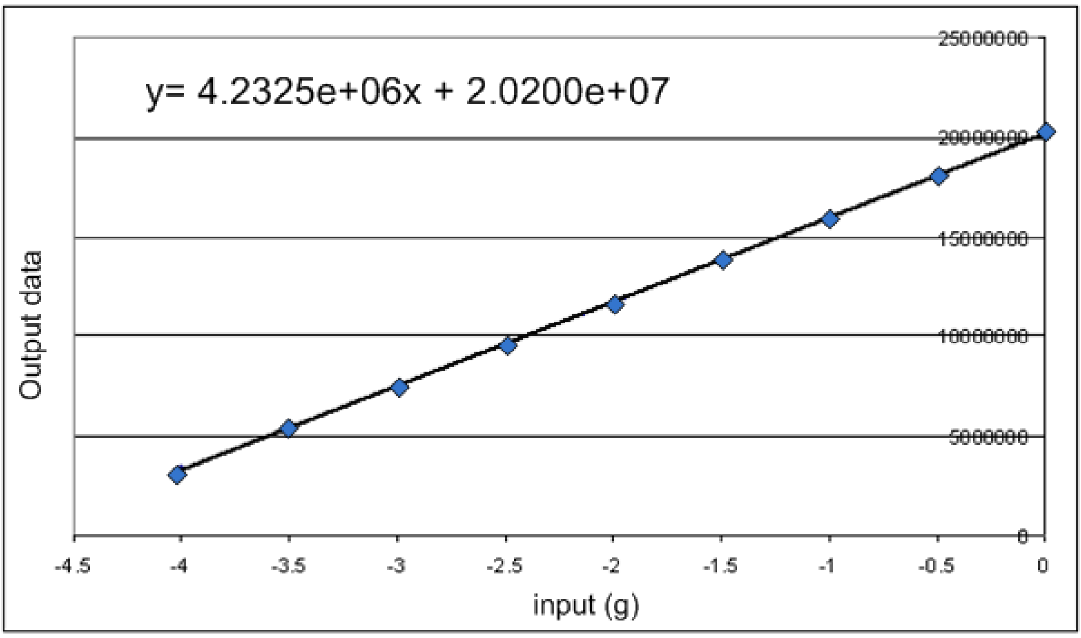

Figure 5.40: Input-output characteristics of DEWP#N_J12 in 0 – -4g range.

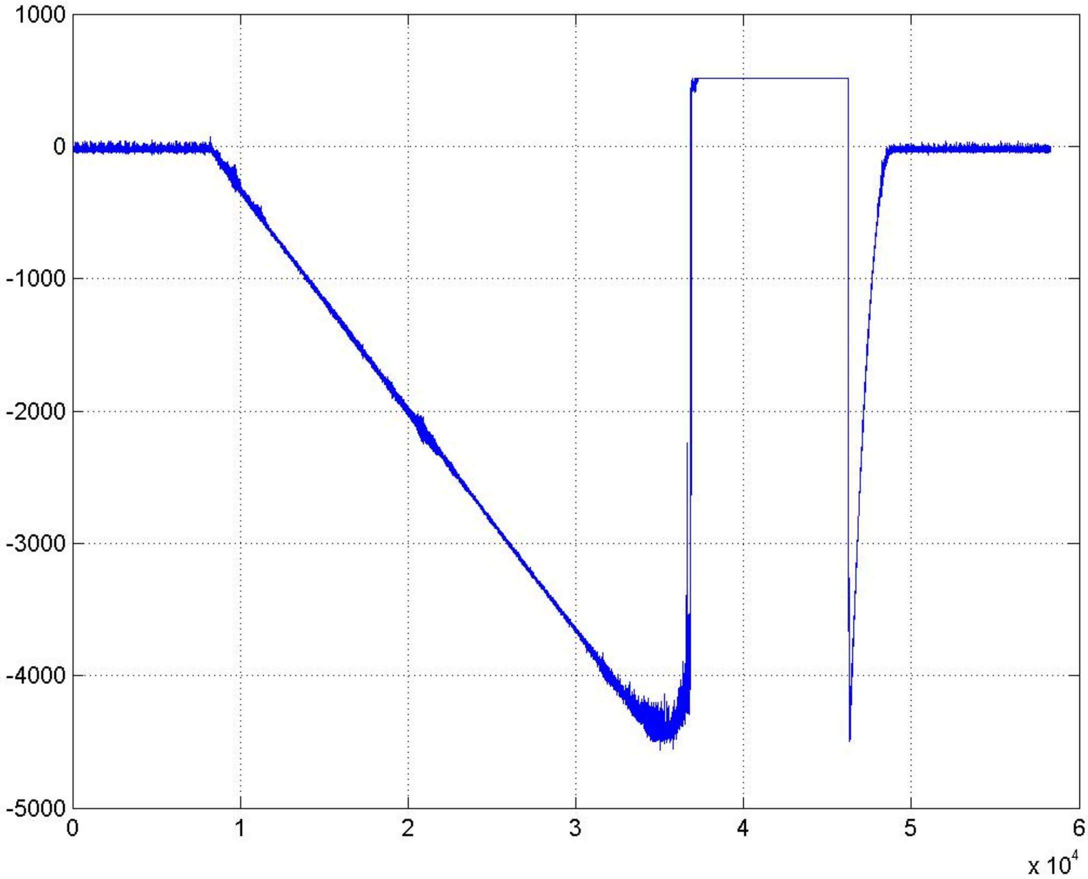

Figure 5.41: Measurement range test result of DEWP#N_J12 accelerometer.

Table 5.16: Measured performance parameters of all DEWP accelerometers.

Sensor ID	**E_I08 1μm**	**H_B06 1μm**	**H_F01 1μm**	**K_J08 1μm**	**N_J12 2μm**
Bias Drift	700	720	910	112	286
Noise Density	160	973	210	255	214
Non-Linearity (%)	0.56	0.34	0.42	0.66	0.36
Measurement Range (g)	-	-	-	>20	4.5

5.5 Three Axes Accelerometer Package and Tests

Finger spacing of the accelerometers are increased to 2μm in order to increase the yield of the fabrication and initial test results showed that accelerometers having 450μm finger lengths, which has 0% yield with 1μm finger spacing has increased to 50-55%. These results are cross checked between 3 DEWP2μm fabrications and 9 DEWP1μm fabrications.

Increase in the yield of fabrication enabled us to find similar accelerometers for three axes systems. Figure 5.42 shows a three axes accelerometer system with three second order sigma delta readout chips wire bonded to three DEWP2μm accelerometers. In this section of the thesis system level tests of three axes accelerometer package are presented.

5.5.1 System Level Tests

5.5.1.1 Allan-Variance Noise and Bias Drift Measurement

During this test, accelerometers should be on rest position but since the packages have three accelerometers measuring in three orthogonal axes, at least one sensor should experience acceleration on its sensitive axis. Figure 5.43 - Figure 5.45 shows the Allan-Variance graphs of x-, y-, and z-axis accelerometers of the three axes accelerometer package which are DEWP#O_K08, DEWP#O_M03, and DEWP#O_M06. Table 5.17 lists the bias drift and noise density values of accelerometers connected to the x-, y-, and z-axis of three axes accelerometer system.

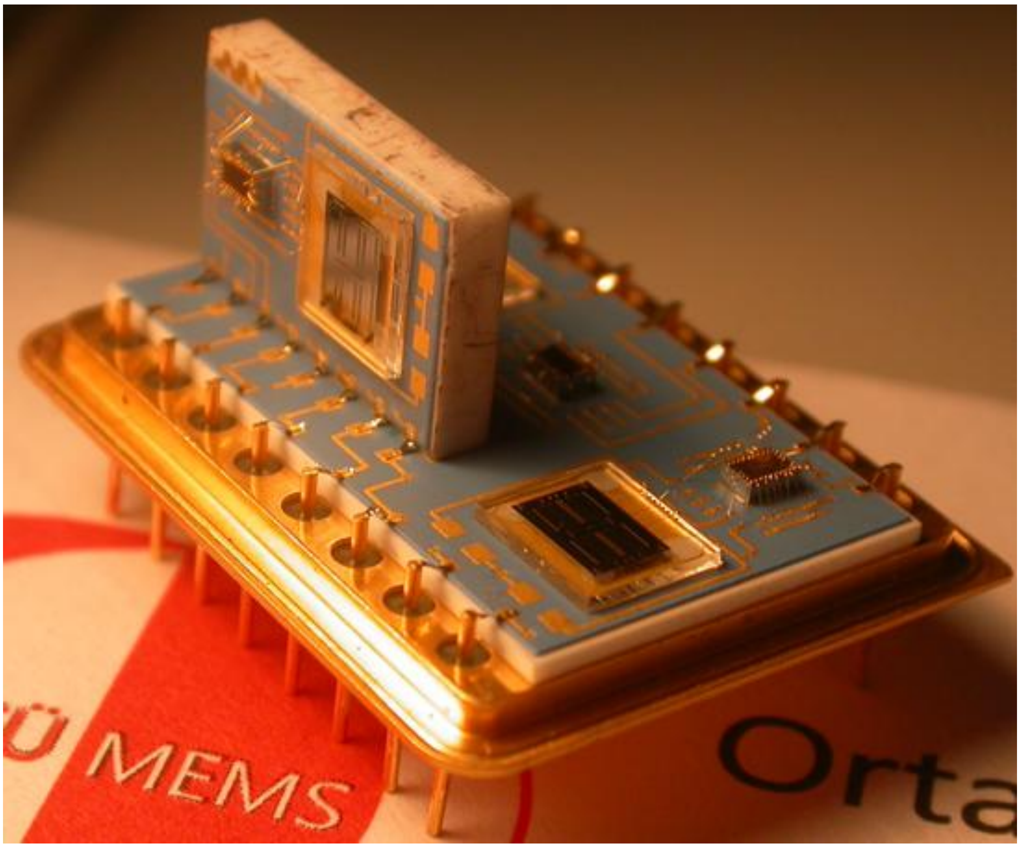

Figure 5.42: Three axes accelerometer system with three second order sigma delta readout chips wire bonded to three DEWP2µm accelerometers

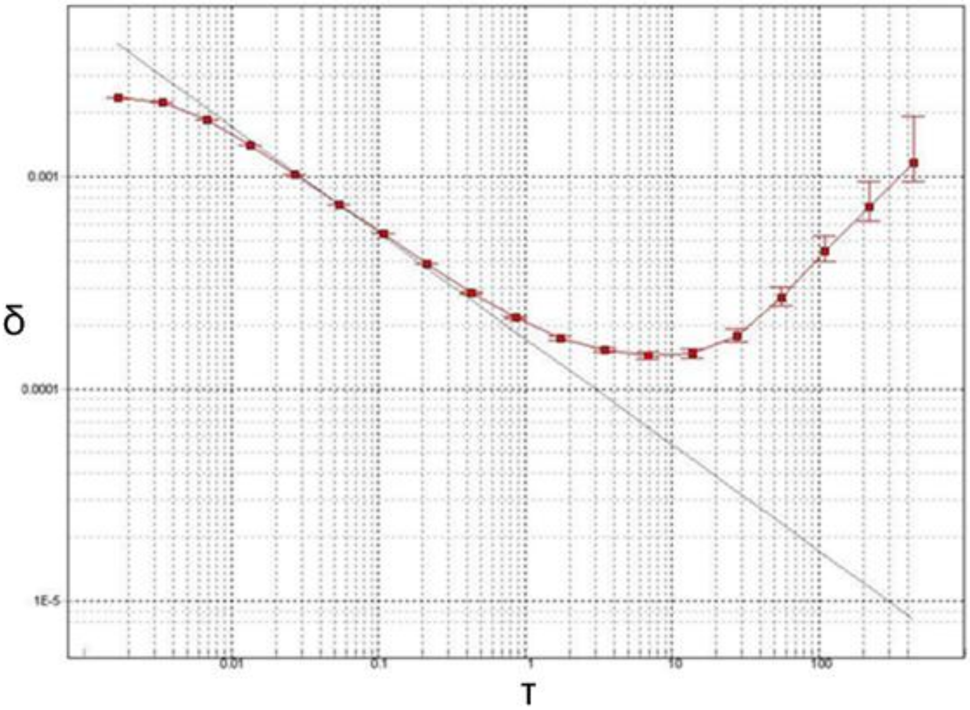

Figure 5.43: Allan variance result of x-axis of three axes package. (DEWP#O_K08)

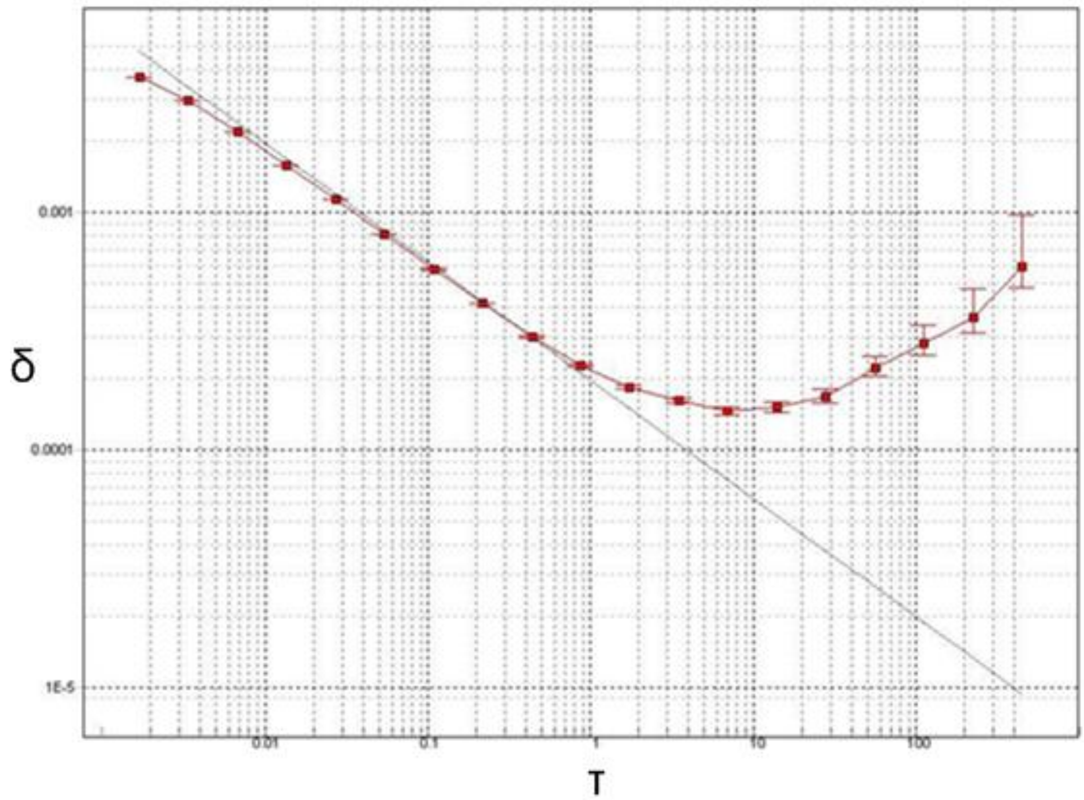

Figure 5.44: Allan variance result of y-axis of three axes package. (DEWP#O_M03)

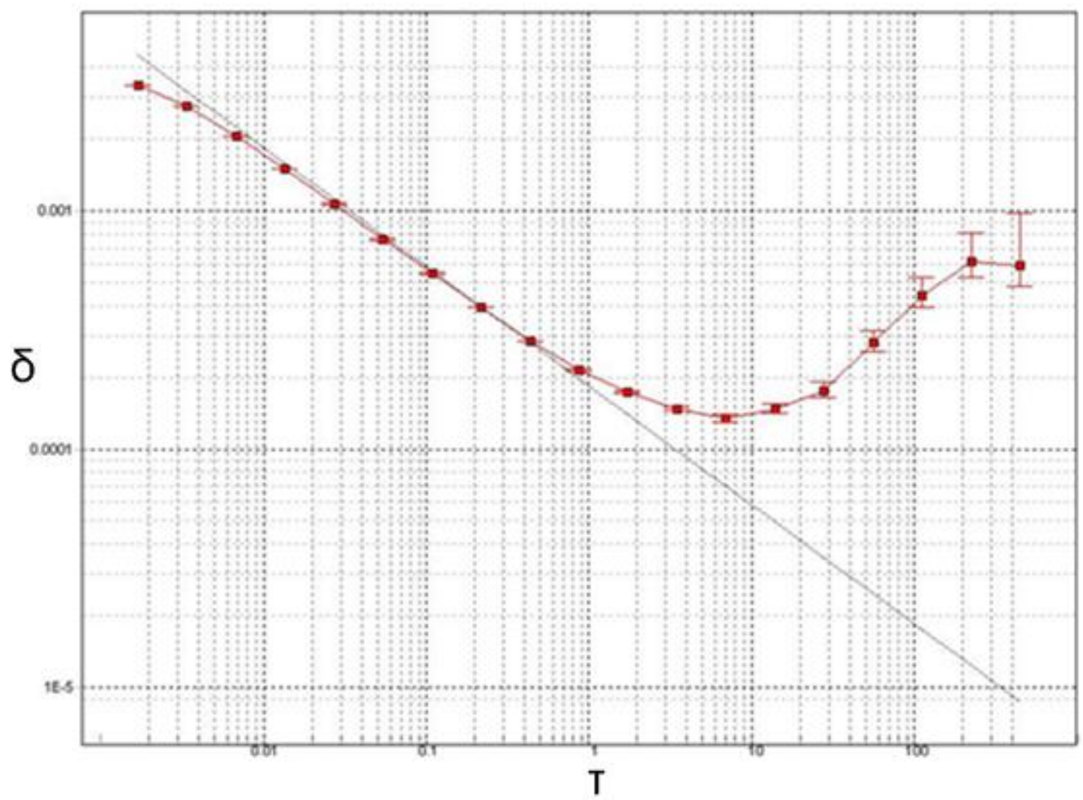

Figure 5.45: Allan variance result of z-axis of three axes package. (DEWP#O_M06)

Table 5.17: Bias drift and noise density values of accelerometers connected to the x-, y-, and z-axis of the three axes accelerometer system.

	x-axis DEWP#O_K08	y-axis DEWP#O_M03	z-axis DEWP#O_M06
Noise Density (µg/√Hz)	173	197	184
Bias Drift (µg)	147	152	142

5.5.1.2 Non-Linearity Measurements

In order to measure full positive range linearity of all three axis accelerometers, input acceleration between 0 – 10g are applied to the sensors by 1g steps. Non-linearity's of the sensors are extracted by fitting a curve to the obtained data from the test results. Figure 5.46 - Figure 5.48 show the non-linearity test data and best fit curves for x-, y-, and z-axis accelerometers. Table 5.18 lists the measured non-linearity's of the accelerometers in three axes accelerometer system

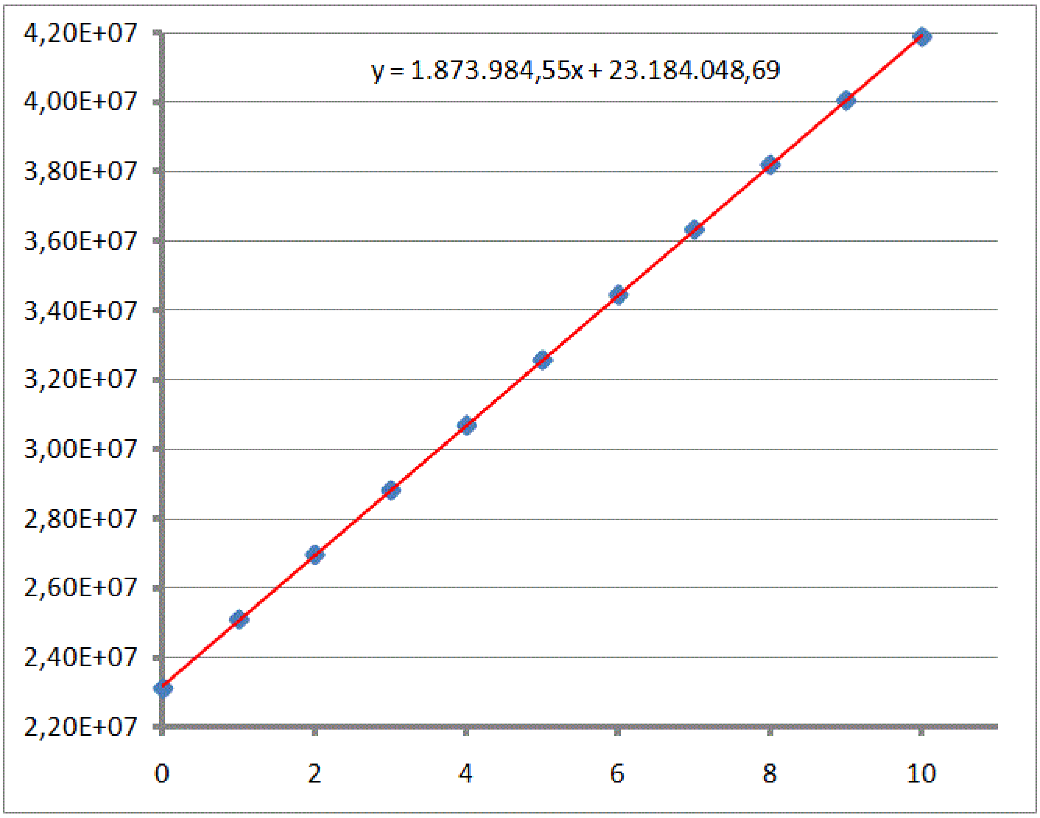

Figure 5.46: Non-linearity test data and best fit curve for DEWP#O_K08.

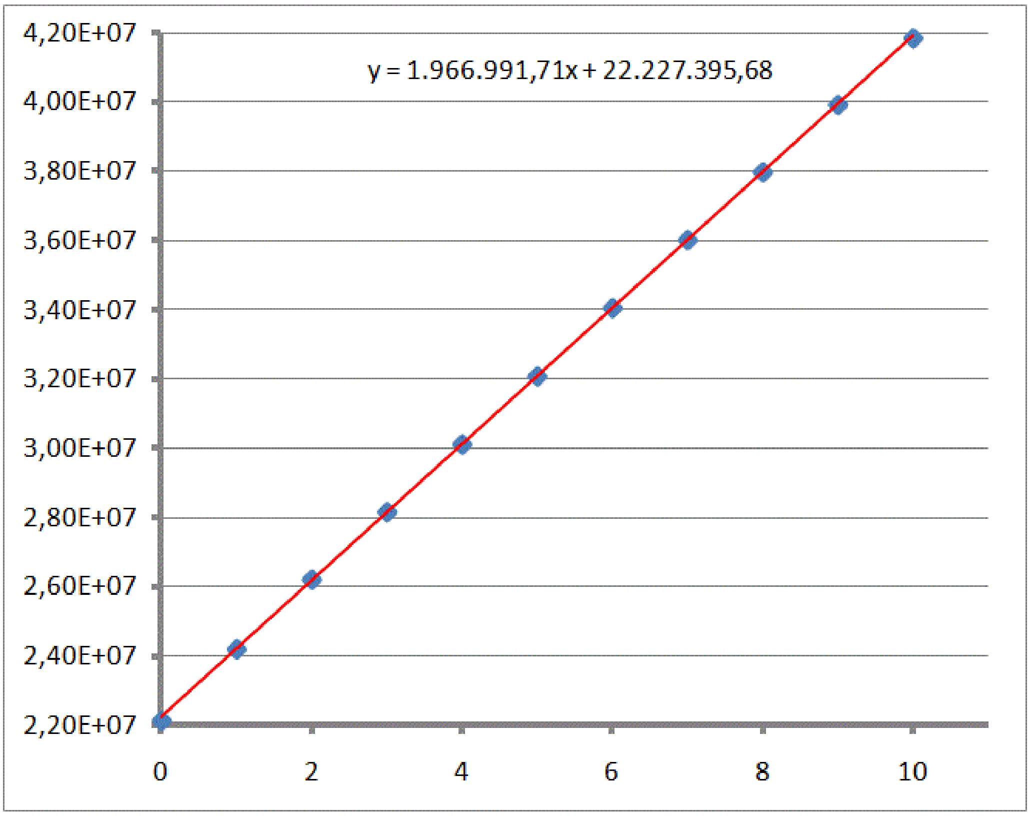

Figure 5.47: Non-linearity test data and best fit curve for DEWP#O_M03.

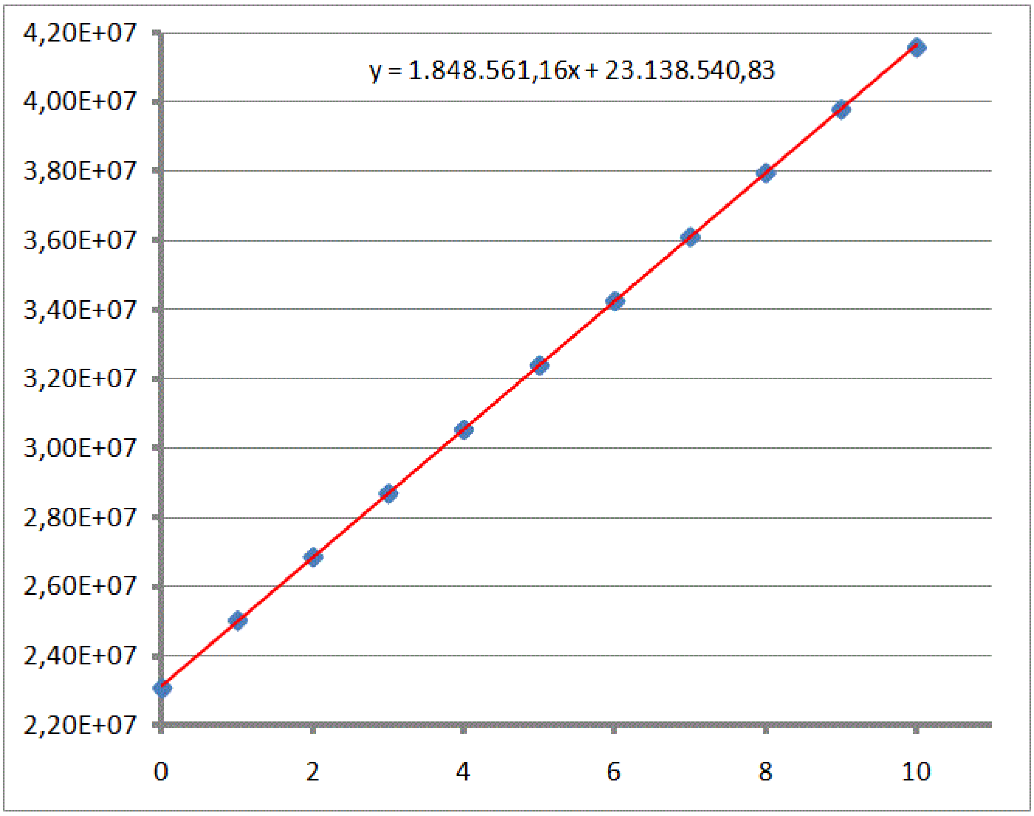

Figure 5.48: Non-linearity test data and best fit curve for DEWP#O_M06.

Table 5.18: Measured non-linearity's of the accelerometers in three axes accelerometer system.

Sensor ID	Axis	Non-Linearity (%)
DEWP#O_K08	x	0.40
DEWP#O_M03	y	0.44
DEWP#O_M06	z	0.38

5.5.1.3 Measurement Range Detection

Measurement range detection tests of the three axes accelerometer system are performed in the three axes motion simulator installed at Akyurt facilities of ASELSAN A.Ş. Expected measurement range values for these accelerometers were ±12.5g's. Accelerations up to 10g are applied on both axes of each accelerometer in three axes accelerometer system and the output saturation values are observed. Table 5.19 lists the measured maximum operation ranges of the accelerometers connected to the three axes accelerometer system. Figure 5.49 - Figure 5.51 shows the positive and negative operation range measurement tests of x-, y- and z-axis accelerometers respectively.

Table 5.19: Measured maximum operation ranges of the accelerometers connected to the three axes accelerometer system

	x-axis DEWP#O_K08	y-axis DEWP#O_M03	z-axis DEWP#O_M06
Positive Axis	>10g	>10	>10
Negative Axis	>-10.5	>-10.2	>-10.2

With these final tests, full functionality of a tactical grade three axes accelerometer system is proved. Increasing the finger spacing and other important changes to the mask set increased the yield of the accelerometer fabrication considerably and all accelerometers on three different axis's demonstrated very similar performance parameters. Table 5.20 lists all the measured performance parameters of accelerometers in the three axes accelerometer system.

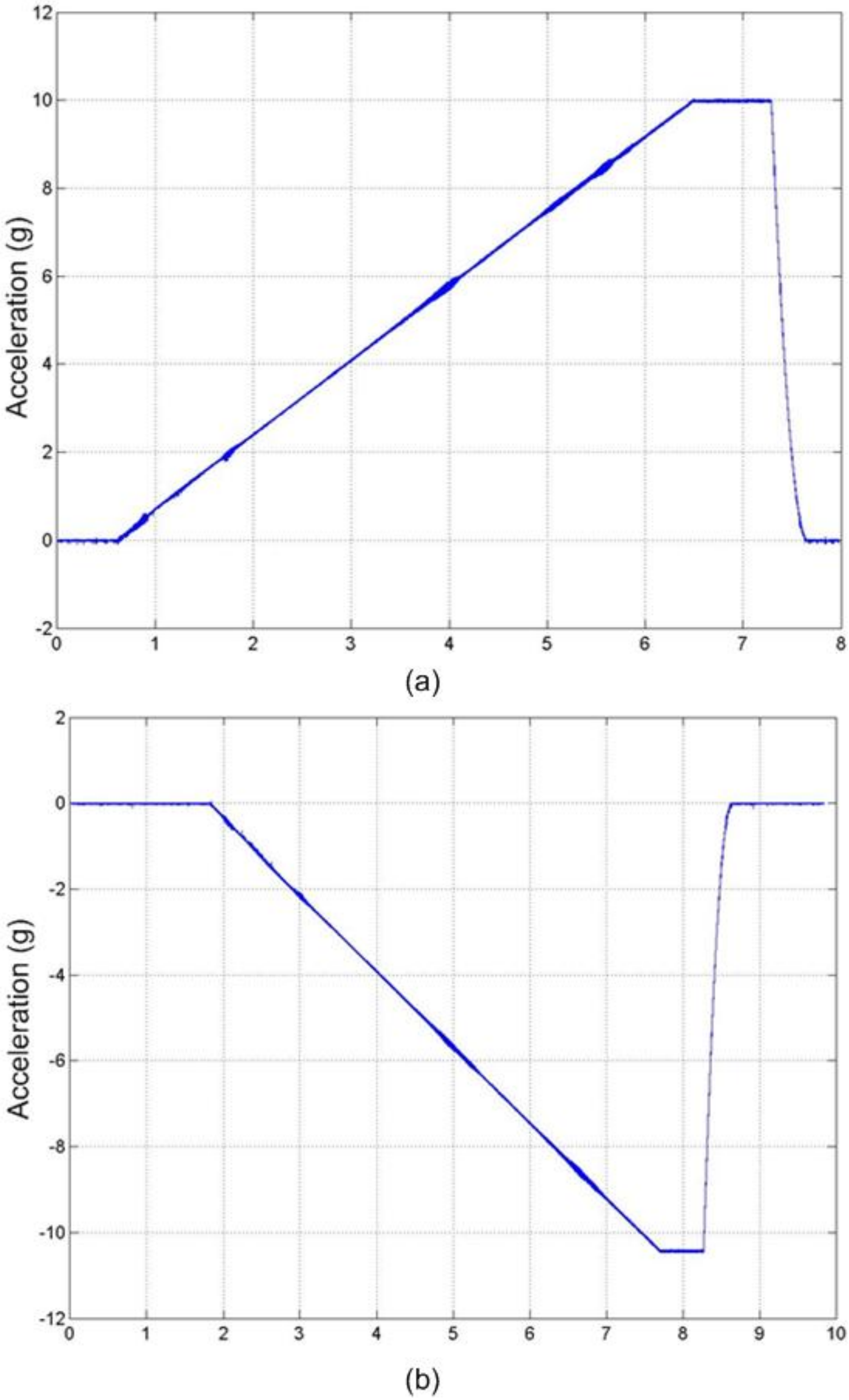

Figure 5.49: (a) Positive and (b) Negative operation range measurement tests of x-axis accelerometer (DEWP#O_K08)

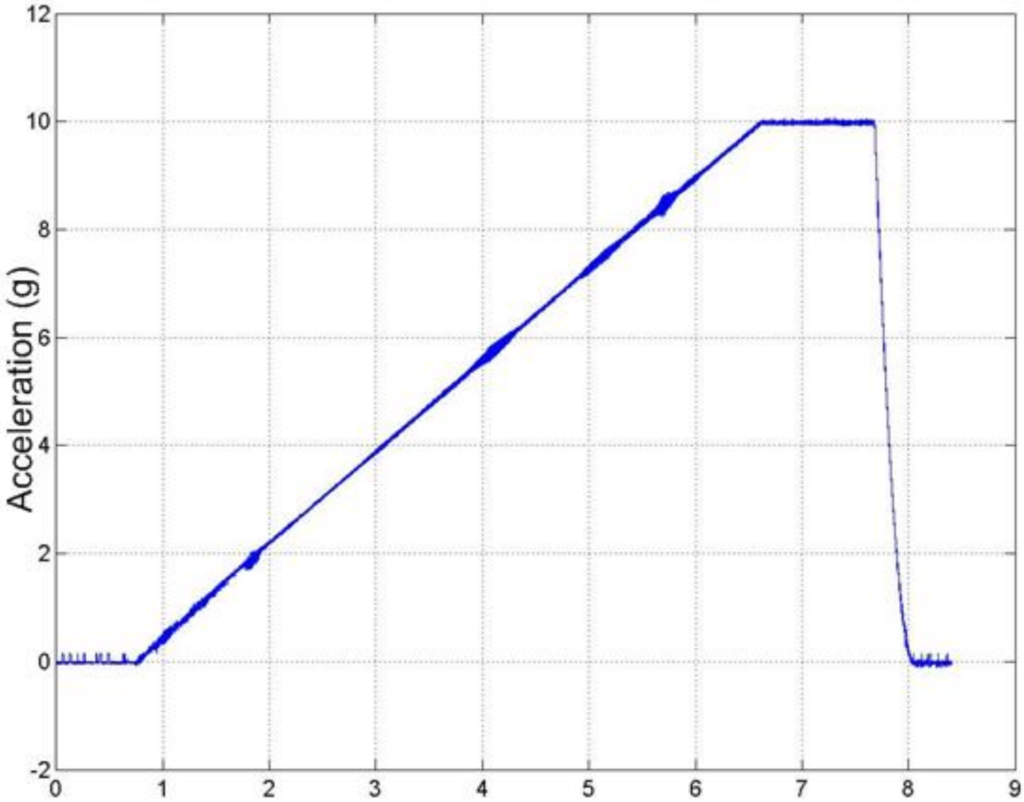

(a)

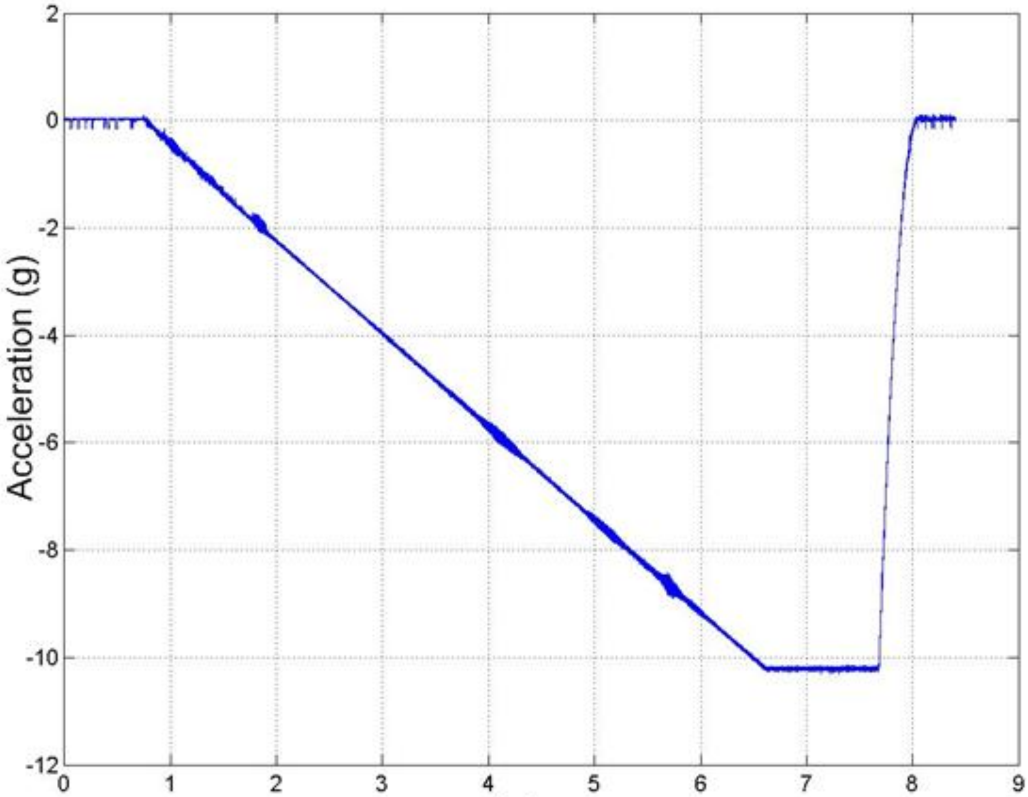

(b)

Figure 5.50: (a) Positive and (b) Negative operation range measurement tests of y-axis accelerometer (DEWP#O_M03)

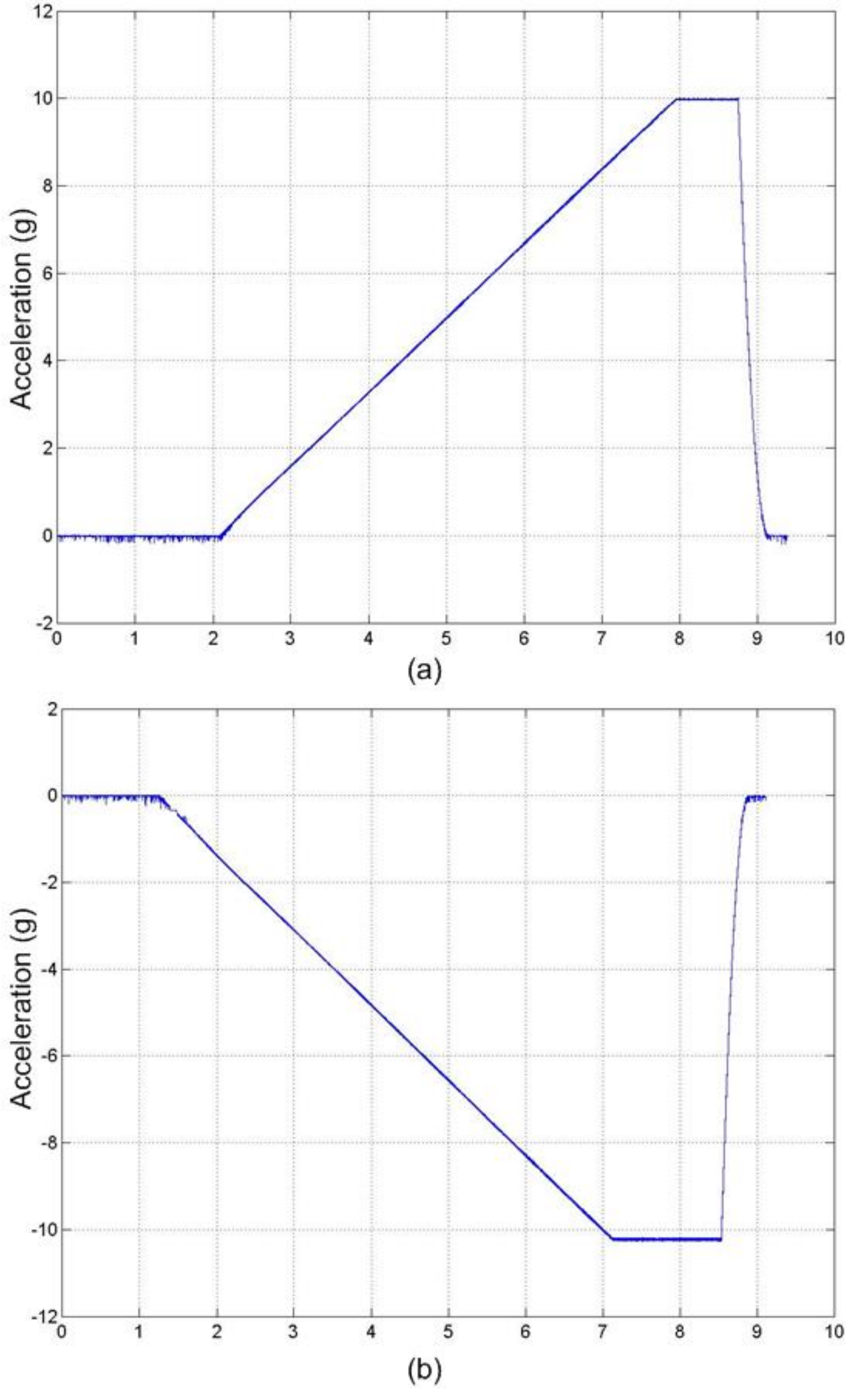

Figure 5.51: (a) Positive and (b) Negative operation range measurement tests of z-axis accelerometer (DEWP#O_M06)

Table 5.20: All measured performance parameters of accelerometers in the three axes accelerometer system

	x-axis DEWP#O_K08	y-axis DEWP#O_M03	z-axis DEWP#O_M06
Bias Drift (µg)	147	152	142
Noise Density (µg/√Hz)	173	197	184
Non-Linearity (%)	0.40	0.44	0.38
Positive Range (g)	>10	>10	>10
Negative Range (g)	>10.5	>10.2	>10.2

5.6 Summary of the Chapter

In this chapter test results of the accelerometers fabricated in the scope of this study are given. Design and fabrication techniques of these accelerometers were presented in the fourth chapter of this thesis in detail.

Chapter starts with a brief summary of each test performed on the accelerometers both at sensor and system level. Test equipment and single axis accelerometer packaging is also introduced. Afterwards, extraction of bias drift and noise density from Allan-Variance graph and non-linearity from 12 position test results are explained.

In the later sections, sensor and system level test results of the accelerometers are presented separately for each fabrication technique and at the end of each section; a table summarizing all sensors in that section is given.

Finally in the last section, three axes accelerometer which was prepared by orthogonally placing three single axis DEWP accelerometers having 2µm finger spacing is described. Allan-Variance, measurement range and non-linearity tests and their results are also given in order to summarize the overall performance of the three axes accelerometer system.

Table 5.21 presents system level performance results of all accelerometers presented in this chapter.

Table 5.21: System level performance results of all accelerometers presented in this chapter.

Sensor ID	Fabrication Process	Noise Density (μg/√Hz)	Bias Drift (μg)	Non-Linearity (%)	Measurement Range (g)
1O02	SOG long finger	17	29	0.90	±2.22
4F03	DWP short finger	353	812	1.10	not tested
4I10	DWP short finger	NA	NA	2.60	not tested
6C03	DWP short finger	342	406	0.25	not tested
5G01	DWP short finger	NA	NA	1.03	NA
5G13	DWP short finger	NA	NA	NA	±35
5K06	DWP short finger	532	588	1.11	±32
5J06	DWP short finger	153	50	0.38	±33.5
5I08	DWP short finger	279	449	0.38	±28
5O06	DWP short finger	880	714	0.34	±33
EI08	DEWP1μm short finger	160	700	0.56	distorted
HB06	DEWP1μm short finger	973	720	0.34	distorted
HF01	DEWP1μm short finger	210	910	0.42	distorted
KJ08	DEWP1μm short finger	255	112	0.66	>±20
NJ12	DEWP2μm long finger	214	286	0.36	±4.5
OK08	DEWP2μm short finger	173	147	0.40	>±10
OM03	DEWP2μm short finger	197	152	0.44	>±10
OM06	DEWP2μm short finger	184	142	0.38	>±10

CHAPTER 6

SOI^2 PROCESS AND SENSOR DESIGN

During the fabrication of a 3 axial accelerometer system for an inertial measurement unit, placing three accelerometers orthogonally is a very challenging task. In addition to this finding three identical accelerometers that will be capable of satisfying the same performance criteria's is very difficult. To solve these problems monolithic accelerometers, integrating all three axes on the same substrate are design and fabricated [101] – [106]. Some of these accelerometers are fabricated with post CMOS processing and since their design parameters are not flexible, they can't achieve high performances [101], [106]. Remaining tri-axially fabricated accelerometer structures either lack high operation range and have difficult fabrication [102] or have process dependent performances with low resolution and high cross axis sensitivity [103] - [105].

In this thesis a new fabrication method is proposed which will eliminate all the problems in the three axes accelerometers reported in the literature. With this process, lateral accelerometers will able to be fabricated as single axis accelerometers by having complete control on the structural layer thickness, finger spacing and die size. In addition to these, vertical axis accelerometers can also be fabricated differentially, by having matched sensitivity, resolution and operation range performances. Drawback of this process is that it contains a total of 9 masks and has a very difficult process flow.

6.1 SOI² Process Flow

Process starts with the etching of the SOI wafer in KOH, in order to open via holes from device layer to the handle layer. For this etching process 0.5µm thick silicon nitride is used on top of the epitaxial surface as a masking layer and it is patterned with the "Via Mask" which is the first mask of the mask set. These via openings will be used to have contact to the rigid proof mass of the z-axis sensor. Finally buried oxide between the epitaxial layer and the handle layer is removed in RIE together with the surface nitride mask. After via's are formed Chromium/Gold metallization layer is sputtered and patterned to have metal contacts between the bottom z-axis electrode and the intermediate rigid proof mass. Metallization layer is patterned with second mask of the mask set which is "Metallization Mask". Than in order to form z-axis accelerometer's bottom electrode, device layer of the SOI wafer is patterned and etched with DRIE using the third mask of the mask set which is the "Bottom Epi Mask". In order to suspend z-axis accelerometer's bottom electrode and remove the unwanted silicon in the dicing streets, SOI wafer is put into HF or vapor HF to completely remove silicon dioxide under the suspended regions. Figure 6.1 shows the process steps of the preparation of first SOI wafer in SOI^2 process.

After the preparation of the first SOI wafer, the preparation of the glass wafer which will be used as the base substrate for all x, y and z axis accelerometers starts. As in DWP, DEWP and SOG processes, glass wafer is etched for recess opening with the "Anchor Mask", which is the fourth mask of the mask set. Then patterned glass wafers are coated with chromium and gold, in order to form the metal connections on the bottom SOI and glass wafers. These stacked metal layers are wet etched with "Glass Metal Mask", which is the fifth mask of the mask set. Prepared glass wafer and device layer of the SOI wafer are than bonded anodically. By this way electrical connections are carried out from the handle layer of the SOI wafer through via's to the metal lines on the glass and then to pad's of the device. Backside of the handle layer of the SOI wafer is than evaporated with Gold and patterned with sixth mask of the mask set, the "Bottom Handle Mask", which is a whole wafer DRIE mask that will separate individual sensors from each other. Like the "Bottom Epi-Mask" whole dicing streets are not etched in this step, instead 20µm lines around each individual device is etched and bulk silicon on the dicing streets is removed as a whole frame.

After the process, gold masking layer is not removed from the surface because this will also be used as the intermediate bonding layer between the top and bottom SOI wafer of the process. Figure 6.2 shows the process steps of the preparation of glass wafer, bonding of SOI and glass wafers and DRIE etch of the SOI handle layer.

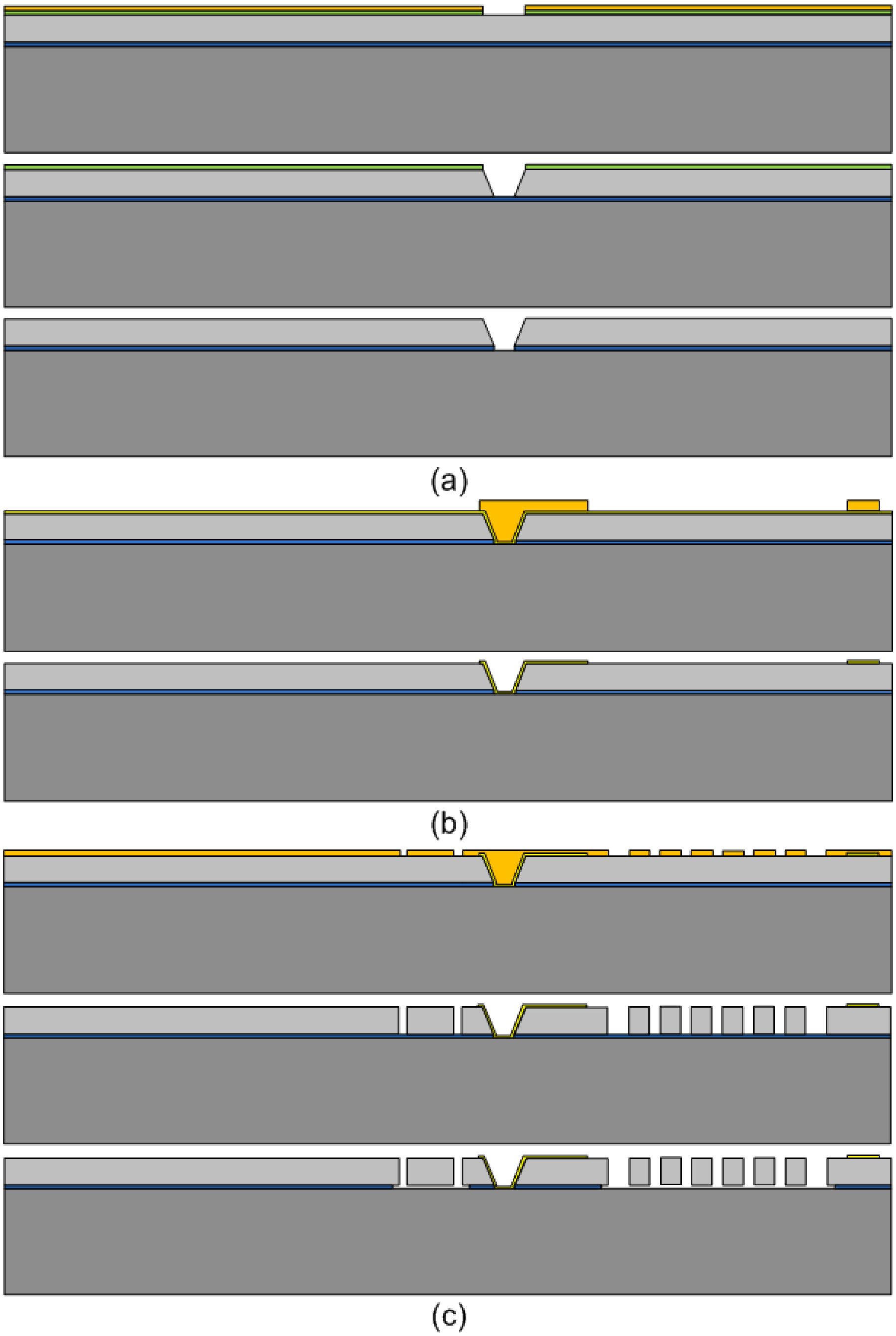

Figure 6.1: Process steps of the first SOI wafer in SOI^2 process. (a) SOI wafer is masked with 0.5μm thick silicon nitride, etched with KOH and mask and buried oxide are removed in RIE. (b) Metallization is done. (c) Device layer is patterned with DRIE and buried oxide is removed in HF or vapor HF.

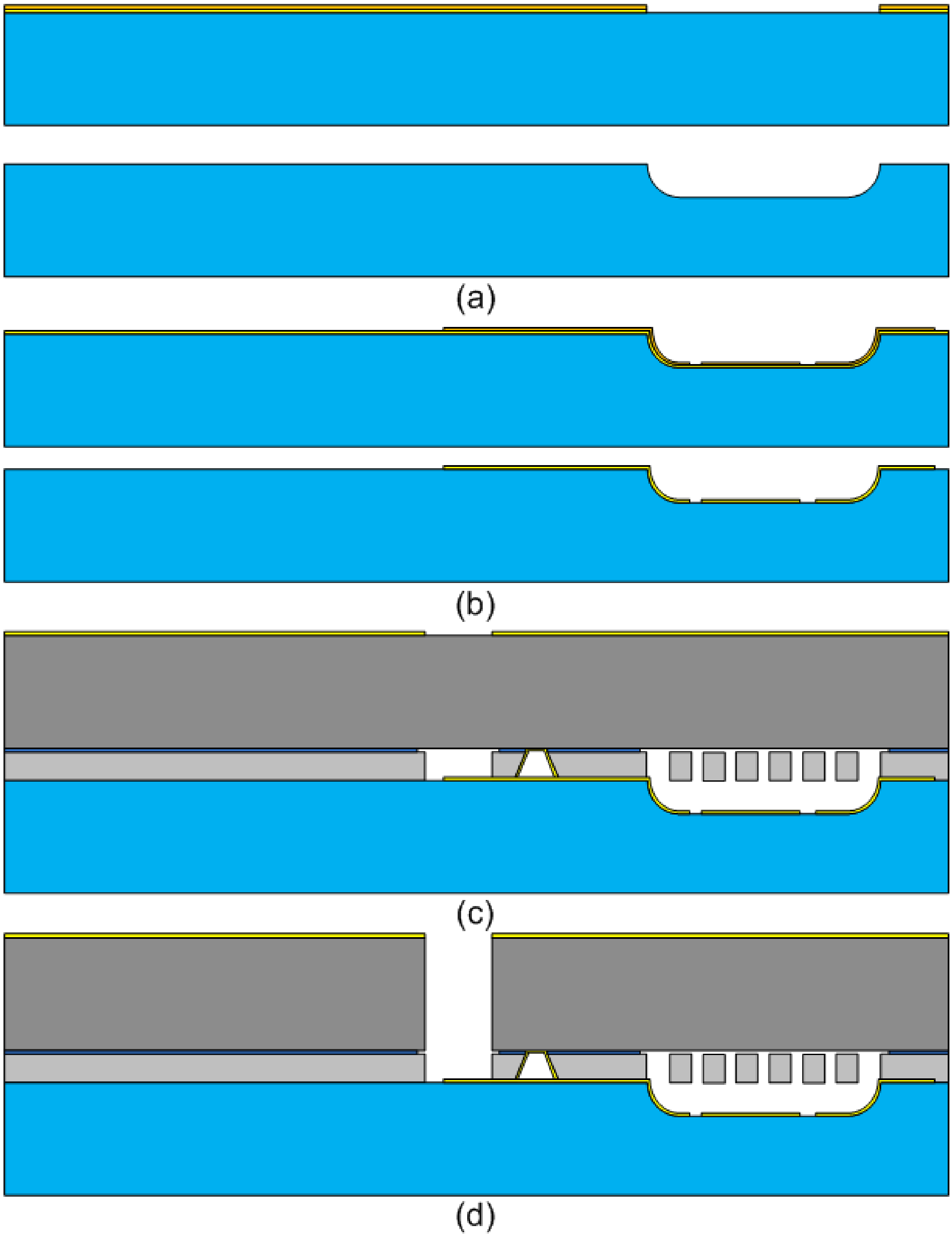

Figure 6.2: Process steps of the glass wafer, bonding of SOI and glass wafers and DRIE etch of the SOI handle layer. (a) Glass recess opening in HF. (b) Metallization of glass wafer. (c) SOI and glass wafers are bonded together and backside of the SOI handle layer is masked with gold. (d) Handle layer is through etched with DRIE. Metal masking layer is left on top of the handle layer as an intermediate bonding medium.

Fabrication of the second SOI wafer is started with the backside etching of the handle layer in order to open pad windows and remove the substrate beneath the lateral axis accelerometers to decrease the parasitic capacitances. Like in the first SOI wafer, 20µm thick lines around each individual device and bottom of the lateral axis accelerometers are etched with seventh mask of the mask set, the "Top Handle Mask". Bulk silicon in the dicing streets remains attached to the intermediate buried oxide layer. During the DRIE, gold is again used as a masking layer and it is not removed from the bottom of the handle layer, since it will be used as the intermediate bonding layer between top and bottom SOI wafers. After backside etching of the top SOI wafer, it is bonded to the handle layer of the bottom SOI wafer. At high temperatures deposited gold layers on both surfaces melt and form a strong bond between two wafers. After bonding, metallization for lateral axis accelerometers and z-axis accelerometer's top electrode is sputtered with chromium and gold and patterned with the eighth mask, "Top Metallization". Final mask of the mask set, the "Top Epi" is used to define the top electrode of z-axis accelerometers and structures of the lateral accelerometers with lithography. Top SOI wafer is then etched with DRIE. After this step some parts of the device and handle layers of top SOI wafer is going to be attached to the devices with the intermediate buried oxide. Therefore with a second oxide removal step with HF or vapor HF, both lateral and vertical axis accelerometers are released and the silicon frames covering the top of pad metallization and dicing streets can be removed physically. With this final step all three axes accelerometer dies become ready for testing.

One important issue that should be carefully considered during fabrication is that, if wet HF is used to remove the buried oxide layers than critical point drier must be used to dry the devices. Because the top or bottom electrodes of the z-axis accelerometers can stick to their own handle layers and it will be impossible to work with that accelerometer after this happens. Therefore without drying the sensor at any stage of the etching process, wafers should be transferred from HF to Di-water, then from Di-water to isopropyl alcohol and should be dried in critical point dryer. Figure 6.3 shows the final steps of the SOI^2 process including bonding of two silicon wafers with intermediate gold layer, metallization and DRIE of the top device layer and buried oxide removal steps.

With this process varying gaps between top and bottom electrodes of z-axis sensor can be fabricated identically by choosing same oxide layer thicknesses for both wafers. By selecting device layer thickness around 35-40µm's high performance lateral axes accelerometers can be fabricated with this procedure and z-axis accelerometers having matched high sensitivity can also be fabricated with varying gap parallel plate capacitance with 1µ oxide thickness.

(a)

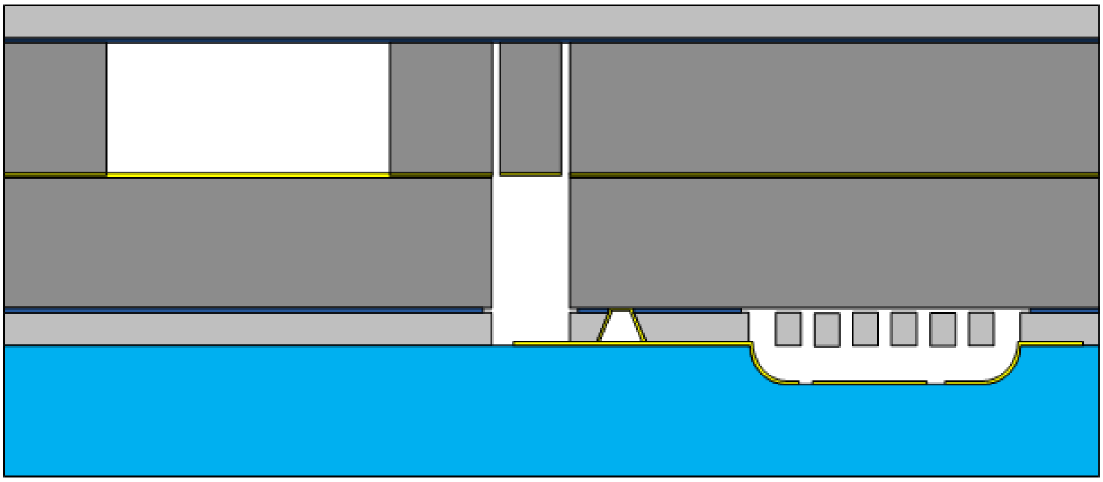

(b)

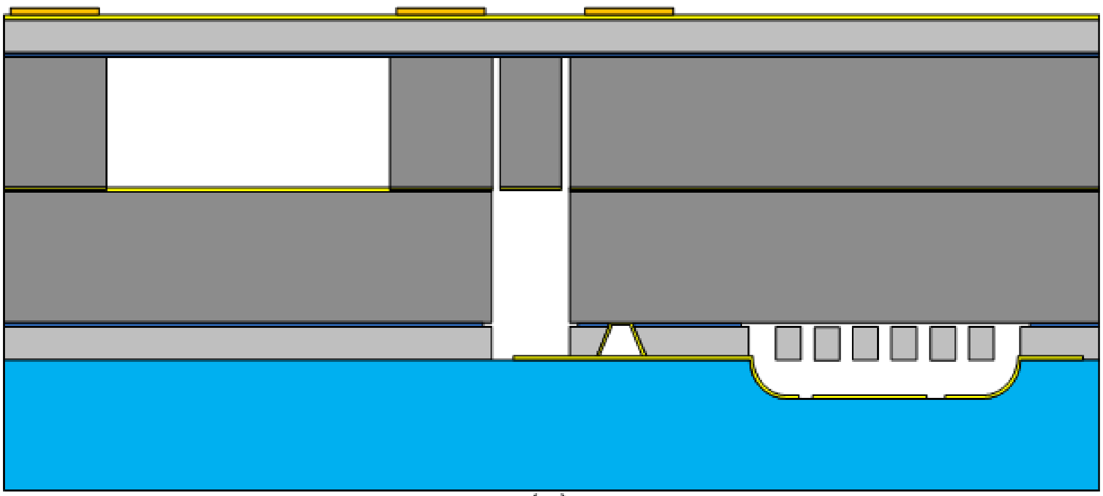

(c)

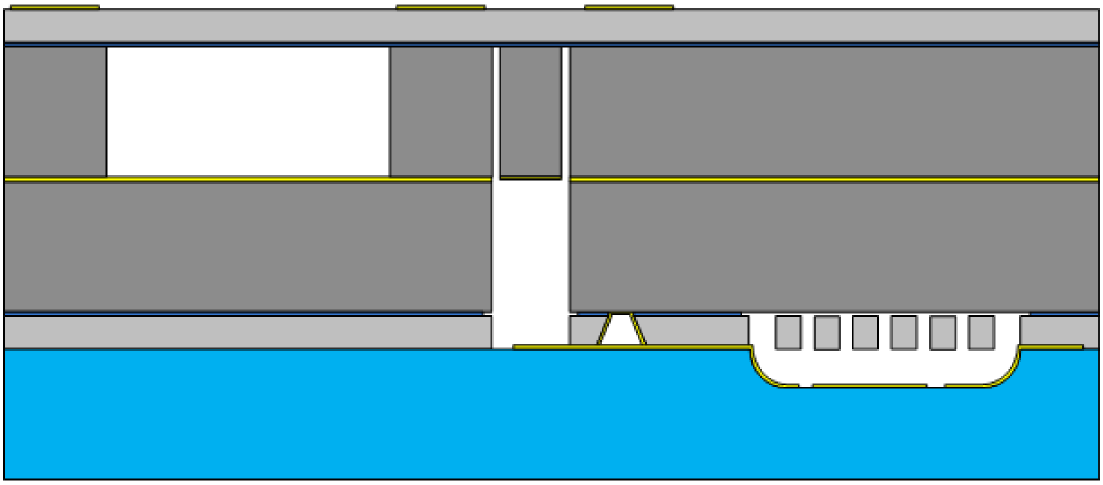

(d)

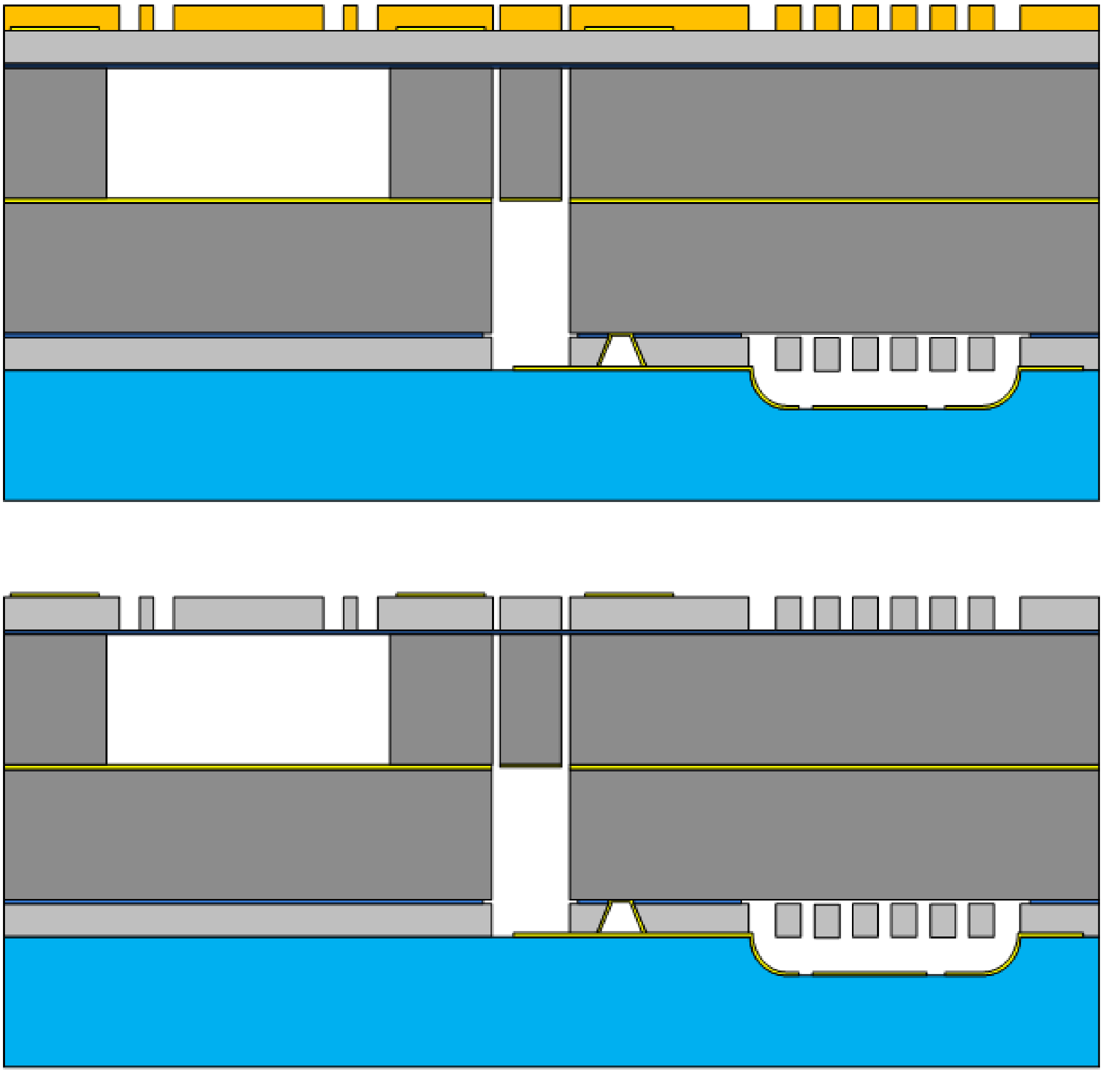

(e)

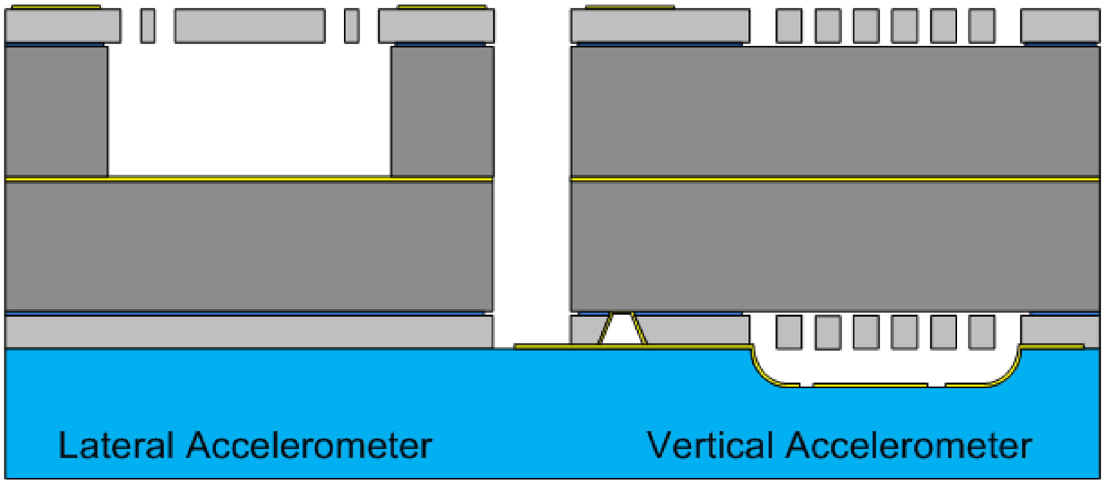

Figure 6.3: Final steps of the SOI^2 process. (a) Bottom surface of the handle layer is sputtered with gold, patterned and etched with "Top Handle Mask". (b) Top SOI wafer and the previously prepared wafers are bonded by using the intermediate gold layer on both surfaces. (c) Top surface is sputtered with chromium and gold and patterned with "Top Metallization Mask". (d) Metal is etched and photoresist is stripped. (e) Top surface is patterned and etched with DRIE using "Top Epi Mask". (f) Top electrode of vertical accelerometers and lateral accelerometers are released in HF or vapor HF.

6.2 SOI^2 Mask Set and Expected Performance Parameters

SOI^2 process consists of 9 masks and in this part of the thesis each mask of the mask set will be described in detail together with the expected performances of each design for lateral and vertical accelerometers.

6.2.1 Via Mask

In SOI^2 process, two SOI wafers are used to form the overall structure and the handle layers of both SOI wafers are bonded to each other to form the rigid mass of the vertical axis accelerometer. Unlike other accelerometers in the literature, this sensor has rigid proof mass as well as moving electrodes for differential capacitive sensing. Via mask is used to get electrical connection to the intermediate rigid proof mass. If these via holes are not opened, both handle layers are surrounded by silicon dioxide from top and bottom. But with these via holes, proof mass is electrically connected to the metal pads on the glass substrate.

Dimensions of these via holes are chosen as 150 μm x 200 μm, because after anisotropic etching with 54.7^{o} in KOH, these holes will narrow down to 115 μm x 165 μm with in 25μm depth, which will be enough for the electrical connections to the handle wafer. Anisotropic etching is preferred instead of DRIE while opening these via holes, because smooth steps with 54.7^{o} angle with the horizontal will give better results compared with the sharp edges of DRIE for step coverage of metals. Figure 6.4 shows the layout of via holes for both vertical and horizontal axis accelerometers.

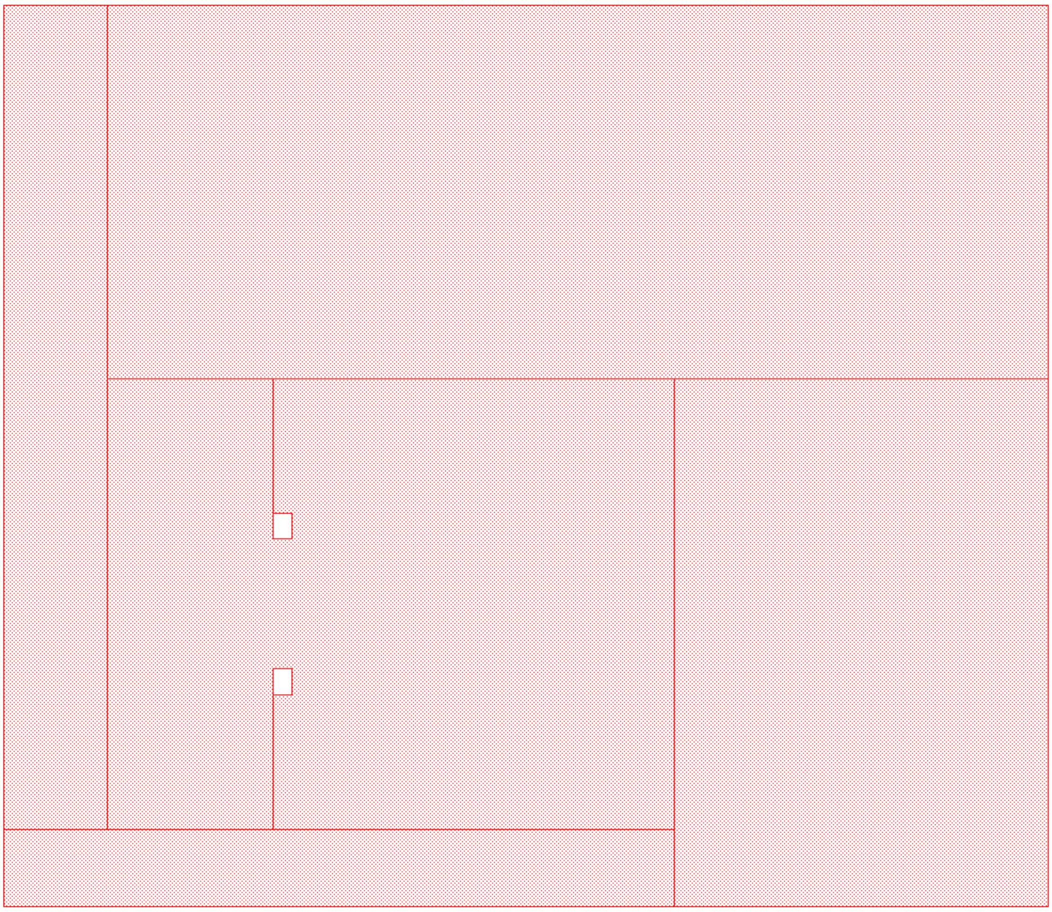

Figure 6.4: Layout of via holes for both vertical and horizontal axis accelerometers.

6.2.2 BMetal (Bottom Metallization) Mask

In order to have electrical connection from via holes, a metal must be coated on the epi (device) layer of the bottom SOI wafer. In this mask, metals are drawn 40μm larger on the sides and 200μm larger on the length compared with via holes, in order to ensure the total coverage of via openings. If the via holes are not properly closed with metal, during the HF etching of the buried oxide layer, oxide beneath via openings are also etched. Figure 6.5 shows the metal lines totally covering the via holes opened on the device layer of the bottom SOI wafer.

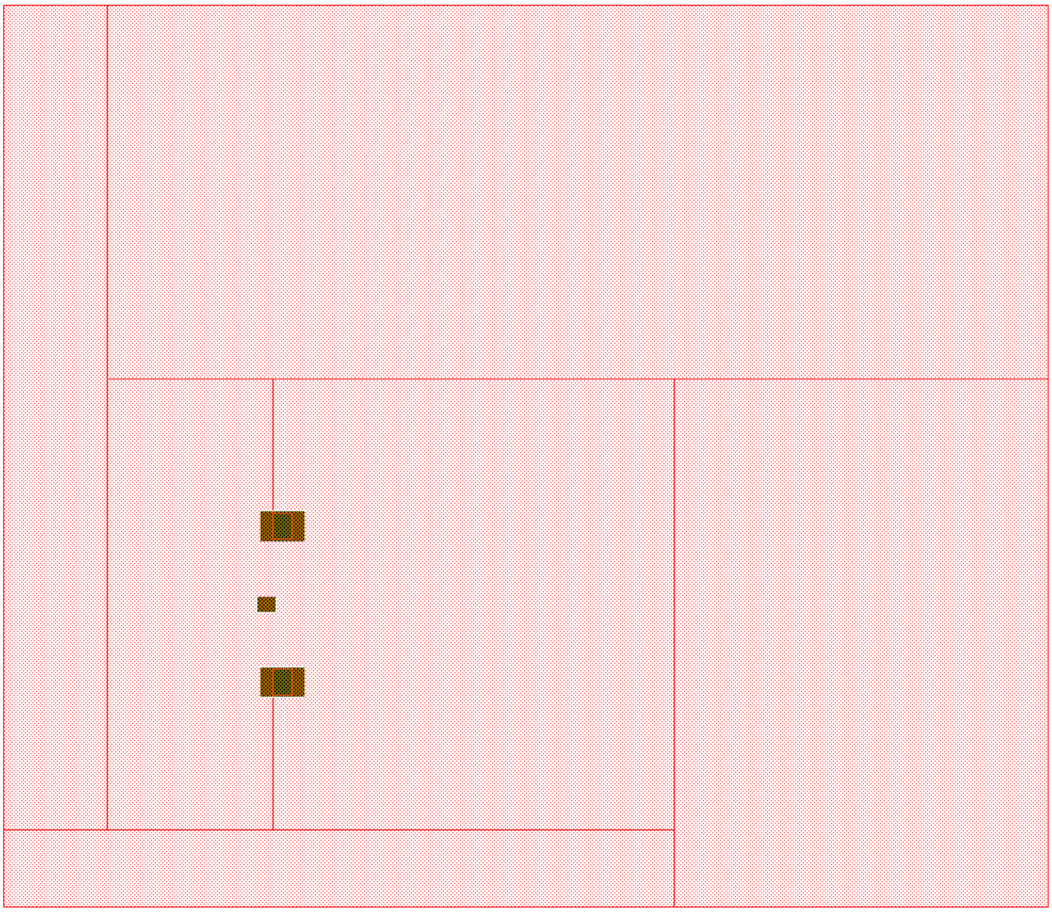

Figure 6.5: Metal lines totally covering via holes opened on the device layer of the bottom SOI wafer.

6.2.3 BEpi (Bottom Epitaxial) Structural Mask

This masking layer defines the bottom electrode of the vertical axis accelerometer. There are etching holes on the suspended regions in order to release the bottom electrode of the DRIE. Same etching holes are also placed in the dicing streets with the same spacing as the suspended bottom electrode. By this way when the bottom electrodes become suspended, frame on the dicing streets will also be detached from the SOI wafer surface and it can be completely removed. Figure 6.6 shows the BEpi

Structural DRIE Mask for both vertical and lateral axis accelerometers. In this figure, regions colored with green shows the anchors, regions colored with red shows the suspended electrodes and regions colored with blue shows the frame on the dicing lines that will be completely removed after the vapor HF or HF release process. The largest spacing between the etch holes are drawn as 91.4µm's and all the anchor regions are drawn larger than this length in order to prevent the accelerometer structure to be completely etched away after HF or vapor HF suspending process. Therefore at least 45.7µm's of silicon dioxide needed to be etched on each edge in order to completely release the structures.

This layer also defines the performance parameters of a vertical axis accelerometer. Table 6.1 lists the design and performance parameters of the vertical axis accelerometers for the suspended electrode on one side of the accelerometer.

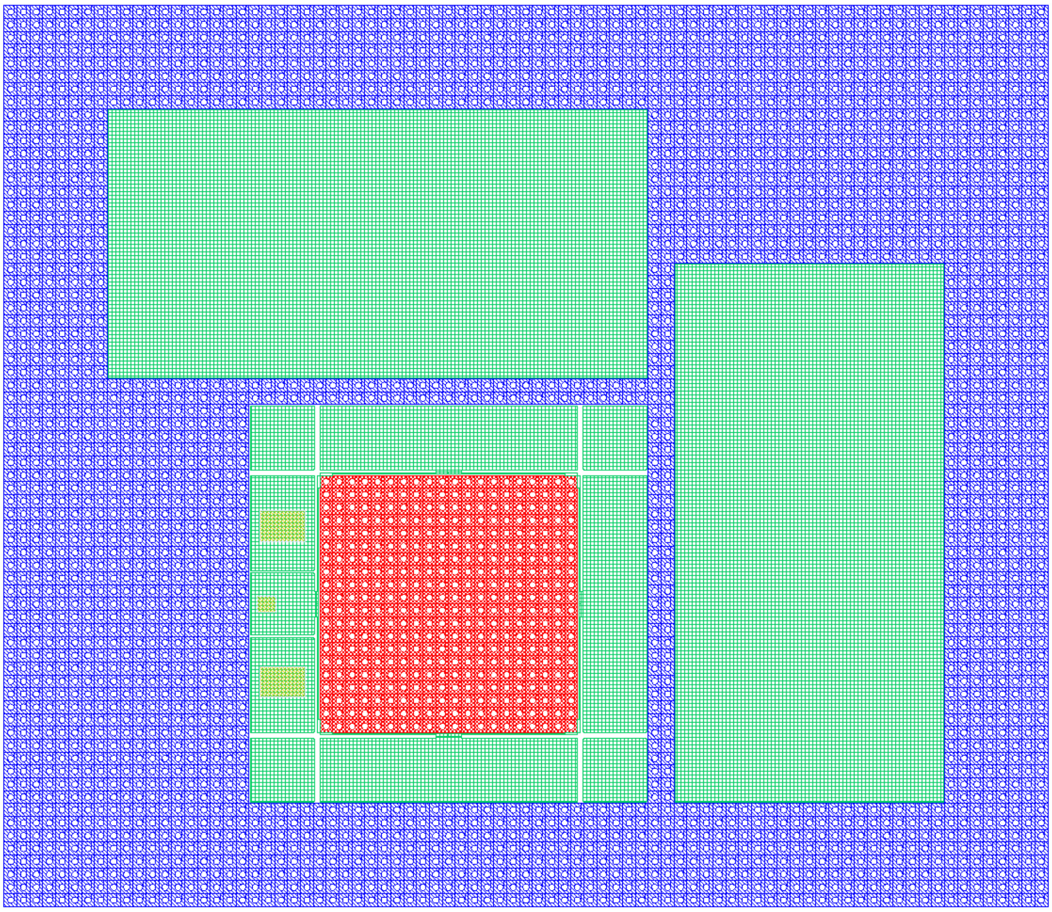

Figure 6.6: BEpi Structural DRIE Mask for both vertical and lateral axis accelerometers.

Table 6.1: Design and performance parameters of the vertical axis accelerometers for the suspended electrode on one side of the accelerometer.

Mechanical Property	Dimension	Performance	Value
Unit Dimensions	100µm x 100µm	Total Mass	1.9×10^{-7} kg
Hole Radius	25µm	Rest Capacitance	28.4 pF
No. of Holes	400	Spring Constant	222 N/m
Thickness	25µm	Resonance Freq.	5482 Hz
Capacitive Spacing	1µm	Cap. Change1g	239 fF
Spring Length	800µm	Open Loop Range	120 g
Spring Height	7µm	Closed Loop Range	116 g
Spring Multiplier	8	Damping	0.055
		Mechanical Noise	161µg/√Hz

6.2.4 Anchor Mask

This mask defines the recesses that will be opened on the glass wafer on which the structures will be anodic bonded. Bottom of the vertical accelerometers and place for the pads are opened using this masking layer. Bottom of the lateral axis accelerometers are not etched in this step since their bottom surface will be directly bonded to the glass substrate. Also three air channels are opened for the bottom electrode of vertical accelerometer which will prevent that region to be in vacuum. Figure 6.7 shows the anchor mask for the vertical and lateral axis accelerometers and the air channels opened on the anchors.

6.2.5 GMetal (Glass Metallization) Mask

Glass metallization mask defines the pads and metal lines of the bottom electrode and proof mass of the vertical axis accelerometer. During the bonding of the first SOI to glass wafer, metal lines on the glass wafer are aligned with the vias opened on the SOI wafer and this way electrical connection to the proof mass is carried to the pads.

There is an additional metal shielding layer just beneath the bottom electrode of the vertical accelerometer. During anodic bonding, high bonding voltages around 1000V is applied between glass and silicon surfaces. This voltage would pull the suspended bottom electrode of the vertical accelerometer towards the glass and since the stiffness of the springs are too high; they would break with this high amount of voltage. In order to prevent this, metal shielding layer is placed under the bottom electrode of the accelerometer which would be charged to same potential during the process and with this additional electrode, pulling potential can be completely canceled.

In order to obtain a high quality bonding, every silicon and glass surface should be electrically connected to the bonding potential. In SOI^2 mask set bottom electrode of the vertical accelerometer is completely isolated from the rest of the structures therefore electrical potential could not be applied to these surfaces. Using the glass metallization mask, bottom electrode and proof mass pads are connected to solve this problem. Metal lines can be trimmed with laser after fabrication. Figure 6.8 shows the glass metallization mask and the shielding layer sputtered below the bottom electrode of the vertical accelerometer.

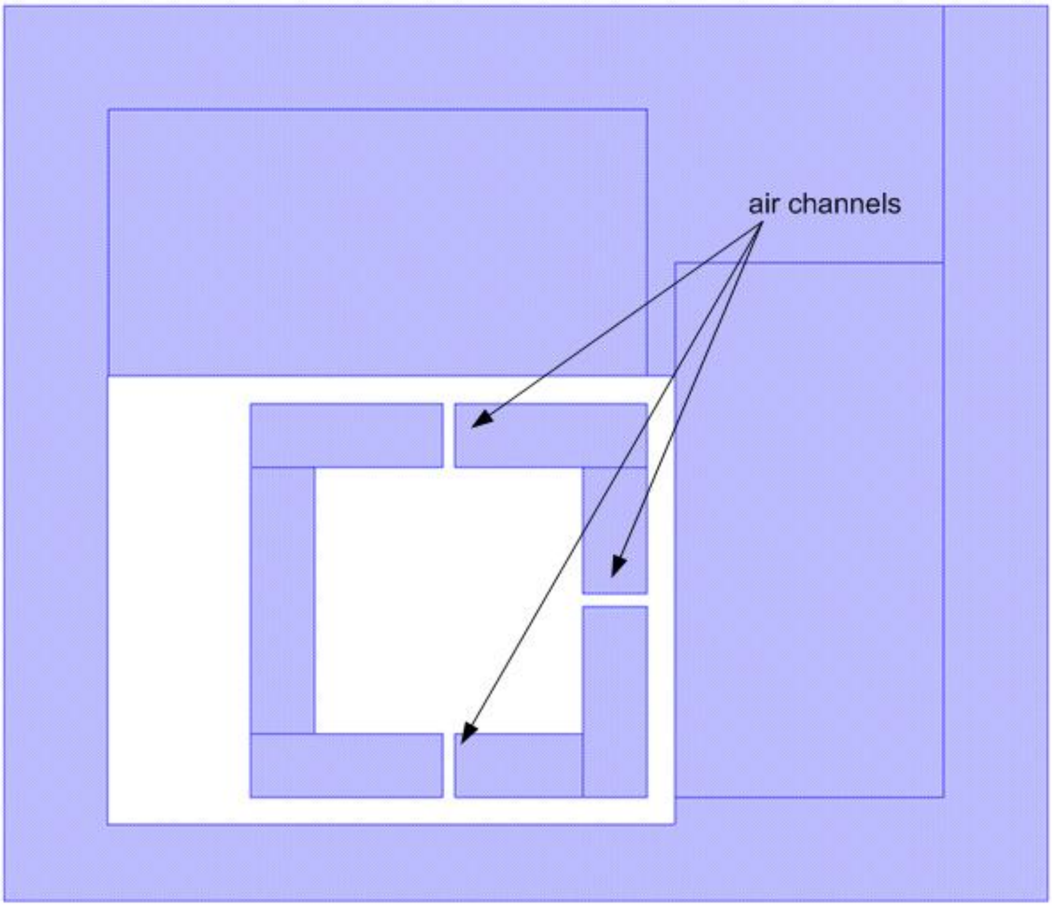

Figure 6.7: Anchor mask for the vertical and lateral axis accelerometers and the air channels opened on the anchors.

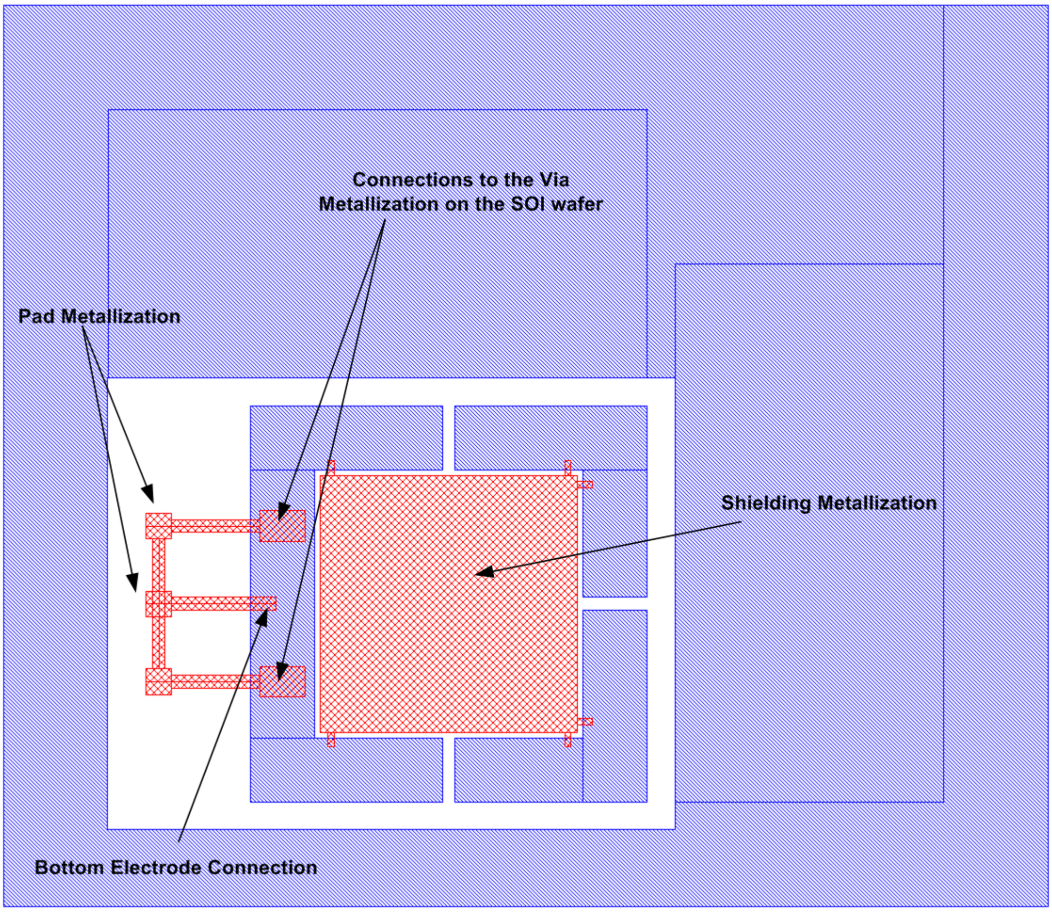

Figure 6.8: Glass metallization mask and the shielding layer sputtered below the bottom electrode of the vertical accelerometer

6.2.6 BHandle (Bottom Handle) Mask

After the bonding of the glass and silicon wafers, handle wafer of the bottom SOI is etched with the "Bottom Handle Mask". Gold sputtered on the handle layer of the SOI wafer is patterned with this mask and remaining gold layer is used as the DRIE mask. Figure 6.9 shows the bottom handle mask that will be used to pattern the handle layer of the bottom SOI wafer. In this figure regions shown with red will be removed as a frame after the DRIE and the regions shown with grey will remain as the anchors for the top SOI wafer. Gold masking layer on top of these grey areas will not be removed after DRIE, since they will be used as the bonding medium between handle layers of the top and bottom SOI wafers.

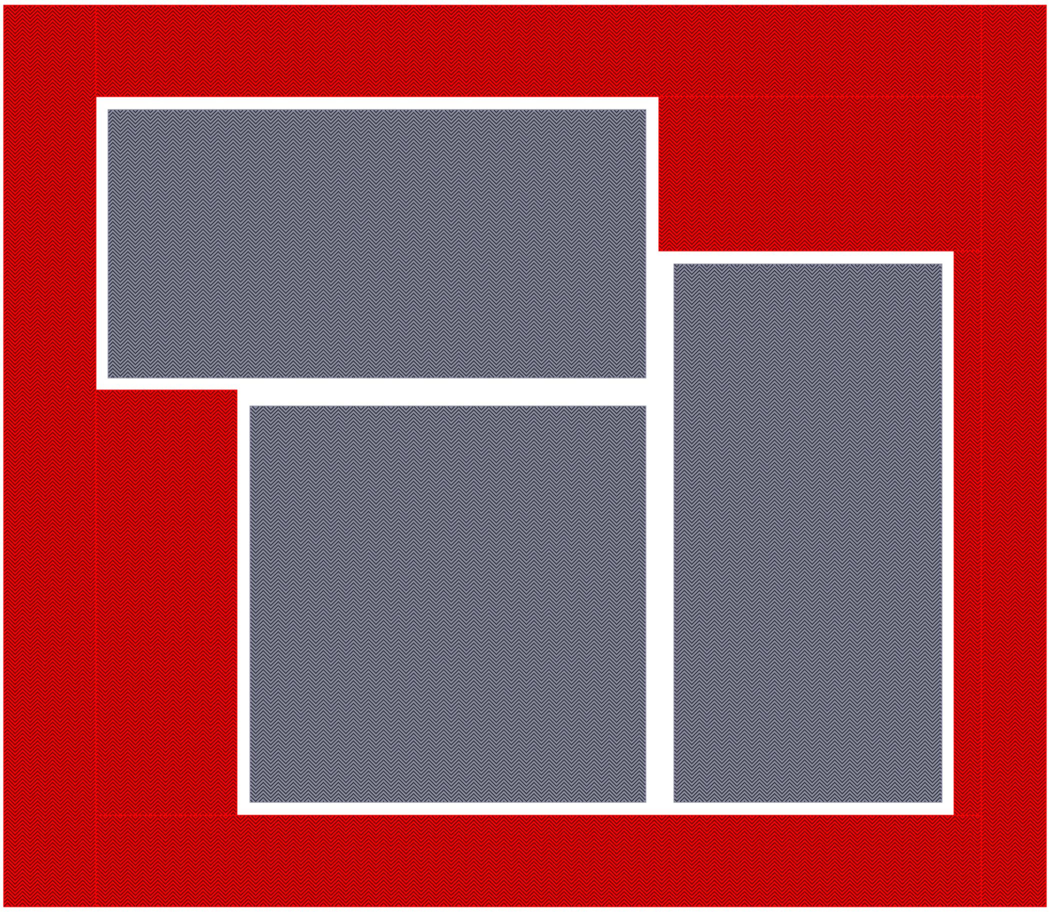

Figure 6.9: Bottom handle mask that will be used to pattern the handle layer of the bottom SOI wafer.

6.2.7 THandle (Top Handle) Mask

Top Handle is the first mask in the process that will be applied to the second SOI wafer. This mask is very similar to the previously used "Bottom Handle Mask" since the regions that are not etched with DRIE will overlap with the regions on the bottom SOI wafer for metal to metal bonding. The only difference between two masks is the bottom of the lateral axis accelerometers which are etched in the top SOI wafer. Parasitic stray capacitances are a very important problem for SOI accelerometers and, by removing the bottom of the lateral accelerometers this problem is reduced significantly. The frame around the structures will also be removed after oxide etching of the top SOI wafer. Figure 6.10 shows the layout of the handle etch mask for the top SOI wafer of SOI^2 process.

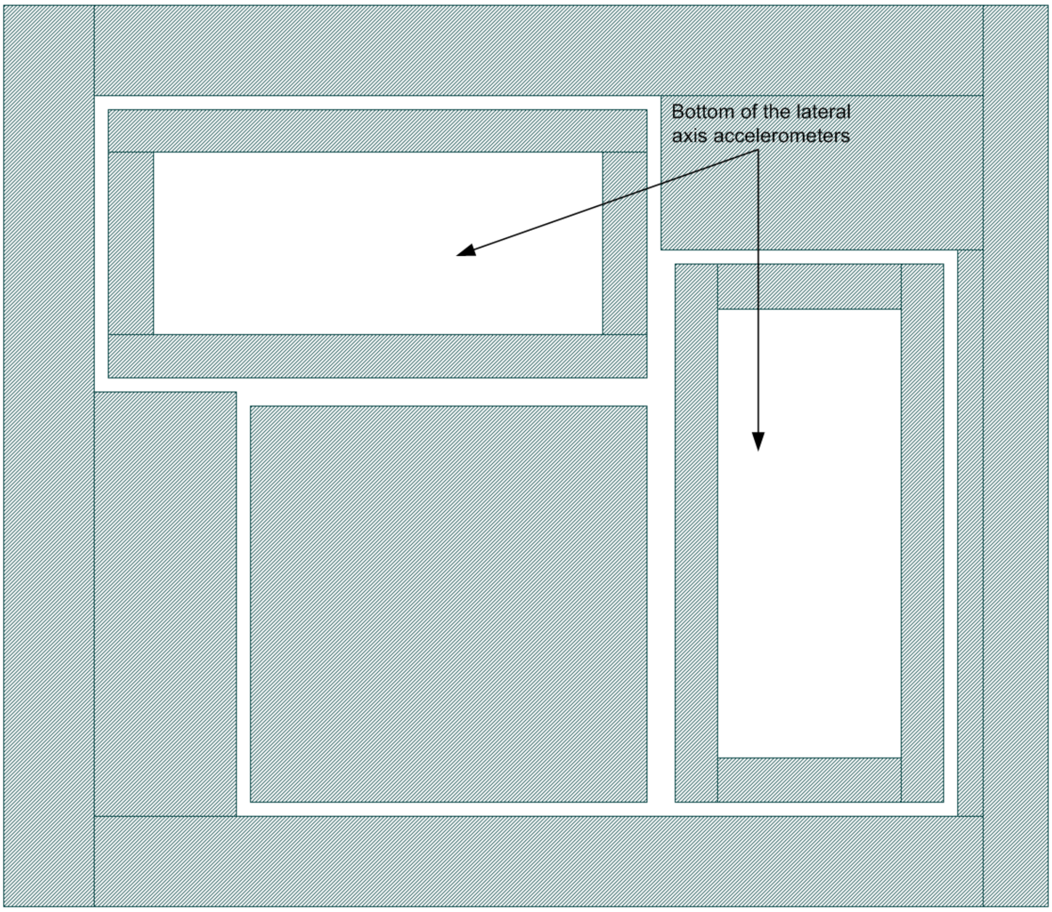

Figure 6.10: Layout of the handle etch mask for the top SOI wafer of SOI^2 process.

6.2.8 TMetal (Top Metal) Mask

After bonding the handle surface of the second SOI wafer to the previously prepared SOI + glass wafer pair, top metallization for the lateral and vertical axis accelerometers is coated over the device surface on the upmost SOI wafer. Figure 6.11 shows the metal connections for the lateral axis accelerometers and top electrode for vertical accelerometers.

6.2.9 TEpi (Top Epitaxial) Structural Mask

This is the second mask defining the properties of the designed accelerometers. In the "Bottom Epitaxial Structural Mask" performance of the vertical axis accelerometer were defined. In "Top Epitaxial Structural Mask", top electrode of the vertical accelerometer, having matched performance parameters with the bottom electrode, is defined and patterned with DRIE. In addition to this, structures of the lateral accelerometers are also defined in this mask layer. For lateral acceleration measurement, capacitive type differential finger architecture is employed during the accelerometer design. Figure 6.12 shows the layout of the "Top Epitaxial Mask" which defines the structures of the lateral accelerometers and top electrode of the vertical accelerometer. Like the "Bottom Epitaxial Structural Mask" regions shown with red is the frame of this layer and it will be removed after HF or vapor HF release of the top epitaxial layer. Regions shown with green are the anchors and regions shown with blue are the structures suspended after the oxide removal process. For this first fabrication trial two different types of lateral accelerometer designs are prepared having 2μm and 3μm capacitive finger spacing's. Table 6.2 lists the design dimensions and performance parameters of the lateral axis accelerometers for 2μm and 3μm finger spacing's.

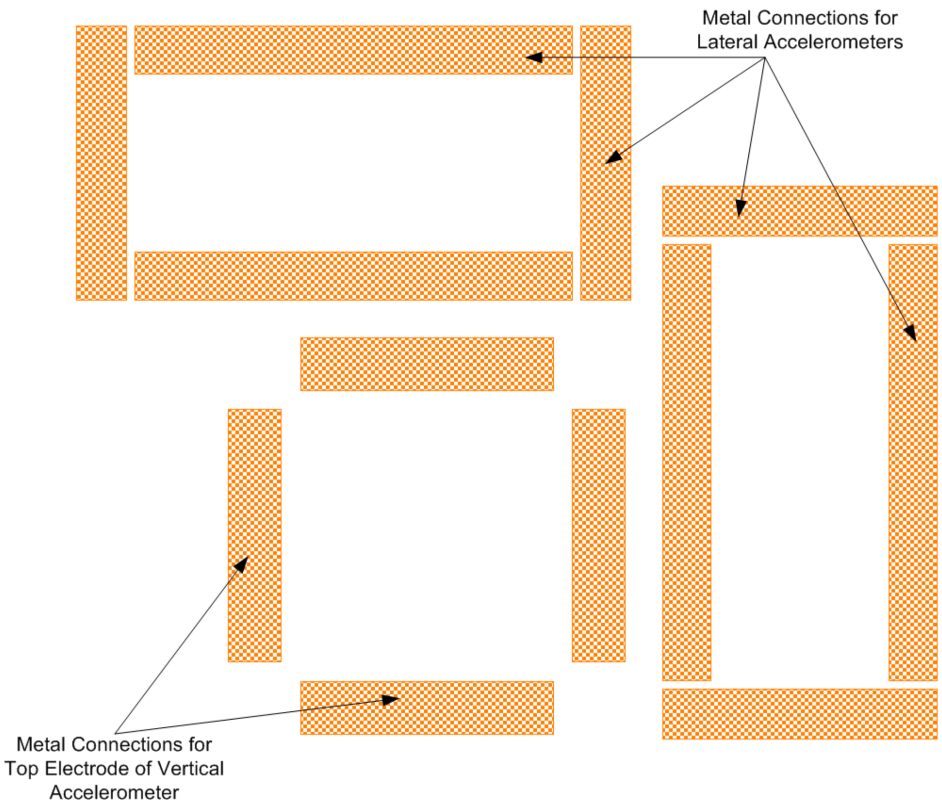

Figure 6.11: Metal connections for the lateral axis accelerometers and top electrode for vertical accelerometers

Table 6.2: Design dimensions and performance parameters of the lateral axis accelerometers for 2µm and 3µm finger spacing's.

DESIGN DIMENSIONS		PERFORMANCE PARAMETERS		
Mechanical Property	Dimension	Performance	2µm	3µm
Unit Dimensions	100x100µm^2	Total Mass	1.2x10^{-7} kg	1.1x10^{-7} kg
Hole Radius	25µm	Damping	19x10^{-4}	4.6x10^{-4}
No. of Holes	33x5	Spring Constant	35	35
Thickness	25µm	Rest Capacitance	7.5pF	4.2pF
Spacing	2µm/3µm	Resonance Freq.	2690Hz	2781Hz
Anti Spacing	8µm/12µm	Cap. Change1g	101fF	34fF
Spring Length	400µm	Open Loop Range	58g	93g
Spring Height	7µm	Closed Loop Range	18g	7g
No. Of Fingers	137/113	Mechanical Noise	45.8µg/√Hz	24.2µg/√Hz

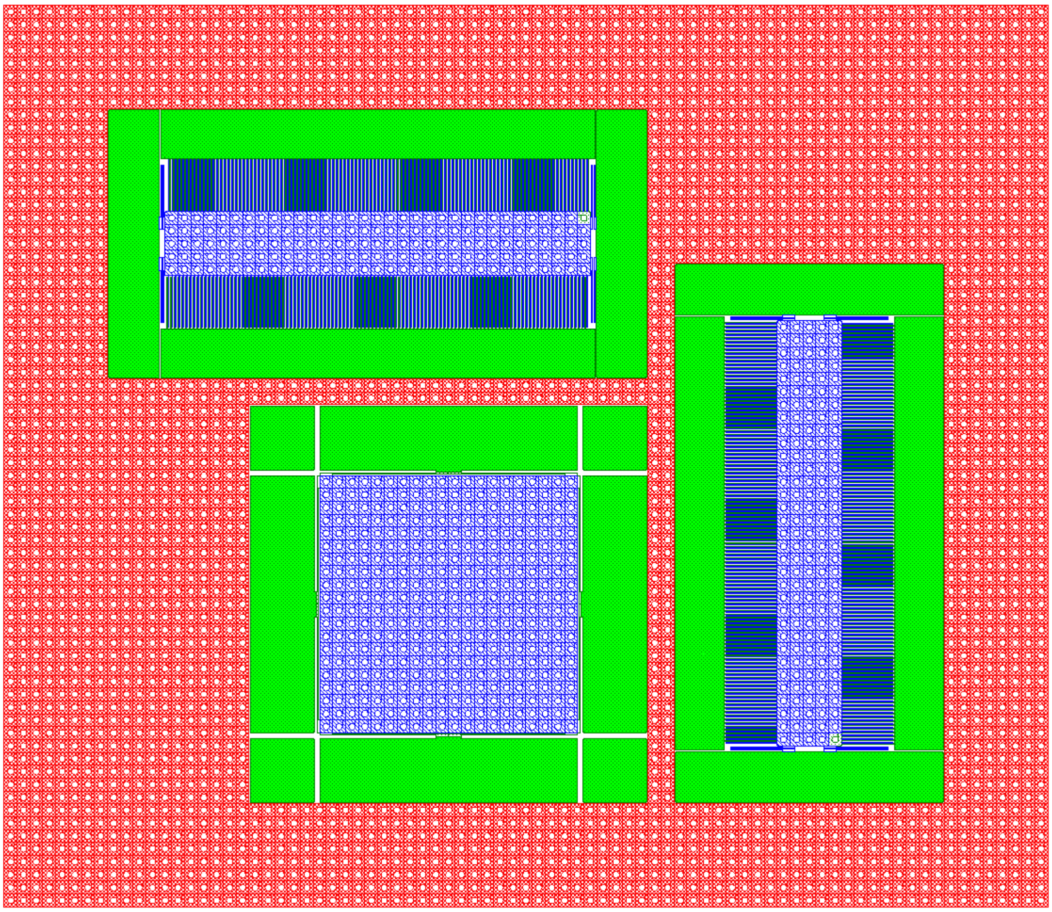

Figure 6.12: Layout of the "Top Epitaxial Mask" which defined the structures of the lateral accelerometers and top electrode of the vertical accelerometer

6.3 First Fabrication Trial

After the sensor design SOI^2 process and mask set is completed, masks are fabricated in the METU MEMS Research Center Facilities and the first fabrication trial was initiated. Process is conducted according to the process flow given in section 6.1 of this thesis and first two masks are successfully completed. First the via holes are opened on the device layer of the first SOI wafer, then whole wafer is sputtered with chromium and gold in order to electrically connect the bottom handle layer of the SOI wafer to the top device layer. After the sputtering, metallization is patterned with “BMetal” mask to remove the excess gold from the surface of the wafer. Figure 6.13 shows via regions formed by etching the 25µm thick device layer with KOH. 1µm thick buried oxide is removed afterwards and whole region is covered with Cr/Au for electrical connection. After the preparation of via holes, glass recess opening and glass metallization processes are also successfully completed.

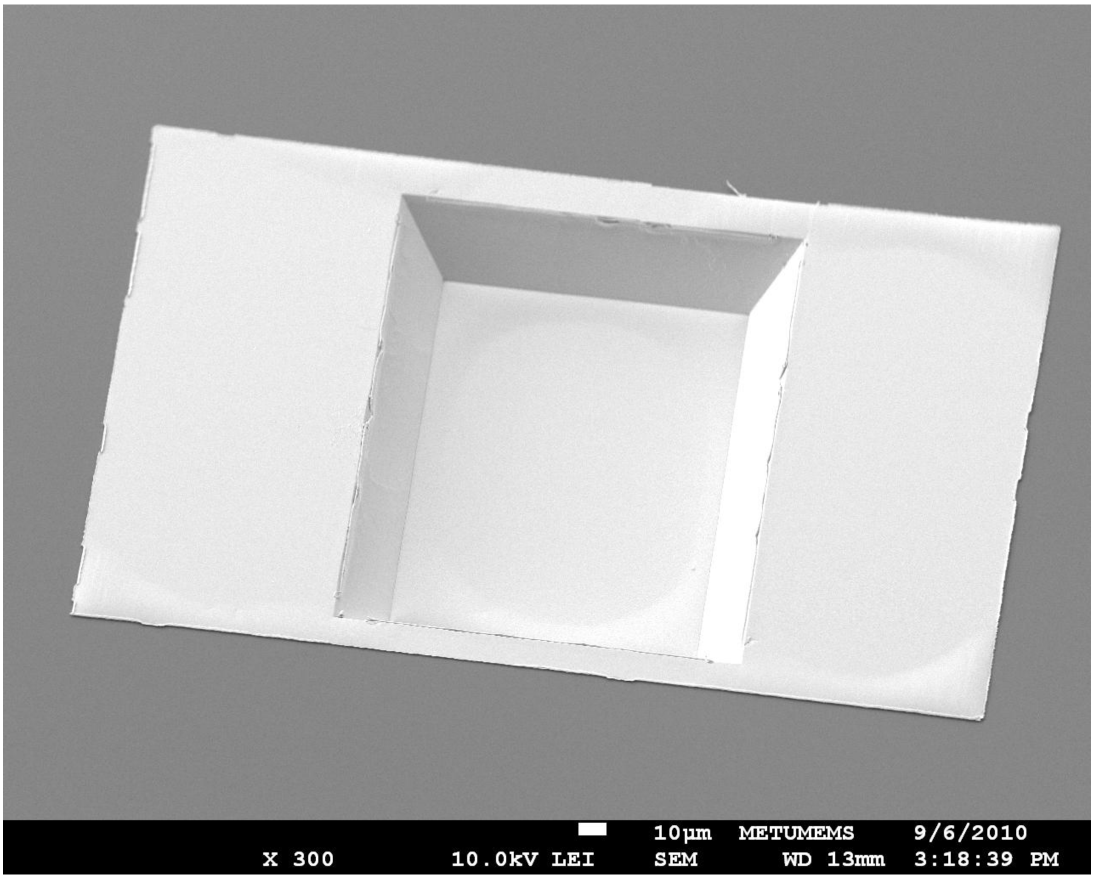

Figure 6.13: Via regions formed by etching the 25µm thick device layer with KOH. 1µm thick buried oxide is removed afterwards and whole region is covered with Cr/Au for electrical connection.

After the metallization for via's are formed, "Bottom Epitaxial Structural Mask" is patterned on the device layer and structures are formed with DRIE. In order to release the suspended structures, and remove the frame around the devices wafer is dipped into 48%HF facing downwards. According to literature etch rate of 48% HF should be ~2.5μm/min. [107] At the end of the required time in the first trial frame of the wafer was not released yet, therefore the etching period is increased up to 30minutes. When 30 minutes is over, huge frame covering all SOI devices were still in place, on the other hand large anchor regions which have 200μm x 200μm dimensions are started to peel off from the SOI wafer surface. This much HF etching also damaged the metal contacts around and inside via regions. Figure 6.14 shows the damaged via regions after 30 minutes of HF etching. In Figure 6.14.a HF tried to strip the metallization from the surface by pushing it upwards from the edges. In Figure 6.14.b metal connection in via region is completely lost.

A quick search in the literature [108], [109] revealed that, capillary forces of the drying liquid cause sticking of the frame to the handle layer of the SOI wafer after the removal of the buried oxide. The main reason of this problem is due to the large surface areas of the frame covering all devices around the wafer surface. According to [109] it is not possible to avoid this problem unless thicker or shorter devices are used. Peeling of the 200μm x 200μm devices also supports this claim. Therefore using this information a new "Bottom Epitaxial Structural Mask" is prepared by dividing the large frame surrounding all devices on the wafer into much smaller pieces which do not exceed 1mm x 1mm in dimensions. Figure 6.15 shows the second "Bottom Epitaxial Structural Mask" which has a frame divided into smaller pieces. With this second mask a new fabrication trial is conducted in order to optimize the HF etching phase. After DRIE wafer is again dipped in to 48% HF facing downwards. This time around 12-13 minutes small suspended frames start to leave the surface as desired. After 2-3 minutes of extra etching wafer is removed from HF and put into Di-water for cleaning. Although around 95% of the frame pieces are removed from the surface there was still few pieces stick to the handle layer of the SOI wafer. Some of these pieces could be removed from the surface of the wafer in buzzer at 10-20% of the full ultrasonic power. But this step may damage the springs and other suspended structures if the ultrasonic power is too high.

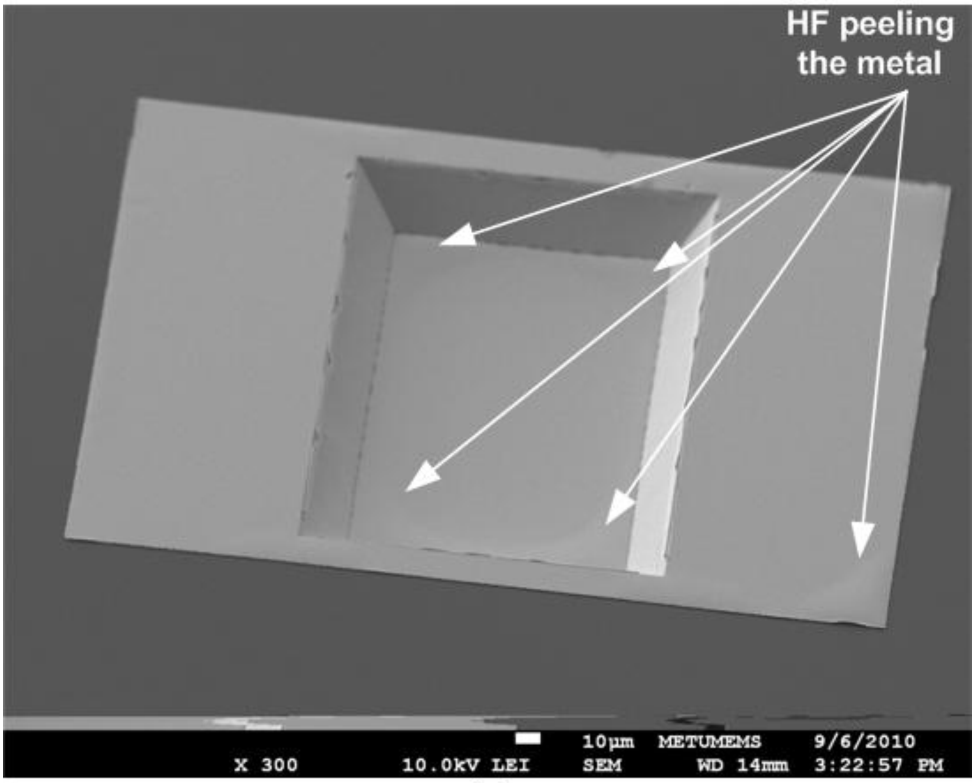

(a)

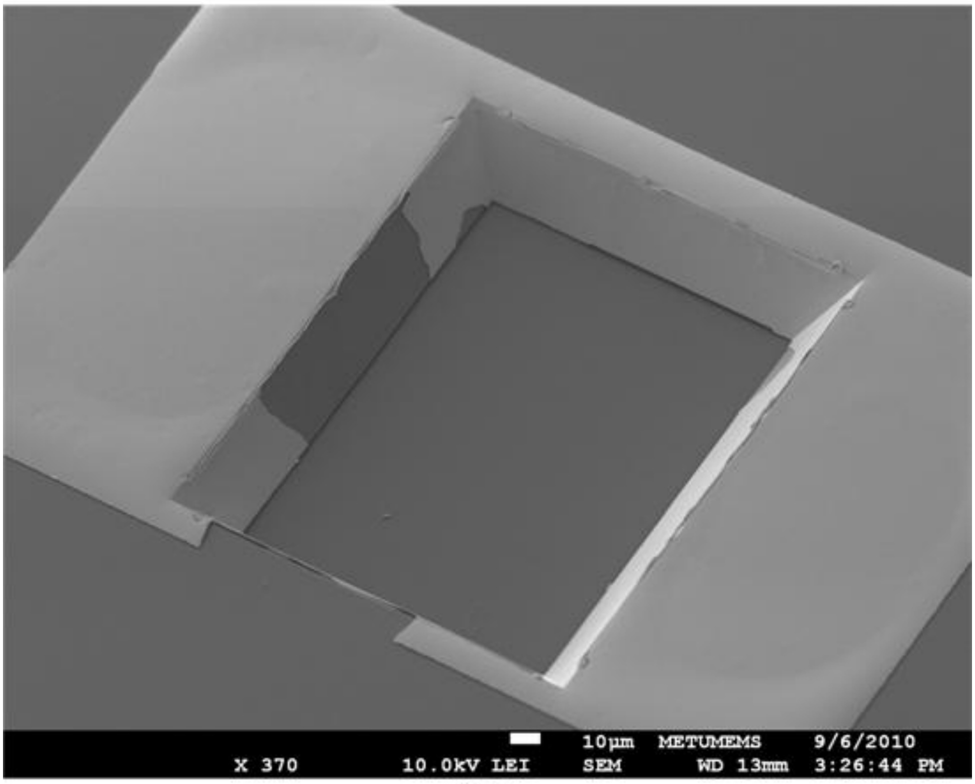

(b)

Figure 6.14: Damaged via regions after 30 minutes of HF etching (a) HF tried to strip the metallization from the surface by pushing it upwards from the edges (b) Metal connection in via region is completely lost

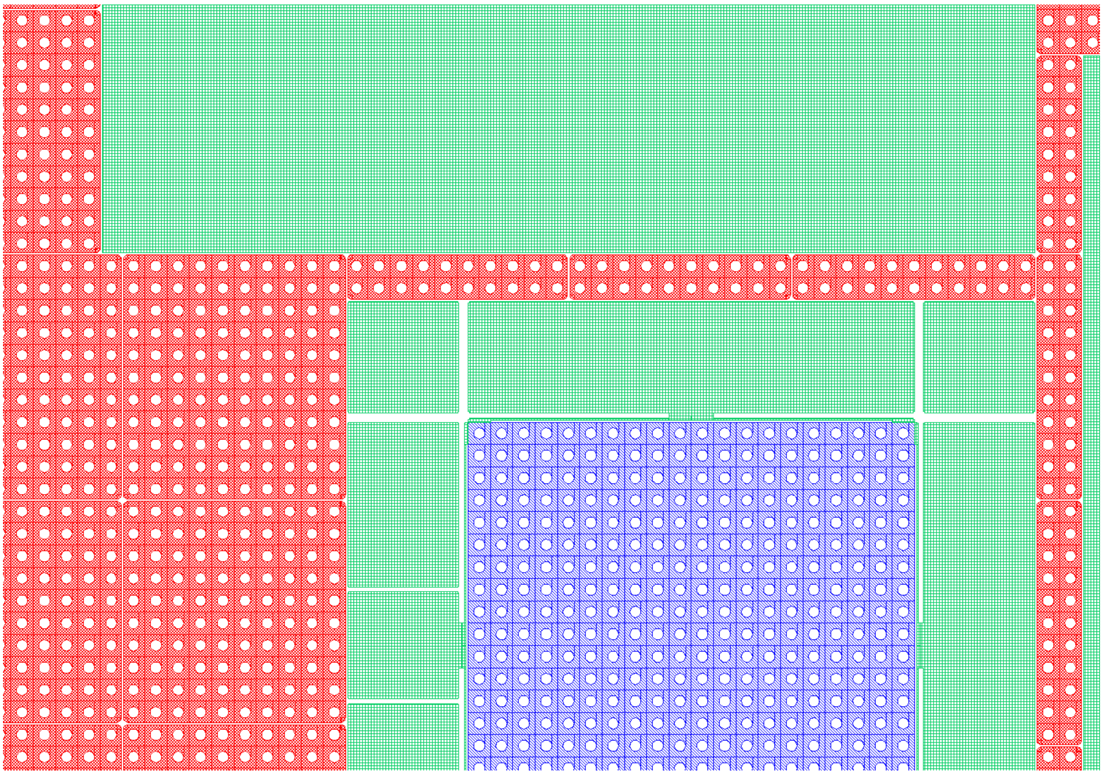

Figure 6.15: Second “Bottom Epitaxial Structural Mask” which has a frame divided into smaller pieces.

After this second fabrication trial, wafers are cleaned in successive acetone, IPA and methanol steps and dried on the hot plate at 80^0C. Capacitive measurements made on the fabricated accelerometers revealed that all electrodes that should be suspended after the fabrication is stuck to the handle layer of the SOI wafer. Figure 6.16 shows the SEM pictures of the fabricated bottom electrodes of vertical accelerometers most of which are stuck to the handle layer of the SOI wafer.

A third fabrication trial is done by drying the released wafer in critical point dryer. Since the surface of the wafer becomes completely hydrophobic during HF etching, it should never leave the liquid during drying procedure. After HF etching, etchant is diluted by adding excess amounts of Di-water. Than the wafer is placed into isopropyl alcohol and placed into critical point dryer for drying. Devices fabricated in this third trial are tested under the probe station for capacitance measurement and it is observed that 4 out of 48 vertical accelerometer electrodes are suspended successfully. But this ratio is still too low for a three axes fabrication and removal of the silicon dioxide with vapor HF is necessary in order to improve the yield.

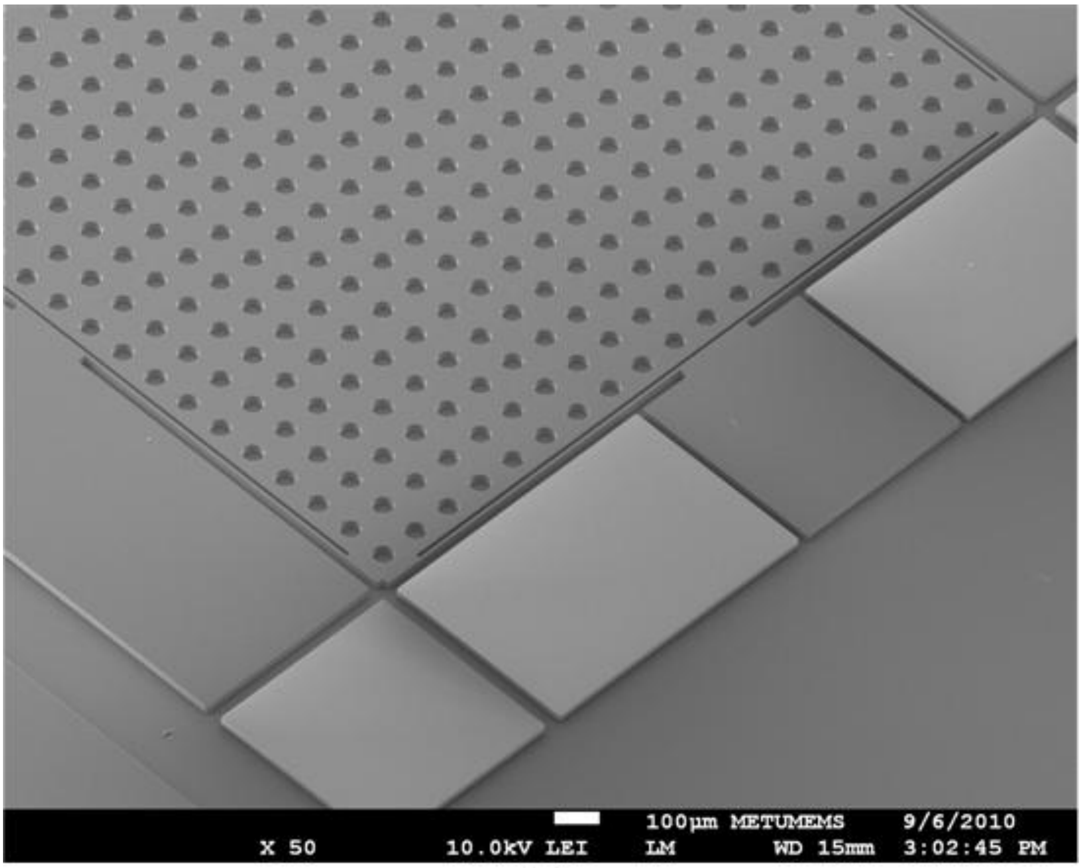
100µm METUMEMS 9/6/2010
X 50 10.0kV LEI LM WD 15mm 3:02:45 PM

(a)

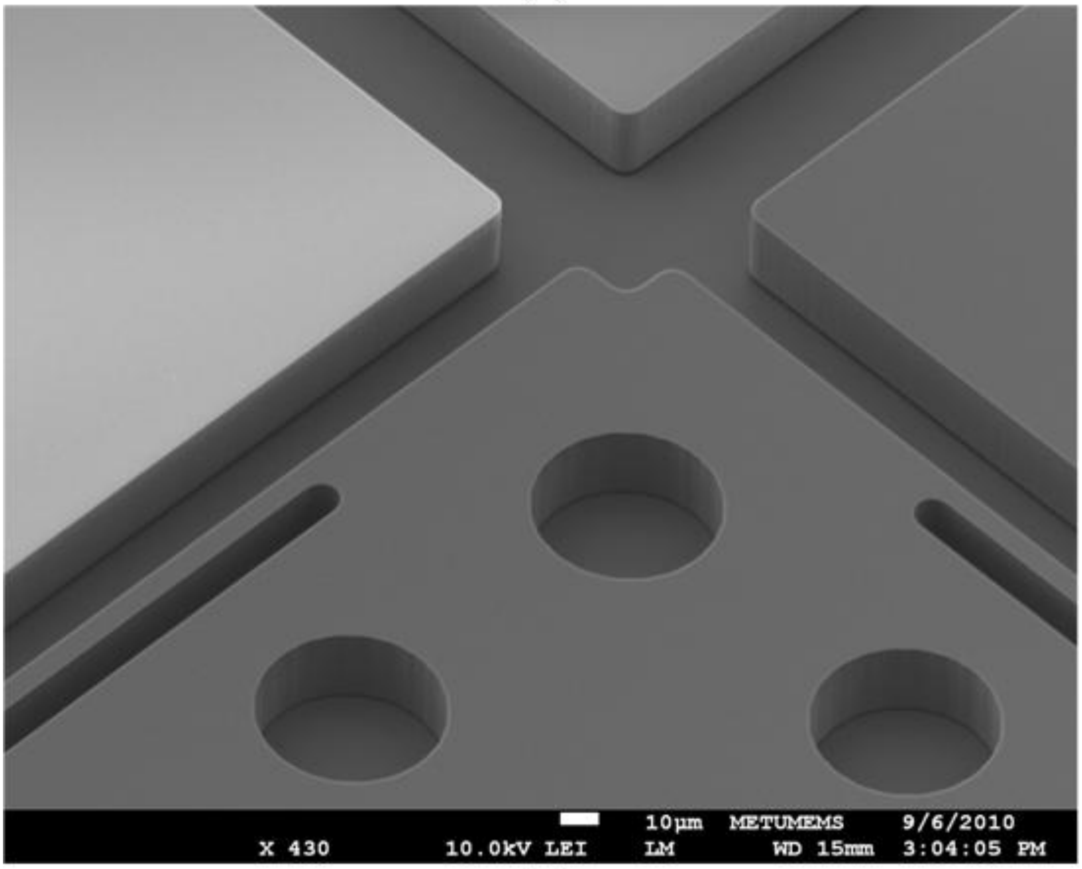
10µm METUMEMS 9/6/2010
X 430 10.0kV LEI LM WD 15mm 3:04:05 PM

(b)

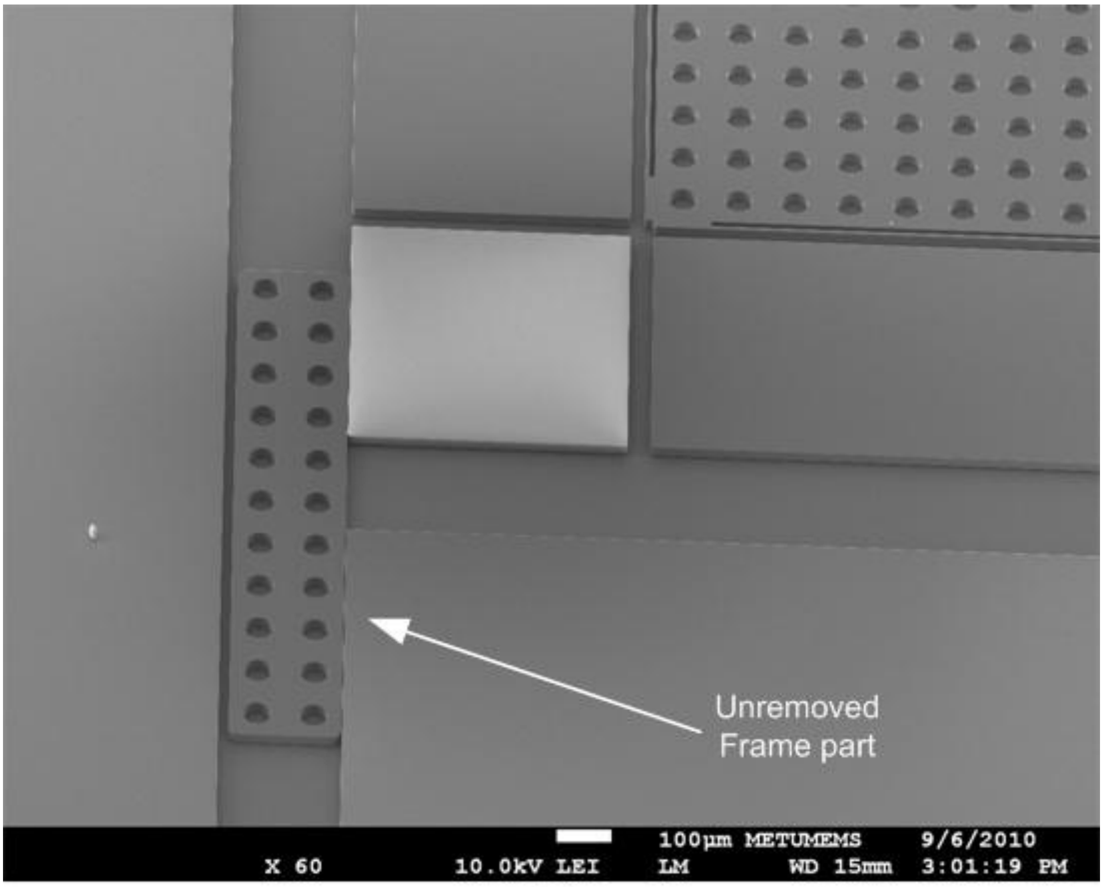

(c)

Figure 6.16: (a), (b), and (c) SEM pictures of the fabricated bottom electrodes of vertical accelerometers most of which are stuck to the handle layer of the SOI wafer.

6.4 Summary of the Chapter

In the scope of this thesis a three axes accelerometer fabrication technique is proposed. Three axis accelerometers in the literature are mostly fabricated with post CMOS surface micromachining techniques, which end up with low structural thicknesses, low sensitivity and buckled structures due to high internal stress of the device layer. The accelerometers fabricated with bulk micromachining have either low measurement range or high cross axis sensitivity.

With the SOI^2 fabrication technique proposed in this thesis highly symmetrical, totally decoupled, high performance monolithic accelerometers can be achieved. In this process two SOI wafers are employed to realize the top and bottom electrodes of the vertical accelerometers and device layer of the top SOI wafer is also used for lateral accelerometers.

After the sensor design and fabrication of the masks, three fabrication trials are conducted. In first two trials several problems are encountered related with the capillary forces of the drying liquids. In order to overcome this problem critical point dryer is employed and problem is partially solved by increasing the bottom electrode release yield from 0% to 8.3% which is still low. At the end of this study it is concluded that employing vapor HF to etch silicon dioxide may be the key to successfully release the suspended structures.

CHAPTER 7

CONCLUSIONS AND FUTURE RESEARCH

Objective of this study is to develop a micromachined three axes accelerometer system for tactical grade applications. There are many different types of micromachined accelerometers in the literature or market, but for this study capacitive MEMS accelerometers are chosen because of their many advantages like low fabrication cost, low power consumption, high sensitivity, and high reliability as well as low nonlinearity, low temperature dependency, low noise, and low drift. A tactical grade accelerometer should be operating in mid range accelerations like 10-30g and with a high linearity. Therefore closed loop readout architecture is preferred to be used for this system since open loop circuits have bad linearity at high operations ranges and they are not suitable for tactical grade accelerometer systems. Three different fabrication procedures are used for the fabrication of these accelerometers. These are silicon-on-glass (SOG) fabrication process, dissolved wafer process (DWP) and dissolved epitaxial wafer process (DEWP). Results of these fabrications are evaluated and compared by a series of tests both at sensor and system level. At the end of these tests, accelerometers having similar performances are brought together and packaged in order to form three axes accelerometer system which is able to measure accelerations applied in three orthogonal axes. All three axes of the fabricated accelerometer package are tested and all performance specifications are extracted. Though operation of the three dimensional accelerometer package is verified, there were problems originating from the packaging of these accelerometers. First problem is that packaging of the accelerometers were extremely difficult, especially during the placement and wire bonding of the z-axis accelerometer, sensors on the other axes can be damaged. In addition to these since these sensors are placed by hand, it is inevitable to have axis misalignment between the three orthogonal axes. In order to solve these problems, a new three dimensional monolithic accelerometer process is proposed. This process was consisting of 9 masks and all three axis accelerometers could be fabricate at the same time which are oriented to each other orthogonally without further packaging effort.

Following conclusions can be drawn based on the studies and goals achieved during these studies:

1. Verification of the performance parameters given in the literature is done by MATLAB simulations. Accelerometer models for both closed loop and open loop are constructed and important performance parameters like measurement range, bandwidth, resolution, non-linearity, and dead-zone concepts are verified during these simulations. Effects of mechanical dimensions and parameters on the performance of the accelerometers are extracted and could be completely formulated. During the verification procedure it was noticed that the formulation given in the literature for mass residual motion was not sufficient to completely model this noise source. Assumptions made during the extraction of this model, like the fixed oscillation frequency was found to be over suppressing the calculated values. Because assuming that the proof mass is oscillating in a single frequency is actually assuming that the accelerometer is operating in the dead zone. In this region proof mass of the sensor is locked in such an oscillating stage that certain acceleration values below dead-zone threshold could not disturb this equilibrium position, therefore externally applied acceleration values could not be successfully measured. From these observations, it can be concluded that in order to estimate noise value of an accelerometer system, simulation results should be taken as a reference instead of equations given in [4], [82], and [84].

2. Silicon on glass (SOG) technique is employed as the first fabrication procedure for accelerometers. This technique utilizes bonding of 100µm thick silicon wafer to a glass wafer. Structures are etched through the silicon wafer and an aluminum shield is used to prevent DRIE notching. With this

process accelerometers could be fabricated at very high yields and they were demonstrating repeatable performances. Measured noise density values were below 20μg/√Hz which is far better than many tactical grade accelerometers in the literature. But the measurement range of the accelerometers was very low. ±2.5g measurement range was not sufficient for a tactical grade accelerometer system. The reason for low measurement range was the structural thicknesses of the sensors fabricated with this process. Due to 100μm thick structures it was not possible to open spacing of fingers less than 3.5 - 4μm's which limits the sensitivity and range of the accelerometers considerably. In addition to this, sensors have high proof masses due to their 100μm structural thickness which decreases the mechanical (Brownian) noise of the devices and increases the closed loop stability, but this is also another limit on the operation range. Therefore it was concluded that in order to reach high operation ranges, a process with narrower finger spacing and lighter mass should be employed to fabricate accelerometers.

3. DWP is conducted in two phases. In the first phase four different accelerometer designs were made and fabricated. Designed accelerometers had 0.8μm finger spacing for high operation ranges. Among these 4 designs only one of them was successfully fabricated with a very low yield. Therefore second phase of the fabrications started with improving the working design from the previous phase. Finger spacing of this design is increased from 0.8μm to 1μm in order to increase the yield. 6 DWP runs with a mask set shared with gyroscopes are completed. Many sensors could be successfully fabricated from these fabrications but very few were demonstrating performances close to their design values. Major reason for the low yield of this design was the 440μm long finger lengths combined with the buckling of the sensors after the fabrication due to the high internal stress of the boron doped layers. It was concluded from these results that a new design should be done in order to decrease the finger lengths and effect of the buckling on the performance of the accelerometers.

4. A MATLAB optimization algorithm is written, in order to find the optimum accelerometer design suitable for DWP. Using this algorithm every changeable physical parameter is swept within its boundaries and process limits are explored. Using the results of this parametric analyzes an optimum design is selected among different possibilities and a new mask set is prepared. This new mask set continues only accelerometers with 80 sensors from the previous design having 440μm finger lengths and 76 sensors from the new optimized design. 5 more fabrication runs with this full wafer accelerometer mask set is finalized in the scope of this study. During these fabrications many accelerometers are fabricated but most of these accelerometers could not even pass sensor level capacitance measurement tests unlike the expectations. Buckling of the devices at the end of the fabrications were still very high, and the fingers were touching each other during the operation which causes undesired voltage spikes at the output of the sensors. 9 accelerometers are tested at system level together with second order closed loop sigma-delta readout circuitry and among these accelerometers, best obtained results was belong to DEWP5J06 with a noise density of 153μg/√Hz and bias drift of 50μg with a nonlinearity of 0.38% operating within ±33.5g range. These performance results achieve highest dynamic range among the tactical grade accelerometers with a second order sigma-delta readout architecture which operates over 30g range. Although achieving such high performances, it was concluded that a new fabrication technique is necessary in order to eliminate the internal stress and the buckling problem of the accelerometers.

5. The internal stress of the DWP wafers were originating from the disorientation of the crystal structure of silicon due to the doped boron atoms. In order to overcome this problem and increase the yield of the DWP, boron doped silicon wafers are replaced with 35μm highly doped epitaxial growth silicon wafers with 1% Ge doping which prevents the buckling of the wafer after the release of the sensors. Mask set is also changed by increasing the finger spacing form 1μm to 2μm's and more access is provided by opening larger holes in the anchor regions to the bottom of the devices. These

changes improved the yield by ~20-25 times from 2-3% up to 45-50% wafer vise. With these changes accelerometers having repeatable performances with noise floor around 150-200μg/√Hz, bias drift around 150μg and operation range higher than 10g could be fabricated in large numbers.

6. High number of accelerometers fabricated with increased process yield enables the construction of a three axes accelerometer system. By orthogonally placing three accelerometers fabricated with DEWP2μm process in a specially designed package, an accelerometer system able to measure in three orthogonal axes is constructed. This system is tested in three axes simulator installed at ASELSAN Akyurt facilities and results showed that all three axes was successfully measuring acceleration in tactical grade performance limits.

7. Knowing that placing three accelerometers orthogonally is a very challenging task without axis misalignment and finding three identical accelerometers that will be capable to satisfy the same performance criteria's is very difficult, a new three axes monolithic accelerometer fabrication process is proposed in this study. In this fabrication technique all three axis accelerometers are fabricated in the same process flow and they are automatically aligned to each other orthogonally without further packaging effort after fabrication. Also accelerometers fabricated with this process are completely immune to cross axis sensitivity since all three axes accelerometers are fabricated on the same substrate as separate dies.

   Although the process steps seem to be very straight forward, few complications are experienced during the fabrication of the accelerometers. During the release of the bottom electrode of the accelerometer, HF is used to remove the buried oxide between the device and handle layers. But wet etching caused adhesion of the suspended structures due to the capillary forces of the drying liquids.

Although many goals are achieved and all objectives are successfully completed within this study, there are still some further improvements that can be done, in order to increase the performance of capacitive MEMS accelerometers. These possible improvements can be listed as follows:

1. In this study, it was observed that decreasing the finger spacing is very crucial to increase the measurement range of the accelerometers. On the other hand decreasing the finger spacing also decreases the yield of the wafers drastically. Yield of the SOG process having 3.5-4μm finger spacing were over 70%, while the yield of the DWP or DEWP having 1μm finger spacing could not exceed 5%. Wafer level test results also proved that increasing the spacing of the fingers from 1μm to 2μm's increased the yield of the fabrication up to 45-50% in DEWP. These results demonstrate a good correlation between the finger spacing and yield of the fabrication process. Therefore while designing an accelerometer system, operation range or system noise should not be the limiting factor for finger spacing. In order to obtain high performance and high yield fabrications, finger spacing should be the key design parameter.

2. It was observed that the mass residual motion of the closed loop accelerometer systems could not be successfully formulated in the literature yet. This problem is also reported in several other publications through the literature [85], [86]. Complete formulization of this motion is a very difficult task due to non-linear architecture of the closed loop readout circuits, but it is very important to fully understand this effect since mass residual motion is the major noise contributor of the closed loop system. Therefore a future study to extract a better theoretical approach would allow better understanding of system for sensor designers.

3. MEMS capacitive sensor fabrication is preferred over other techniques due to its high yield and low sensor cost. By taking this into account, several precautions are taken to increase the yield of the fabrication processes like increasing the finger spacing, opening holes through the anchors for easier access to the bottom of the suspended structures or adding more cleaning procedures to the fabrication processes. But none of these precautions stops the contamination of the sensors after fabrication. During testing, sensors are

heavily contaminated from the surrounding. In order to overcome this problem a wafer level packaging is necessary for protecting the dies after the fabrication. As a future study, a protective cap wafer can be designed, fabricated and integrated into the processes described in this thesis, in order to prevent further contamination.

4. In this study, a high performance tactical grade accelerometer was successfully fabricated with 33.5g operation range, 153μg/√Hz noise floor, 50μg bias drift and 0.38% non-linearity. When the performance results of this sensor are compared with literature, it surpasses all of its counterparts. But the yield of these fabrications was very low. In order to increase the yield, spacing of the fingers are increased but this time the accelerometers could not reach higher operation range values. As a conclusion it is understood that operation range and the yield of the sensor in inversely proportional and cannot be both maximized by just adjusting the mechanical dimensions of the designs.

   Therefore, an improvement in the accelerometer readout is necessary. According to equation 3.2 readout circuit has two important parameters affecting the operation range of the accelerometer. These are the feedback voltage and the pulse width percentage of the applied feedback voltage. Operation range is directly proportional with the pulse width percentage and the square of the feedback voltage. By increasing the feedback supply voltage from 5V to 10V the measurement range of the accelerometer can be increased by 4 times from 12.5g to 50g. Like every improvement made on the system, this one will also have an important drawback which is a linear increase of the major noise sources. But this drawback can also be overcome by changing the readout architecture from 2^{nd} order to 4^{th} order sigma-delta circuit. Simulations indicate that the noise density of the system can decrease below 40μg/√Hz as well as its operation range can increase over 30g with a fourth order sigma-delta readout architecture and DEWP accelerometers having 2μm finger spacing.

5. During the fabrication of the three axes SOI[2] process, release of the top and bottom electrodes of the z-axis accelerometer was a major difficulty. Due to the capillary forces of the drying liquid, capacitive electrodes having huge surface areas are sticking to the handle layer because of the thin 1μm spacing between these layers. According to the literature this effect cannot be completely prevented unless the dimensions of the devices are drawn very small [107]. In order to prevent this effect epitaxial layer in the dicing streets are divided into small parts which can be easily removed in HF etching but the 2mm x 2mm electrodes of the vertical accelerometers could not be decreased to this dimension since this time design will be effected and desired performance parameters could not be met. Therefore as a future study instead of wet removal of the intermediate oxide layer, vapor HF can be employed to solve this problem which requires special equipment.

As a conclusion, during this study many different designs and fabrication techniques are used to both improve the fabrication and performance of the accelerometers. In addition to these, using the theoretical approaches, an optimization algorithm is developed and high performance tactical grade accelerometers are designed. Test results of the fabricated accelerometers which are close to their design parameters, showed better performance than all of its counterparts in the literature. Also a new three axial monolithic accelerometer fabrication process is proposed in this study which is able to measure in three orthogonal axes and all three axes are fabricated on the same substrate.

REFERENCES

[1] Volant Technologies Web Site, “Accelerometer and Pressure Sensor MEMS History”, http://terahz.org/_html/22SensorChronology.html, last access: 28.08.2010.

[2] iSuppli Market Research Firm, newsletter June 2009. http://www.isuppli.com/Pages/Market-Research-Search-News.aspx, http://www.memsindustrygroup.org/images/newsletter/June2009/isuppli_figure1.jpg, http://www.memsindustrygroup.org/images/newsletter/June2009/isuppli_figure2.jpg, last access: 28.08.2010.

[3] M. Kraft, “Micromachined Inertial Sensors State of the Art and a Look into the Future”, University of Southampton.

[4] N. Yazdi, F. Ayazi, and K. Najafi, “Micromachined Inertial Sensors,” Proc. of the IEEE, Vol. 86, No 8, pp. 1640-1659, August 1998.

[5] C. Song, and M. Shinn, “Commercial vision of silicon-based inertial sensors,” *Sensors and Actuators*, A66, Samsung Advanced Institute of Technology, 1998.

[6] M. D. Pottenger, “Design of Micromachined Inertial Sensors,” PhD. Dissertation, Univ. of California, 2001.

[7] J. E. D. Williams, “From Sails to Satellites: The Origin and Development of Navigational Science,” New York, Oxford University Press, 1994.

[8] R. S. Seeley, “Micromachines Rev Up for Fast Growth,” Electronic Business Today, pp- 33-38, April 1996.

[9] R. L. Craik and C. A. Oatis (Eds.), “Gait Analysis: Theory and Applications,” Mosby, 1995.

[10] K. Miller, D. Hendelman, C. Baggett, E. Debold, and P. Freedson, "Validation of Accelerometry to Assess Moderate Intensity Physical Activity in the Field," Medicine & Science in Sports & Exercise, 31(5), pp.43, May 1999.

[11] Baldwin, C., Niemczuk, J., Kiddy, J., and Slater, T., "Review of fiber optic accelerometers," Proceedings of IMAC XXIII Conference & Exposition on Structural Dynamics, Society for Experimental Mechanics, January 31 - February 3, 2005

[12] R. F. Yazıcıoğlu, "Surface Micromachined Capacitive Accelerometers Using MEMS Technology," *M.S. Thesis*, Middle East Technical Univ., 2003

[13] V. Milanovi, E. Bowen, N. Tea, J. Suehle, B. Payne, M. Zaghloul, and M. Gaitan, "Convection-Based Accelerometer and Tilt Sensor Implemented in Standard CMOS," *Proc. Int. Mech. Eng. Conf. and Exp., MEMS Symposium*, Anaheim, Nov. 1998.

[14] A. A. Seshia, M. Palaniapan, T. A. Roessing, R. T. Howe, R. W. Gooch, T. R. Schimert, and S. Montague, "A Vacuum Packaged Surface Micromachined Resonant Accelerometer," *J. Microelectromechanical Sys*., Vol. 11, No. 6, pp. 784-793, Dec 2002.

[15] C.–H. Lui, and T. H. Kenny, "A High-Precision, Wide-Bandwidth Micromachined Tunneling Accelerometer," *J. Microelectromechanical Sys*., Vol. 10, No. 3, pp. 425-433, Sept. 2001.

[16] B. E. Boser, "Electronics for micromachined inertial sensors," International Conference on Solid State Sensors and Actuators, 1997, vol. 2, pp. 1169 – 1172.

[17] F. Rudolf, "A micromechanical capacitive accelerometer with a two-point inertial-mass suspension", Sensors and Actuators, 1983, pp. 191-198.

[18] M. Van Paemel, "Interface circuit for capacitive accelerometer," Sensors and actuators, 1989, vol. 17 (3 -4 PT2), pp. 629-637.

[19] H. Seidel, H. Riedel, R. Kolbeck, G. Mück, W. Kupke, and M. Königer, "Capacitive silicon accelerometer with highly symmetrical design", Sensors and Actuators: A. Physical, 1990, vol. 21 (1-3), pp. 312-315

[20] F. Rudolf, A. Jornod, J. Bergqvist, and H. Leuthold, “Precision accelerometers with μg resolution”, Sensors and Actuators: A. Physical, 1990, vol. 21 (1-3), pp. 297-302.

[21] E. Peeters, S. Vergote, B. Puers, and W. Sansen, “A Highly Symmetrical Capacitive Micro-Accelerometer with Single Degree-of-Freedom Response”, Transducers '91 , pp. 97-100.

[22] W. Yun, R. T. Howe, and P. R.Gray, “Surface micromachined, digitally force-balanced accelerometer with integrated CMOS detection circuitry”, Technical Digest- IEEE Solid-State Sensor and Actuator Workshop, 1992, pp. 126-131

[23] E. Abbaspour-Sani, R.-S. Huang, C. Yee Kwok, “Novel electromagnetic accelerometer”, IEEE Electron Device Letters, 1994, vol. 15 (8), pp. 272-273.

[24] Y. Matsumoto, M. Iwakiri, H. Tanaka, M. Ishida, and T. Nakamura, “Capacitive accelerometer using SBD-SOI structure”, International Conference on Solid-State Sensors and Actuators, and Eurosensors IX, Proceedings 2, 1995, pp. 550-553

[25] K.H.-L. Chau, S.R. Lewis, Y. Zhao, R.T. Howe, S.F. Bart, and R.G. Marcheselli, “Integrated force-balanced capacitive accelerometer for low-G applications”, International Conference on Solid-State Sensors and Actuators, 1995, and Eurosensors IX, Proceedings 1, pp. 593-596.

[26] B. Wenk, J. Ramos-Martos, M. Fehrenbach, P. Lange, M. Offenberg, and W. Riethmüller, “Thick polysilicon based surface micromachined capacitive accelerometer with force feedback operation”, Proceedings of SPIE - The International Society for Optical Engineering, 1995, pp. 84-94.

[27] M. Lemkin, B. E. Boser, “Micromachined fully differential lateral accelerometer”, Proceedings of the Custom Integrated Circuits Conference, 1996, pp. 315-318.

[28] B.P. van DrieEnhuizen, N.I. Maluf, I.E. Opris, and G.T.A. Kovacs, “Force-Balanced Accelerometer with mG Resolution, Fabricated using Silicon Fusion Bonding and Deep Reactive Ion Etching,” International Conference on Solid-State Sensors and Actuators, Proceedings 2, 1997, pp. 1229-1232.

[29] N. Yazdi and K. Najafi, “An All-Silicon Single-Wafer Fabrication Technology for Precision Microaccelerometers”, International Conference on Solid-State Sensors and Actuators, Proceedings 2, 1997, pp. 1181-1184

[30] B. P. Van Drieënhuizen, N. I. Maluf, “High resolution single crystal silicon accelerometer using silicon fusion bonding and deep reactive ion etching”, American Society of Mechanical Engineers, Dynamic Systems and Control Division (Publication) DSC 62, 1997, pp. 9-12

[31] B. Ha, B. Lee, S. Sung, S. Choi, M. Shinn, Y. Oh, C. Song, “A Area variable capacitive microaccelerometer with force-balancing electrodes”, Proceedings of SPIE - The International Society for Optical Engineering 3242, 1997, pp. 181-190.

[32] G. Zhang, H. Xie, L.E. de Rosset, and G.K. Fedder, "Lateral capacitive CMOS accelerometer with structural curl compensation", Proceedings of the IEEE Micro Electro Mechanical Systems (MEMS), 1999, pp. 606-611.

[33] N. Yazdi, A. Salian, K. Najafi, "High sensitivity capacitive microaccelerometer with a folded-electrode structure", Proceedings of the IEEE Micro Electro Mechanical Systems (MEMS), 1999, pp. 600-605

[34] H. Xie, G.K. Fedder, "CMOS z-axis capacitive accelerometer with comb-finger sensing", Proceedings of the IEEE Micro Electro Mechanical Systems (MEMS), 2000, pp. 496-501.

[35] H. Luo, G.K. Fedder, L.R. Carley, "1 mG lateral CMOS-MEMS accelerometer", Proceedings of the IEEE Micro Electro Mechanical Systems (MEMS), 2000, pp. 502-507.

[36] A. Salian, H. Kulah, N. Yazdi, G. He, and K. Najafi, "A hybrid silicon microaccelerometer system with CMOS interface circuit", Midwest Symposium on Circuits and Systems 1, 2000, pp. 228-231.

[37] H. Goldberg, J. Gannon, and J. Marsh, "An extremely low-noise micromachined accelerometer with custom ASIC circuitry," Sensors (Peterborough, NH) 18 (5), 2001, pp. 52-56.

[38] W. Su, M. Li, and X.-P. He, "Design and test of a low drift, low noise and large range micro-accelerometer", Proceedings of SPIE - The International Society for Optical Engineering 4591, 2001, pp. 281-291

[39] N. Takeda, “Ball Semiconductor Technology and Its Application to MEMS”, lEEE MEMS 2000, Miyazaki, pp. 11-16

[40] R. Toda, N. Takeda, T. Murakoshi, S. Nakamura, M. Esashi, "Electrostatically levitated spherical 3-axis accelerometer," Proceedings of the IEEE Micro Electro Mechanical Systems (MEMS), 2002, pp. 710-712.

[41] K. -H. Han, Y. -H. Cho, "Self-balanced navigation-grade capacitive microaccelerometers using branched finger electrodes and their performance for varying sense voltage and pressure," Journal of Microelectromechanical Systems, 2003, vol. 12 (1), pp. 11-20

[42] J. Chae, H. Kulah, K. Najafi, "An in-plane high-sensitivity, low-noise micro-g silicon accelerometer," Proceedings of the IEEE Micro Electro Mechanical Systems (MEMS), 2003, pp. 466-469

[43] H. Kulah, J. Chae, N. Yazdi, and K. Najafi, "A multi-step electromechanical ΣΔ converter for micro-g capacitive accelerometers," Digest of Technical Papers - IEEE International Solid-State Circuits Conference, 2003, pp. 191+202-203+488

[44] B.V. Amini, S. Pourkamali, F. Ayazi, "A 2.5V 14-bit ΣΔ CMOS-SOI capacitive accelerometer," Digest of Technical Papers - IEEE International Solid-State Circuits Conference 47, 2003, pp. 250-251+556

[45] J. Wu, G.K. Feeder, L.R. Carley, "A low-noise low-offset capacitive sensing amplifier for a 50-μg/√hz monolithic CMOS MEMS accelerometer," IEEE Journal of Solid-State Circuits, 2004, vol. 39 (5), pp. 722-730.

[46] B.V. Amini, S. Pourkamali, M. Zaman, and F. Ayazi, "A new input switching scheme for a capacitive micro-G accelerometer," IEEE Symposium on VLSI Circuits, Digest of Technical Papers (CIRCUITS SYMP.), 2004, pp. 310-313.

[47] T. Tsuchiya, and H. Funabashi, "A Z-axis differential capacitive soi accelerometer with vertical comb electrodes," Proceedings of the IEEE International Conference on Micro Electro Mechanical Systems (MEMS), 2004, pp. 524-527.

[48] J. Chae, H. Kulah, and K. Najafi, "A monolithic three-axis micro-g micromachined silicon capacitive accelerometer," Journal of Microelectromechanical Systems, 2005, vol. 14 (2), pp. 235-242.

[49] J. Chae, H. Kulah, and K. Najafi, "A CMOS-compatible high aspect ratio silicon-on-glass in-plane micro-accelerometer," Journal of Micromechanics and Microengineering, 2005, vol. 15 (2), pp. 336-345.

[50] H. Rödjegård, C. Johansson, P. Enoksson, and G. Andersson, "A monolithic three-axis SOI-accelerometer with uniform sensitivity," Sensors and Actuators, A: Physical 123-124, 2005, pp. 50-53.

[51] H. Ko, S. Park, B.-D. Choi, Y. Park, G. Lim, S.-J. Paik, A. Lee, K. Yoo, S. Lee, Y.K. Roh, and D.-I. Cho, "Two-chip implemented, wafer-level hermetic packaged accelerometer for tactical and inertial applications," Digest of Technical Papers - International Conference on Solid State Sensors and Actuators and Microsystems, TRANSDUCERS, 2005, art. no. 2E4.14, pp. 507-510.

[52] C. Weiping, H. Mingxue, L. Yumin, L. Xiaowei, Z. Ruichao, "A novel Z-axis capacitive accelerometer using SOG structure," 6th International Conference on Electronics Packaging Technology, 2005, art. no. 1564703.

[53] H. Yang, Z. Yu, X. Li, and Y. Wang, "A novel pull-in accelerometer based on cantilever beam mass structure," Proceedings of IEEE Sensors, 2005, art. no. 1597781, pp. 644-647.

[54] B. Bais, A. Ahanchian, and B.Y. Majlis, "A low-g bulk micromachined silicon accelerometer with area-changed differential capacitance," Proceedings of SPIE - The International Society for Optical Engineering 5836, 2005, art. no. 77, pp. 675-685

[55] Y. Liu, Z. Wen, Z. Wen, Z., L. Zhang, and H. Yang, "Design and fabrication of a high-sensitive capacitive biaxial microaccelerometer," Journal of Micromechanics and Microengineering, 2007, 17 (1), art. no. 005, pp. 36-41

[56] D. Fang, H. Qu, H. Xie, "A 1mW dual-chopper amplifier for a 50-μg/√Hz monolithic CMOS-MEMS capacitive accelerometer," IEEE Symposium on VLSI Circuits, Digest of Technical Papers, 2006, art. no. 1705311, pp. 59-60.

[57] Y. Wang, J. Jiao, F. Duan, Y. Zhang, B. Mi, J. Li, Q. Qian, and Y. Wang, "Design and fabrication of an accelerometer with novel '8-beams/mass' structure," Pan Tao Ti Hsueh Pao/Chinese Journal of Semiconductors, 2007, vol. 28 (5), pp. 783-788

[58] H. Hamaguchi, K. Sugano, T. Tsuchiya, O. Tabata, "A differential caeacitive three-axis SOI accelerometer using vertical comb electrodes," TRANSDUCERS and EUROSENSORS '07 - 4th International Conference on Solid-State Sensors, Actuators and Microsystems, 2007, art. no. 4300425, pp. 1483-1486.

[59] R. Abdolvand, B.V. Amini, and F. Ayazi, "Sub-micro-gravity in-plane accelerometers with reduced capacitive gaps and extra seismic mass," Journal of Microelectromechanical Systems, 2007, vol. 16 (5), pp. 1036-1043.

[60] M. Paavola, M. Kämäräinen, J. Järvinen, M. Saukoski, M. Laiho, and K. Halonen, "A 62μA interface ASIC for a capacitive 3-axis micro-accelerometer," Digest of Technical Papers - IEEE International Solid-State Circuits Conference, 2007, art. no. 4242393, pp. 318-319+605+301

[61] L. Aaltonen, P. Rahikkala, M. Saukoski, and K. Halonen, "Continuous time interface for ±1.5 g closed-loop accelerometer," Proceedings 2007 IEEE International Conference on Integrated Circuit Design and Technology, ICICDT, 2007, art. no. 4299571, pp. 187-190

[62] Y.W. Hsu, H.T. Chien, C.S. Lin, L.P. Liao, S. Chen, and P. Chang, "A capacitive low-g three-axis accelerometer," 2008 10th International Conference on Electronic Materials and Packaging, EMAP 2008, art. no. 4784294, pp. 325-328.

[63] A. Wung, R.V. Park, K.J. Rebello, and G.K. Fedder, "Tri-axial high-G CMOS-MEMS capacitive accelerometer array," Proceedings of the IEEE International Conference on Micro Electro Mechanical Systems (MEMS), 2008, art. no. 4443796, pp. 876-879

[64] C.-M. Sun, C. Wang, and W. Fang, "On the sensitivity improvement of CMOS capacitive accelerometer", Sensors and Actuators, A: Physical, 2008, vol. 141 (2), pp. 347-352.

[65] W. Huang, Z. He, L. Liu, Y. Zhong, K. Li, and W. Wu, "A±15V interface IC for capacitive accelerometer," International Conference on Solid-State and Integrated Circuits Technology Proceedings, ICSICT, 2008, art. no. 4734895, pp. 1761-1764.

[66] Y. Hirata, N. Konno, T. Tokunaga, M. Tsugai, and H. Fukumoto, "A new z-axis capacitive accelerometer with high impact durability," TRANSDUCERS 2009 - 15th

International Conference on Solid-State Sensors, Actuators and Microsystem , art. no. 5285908, pp. 1158-1161

[67] C.-P. Hsu, M.-C. Yip, and W. Fang, "A novel SOI Z-axis accelerometer with gap closing differential sensing electrodes," TRANSDUCERS 2009 - 15th International Conference on Solid-State Sensors, Actuators and Microsystems , art. no. 5285935, pp. 1154-1157

[68] L. Dong, H. Yan, W. Huo, L. Xu, Y. Li, and L. Sun, "A novel MEMS inertial sensor with enhanced sensing capacitors," Journal of Semiconductors, 2009, vol. 30 (5), art. no. 054003.

[69] C.-M. Sun, M.-H. Tsai, and W. Fang, "Design and implementation of a novel CMOS-MEMS single proof-mass TRI-axis accelerometer," Proceedings of the IEEE International Conference on Micro Electro Mechanical Systems (MEMS), 2009, art. no. 4805506, pp. 809-812

[70] C.-M. Sun, M.-H. Tsai, Y.-C. Liu, and W. Fang, W., "Implementation of a monolithic single proof-mass tri-axis accelerometer using CMOS-MEMS technique," IEEE Transactions on Electron Devices,2010, vol. 57 (7), art. no. 5467179, pp. 1670-1679

[71] Y. Dong, P. Zwahlen, A.-M. Nguyen, F. Rudolf, and J.-M. Stauffer," High performance inertial navigation grade sigma-delta MEMS accelerometer," Record - IEEE PLANS, Position Location and Navigation Symposium, 2010, art. no. 5507135, pp. 32-36

[72] C. Acar, PhD. Dissertation, University of California Irvine, 2004.

[73] J.Chae, H. Kulah, K. Najafi, “A Hybrid Silicon-On-Glass (SOG) Lateral Micro-Accelerometer”, 2002, pp.623-626.

[74] H. Kulah, J. Chae, N. Yazdi, K. Najafi, “Noise Analysis and Characterization of a Sigma-Delta Capacitive Microaccelerometer”, IEEE JSSC 2006, vol.41-2, pp. 352-361.

[75] M. Lemkin, B.E. Boser, “A Three Axis Micromachined Accelerometer with a CMOS Position-Sense Interface and Digital Offset-Trim Electronics”, IEEE JSSC 1999, vol. 34-4, pp.456-468.

[76] H. Kulah, J. Chae, N. Yazdi, and K. Najafi, "A multi-step electromechanical ΣΔ converter for micro-g capacitive accelerometers," Digest of Technical Papers - IEEE International Solid-State Circuits Conference, 2003, pp. 191+202-203+488

[77] R. Kepenek, PhD. Dissertation, METU, Feb. 2008.

[78] H. Seidel, L. Csepregi, “Design optimization for cantilever-type accelerometers”, Sensors and Actuators, 1984, vol. 6 (2), pp. 81-92.

[79] P. M. Aziz, H. V. Sorensen, J. V. Spiegel, “An overview of Sigma-Delta Converters – How a 1 bit ADC achieves more than 16-bit resolution”, IEEE Signal Processing Magazine, Jan’1996, pp.61-70.

[80] T. B. Gabrielson, “Mechanical-Thermal Noise in Micromachined Acoustic and Vibration Sensors”, IEEE Trans. Electron Dev., vol. 40, no. 5, pp. 903-909, 1993.

[81] V. Kaajakari, “Mechanical Noise in Microelectromechanical Systems”, MEMS Tutorial, http://www.kaajakari.net.

[82] H. Külah, J. Chae, K. Najafi, “Noise Analysis and Characterization of a Sigma-Delta Capacitive Silicon Microaccelerometer”, Transducers’03, pp. 95-98.

[83] Yazdi N and Najafi K “Performance limits of a closed-loop,micro-g silicon accelerometer with deposited rigid electrodes” Proc. Int. Conf. Microelectronics 2000, pp 313–316.

[84] Chae J, Kulah H and Najafi K “An in-plane high sensitivity, low noise micro-g silicon microaccelerometer with CMOS readout circuitry” IEEE J. Microelectromech. Syst. 2004, vol. 13, 628–635.

[85] V. P. Petkov, B. E. Boser, “Forth order $\Sigma-\Delta$ Interface for Micromachined Inertial Sensors”, IEEE Jour. of Solid-State Circuits'05, vol. 40-8, pp.1602-1609.

[86] J. Raman, P. Rombouts, L. Weyten, “An Unconstrained Architecture for Systematic Design of Higher Order $\Sigma-\Delta$ Force-Feedback Loops”, IEEE Trans on Circuits and Systems’08, vol55-6, pp.1601-1614.

[87] B. E. Boser, R. T. Howe, “Surface Micromachined Accelerometers”, IEEE Jour. of Solid State Circuits'96, vol. 31, pp.366-375

[88] G. HE and K. Najafi, “A Single Crystal Silicon Vibrating Gyroscope,” Proc. IEEE Micro Electro Mechanical Systems Workshop (MEMS’02), Las Vegas, CA, January 2002, pp. 718-721.

[89] J. Chae, H. Külah and K. Najafi, “A Hybrid Silicon-on-Glass (SOG) Lateral Micro-Accelerometer with CMOS Readout Circuitry,” Proc. IEEE Micro Electro Mechanical Systems Workshop (MEMS’02), Las Vegas, CA, January 2002, pp. 623-626.

[90] S. E. Alper, PhD. Dissertation, Middle East Technical University, 2005.

[91] J. C. Arnold, and H. H. Sawin, “Charging of Pattern Features During Plasma Etching,” J. Appl. Phys., vol.70, no. 10, pp. 5314-5317, November 1991.

[92] G. S. Hwang, and K. P. Giapis, “Aspect-Ratio-Dependent Charging in High-Density Plasmas,” J. Appl. Phys., vol. 82, no.2, pp. 566-571, July 1997.

[93] T. Kinoshita, M. Hane, and J. P. McVittie, “Notching as an Example of Charging in Uniform High Density Plasmas,” J. Vac. Sci. Technol. B, vol. 14, no. 1, pp. 560-565, January / February 1996.

[94] S. Horiuchi, and R. Blanchard, “Boron Diffusion in Polycrystalline Silicon Layers,” Solid-State Elecrtonics, vol. 18, no. 6, pp. 529-532, June 1975.

[95] R. B. Fair, “Boron diffusion in silicon-concentration and orientation dependence, background effects, and profile estimation,” J. Electrochem. Soc., vol. 122, pp. 800-805, June 1975.

[96] H. Seidel, L. Csepregi, A. Heuberger, and H. Baumgartel, “Anisotropic Etching of Crystalline Silicon in Alkaline Solutions, I. Orientation Dependence and Behavior of Passivation Layers” J. Electrochem. Soc., vol. 197, no. 11, pp. 3612-3625, November 1990.

[97] H. Seidel, L. Csepregi, A. Heuberger, and H. Baumgartel, “Anisotropic Etching of Crystalline Silicon in Alkaline Solutions, I. Orientation Dependence and Behavior of Passivation Layers” J. Electrochem. Soc., vol. 197, no. 11, pp. 3625-3632, November 1990.

[98] Wen Lin, Lower Macungie Toenship, Leigh Country, Pa, Stress relief in epitaxial wafer, United States Patent, 4,769,689, Sep. 6, 1988

[99] S. E. Alper, A. Aydemir and T. Akin, “Stepped Etching for Preserving Critical Dimensions in Through Wafer Deep Reactive Ion Etching of Thick Silicon”, in Proc. Transducers’09, Denver, CO, June 2009, pp. 1110-1113

[100] H. Siedel, “The Mechanism of Anisotropic Silicon Etching and Its Relevance for Micromachining”, in Proc. Transducers’87, Tokyo, Japan, June 1987, pp. 120-125

[101] M. A. Lemkin, B. E. Boser, D. Auslander and J. H. Smith, “A 3-Axis Force Balanced Accelerometer Using a Single Proof Mass”, in Proc. Transducers’ 97, Chicago, June 1997, pp. 1185-1188.

[102] J. Chae, H. Külah, K. Najafi, “A Monolithic Three-Axis Micro-g Micromachined Silicon Capacitive Accelerometer”, Jour. of Microelectromechanical Systems, Vol. 14, April 2005, pp. 235-242.

[103] S. Bütefisch, A. Schoft, and S. Büttgenbach, “Three-Axes Monolithic Silicon Low-g Accelerometer”, Jour. of Microelectromechanical Systems, Vol. 9, December 2000, pp. 551-556.

[104] G. I. Anderson, “A Novel 3-Axis Monolithic Silicon Accelerometer”, in Proc. Transducers’95, Stockholm, Sweden, June 1995, pp. 558-561

[105] R. Puers, S. Reyntjens, “Design and processing experiments of a new miniaturized capacitive triaxial accelerometer”, Jour. Sensors and Actuators A, Vol. 68, 1998, pp. 324-328

[106] M. A. Lemkin, M. A. Ortiz, N. Wongkomet, B. E. Boser and J. H. Smith, “A 3-Axis Surface Micromachined ΣΔ Accelerometer” in Proc. ISSCC’97, 1997.

[107] K.R. Williams, and R.S. Muller, "Etch Rates for Micromachining Processing," Jour. of Microelectromechanical Systems, 1996, vol. 5, no. 4, pp. 256-269.

[108] C.M. Mastrangelo, and C.H. Hsu, ”Mechanical stability and adhesion of microstructures under capillary forces—part I: basic theory,” J. Microelectromech. Syst., 1993, vol. 2, pp. 33–43.

[109] N. Tasy, T. Sonnenberg, H. Jansen, R. Legtenberg and M. Elwenspoek, "Stiction in surface micromachining," J. Micromech. Microeng., 1996, vol. 6, pp. 385–397